Subsurface Indicators of Active Faulting in the Central Strait of Georgia, British Columbia and Implications for Hazard and Risk

by

Anna A. Podhorodeski
B.Sc., University of Victoria, 2021

A Thesis Submitted in Partial Fulfillment of the
Requirements for the Degree of

MASTER OF SCIENCE

in the School of Earth and Ocean Sciences

© Anna A. Podhorodeski, 2025
University of Victoria

All rights reserved. This thesis may not be reproduced in whole or in part, by photocopying or other means, without the permission of the author.

We acknowledge with respect the Lək´ʷəŋən (Songhees and Esquimalt) Peoples on whose traditional territory the university stands, and the Lək´ʷəŋən and W̱SÁNEĆ Peoples whose historical relationships with the land continue to this day.

Subsurface Indicators of Active Faulting in the Central Strait of Georgia, British Columbia and Implications for Hazard and Risk

by

Anna A. Podhorodeski
B.Sc., University of Victoria, 2021

Supervisory Committee

Dr. Lucinda Leonard, Co-Supervisor
(School of Earth and Ocean Sciences)

Dr. Andrew Schaeffer, Co-Supervisor
(Geological Survey of Canada - Pacific and School of Earth and Ocean Sciences)

Dr. Tiegan Hobbs, Committee Member
(Geological Survey of Canada - Pacific and School of Earth and Ocean Sciences)

ABSTRACT

This thesis investigates whether previously unidentified active faulting occurs beneath the central Strait of Georgia, a region located between Metro Vancouver, Nanaimo, and British Columbia's Sunshine Coast. It also aims to evaluate the implications of such faulting for seismic and tsunami hazard in southwestern British Columbia. To address these objectives, ~2200 km of seismic reflection data are systematically interpreted to identify and catalogue subsurface evidence of active faulting across the study area. Fault interpretation is based on eight objective criteria: reflection offsets, reflection discontinuities, abrupt lateral changes in seismic unit, reflection truncations, associated folding and deformation, abrupt changes in dip, fault shadow, and fault plane reflections. Some criteria appear highly localized and unlikely to delineate structures, whereas others exhibit consistency and lateral continuity across multiple seismic reflection profiles and along linear trends. This analysis enables the delineation of the Central Salish Sea fault zone (CSSFZ; referred to previously as the Fraser Delta fault) beyond its previously mapped surface expression to a length of 12 km, with a possible extension up to 25 km. Subsurface evidence of active faulting is also present beneath a seafloor scarp offshore Bowen Island and a seafloor lineament near Gabriola Island.

Given the CSSFZ's proximity to densely populated areas of British Columbia, deterministic seismic hazard and risk modelling is conducted herein for various rupture scenarios. The CSSFZ's main strand is modelled with an average dip of ~75° southwest and strike of ~123°. Based on the fault's strike relative to the orientation of local maximum horizontal compressive stress (S_{Hmax}), the fault is presumed to accommodate oblique right-lateral slip with a reverse component, although scenarios ranging from pure right-lateral to pure reverse slip are considered. The most impactful modelled scenario – a magnitude 6.7 daytime oblique or reverse rupture – is projected to result in 1,300 deaths, 5,600 uninhabitable buildings, and $18.5 billion CAD (2019) in economic losses across southwest British Columbia due to ground shaking and building damage alone. These hazard and risk results establish a baseline assessment for a fault rupture offshore of Metro Vancouver; secondary hazards (e.g., aftershocks, liquefaction, fires, slope failures) and damage to critical infrastructure could result in further damage and casualties. In addition, the proximity of the CSSFZ to the Fraser River delta, an area prone to submarine slope failure, along with its potential for right-lateral oblique slip, suggests that a rupture may be tsunamigenic. Empirical relations indicate that seafloor displacement during a magnitude 6.7 rupture could generate damaging tsunami runups, with potential impacts for several coastal communities around the central Strait of Georgia. The results in this thesis have demonstrated hazard and risk

implications for southwest British Columbia. It is therefore recommended that the CSSFZ be incorporated into future seismic and tsunami hazard and risk assessments.

Table of Contents

Supervisory Committee ii

Abstract iii

Table of Contents v

List of Tables ix

List of Figures x

Acknowledgements xxiv

Dedication xxvi

Chapter 1 Introduction 1
1.1 Motivation and Objectives . . . 1
1.2 Outline . . . 5

Chapter 2 Background 6
2.1 Tectonic Setting and Geologic Context . . . 6
2.1.1 Regional Tectonic Setting . . . 6
2.1.1.1 Crustal Seismicity . . . 8
2.1.2 Geologic Context . . . 10
2.2 Previous Studies of Faults in the Central Strait of Georgia and Adjacent Areas . . . 13
2.2.1 Faults Within the Central Strait of Georgia Study Area . . . 14
2.2.1.1 Strait of Georgia Fault . . . 14
2.2.1.2 Central Salish Sea/Fraser Delta Fault . . . 18
2.2.2 Faults Adjacent to the Study Area . . . 20
2.2.2.1 Fraser River Delta Fault . . . 20
2.2.2.2 Outer Islands Fault . . . 20

Chapter 3 Seismic Reflection Interpretation Framework 23
3.1 Theory . . . 23
3.2 Fault Interpretation . . . 25
3.3 Seismic Unit and Horizon Interpretation . . . 30
3.3.1 Unit Descriptions . . . 31

Chapter 4 Near-Surface Indicators of Active Faulting in the Central Strait of Georgia, Canada 33
4.1 Abstract . . . 33
4.2 Introduction . . . 34
4.2.1 Motivation and Objectives . . . 34
4.2.2 Geologic/Glacial Context . . . 36
4.2.3 Tectonic Context . . . 36
4.2.4 Previous Work on Crustal Faults in the Central Strait of Georgia 37
4.3 Methods and Data . . . 38
4.3.1 Seismic Reflection Dataset . . . 38
4.3.1.1 Legacy Data and Geological Survey of Canada Holdings 39
4.3.1.2 Iona Spit Sub-Bottom Dataset . . . 41
4.3.1.3 3D Seismic Dataset (2002002PGC) . . . 42
4.3.2 Additional Data Sources . . . 42
4.3.3 Seismic Interpretation Framework . . . 43
4.3.3.1 Active Fault Interpretation Criteria . . . 43
4.3.3.2 Seismic Units . . . 44
4.3.4 Data and Methodological Considerations . . . 45
4.4 Results . . . 46
4.4.1 Subarea 1: Fraser Prodelta . . . 49
4.4.1.1 Evidence for Faulting Beneath Escarpment . . . 50
4.4.1.2 Pockmark Chain . . . 51
4.4.1.3 Relationship between Fault Traces - Interpreted Flower Structure . . . 54
4.4.2 Subarea 2: Sturgeon Bank . . . 58
4.4.3 Subarea 3: Point Grey Dredge Disposal Area . . . 59
4.4.4 Subarea 4: Offshore NE Gabriola Island and Vicinity of the 1997 and 1975 Earthquake Clusters . . . 64
4.4.5 Subarea 5: Halibut Bank . . . 65
4.5 Discussion . . . 68
4.5.1 Study Limitations . . . 68
4.5.2 Hazard Implications . . . 69
4.6 Conclusions . . . 70

Chapter 5 Characterization of the Central Salish Sea Fault near Vancouver, Canada 71
5.1 Abstract . . . 71
5.2 Introduction . . . 72
5.2.1 Tectonic Setting . . . 74
5.2.2 Previous Studies . . . 75
5.2.3 Linear Pockmark Chains and Their Relationship to Subsurface Faults . . . 76
5.3 Data and Methods . . . 77
5.3.1 Multibeam Bathymetry and Water Column Data . . . 77
5.3.2 Seismic Hazard and Risk Calculations . . . 78

5.4 Results and Discussion . . . 79
5.4.1 Seafloor Pockmarks . . . 79
5.4.1.1 Pockmark Morphology and Venting . . . 79
5.4.1.2 Hazards Associated with Pockmarks . . . 81
5.4.2 Fault Characterization and Input Parameters . . . 82
5.4.2.1 Lateral Extent, Strike, and Dip . . . 82
5.4.2.2 Faulting Mechanism and Rake . . . 84
5.4.2.3 Seismogenic Depth . . . 85
5.4.3 Seismic Hazard and Risk . . . 86
5.4.4 Implications for Tsunami Hazard . . . 91
5.4.4.1 Shaking-Induced Slope Failures . . . 91
5.4.4.2 Seafloor Tectonic Offset . . . 92
5.5 Conclusions . . . 94

Chapter 6 Process and Rationale for Fault Renaming 96
6.1 Indigenous Name Usage in Geoscience Publications . . . 96
6.2 Central Salish Sea Fault . . . 97
6.2.1 Engaging Indigenous Communities and Interim Renaming . . . 98
6.2.2 Initial Letter to Nations . . . 99

Chapter 7 Conclusions 100
7.1 Summary . . . 100
7.2 Recommendations for Future Work . . . 101
7.2.1 Hazard and Risk Assessment . . . 101
7.2.2 Estimates of Fault Recurrence / Slip Rate . . . 102
7.2.3 Additional Data Analysis for Marine Faults . . . 104
7.2.4 Sub-bottom Surveying and Coastal Studies . . . 104
7.2.5 Additional Seismic Reflection Data Collection . . . 105

Bibliography 108

Appendix A Interpretations of Seismic Reflection Data 123
A.1 Preliminary Information . . . 123
A.2 Data and Interpretations . . . 124
A.2.1 Cruise ID 82003PGC . . . 124
A.2.2 Cruise ID 86008PGC . . . 149
A.2.3 Cruise ID 89010PGC . . . 154
A.2.4 Cruise ID 91004PGC . . . 160
A.2.5 Cruise ID 91008PGC . . . 165
A.2.6 Cruise ID 95001PGC . . . 168
A.2.7 Cruise ID 2002002PGC . . . 168
A.2.8 Cruise ID 2003002PGC . . . 195
A.2.9 Cruise ID 2009009PGC . . . 197
A.2.10 Cruise ID 2013003PGC . . . 200
A.2.11 Cruise ID 2023004PGC . . . 204

A.2.12 Cruise ID 2024006PGC (Iona Spit Sub-bottom Dataset) 205

Appendix B Input Files for Seismic Hazard and Risk Models 220
B.1 Input Files for M 6.3 Strike-Slip Scenario 220
B.2 Input Files for M 6.3 Oblique/Reverse Scenario 223
B.3 Input Files for M 6.7 Strike-Slip Scenario 227
B.4 Input Files for M 6.7 Oblique/Reverse Scenario 231

List of Tables

Table 5.4.1 Summary of input parameters for all modelled fault rupture scenarios. 86
Table 5.4.2 Key results for seismic hazard and risk for CSSF scenarios.[1] . . . 88
Table 5.4.3 Calculated local mean and maximum tsunami runups for select locations near the central SoG for two CSSF rupture scenarios.[2] 93

List of Figures

Figure 1.1.1 Tectonic map of the Cascadia subduction zone. The study area location is indicated with a yellow box. Volcanoes are shown as red triangles. The direction of Juan de Fuca plate motion relative to North America is shown with a black arrow (DeMets et al., 2010). Basemap created from GEBCO (2020) data. 2

Figure 1.1.2 Map showing locations of earthquakes and sediment core studies discussed in Chapters 1 and 2. Large (M>7) earthquakes are indicated with orange stars, while moderate-magnitude earthquakes within the study area are shown with a yellow star. Recent earthquakes around the Salish Sea are indicated with red stars. Basemap created from GEBCO (2020) data. . 3

Figure 1.1.3 Map of the study area (red box) and surrounding locations. UBC: University of British Columbia campus; YVR: Vancouver International Airport. 4

Figure 2.1.1 Schematic tectonic map illustrating the Washington (green), Oregon (pink), and Sierra Nevada (purple) blocks of the Cascadia forearc (from Wells et al., 1998). Triangles indicate locations of major volcanoes along the Cascade volcanic arc. Arrows indicate motion relative to a stable North America. . . 7

Figure 2.1.2 Geodetic, seismicity, and stress data in northern Cascadia (from Harrichhausen et al., 2021). A: Juan de Fuca plate motion with respect to North America shown in black arrows (DeMets et al., 2010), as well as GNSS-derived clockwise (navy) and counterclockwise (red) rotations on the southern and northern sides, respectively, of the Olympic Mountains (Finley et al., 2019). B: GNSS velocity data along the Cascadia forearc illustrating a decrease in northward velocity across the Olympic Mountains (Mazzotti et al., 2002). C: Crustal seismicity from January 1970 to April 2015, S_{Hmax} directions from inversion of crustal earthquake mechanisms shown as pairs of black arrows (Balfour et al., 2011). 8

Figure 2.1.3 Approximate ice flow directions in southwest BC and northwest Washington during the Last Glacial Maximum and glacial extents at the end of and following the Fraser Glaciation (9500, 12000, and 15000 BP). Modified from Figures 4 and 5 of Clague and James (2002). 11
Figure 2.1.4 Seafloor relief illustrating prominent glacial features in the central SoG including Halibut and McCall Banks. A fault and associated pockmark chain display a similar northwest-southeast trend. The approximate extent of the Fraser River delta (FRD) is shown with a black dotted line (adapted from LaCroix et al., 2024). Inset image indicates the main map extent with a black box. Metro Vancouver and Nanaimo are indicated with red dots. Modified from Figure 6 of Barrie et al. (2005). 12
Figure 2.2.1 Map of the Strait of Georgia showing known faults. Faults are shown in black, with inferred faults indicated by dashed lines. Faults within or trending towards the Central SoG are labelled. CSS/FD fault: Central Salish Sea/Fraser Delta fault. The central SoG study area is indicated with a red polygon. . 14
Figure 2.2.2 Map of shallow ($<$ 6 km depth) crustal earthquakes in the northern Cascadia forearc from 1975-1999 (from Cassidy et al., 2000). Note the seismicity in the central SoG, including earthquake sequences in 1975 and 1997. From Cassidy et al. (2000). 15
Figure 2.2.3 Map of the SHIPS multichannel seismic (MCS) line, aeromagnetic data, and crustal seismicity (adapted from Mosher et al., 2000). Areas of interest along the line are denoted A-A' and B-B' and are shown in Figure 2.2.4. Aeromagnetic data range from -500 nT to +1660 nT (black to white). A magnetic high resultant from strong interference of an underwater cable is labelled as MH. Crustal seismicity is shown with grey dots. . . 16
Figure 2.2.4 Seismic reflection data and interpretations of SHIPS data (adapted from Figures 2a and 4d of Mosher et al., 2000). Line locations are shown in Figure 2.2.3. Line A-A‘ shows seismic data (upper) and interpretations (lower) corresponding to data within the central Strait of Georgia study area. Deformation zone 2 (DZ2) is located near the 1997 sequence. Line B-B‘ shows a zoomed and depth-migrated seismic section over an area of significant bedrock faulting and deformation near the approximate area of the 1997 earthquake sequence. Abbreviations: DZ - deformation zone; Unit 1 - Bedrock; Unit 2 - Glacial deposits; Unit 3 - Glacial outwash turbidite sequences; Unit 4 - Fraser River deposits. 17

Figure 2.2.5 Seafloor relief and contours (blue; metres below sea level) showing a scarp and large pockmark chain (adapted from Barrie and Hill, 2004). Additional smaller pockmark chains and randomly oriented features are also present. Locations of follow-up seismic reflection profiles are indicated with thick black lines. 18
Figure 2.2.6 Airgun seismic reflection data over fault-related features (adapted from Barrie and Hill, 2004). Locations shown in Figure 2.2.5. A) Apparent offset of Holocene and Pleistocene strata beneath the seafloor scarp. B) Profile over the linear pockmark chain, showing a notable increase in acoustic turbidity southwest of the feature. Adapted from Barrie and Hill (2004). 19
Figure 2.2.7 Seismic reflection data identifying the Outer Islands Fault. Modified from Figure 14 of England and Bustin (1998) to more clearly display boundaries between units. Cretaceous unit (Nanaimo Group sedimentary strata) is shown in yellow; Tertiary unit (non-marine sedimentary Huntingdon formation) is shown in green; Quaternary deposits are shown in blue. Note the lack of Quaternary sediment coverage over the fault, which prevents an assessment of Quaternary offsets or deformation at this location. 22

Figure 3.1.1 A) Schematic diagram of marine seismic reflection data acquisition. Hypothetical seismic ray paths are shown in black. Waves propagate from a seismic source towed behind a vessel (shown as a yellow dot). These waves reflect off the seafloor and subsequent layers, before returning to the surface where they are received by an array of hydrophones (shown as blue dots). B) Resultant seismic reflection profile. Black lines indicate interpreted faults, purple arrow indicates the seafloor reflection, red arrow indicates a high amplitude reflection off of a strong bedrock reflector, and the yellow arrow indicates an unconformity. C) A high contrast in acoustic impedance (Z) between seawater ($\rho_1 V_{p1}=Z_1$) and seafloor sediment ($\rho_2 V_{p2}=Z_2$), represented by the reflection coefficient (RC), results in the high amplitude seafloor reflection visible in B. From Crutchley and Kopp (2018). 24

Figure 3.2.1 Examples of fault identification criteria in seismic reflection data (adapted from Brandes et al., 2022). Faults are delineated in the lower images with black lines. Yellow arrows show the sense of movement. A) Offset reflectors, shown with yellow circles, are used to identify the location of multiple faults. Given the downward displacement of hanging wall strata, the faults are interpreted as normal faults. B) Discontinuities, indicated with a yellow oval, imply the presence of a fault. C) Dimmed reflectors near bottom of the image are characteristic of fault shadow, labelled in the lower image in yellow. C also shows an abrupt change in seismic facies indicated with two black arrows. 26
Figure 3.2.2 Uninterpreted (left) and interpreted (right) multichannel seismic reflection profiles (from Han et al., 2016). Fault plane reflections are shown in pink. Dashed lines indicate weak reflections. Blue and green lines indicate the seafloor and top of basement, respectively. The Moho is shown in red. 28
Figure 3.2.3 A fault, indicated with a black line, interpreted based on reflector truncations in a cross-bedded unit paired with an abrupt change in seismic facies from a well-layered, cross-bedded unit in the north contrasted with an acoustically transparent unit to the south (from Greene and Barrie, 2020). . . . 28
Figure 3.2.4 Uninterpreted (A) and interpreted (B) seismic profile of a fault and fault propagation fold (adapted from Misra, 2018). The fault is indicated with dark orange. Clearly offset and folded horizons are delineated in B. 29
Figure 3.2.5 Uninterpreted (A) and interpreted (B) seismic profile illustrating a set of closely-spaced normal faults (modified from Butler, 2021). Short monoclinal folds can be seen throughout (e.g., dark blue boxes in A). Areas that may contain faults with spacing or offsets too small to resolve, apparent as successive small monoclinal folds, are highlighted with dotted light blue boxes in A. Interpreted faults are indicated in B. . . 30
Figure 3.3.1 Simplified summary of seismic units with example images and geological interpretations. UPG: upper post-glacial, LPG: lower post-glacial (top of unit indicated with orange arrow), G: glacial, B: bedrock. 32

Figure 4.2.1 Tectonic setting in northern Cascadia. a) Overview of Cascadia subduction zone and Juan de Fuca plate motion with respect to North America (black arrow; DeMets et al., 2010). b) Study area within the SoG (red box) with crustal seismicity (grey dots; S and A grade events from Merrill et al., 2022) and epicentral location of the 1997 earthquake cluster (black star). Approximate extent of the Fraser River delta is shown with a black dotted line (La Croix et al., 2024). c) 5-m resolution multibeam bathymetry from 2000 detailing fault-related morphology first identified in Barrie and Hill (2004). Basemap created from Kung et al. (2023) and GEBCO (2020). 35
Figure 4.3.1 Map of ship track lines for all seismic reflection profiles. Dark purple, light and dark orange lines represent data collected digitally; light purple lines represent digitized analogue legacy data. Study area extent indicated with grey polygon. 39
Figure 4.4.1 Spatial distribution of indicators of potential faults identified across the central SoG, categorized by fault criteria. A) Reflection discontinuities (yellow teardrops), B) reflection truncations (green circles), C) apparent reflection offsets (orange triangles), D) associated folds and deformation (deep blue four-point stars), E) abrupt change in seismic facies (red asterisks), F) abrupt change in dip (light blue diamonds). Seismic reflection profile locations are denoted by white lines. 47
Figure 4.4.2 Simplified fault map based on seismic reflection and MBES interpretations. Inferred faults are indicated with dashed lines. References to relevant subsections for each segment are denoted within the figure. 48
Figure 4.4.3 Map of subarea locations discussed in sections 4.4.1-4.4.5. 1) Fraser Prodelta, 2) Sturgeon Bank, 3) Point Grey Dredge Disposal Area, 4) Offshore NE Gabriola Island and Vicinity of the 1997 and 1975 Earthquake Clusters, 5) Halibut Bank. 48
Figure 4.4.4 Fraser Prodelta subarea and seismic reflection data coverage (white lines). The locations of Figures 4.4.5 to 4.4.13 are indicated with coloured lines in the main map and inset. . . . 49
Figure 4.4.5 3.5 kHz sub-bottom profile along the pockmark chain of the CSSF. Line 19 from cruise 2023004PGC. A) Interpreted profile showing upper post-glacial unit (horizon marked in yellow at seafloor) with significant acoustic turbidity and multiple pockmarks. B) Uninterpreted profile. See Figure 4.4.4 for location. 50
Figure 4.4.6 MBES data over the seafloor scarp, main pockmark chain and associated field. Line locations (white lines) and extent of main figure (black box) are shown in inset map. 50

Figure 4.4.7 Huntec (external receiver) seismic reflection profile across the seafloor scarp. Line A5-B7 from cruise 91004PGC. A) Interpreted profile showing an inferred fault (purple) beneath the seafloor scarp. Tops of upper post-glacial and glacial units are shown in yellow and red, respectively. B) Uninterpreted profile. See Figure 4.4.4 for location. 51
Figure 4.4.8 Airgun seismic reflection profile located approximately 2 km east of the scarp. Profile is from the transit between lines 473 and 474 from cruise 91008PGC; note the start of line 474 is hand-written on the profile as 'SOL 474'. A) Interpreted profile showing a possible fault (purple) based on reflection truncations. Tops of upper post-glacial and glacial units are shown in yellow and red, respectively. B) Uninterpreted profile. See Figure 4.4.4 for location. 52
Figure 4.4.9 Airgun seismic reflection profile located approximately 3 km southeast of the scarp. Line Fraser Bowen from cruise 82003PGC. A) Interpreted profile showing an possible fault (purple) based on reflection truncations across multiple seismic units. Additional inferred faults are based on reflection discontinuities, truncations, and associated deformation. Horizon interpretations are shown in yellow (top of upper post-glacial), orange (top of lower post-glacial), red (top of glacial), and blue (top of bedrock). B) Uninterpreted profile. See Figure 4.4.4 for location. 53
Figure 4.4.10 Huntec (A, B) and airgun (C, D) seismic reflection profiles crossing perpendicularly over the pockmark chain. Line 60 from cruise 2002002PGC. Horizon interpretations are shown in yellow (top of upper post-glacial), orange (top of lower post-glacial), red (top of glacial), and blue (top of bedrock). A) Interpreted Huntec profile showing an interpreted fault (purple). Pockmarks are evident on the seafloor, and acoustic turbidity increases southwest of the interpreted fault contact. Locally brightened reflections are indicated with a black double-pointed arrow. B) Uninterpreted Huntec profile. C) Interpreted airgun profile showing the same interpreted fault, as well as additional deeper faults not resolved in the Huntec profile (purple). Inferred faults are based on reflection discontinuities, truncations, and apparent offsets. Note increased signal degradation with depth beneath areas with high acoustic turbidity, which partially or fully obscures underlying units. D) Uninterpreted airgun profile. See Figure 4.4.4 for location. . . 54

Figure 4.4.11 Airgun seismic reflection profiles located approximately 2.5-4.5 km west of the scarp. Lines 19 (east, i) and 20 (west, ii) from cruise 82003PGC. A) Profile showing interpreted faults (purple) associated with the proposed fault zone. Horizon interpretations are shown in yellow (top of upper post-glacial), orange (top of lower post-glacial), red (top of glacial), and blue (top of bedrock). B) Uninterpreted profile. See Figure 4.4.4 for location. 55
Figure 4.4.12 Huntec (external receiver) seismic reflection profile across the pockmark chain and seafloor scarp. Line 99 from cruise 2002002PGC. A) Interpreted profile showing an inferred fault (purple) beneath a seafloor scarp. The tops of upper post-glacial and glacial units are shown in yellow and red, respectively. Upper post-glacial deformation and upward bending of the seafloor is apparent between the scarp and pockmark chain. Note acoustic turbidity and local brightened reflections southwest of the inferred fault contact. B) Uninterpreted profile. See Figure 4.4.4 for location. 56
Figure 4.4.13 Airgun seismic reflection profile across the pockmark chain and seafloor scarp. Line 18 from cruise 83002PGC. A) Interpreted profile showing an inferred flower structure and faults (purple) between a scarp and a pockmark chain. The tops of upper post-glacial and glacial units are shown in yellow and red, respectively. Upper post-glacial deformation and upward bending of the seafloor is apparent between the scarp and the pockmark chain. B) Uninterpreted profile. See Figure 4.4.4 for location. 57
Figure 4.4.14 LiDAR and sub-bottom data along the Sturgeon Bank subarea. A) Regional map showing the location of profile C (red line), other seismic reflection profiles (white lines) and the extent of B. B) Zoomed view of LiDAR data collected offshore of Vancouver in 2021, with the location of profile C shown in red. Note the bedforms visible in surface morphology. C) Sub-bottom profile (Line U5) along the Sturgeon Bank subarea exhibiting gently inclined and variably dipping reflections in the upper $\sim$10 ms. Yellow marks the top of the upper post-glacial unit (seafloor). Line U5 is shown to represent the subarea, as it exhibits minimal noise and is in an area of complete LiDAR coverage. Data along strike of the CSSF are similar but lack full LiDAR coverage. 58

Figure 4.4.15 MBES data and line locations over the Point Grey Dredge Disposal Subarea. Profiles shown in subsequent figures are indicated with red, yellow, and orange lines. A) Overview map illustrating locations of all seismic profiles (white). B) Geomorphology of subarea, with key features indicated. Profiles shown in subsequent figures are delineated; other lines are omitted to avoid obscuring geomorphic features. 60
Figure 4.4.16 Airgun seismic reflection profile across a pockmark and lineament. This profile is from line 207 of cruise 89010PGC. A) Profile showing interpreted faults or fluid conduits (purple). Tops of upper post-glacial, lower post-glacial, glacial, and bedrock units are shown in yellow, orange, red, and blue, respectively. B) Uninterpreted profile. See Figure 4.4.15 for profile location. 61
Figure 4.4.17 Airgun seismic reflection profile across pockmark and lineament. Line 471, 472 and turn from cruise 91008PGC. A) Interpreted profile showing inferred fluid conduits (purple). Tops of upper post-glacial and glacial units are indicated in yellow and red, respectively. B) Uninterpreted profile. See Figure 4.4.15 for profile location. 62
Figure 4.4.18 Huntec external seismic reflection profile across seafloor scarp. Line A7-B8 from cruise 91004PGCPGC. A) Interpreted profile showing a fault (purple) interpreted based on truncated upper post-glacial and glacial reflections, along with deformed upper post-glacial reflections. Tops of upper post-glacial and glacial units are shown in yellow and red, respectively. B) Uninterpreted profile. See Figure 4.4.15 for profile location. . . 63
Figure 4.4.19 Map of MBES data and seismic reflection lines discussed in the text. A) Regional map showing seismic reflection lines (white) analysed for this study. Locations for Figures 4.4.20 (Line 25R, 82003PGC) and 4.4.21 (Line 24, 82003PGC) are shown in orange and red, respectively. The location of the 1997 mainshock is shown with a black star. B) Zoomed-in view of MBES data offshore Gabriola Island, highlighting seafloor geomorphology. Seismic reflection lines are omitted to enhance clarity of the seafloor, except for those shown in Figures 4.4.20 and 4.4.21 (orange and red, respectively). White arrow indicates the location of apparent offsets interpreted in seismic reflection data. Black dashed line illustrates the location of a mapped fault on Gabriola Island (from Denny et al., 2007; Muller and Jeletzky, 1970). 65

Figure 4.4.20 Airgun seismic reflection profile offshore Gabriola Island, zoomed to illustrate features mentioned in the text. Line 25R from cruise 82003PGC. A) Interpreted profile showing inferred faults (purple). The southwesternmost fault, located approximately 7 km from Gabriola Island, exhibits apparent offsets in upper post-glacial, glacial, and bedrock units (yellow, red, and blue, respectively). The top of the lower post-glacial unit is denoted in orange. A digitizing artifact, which creates false offsets, is marked with an arrow. The region near the 1997 earthquake cluster is indicated with a double-pointed arrow. B) Uninterpreted profile. See Figure 4.4.19 for location. 66

Figure 4.4.21 Airgun seismic reflection profile spanning the width of the SoG. Line 24 from cruise 82003PGC. A) Interpreted profile showing inferred faults (purple) along strike of the Central Salish Sea fault zone (left) and approximately 3 km SW of the 1997 SoG earthquake sequence (rightmost faults). Tops of upper post-glacial, lower post-glacial, glacial, and bedrock units are shown in yellow, orange, red, and blue, respectively. The region over the 1997 earthquake cluster is indicated with a double-pointed arrow. B) Uninterpreted profile. See Figure 4.4.19 for location. 67

Figure 5.2.1 A) Tectonic setting of Cascadia. Plate motion with respect to North America is indicated with a black arrow (DeMets et al., 2010). Volcanoes are shown as red triangles. B) Regional map of southwest BC and northwest Washington. Locations for earthquakes discussed in text are shown as asterisks. CSSFZ: Central Salish Sea fault zone. 73

Figure 5.4.1 MBES survey extents are indicated with white, green, red, and black dashed lines for the 2023, 2021, 2010 and 2000 datasets, respectively. A) Location map, indicating the location of panel B with respect to Metro Vancouver. Basemap modified from Kung et al. (2023). B) Multibeam bathymetry datasets over the linear pockmark chain. The extent of the original survey, collected in 2000, covers the entirety of the subfigure, whereas the 2010 and 2021 surveys lack data for the northwestern part of the pockmark chain. C) Difference map, calculated from the 2023 and 2000 datasets. Features interpreted as new pockmarks having developed since the 2000 survey are indicated with white arrows. Map extent matches the extent of the 2023 survey, indicated in panels A and B. . . 80

Figure 5.4.2 Simplified extent of the CSSF based on interpretations of active fault indicators in Chapter 4. Fault segment traces are shown with solid black lines. The fault's inferred extension to the northwest is shown with a dashed black line. Orientation of local maximum horizontal compressive stress is shown with black arrows (Balfour et al., 2011). Basemap modified from Kung et al. (2023). YVR: Vancouver International Airport; UBC: University of British Columbia campus. 83
Figure 5.4.3 Distribution of earthquake events by depth in the central Strait of Georgia study area. Seismicity data from the REST catalogue (Merrill et al., 2022). 85
Figure 5.4.4 Seismic hazard maps for each daytime CSSF rupture scenario. Ground shaking values were converted to the MMI scale from mean PGA based on empirical relationships outlined in Worden et al. (2012). Canada-US border is shown with a dotted black line. Simplified fault traces for each scenario are indicated with an orange line. Seismic hazard results were not calculated for areas outside of Canada. Areas beyond the map extent are expected to experience MMI values of 0-IV, corresponding to no to light perceived shaking and no expected damage. G: Gibsons; GI: Gabriola Island; MV: Metro Vancouver; N: Nanaimo; SC: Sunshine Coast; UBC: University of British Columbia Campus; V: Valdes Island; YVR: Vancouver International Airport. 87
Figure 5.4.5 Modelled results summarized by census subdivision for the most (right panels; b, d, f) and least (left panels; a, c, e) impactful modelled daytime scenarios. For all panels, a simplified fault trace is denoted with a black line, and the Canada-US border is shown with a dotted line. A and B: Number of buildings in a state of complete damage. C and D: Estimated deaths. E and F: Estimated economic losses. Dollar values are in Canadian currency as of 2019. 89
Figure 5.4.6 Estimated hospital demand for the 10 most impacted census subdivisions. Results are summarized for the magnitude 6.3 strike-slip and magnitude 6.7 oblique/reverse daytime scenarios. Note that Greater Vancouver A corresponds to the UBC campus. Values are rounded to the closest ten. 90
Figure 5.4.7 Zone for potentially damaging tsunami waves, based on empirical relations from Abe (1995) assuming an M_W 6.7 event. Areas within the blue polygon may experience a local maximum runup of $\geq$1.5 m. Fault trace is shown as a black line. Basemap modified from Kung et al. (2023). 94

Figure A.2.1 Lines 13 and 14, cruise 82003PGC 124
Figure A.2.2 Line 14 A, cruise 82003PGC 125

Figure A.2.3 Line 15, cruise 82003PGC. Excluded from results due to discrepancies between the seafloor reflector in profile and seafloor relief in MBES data, suspected navigation and/or georeferencing errors. . . . 126
Figure A.2.4 Line 16, cruise 82003PGC . . . 127
Figure A.2.5 Line 17, cruise 82003PGC . . . 127
Figure A.2.6 Line 18, cruise 82003PGC . . . 128
Figure A.2.7 Lines 19 and 20, cruise 82003PGC . . . 129
Figure A.2.8 Lines 21 and 22, cruise 82003PGC . . . 130
Figure A.2.9 Line 23, cruise 82003PGC . . . 131
Figure A.2.10 Line 24, cruise 82003PGC . . . 131
Figure A.2.11 Line 25R, cruise 82003PGC. Black line indicates the extent of detailed profile shown in Figure A.2.12. . . . 132
Figure A.2.12 Magnified profile of line 25R near Gabriola Island and the 1975/1997 Strait of Georgia earthquake clusters. . . . 133
Figure A.2.13 Line 26, cruise 82003PGC . . . 134
Figure A.2.14 Line 27, cruise 82003PGC . . . 135
Figure A.2.15 Line 28, cruise 82003PGC . . . 136
Figure A.2.16 Lines 29 and 30, cruise 82003PGC . . . 137
Figure A.2.17 Line 31, cruise 82003PGC . . . 138
Figure A.2.18 Line 32, cruise 82003PGC . . . 139
Figure A.2.19 Line 33, cruise 82003PGC . . . 140
Figure A.2.20 Line 34, cruise 82003PGC . . . 141
Figure A.2.21 Line 35, cruise 82003PGC . . . 142
Figure A.2.22 Line 36, cruise 82003PGC . . . 143
Figure A.2.23 Line 37, cruise 82003PGC . . . 144
Figure A.2.24 Line Fraser Bowen, cruise 82003PGC . . . 145
Figure A.2.25 Line Gabriola (Part 1), cruise 82003PGC. Line has been cropped to match study area; full line extends further northwest. . . . 146
Figure A.2.26 Line Gabriola (Part 2), cruise 82003PGC . . . 147
Figure A.2.27 Line McCall, cruise 82003PGC . . . 148
Figure A.2.28 Line 25, cruise 86008PGC . . . 149
Figure A.2.29 Line 36, cruise 86008PGC . . . 150
Figure A.2.30 Lines 41-49 (Part 1), cruise 86008PGC . . . 151
Figure A.2.31 Lines 41-49 (Part 2), cruise 86008PGC . . . 152
Figure A.2.32 Lines 41-49 (Part 3), cruise 86008PGC . . . 153
Figure A.2.33 Lines 41-49 (Part 4), cruise 86008PGC . . . 153
Figure A.2.34 Profile 151-743 (Section 1), cruise 89010PGC. Profile cropped to study area; full profile originates in the Strait of Georgia (Section 1), extends into Howe Sound, returns to the central Strait of Georgia (subsequent figure; Section 2), and continues further south.Thick vertical lines along top of profile indicate locations of turns and transits between straight sections. . . . 154

Figure A.2.35 Line 151-743 (Section 2), cruise 89010PGC. Profile cropped to study area; full profile originates in the Strait of Georgia (previous figure; Section 1), extends into Howe Sound, returns to the central Strait of Georgia (Section 2), and continues further south. Thick vertical lines along top of profile indicate locations of turns and transits between straight sections. . . . 155
Figure A.2.36 Line 126, cruise 89010PGC. Line located along Fraser River delta slope; Reflector truncations and discontinuities are interpreted as heavily reworked delta sediments. Profile is cropped to study area; full profile extends further south. 156
Figure A.2.37 Line 207, cruise 89010PGC. Thick vertical lines along top of profile indicate locations of line turns and transits between straight sections. Black horizontal double-ended line indicates the extent of detailed profile shown in Figure A.2.38. Profile is cropped to study area; full profile extends NE into Howe Sound. 157
Figure A.2.38 Magnified profile of line 207, cruise 89010PGC 158
Figure A.2.39 Line 221, cruise 89010PGC. Profile is cropped to study area; full profile continues further south and further west. 159
Figure A.2.40 Line A5-B7, cruise 91004PGC. Line is cropped to study area; full line extends further south. Black line indicates the extent of detailed profile shown in Figure A.2.42 160
Figure A.2.41 Line A7-B8, cruise 91004PGC. Line is cropped to study area; full line extends further south. Black line indicates the extent of detailed profile shown in Figure A.2.43 161
Figure A.2.42 Magnified profile of line A5-B7, cruise 91004PGC 162
Figure A.2.43 Magnified profile of line A7-B8, cruise 91004PGC 162
Figure A.2.44 Line A8-B11, cruise 91004PGC. Line is cropped to study area; full profile extends further south. Excluded from results due to discrepancies between the seafloor reflector in profile and seafloor relief in MBES data, suspected navigation and/or georeferencing errors. 163
Figure A.2.45 Lines 470, 471, 472, and 473, cruise 91008PGC. Black line indicates the extent of detailed profile shown in subsequent figure. 164
Figure A.2.46 Magnified profile of line 471, cruise 91008PGC 165
Figure A.2.47 Lines 474, 475, 476, and 477, cruise 91008PGC. Black line indicates the extent of detailed profile shown in subsequent figure. 166
Figure A.2.48 Magnified profile of line 474, cruise 91008PGC 167
Figure A.2.49 Line 4b, cruise 95001PGC. Profile is cropped to study area; full profile extends further south. 168
Figure A.2.50 Line 10 (Huntec DTS external), cruise 2002002PGC 169
Figure A.2.51 Line 10 (Huntec DTS internal), cruise 2002002PGC 170
Figure A.2.52 Line 10 (airgun), cruise 2002002PGC 171

Figure A.2.53 Line 30 (Huntec DTS external), cruise 2002002PGC 172
Figure A.2.54 Line 30 (Huntec DTS internal), cruise 2002002PGC 173
Figure A.2.55 Line 30 (airgun), cruise 2002002PGC 174
Figure A.2.56 Line 40 (Huntec DTS external), cruise 2002002PGC 175
Figure A.2.57 Line 40 (Huntec DTS internal), cruise 2002002PGC 176
Figure A.2.58 Line 40 (airgun), cruise 2002002PGC 177
Figure A.2.59 Line 50b (Huntec DTS external), cruise 2002002PGC 178
Figure A.2.60 Line 50b (Huntec DTS internal), cruise 2002002PGC 179
Figure A.2.61 Line 50b (airgun), cruise 2002002PGC 180
Figure A.2.62 Line 60 (Huntec DTS external), cruise 2002002PGC 181
Figure A.2.63 Line 60 (Huntec DTS internal), cruise 2002002PGC 182
Figure A.2.64 Line 60 (airgun), cruise 2002002PGC 183
Figure A.2.65 Line 70 (Huntec DTS external), cruise 2002002PGC 184
Figure A.2.66 Line 70 (Huntec DTS internal), cruise 2002002PGC 185
Figure A.2.67 Line 70 (airgun), cruise 2002002PGC 186
Figure A.2.68 Line 80 (Huntec DTS external), cruise 2002002PGC 187
Figure A.2.69 Line 80 (Huntec DTS internal), cruise 2002002PGC 188
Figure A.2.70 Line 80 (airgun), cruise 2002002PGC. Profile was not fully acquired in conjunction with the Huntec internal and external profiles. The airgun line is located further southwest relative to the Huntec lines; However, the final 3 km of the airgun line and the initial 3 km of the Huntec lines were acquired simultaneously. 189
Figure A.2.71 Line 90 (Huntec DTS external), cruise 2002002PGC 190
Figure A.2.72 Line 90 (Huntec DTS internal), cruise 2002002PGC 191
Figure A.2.73 Line 90 (airgun), cruise 2002002PGC 192
Figure A.2.74 Line 99 (Huntec DTS external), cruise 2002002PGC 193
Figure A.2.75 Line 99 (Huntec DTS internal), cruise 2002002PGC 194
Figure A.2.76 Line 30 (Huntec DTS external), cruise 2003002PGC 195
Figure A.2.77 Line 30 (Huntec DTS internal), cruise 2003002PGC 196
Figure A.2.78 Line DTS001, cruise 2009009PGC 197
Figure A.2.79 Line DTS022 (part 1), cruise 2009009PGC. Thick lines at the top of the profile indicate locations of line turns. 198
Figure A.2.80 Line DTS022 (part 2) and DTS023 (part 1), cruise 2009009PGC. Thick lines at the top of the profile indicate locations of line turns. 199
Figure A.2.81 DTS023 (part 2), cruise 2009009PGC. 200
Figure A.2.82 Line 7-1, cruise 2013003PGC 201
Figure A.2.83 Line WP7-8, cruise 2013003PGC 202
Figure A.2.84 Line WP27-28, cruise 2013003PGC 203
Figure A.2.85 Line 19, cruise 2023004PGC 204
Figure A.2.86 Lines A1, A2, and A3, cruise 2024006PGC 205
Figure A.2.87 Lines C1, C2, and C3, cruise 2024006PGC 206
Figure A.2.88 Lines E1, E2, E3, and E4, cruise 2024006PGC 207
Figure A.2.89 Lines G1, G2, and G3, cruise 2024006PGC 208

Figure A.2.90 Lines J1, J2, and J3, cruise 2024006PGC 209
Figure A.2.91 Lines K1, K2, and K3, cruise 2024006PGC 210
Figure A.2.92 Lines M1, M2, M3, M4, and M5, cruise 2024006PGC 211
Figure A.2.93 Lines O1, O2, and O3, cruise 2024006PGC 212
Figure A.2.94 Lines Q1, Q2, Q3, Q4, and Q5, cruise 2024006PGC 213
Figure A.2.95 Lines S1 and S2, cruise 2024006PGC 214
Figure A.2.96 Lines S3, S4, and S5 215
Figure A.2.97 Lines U1, U2, U3, and U4, cruise 2024006PGC 215
Figure A.2.98 Lines U4, U5, U6, and U7, cruise 2024006PGC 216
Figure A.2.99 Lines W2, W3, and W4, cruise 2024006PGC. Line W1 is excluded due to its short length. 216
Figure A.2.100 Lines W5, W6, and W7, cruise 2024006PGC 217
Figure A.2.101 Transit lines from U4 to W7 (X1) and U6 to W5 (X2), cruise 2024006PGC 218
Figure A.2.102 Transit line (X3) from O3 to Q5, cruise 2024006PGC 219

ACKNOWLEDGEMENTS

Most thesis acknowledgements begin with thanks to supervisors and committee members, but I truly believe Karen Douglas deserves thanks first and foremost. She, for all intents and purposes, served as an unofficial supervisor for this project. Karen has been absolutely instrumental - from helping find supervisors and funding, to project conceptualization, setting up access to data and software, helping with data interpretations, attending committee and supervisory meetings in an unofficial capacity, and providing thoughtful, meticulous feedback on my research and writing (even, in one instance, while on an expedition in Antarctica). All of this despite having absolutely no obligation to do so. Thank you.

I would like to thank my supervisors and committee members, Lucinda Leonard, Andrew Schaeffer, and Tiegan Hobbs, for their guidance, patience, encouragement, and support. I couldn't have asked for a better team. This research was supported by funding through the Geological Survey of Canada's Research Affiliate Program and NSERC from Tiegan Hobbs and Andrew Schaeffer, respectively. I am also grateful to David Mosher for his time and effort as my external examiner.

This work would not have been possible without decades of prior research and data collection from scientists, technicians, students, and staff. There are countless individuals to thank, and I sincerely apologize for not knowing them all. However, I can offer acknowledgements to those I know personally. The work in this thesis utilizes datasets collected in the Strait of Georgia – including those collected by Tark Hamilton, Vaughn Barrie, Michael Riedel and others over a period of about 40 years. These three specifically provided useful discussions, interpretations, and advice for this project, and I am so grateful for their willingness to share their knowledge whenever asked. Interpretations of the seismic reflection dataset in this thesis were started by Karen Douglas and Tark Hamilton. Their work first identified a possible flower structure beneath the structures outlined in Barrie and Hill (2004) and directly led to the research in this thesis.

For their advice and encouragement on renaming the Central Salish Sea fault, I would like to thank Rhy McMillan, Michelle Côté, and Mike Ellerbeck from Natural Resources Canada's Indigenous Relations Network. I am also deeply grateful to all twelve First Nations that we contacted for their time and thoughtful responses.

Frontier Geosciences Inc. conducted data collection and processing for the Iona Spit sub-bottom dataset. Many thanks to them, especially Laysa Viera and Ralf Hansen, for their work on these data and for allowing me to tag along during data collection.

The Pacific Geoscience Centre (PGC) is brimming with talented and enthusiastic researchers and staff who provided constant support throughout my graduate studies. I'd like to especially thank my (extensive list of) past co-op supervisors at PGC who encouraged me to pursue graduate studies: Randy Enkin, Cooper Stacey, Michelle Côté, Robert Kung, Scott Dallimore, and Karen Douglas. Karen and Scott kindly acted as references in my UVic application, and I remain humbled by their generous words and belief in me.

Through UVic and the PGC, I have been fortunate to be part of two excellent graduate student groups: the Hobbit Crew™ with Meg and Raul and the UVic/PGC student group. Thanks for many great conversations, suggestions, and constructive comments. Also, a quick shout-out to my fellow night-shift grad students, Megan and Lekima, who kept me (mostly) sane during research cruises in 2023 and 2024.

Finally, I would like to thank my friends and family. In particular: Devon for proof-reading, re-proof-reading, and (after an eye-roll or two) re-re-proof-reading my drafts; Sam for invaluable advice on approaching Nations; Tyson, Emily, Olya, and Maryna for reassuring me during episodes of imposter syndrome; my dogs, Polly and Bottle, for reminding me to step away from work now and then; and my Grandpa Peter for offering lots of unprompted - but always welcome - advice at the start of my MSc program.

DEDICATION

This work is dedicated to those I have lost recently: Mom, Dad, Grandpa Peter, and my dog, Polly. Although none are here today, their unwavering love, curiosity, and guidance continue to shape everything that I do.

Chapter 1

Introduction

1.1 Motivation and Objectives

The southwestern coast of Canada is located within the forearc of the Cascadia subduction zone (Figure 1.1.1). As such, it is prone to large earthquakes generated by the sudden rupture of crustal faults, as well as megathrust earthquakes on plate-boundary faults and intraslab earthquakes within the subducting Juan de Fuca plate. Comprehensive mapping and characterization of faults within the North America plate crust are essential to properly assess the seismic hazard and risk posed to local communities, yet relatively few active crustal faults have been conclusively identified in southwestern BC (e.g., Caston, 2021; Greene et al., 2018; Harrichhausen et al., 2023; Morell et al., 2018). This is demonstrated well by a magnitude 7.3 earthquake which occurred on Vancouver Island in 1946 (Figure 1.1.2); despite widespread shaking, locally dangerous tsunami waves, and well-documented damage (Hodgson, 1946; Rogers and Hasegawa, 1978), the causative fault for this event is not conclusively known (Lynch et al., 2023). The southwest coast of Canada and nearby Washington state have experienced ongoing crustal seismicity over the length of the instrumental record (∼150 years; e.g., Cassidy et al., 2000). This is highlighted by recent moderate-magnitude events in February and March, 2025, including an M_w 4.7 event on the Sunshine Coast and an M_w 4.1 event near the San Juan Islands, both of which were widely felt across the region (Figure 1.1.2; Natural Resources Canada, 2025a; 2025b).

The central Strait of Georgia (SoG), situated within the Salish Sea on the Cascadia forearc, is home to multiple population centres including the cities of Metro Vancouver, Nanaimo, and communities situated along the Sunshine Coast (Figure 1.1.3). Communities surrounding the SoG together contain Canada's largest coastal population, exceeding 3.5 million people (Statistics Canada, 2023). Large earthquakes generated along any given crustal fault in the region likely have long recurrence intervals (e.g., between 5,000 and 15,000 years; Personius et al., 2014; Rockwell et al., 2000;

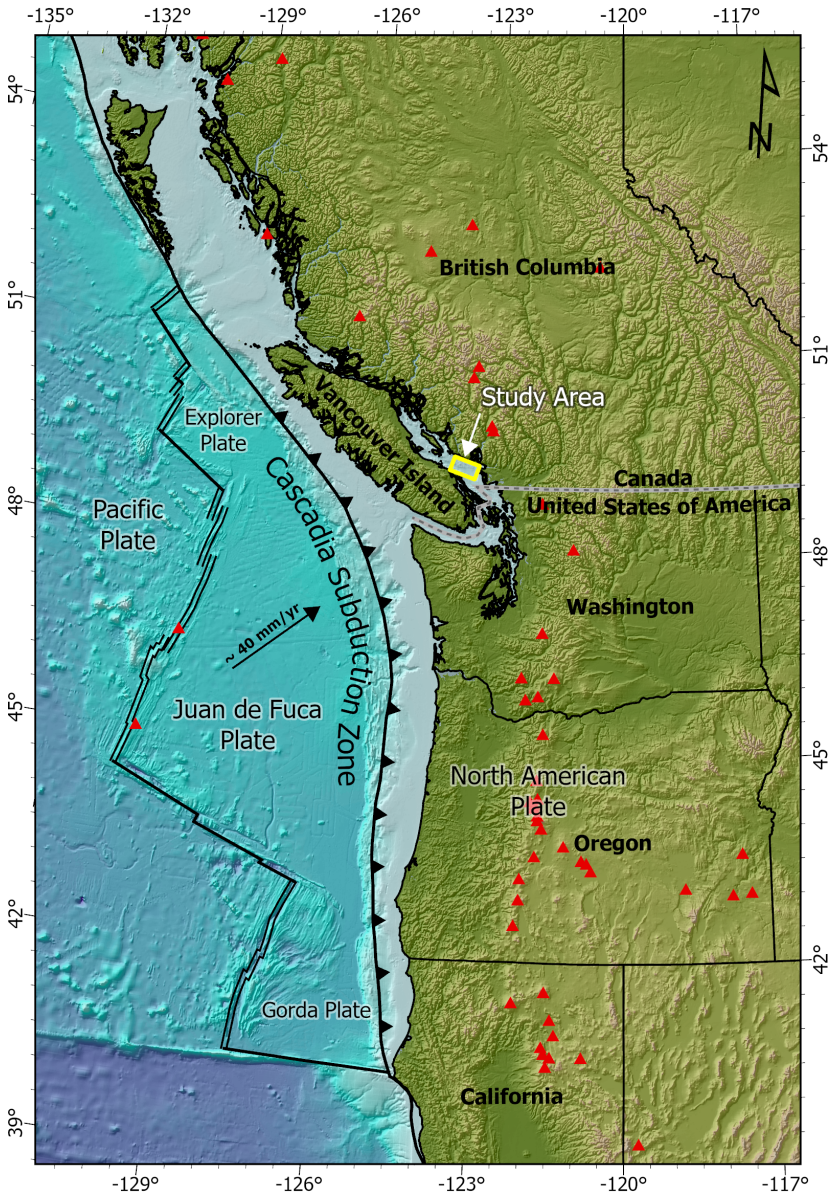


Figure 1.1.1: Tectonic map of the Cascadia subduction zone. The study area location is indicated with a yellow box. Volcanoes are shown as red triangles. The direction of Juan de Fuca plate motion relative to North America is shown with a black arrow (DeMets et al., 2010). Basemap created from GEBCO (2020) data.

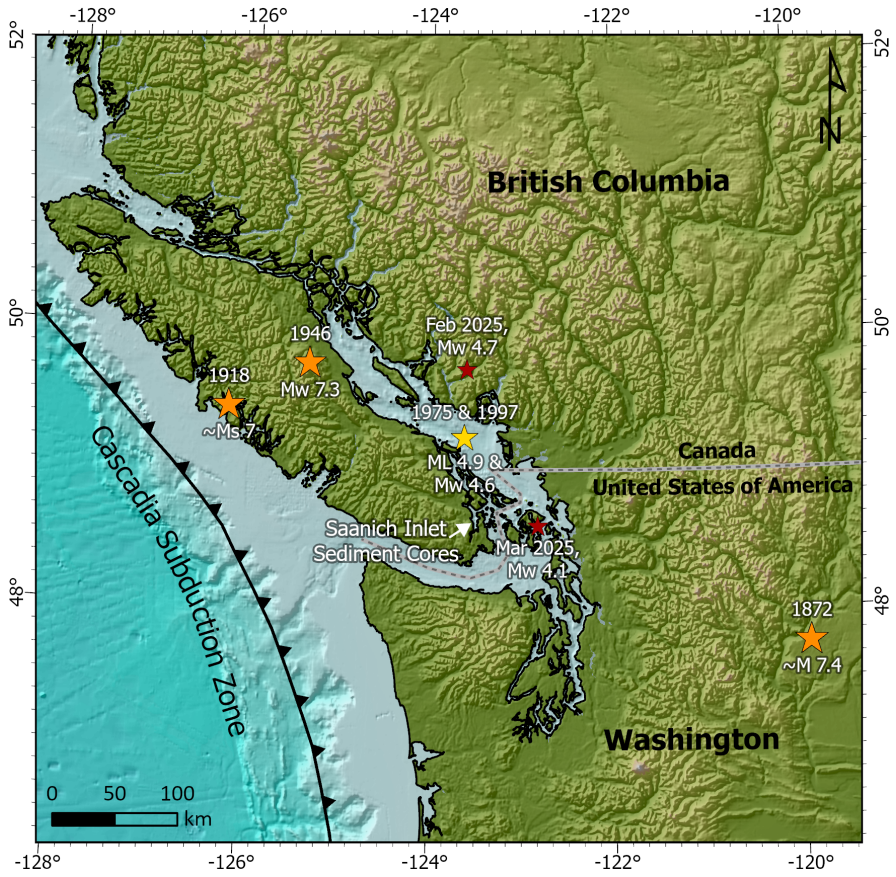


Figure 1.1.2: Map showing locations of earthquakes and sediment core studies discussed in Chapters 1 and 2. Large (M>7) earthquakes are indicated with orange stars, while moderate-magnitude earthquakes within the study area are shown with a yellow star. Recent earthquakes around the Salish Sea are indicated with red stars. Basemap created from GEBCO (2020) data.

Vargas et al., 2014); however, the proximity of the central SoG to dense coastal populations heightens the potential impacts of a submarine crustal earthquake or associated tsunami should they occur. Deterministic seismic risk modelling for hypothetical, large magnitude (∼M 7) crustal earthquakes in southwest BC projects that a single such event could result in an estimated 770-990 deaths, 6-10 thousand buildings damaged and $20-30 billion (CAD) in economic losses due to ground shaking and building damage alone (Hobbs et al., 2022). Despite these risks, the extent, activity, and subsurface characteristics of crustal faults in the central SoG remain poorly constrained, in part due to a limited number of studies and unresolved links between surface features, seismicity, and subsurface deformation (Chapter 2, e.g., Barrie and Hill, 2004; Cassidy et al., 2000; Mosher et al., 2000). Thus, the full scope of hazard and risk associated with crustal faults in the region is under-quantified.

To help address these knowledge gaps, this study tests the hypothesis that previously unrecognized active faults exist within the central Strait of Georgia, and that, if present, such faults could pose a significant hazard to coastal communities of British Columbia. To address this hypothesis, evidence for active faulting within the study area (Figure 1.1.3) is systematically identified, primarily through the interpretation of seismic reflection data. Seismic reflection analysis is supplemented by sub-bottom profiles collected over the Fraser River delta and by multibeam bathymetry. These interpretations are used to delineate a crustal fault near Metro Vancouver beyond its previously recognized extent. Referred to as the Fraser Delta fault in previous work (Barrie and Hill, 2004), the name Central Salish Sea fault zone (CSSFZ) is adopted within this thesis to distinguish it from the Fraser River Delta fault, another crustal fault in southwest BC. Seismic hazard and risk associated with the CSSFZ are then modelled for southwestern BC to better understand the implications for surrounding communities.

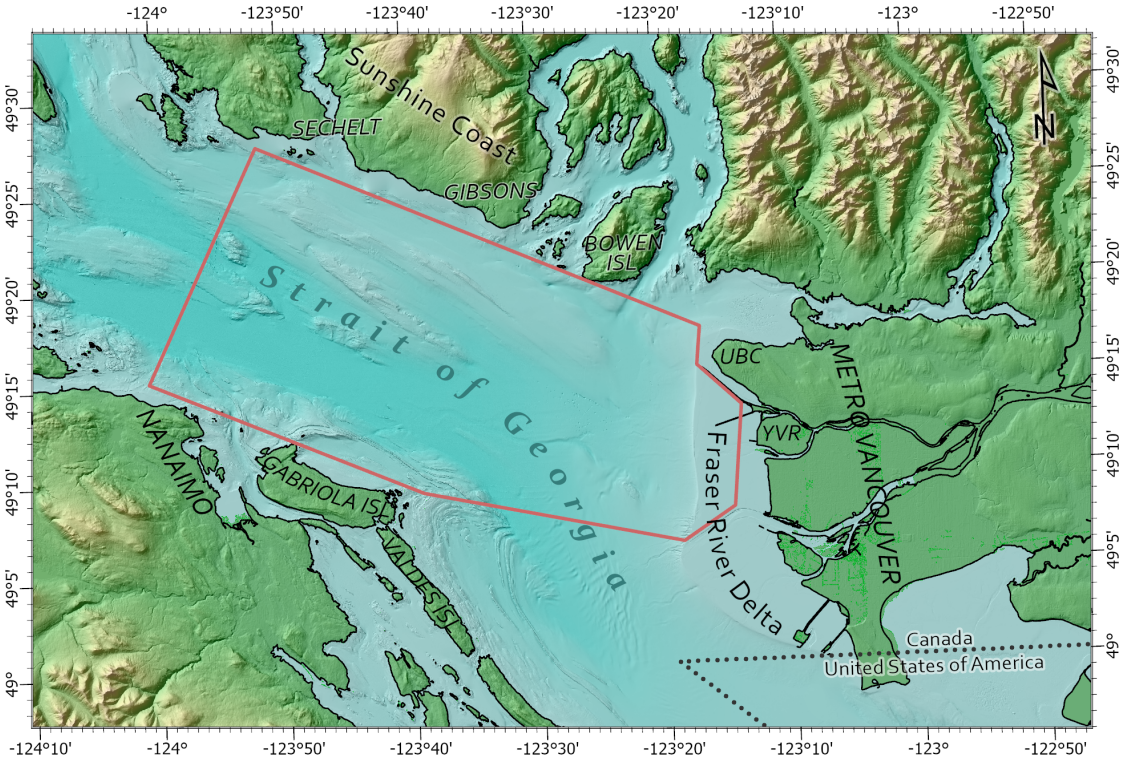


Figure 1.1.3: Map of the study area (red box) and surrounding locations. UBC: University of British Columbia campus; YVR: Vancouver International Airport.

1.2 Outline

This thesis consists of seven chapters, two of which (Chapters 4 and 5) are stand-alone papers intended for submission to peer-reviewed journals. Chapter 2 outlines the tectonic setting, geologic context, and previous active fault studies within the central Strait of Georgia. Chapter 3 provides details of the seismic reflection interpretation framework employed in this study, including definitions of active fault criteria and seismic units. Some material contained within these preliminary chapters is repeated within the introductions of Chapters 4 and 5.

Chapter 4 presents an analysis of seismic reflection data collected within the central Strait of Georgia. A set of objective criteria is employed to assess the presence of active faulting within the study area, including apparent offsets, reflection discontinuities, reflection truncations, abrupt lateral changes in facies, abrupt changes in dip, and associated folds and deformation. Seismic interpretation enables the delineation of the CSSFZ beyond its previously recognized extent. Additional evidence for active faulting in the study area is presented and discussed, including offshore Bowen Island and near Gabriola Island.

Chapter 5 presents further analysis of the CSSFZ and characterization of its main strand for modelling purposes. Multibeam bathymetry and water column data are analysed for signs of active venting along a fault-strike pockmark chain associated with the CSSFZ, a potential hazard for local seafloor infrastructure. Seismic hazard and risk are modelled for four rupture scenarios on the CSSFZ, and estimates for resultant deaths, hospital demand, building damage, and economic losses are presented. A discussion on tsunamigenic implications is also presented, along with selected calculations for potential tsunami runups resulting from tectonic offset of the seafloor during a large earthquake on the CSSFZ.

Within this thesis, the Fraser Delta fault, first identified by Barrie and Hill (2004), is renamed to the CSSFZ. Chapter 6 provides a short description of the rationale behind this choice and of the process used to rename the fault. It contains a brief overview on uses of Indigenous names within geoscientific publications and challenges faced in determining a new fault name in this project.

Chapter 7 provides a general summary of the thesis findings as well as recommendations for future studies.

Chapter 2

Background

2.1 Tectonic Setting and Geologic Context

2.1.1 Regional Tectonic Setting

Off the west coast of North America, the Juan de Fuca plate is subducting northeastward beneath the North America plate at a rate of ∼40 mm/year (DeMets et al., 2010). This forms the Cascadia subduction zone (Figure 1.1.1). Regional tectonics of the Cascadia forearc are largely the result of the oblique relative motion occurring along the subduction zone (Figure 1.1.1; Wells et al., 1998).

Relative plate motions vary along the length of the curved subduction zone, resulting in different deformation regimes in the forearc, with subduction obliquity being greatest in the south and decreasing northward (Figure 2.1.1; Figure 2.1.2A). The oblique relative motion of the Juan de Fuca plate partially results in northward migration of the Oregon and Washington forearc blocks (Figure 2.1.1). Decreased subduction obliquity further north, in turn, reduces the rate of northward migration of the forearc, resulting in north-south margin-parallel shortening in northwest Washington and southwest British Columbia (Wells et al., 1998; Mazzotti et al., 2002). Global Navigation Satellite System (GNSS) data indicate a rate of shortening of ∼5 mm/yr between 46.5°N and 48°N, with a significant decrease in shortening north of the Olympic Mountains (Figure 2.1.2B; Mazzotti et al., 2002).

The margin-parallel shortening occurring in southwest British Columbia and northwest Washington results in oroclinal bending of the Olympic Mountains in northwest Washington, a process in which a previously linear orogenic belt is deformed after its formation (Finley et al., 2019). GNSS data show that the Cascadia forearc rotates counterclockwise north of the Juan de Fuca Strait relative to stable North America (Finley et al., 2019). This marks a transition northward across the Olympic Peninsula

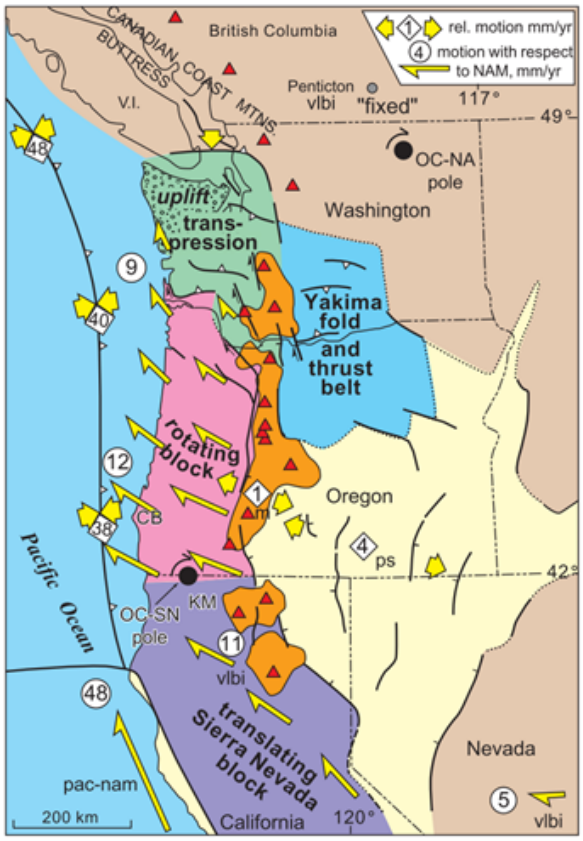


Figure 2.1.1: Schematic tectonic map illustrating the Washington (green), Oregon (pink), and Sierra Nevada (purple) blocks of the Cascadia forearc (from Wells et al., 1998). Triangles indicate locations of major volcanoes along the Cascade volcanic arc. Arrows indicate motion relative to a stable North America.

from clockwise rotation in the south to counterclockwise rotation in the north (Figure 2.1.2A; Finley et al., 2019). In the Pacific Northwest, oroclinal bending is believed to be accommodated by flexural slip on the orocline limbs, with the NE-trending axial trace of the orocline being located through the Olympic Mountains in northwest Washington (Finley et al., 2019). Flexural slip is consistent with the mainly right-lateral Quaternary-active faulting observed on southern Vancouver Island and in the southern Salish Sea versus the mainly left-lateral faulting to the south of the Olympic Mountains (Finley et al., 2019).

The Leech River – Devils Mountain fault was suggested as the northern limit of forearc shortening in Cascadia, controlled by a buttress at the Coast Mountains (Figure 2.1.1; Johnson et al., 2001; Wells et al., 1998). This hypothesis placed the leading edge of deformation in the southern Strait of Georgia (SoG); however, at present, this boundary is not well constrained (Kelsey et al., 2012). Several studies, includ-

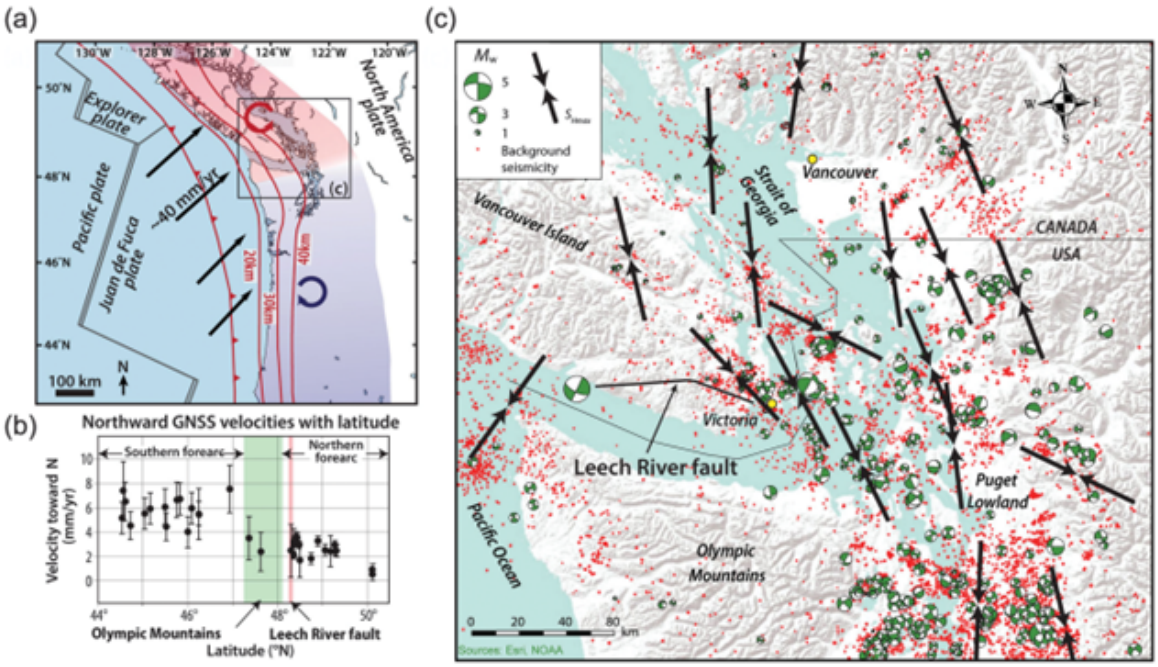


Figure 2.1.2: Geodetic, seismicity, and stress data in northern Cascadia (from Harrichhausen et al., 2021). A: Juan de Fuca plate motion with respect to North America shown in black arrows (DeMets et al., 2010), as well as GNSS-derived clockwise (navy) and counterclockwise (red) rotations on the southern and northern sides, respectively, of the Olympic Mountains (Finley et al., 2019). B: GNSS velocity data along the Cascadia forearc illustrating a decrease in northward velocity across the Olympic Mountains (Mazzotti et al., 2002). C: Crustal seismicity from January 1970 to April 2015, S_{Hmax} directions from inversion of crustal earthquake mechanisms shown as pairs of black arrows (Balfour et al., 2011).

ing those by Kelsey et al. (2012), Greene et al. (2018), and Caston (2021), have identified Holocene- and Quaternary-active faults farther north in the southern SoG, progressively extending the recognized boundary of active deformation in the northern Cascadia forearc. More recent studies present evidence for Holocene forearc faulting even farther north, beyond the southern SoG towards central Vancouver Island (e.g., Cape Lazo, Douglas et al., 2022; Beaufort Range, Lynch et al., 2023).

2.1.1.1 Crustal Seismicity

Three types of earthquakes occur in southwestern BC: subduction megathrust events on the interface between the North America plate and the subducting Juan de Fuca plate, intraslab events within the subducted Juan de Fuca plate, and shallow crustal earthquakes within the overlying North America plate. In the northern Casca-

dia forearc, crustal earthquakes are the most common type, although rates of crustal seismicity are higher in Washington State than British Columbia (Rogers, 1998). Since 1850, three earthquakes of magnitude 7 or larger have been generated by Holocene-active crustal faults in the northern forearc (Figure 1.1.2). The most recent, the 1946 M_w (moment magnitude) 7.3 earthquake near central Vancouver Island, resulted in extensive, well-documented infrastructure damage, slope failures, and tsunami waves (Hodgson, 1946; Rogers and Hasegawa, 1978; Mosher et al., 2004). Along with the 1918 M_s (surface wave magnitude) ∼7 event and the 1872 M (estimated magnitude) ∼7.4 event, these comprise the largest recorded earthquakes in the northern Cascadia forearc (Rogers and Hasegawa, 1978; Malone and Bor, 1979; Cassidy et al., 1988). Given that nearly 80 years have passed since the last major event, most of the region's population have no direct memory of very strong earthquake shaking.

The SoG has been subject to persistent light to moderate magnitude seismicity since earthquakes started being recorded on Canada's west coast (e.g., Figure 2.1.2C). Of note, two shallow earthquake sequences have occurred within the last 50 years in the central SoG, mid-way between Vancouver and Nanaimo, British Columbia: an M_L(Richter local magnitude) 4.9 event in 1975 and an M_w 4.6 event in 1997 (Figure 1.1.2; Rogers, 1979; Cassidy et al., 2000). These moderate-magnitude events were felt as far as Seattle and southern Vancouver Island, and the 1997 event resulted in two power outages and minor damage (Rogers, 1979; Cassidy et al., 2000). Recent seismic activity further highlights ongoing crustal seismicity surrounding the SoG. In early 2025, two considerable earthquakes occurred: an M_w 4.7 event on February 21, approximately 30 km north of the central SoG, and an M_w 4.1 event on March 3 near the San Juan Islands (Figure 1.1.2; Natural Resources Canada, 2025a, b). Both events were felt across southwest BC, although no damage was reported (Natural Resources Canada, 2025a, b).

The relatively short seismicity record in northern Cascadia presents challenges when estimating recurrence rates for large crustal earthquakes. However, paleoseismic data have been used to approximate recurrence rates in the region. For example, Blais-Stevens et al. (2011) conducted varve and debris flow analyses on sediment cores obtained in the Saanich Inlet, a fjord along southern Vancouver Island that opens into the SoG (Figure 1.1.2). Debris flows, thought to originate from strong shaking such as subduction events and large local earthquakes over a 4000-year period, were dated and correlated across the dataset. These events were then compared with other paleoseismic studies in the region (e.g., Atwater et al., 2004). The Saanich Inlet study

revealed 18 events which occurred across two or more cores: nine linked to subduction events and nine to local strong shaking events, the most recent of which correlates to the 1946 Vancouver Island earthquake (Blais-Stevens et al., 2011). Their analysis suggests a recurrence interval of approximately 200 years for strong shaking and 470 years for significant local (crustal or intraslab) events (Blais-Stevens et al., 2011). These findings align with those of Hyndman et al. (2003), who applied Gutenberg-Richter statistics and geodetic deformation rates to estimate recurrence intervals for M$\sim$7 or greater crustal earthquakes in the Puget Sound - southern Strait of Georgia region. Based on a seismicity catalogue of small crustal earthquakes, Hyndman et al. (2003) extrapolated a recurrence interval of approximately 420 years for M$\sim$7 crustal events, while GPS data indicated a similar interval of 400 years.

2.1.2 Geologic Context

The SoG sits within the Georgia Basin, a sedimentary and structural forearc basin located between Vancouver Island and the mainland of southern British Columbia, Canada. The shallow bedrock of the central SoG is largely composed of Jurassic, Cretaceous, and Paleogene rocks of the Coast Plutonic Complex, Nanaimo Group, and Huntingdon Formation (Clague, 1998; England and Bustin, 1998; White and Clowes, 1984). The Upper Cretaceous Nanaimo Group, composed of marine sedimentary shales, sandstones, and conglomerates, outcrops along the southwest edge of the SoG (England and Bustin, 1998). Non-marine Paleogene sedimentary strata of the Huntingdon Formation overlie Nanaimo Group rocks and form the acoustic basement along the eastern section of the central SoG (England and Bustin, 1998). Jurassic to Cretaceous granitic rocks of the Coast Plutonic Complex occupy the northeastern section of the central SoG (Clague, 1998; White and Clowes, 1984). Bedrock is overlain by up to 1 km of Quaternary sediments (England and Bustin, 1998).

The west coast of Canada has a complex history of successive glaciations due to the advance and retreat of the Cordilleran Ice Sheet throughout the Pleistocene. The most recent, locally known as the Fraser Glaciation (corresponding to the Late Wisconsinan), began around 25 to 30 ka before present (BP), with the Last Glacial Maximum (LGM) occurring around 14 to 15 ka BP (Clague and James, 2002; Figure 2.1.3). Deglaciation following the LGM was rapid, and the SoG was ice-free by 11.3 ka BP (Barrie and Conway, 2002).

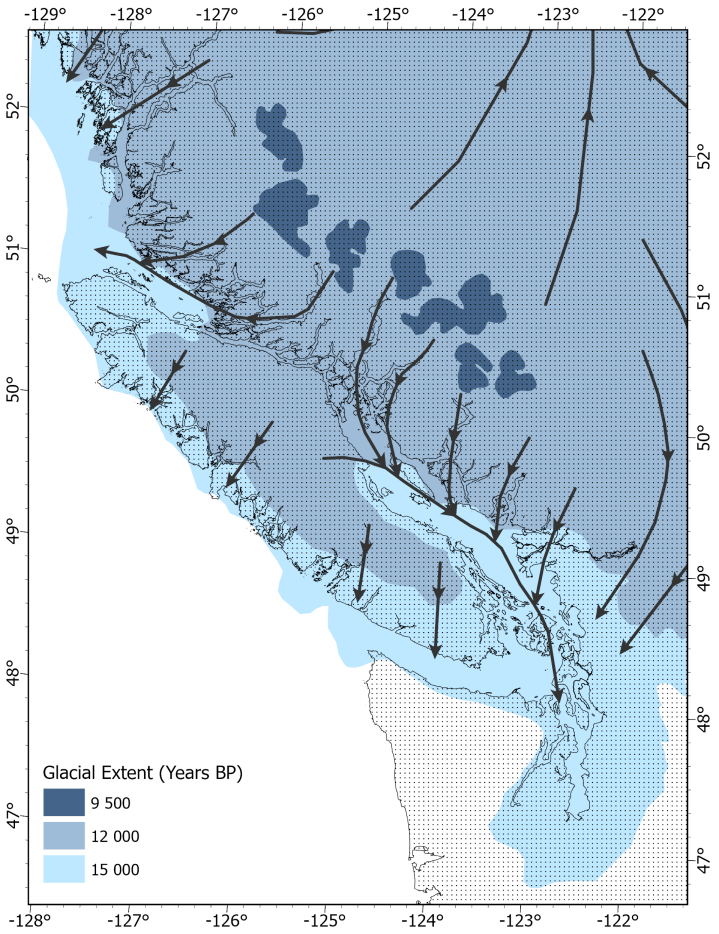


Figure 2.1.3: Approximate ice flow directions in southwest BC and northwest Washington during the Last Glacial Maximum and glacial extents at the end of and following the Fraser Glaciation (9500, 12000, and 15000 BP). Modified from Figures 4 and 5 of Clague and James (2002).

Throughout deglaciation, relative sea level in the central SoG experienced considerable variation. At the LGM, relative sea level was approximately 150 m higher than present (Hutchinson et al., 2004). Regional variation has been observed in other studies, reflecting differences in ice thickness and consequent isostatic response, with generally lower highstands reported farther southwest (e.g., Mosher and Hewitt, 2004). As deglaciation progressed, rapid isostatic rebound resulted in a substantial sea level fall, reaching approximately -15 m by ∼11.5 ka BP, roughly coinciding with the timing of ice-free conditions in the SoG (Hutchinson et al., 2004; Barrie and Conway, 2002). This lowstand was followed by a subsequent rise, with sea level peaking at ∼+1 m around 9 to 8.5 ka BP, before gradually stabilizing to present-day levels (Hutchinson et al., 2004).

The successive glaciations in the SoG deposited large amounts of sediment and reworked the seafloor. As a result, the region's present-day morphology and shallow subsurface composition have been moulded by its glacial past. Ice flow during the Fraser Glaciation in the SoG was oriented along the axis of the strait (100-110°), moving from the northwest to the southeast (Barrie et al., 2005; Figure 2.1.3). As a result of glacial ice flow, bedrock within the Georgia Basin was eroded into NW-SE oriented ridges and troughs (Clague et al., 1998). Northwest-southeast-oriented geomorphological features, such as banks and glacial flutes, occur throughout the central SoG and are readily apparent in multibeam bathymetry data (Figure 2.1.4). McCall Bank, composed of interglacial silts which have been carved and fluted by subsequent glaciation, is a prominent example of one such feature in the region, as shown in Figure 2.1.4. Based on seafloor relief alone, it is difficult to interpret the origin of linear northwest-southeast-oriented geomorphological features, i.e., whether glacial and/or tectonic.

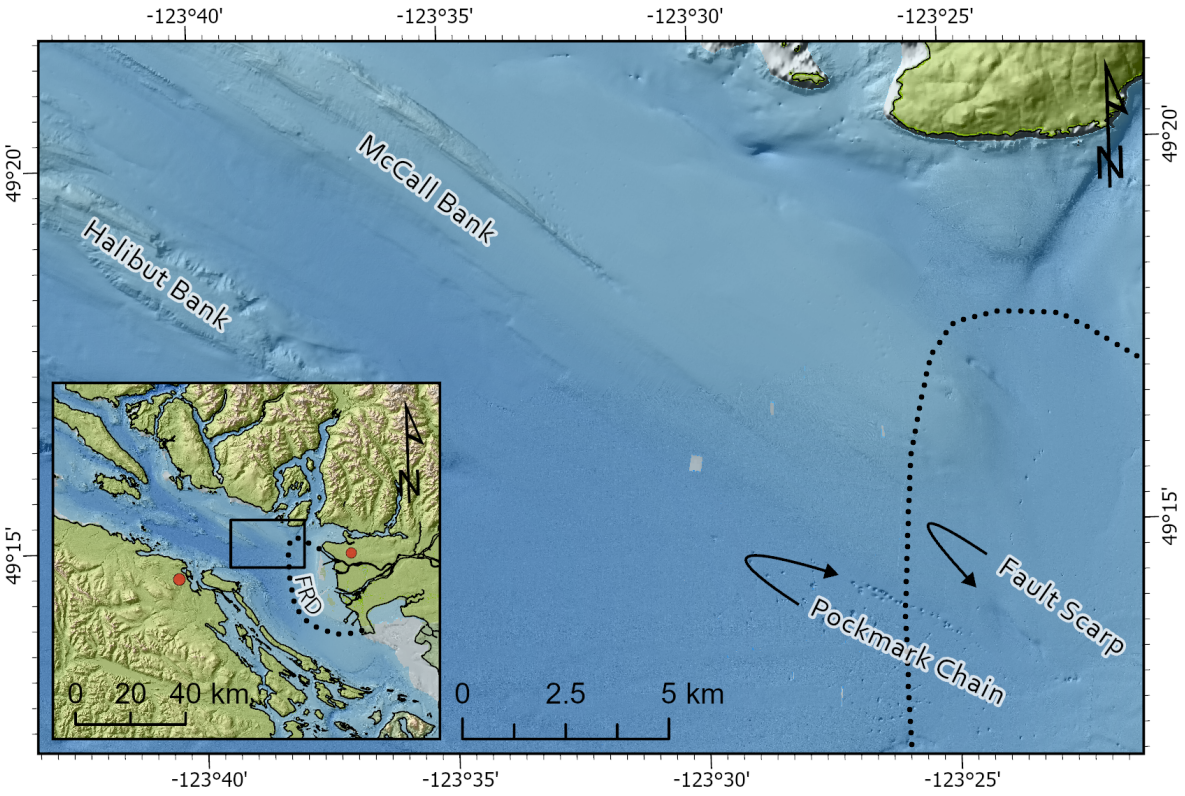


Figure 2.1.4: Seafloor relief illustrating prominent glacial features in the central SoG including Halibut and McCall Banks. A fault and associated pockmark chain display a similar northwest-southeast trend. The approximate extent of the Fraser River delta (FRD) is shown with a black dotted line (adapted from LaCroix et al., 2024). Inset image indicates the main map extent with a black box. Metro Vancouver and Nanaimo are indicated with red dots. Modified from Figure 6 of Barrie et al. (2005).

The rapid deglaciation and isostatic rebound of the SoG was accompanied by ice-proximal and ice-distal glaciomarine deposition (Barrie and Conway, 2002). The glaciomarine deposits have since been buried by subsequent Holocene deposits but remain visible in subsurface data (Hamilton, 1991). Following the end of the Fraser Glaciation, the Fraser River delta (Figure 2.1.4) formed at the mouth of the Fraser River at approximately 10 ka BP. Throughout the Holocene, the Fraser River has been the dominant source of sediment for the central SoG, with sedimentation across the study area being dominated by sands and silts (Johannessen et al., 2003; LaCroix et al., 2024). Coarser sediments, primarily sand, deposit near the delta front, while thick muddy sediments deposit throughout the remainder of the study area (Hill et al., 2008). Present-day sedimentation rates in the region vary with proximity to the Fraser River delta, ranging from 3 to 10 cm/yr (Hart et al., 1998).

2.2 Previous Studies of Faults in the Central Strait of Georgia and Adjacent Areas

In southwest British Columbia and northwest Washington, there is increasing evidence for Holocene activity on a widespread network of crustal faults. As discussed in the previous section, several studies have placed the leading edge of forearc deformation in the southern Strait of Georgia (SoG); however, this boundary remains poorly constrained (Kelsey et al., 2012). Consequently, most research on crustal faults in southwest BC has focused on regions near this inferred boundary (e.g., Greene et al., 2018; Kelsey et al., 2012; Morell et al., 2018; Personius et al., 2014).

In contrast, the central and northern SoG have received less attention, despite evidence of Holocene-active faulting (e.g., Barrie and Hill, 2004) and persistent low to moderate magnitude crustal seismicity (e.g., Cassidy et al., 2000). The following literature review focusses on the study area for this thesis (Figure 2.2.1), a region of the central Strait of Georgia characterized by its proximity to population centres such as Metro Vancouver, Nanaimo, and the Sunshine Coast and with a high concentration of seismic reflection data. The review in this chapter discusses prior studies within the study area, as well as faults which trend toward it that may warrant further investigation. Within the study area, two faults have previously been identified: the Central Salish Sea/Fraser Delta fault (Barrie and Hill, 2004) and an unnamed Strait of Georgia fault (Cassidy et al., 2000), the latter responsible for an earthquake sequence

(mainshock M_w 4.6) in 1997. Additionally, two other faults appear to trend toward the study area: the Fraser River Delta fault and the Outer Islands fault.

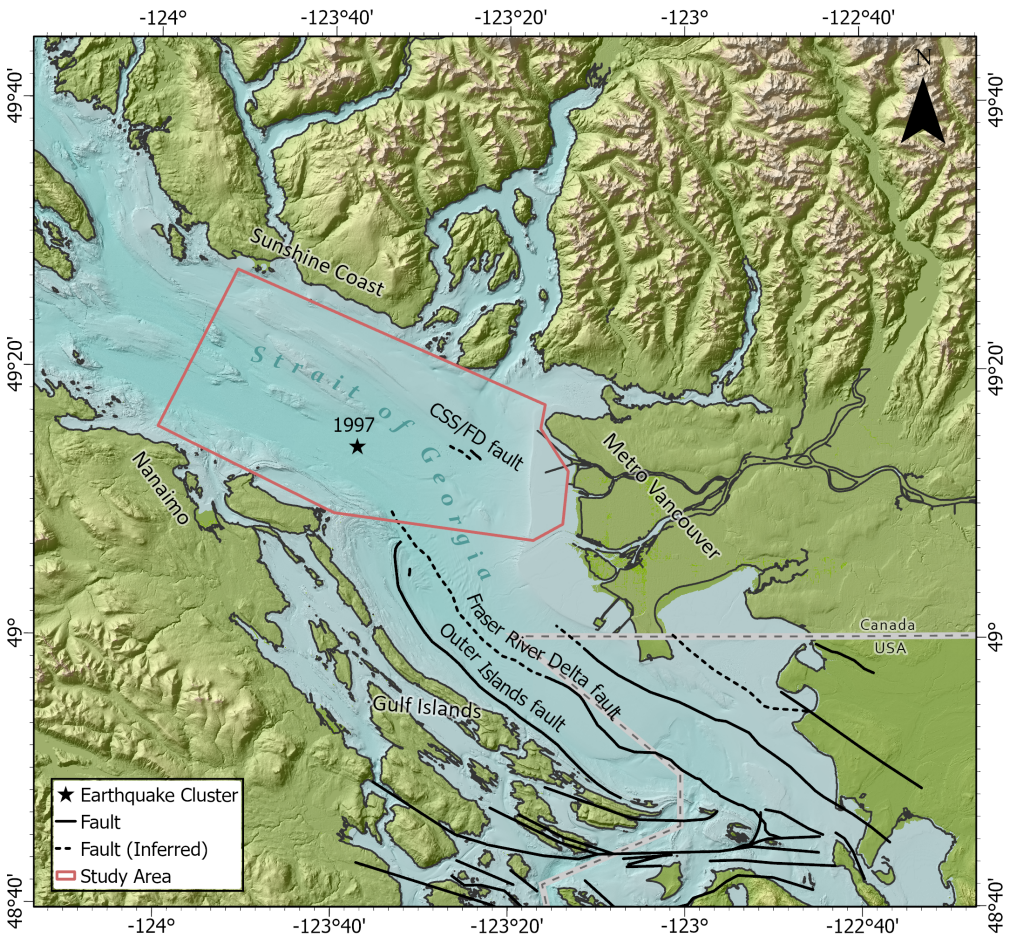


Figure 2.2.1: Map of the Strait of Georgia showing known faults. Faults are shown in black, with inferred faults indicated by dashed lines. Faults within or trending towards the Central SoG are labelled. CSS/FD fault: Central Salish Sea/Fraser Delta fault. The central SoG study area is indicated with a red polygon.

2.2.1 Faults Within the Central Strait of Georgia Study Area

2.2.1.1 Strait of Georgia Fault

On June 24, 1997, a mainshock M_w 4.6 earthquake occurred under the central SoG with associated foreshock (M_L 3.4) and aftershock (M_L 0.3-1.8) events (Figures 2.2.1, 2.2.2; Cassidy et al., 2000). Cassidy et al. (2000) used relocated hypocentres and focal mechanism solutions from P-nodal and centroid moment tensors to characterize

the causative fault. Results showed an east-west trending, 53° north-dipping reverse fault located at a depth of 2-4 km (Cassidy et al., 2000). The characterized plane aligns well with an 8 km long aeromagnetic anomaly in the SoG (Figure 2.2.3; Cassidy et al., 2000; Mosher et al., 2000). Previously, a similar magnitude sequence (main-shock M_L 4.9) occurred in the same location, approximately 30 km from the cities of Vancouver and Nanaimo, in 1975 (Figure 2.2.2; Rogers, 1979). P-nodal solutions for the two events are similar, both suggesting reverse faulting on an east-west trending, northward dipping fault. However, to date, no surface expression of this fault has been documented.

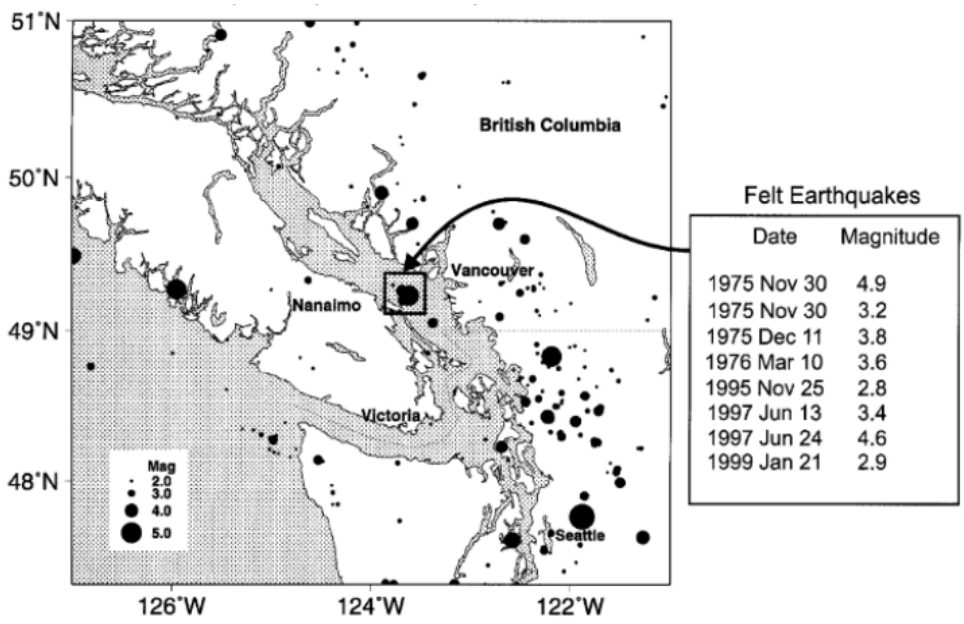


Figure 2.2.2: Map of shallow (< 6 km depth) crustal earthquakes in the northern Cascadia forearc from 1975-1999 (from Cassidy et al., 2000). Note the seismicity in the central SoG, including earthquake sequences in 1975 and 1997. From Cassidy et al. (2000).

Following the 1997 earthquake cluster under the SoG, multichannel seismic reflection surveying was conducted in the Salish Sea as part of the Seismic Hazard Investigations in Puget Sound (SHIPS) program in March 1998 (Figure 2.2.3). A 100-km-long multichannel seismic line was collected through the central and southern SoG, the northern third of which was located within the central Strait (Figure 2.2.4). One of the goals of the program was to investigate subsurface structures near the 1997 and 1975 earthquake clusters (Mosher et al., 2000).

Mosher et al. (2000) interpreted two zones of deformation within the bedrock unit from the resultant data based on the presence of disrupted, offset, and variably

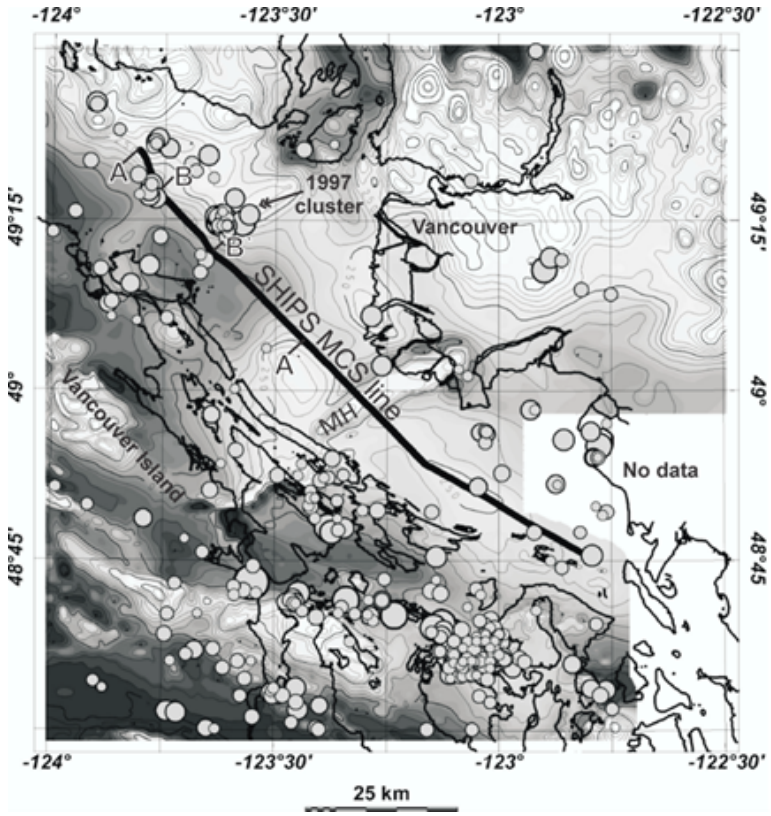


Figure 2.2.3: Map of the SHIPS multichannel seismic (MCS) line, aeromagnetic data, and crustal seismicity (adapted from Mosher et al., 2000). Areas of interest along the line are denoted A-A' and B-B' and are shown in Figure 2.2.4. Aeromagnetic data range from -500 nT to +1660 nT (black to white). A magnetic high resultant from strong interference of an underwater cable is labelled as MH. Crustal seismicity is shown with grey dots.

dipping reflectors (Figure 2.2.4). The northernmost of the two deformation zones was located in the area of the 1997 events and had two interpreted faults with apparent northward dips. This orientation is consistent with the analyses of Cassidy et al. (2000); however, offsets within the deformation zones were interpreted as indicative of normal or listric normal faulting, contrasting with the reverse focal mechanisms of Cassidy et al. (2000) (Figure 2.2.4). The modern stress regime suggests that reverse faulting would be expected on such a structure (Balfour et al., 2011). However, because the seismic profile did not traverse directly over the hypocentres of the 1997 events, a definitive correlation between these faults and the earthquake cluster could not be established (Mosher et al., 2000). The authors did not address whether this may indicate a reactivation of older bedrock structures with reversed kinematics or if the 1997 sequence could have occurred on a different structure altogether.

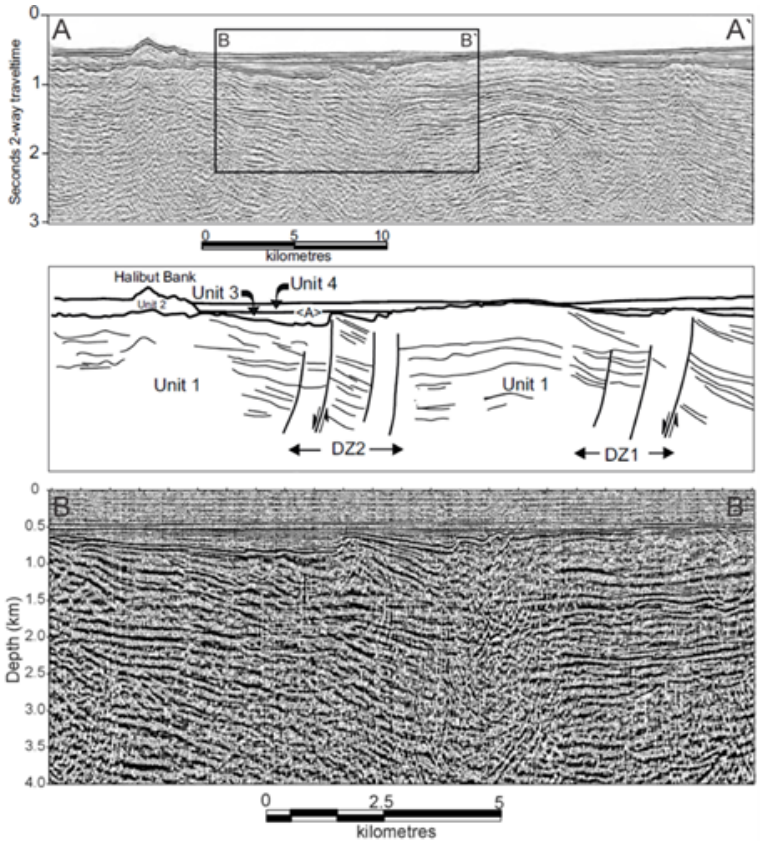


Figure 2.2.4: Seismic reflection data and interpretations of SHIPS data (adapted from Figures 2a and 4d of Mosher et al., 2000). Line locations are shown in Figure 2.2.3. Line A-A‘ shows seismic data (upper) and interpretations (lower) corresponding to data within the central Strait of Georgia study area. Deformation zone 2 (DZ2) is located near the 1997 sequence. Line B-B‘ shows a zoomed and depth-migrated seismic section over an area of significant bedrock faulting and deformation near the approximate area of the 1997 earthquake sequence. Abbreviations: DZ - deformation zone; Unit 1 - Bedrock; Unit 2 - Glacial deposits; Unit 3 - Glacial outwash turbidite sequences; Unit 4 - Fraser River deposits.

No faults, folds, or associated deformation were observed in the overlying Quaternary sediments by Mosher et al. (2000), and the authors note that the 1997 event may not have resulted in surface rupture. The apparent lack of Pleistocene and Holocene deformation may indicate blind ruptures or a lack of significant faulting during the Quaternary (Mosher et al., 2000). However, these results have some key limitations: the relatively low resolution of the uppermost 1 km in multichannel seismic data compared to high-resolution sub-bottom profiling records, combined with the Quaternary units' acoustic transparency in the dataset, would make faulting and deformation within the Quaternary units difficult to assess. As such, the lack of visible deformation and faulting within Quaternary units may be the result of method limitations rather than

confirmation of a lack of deformation and faulting.

2.2.1.2 Central Salish Sea/Fraser Delta Fault

In an effort to obtain contiguous multibeam bathymetry coverage of the Salish Sea, Canadian federal government field programs collected approximately 5000 km^2 of data between 2000 and 2004 (Barrie et al., 2005). These data led to the identification of several seabed features based on seafloor relief, including a seafloor scarp and linear pockmark chain approximately 10-15 km west of Vancouver (Figures 2.2.1, 2.2.5). Pockmarks are seafloor depressions that form in soft sediment due to the escape of subsurface fluids (Hovland and Judd, 1988). Previous studies, globally, have shown associations between linear pockmark chains and faults (e.g., Acosta et al., 2001; Barrie et al., 2005; Pilcher and Argent, 2007; Zhang et al., 2020). The presence of a linear pockmark chain alone cannot confirm subsurface faulting; however, such features can serve as indicators for underlying structures when considered in conjunction with geo-

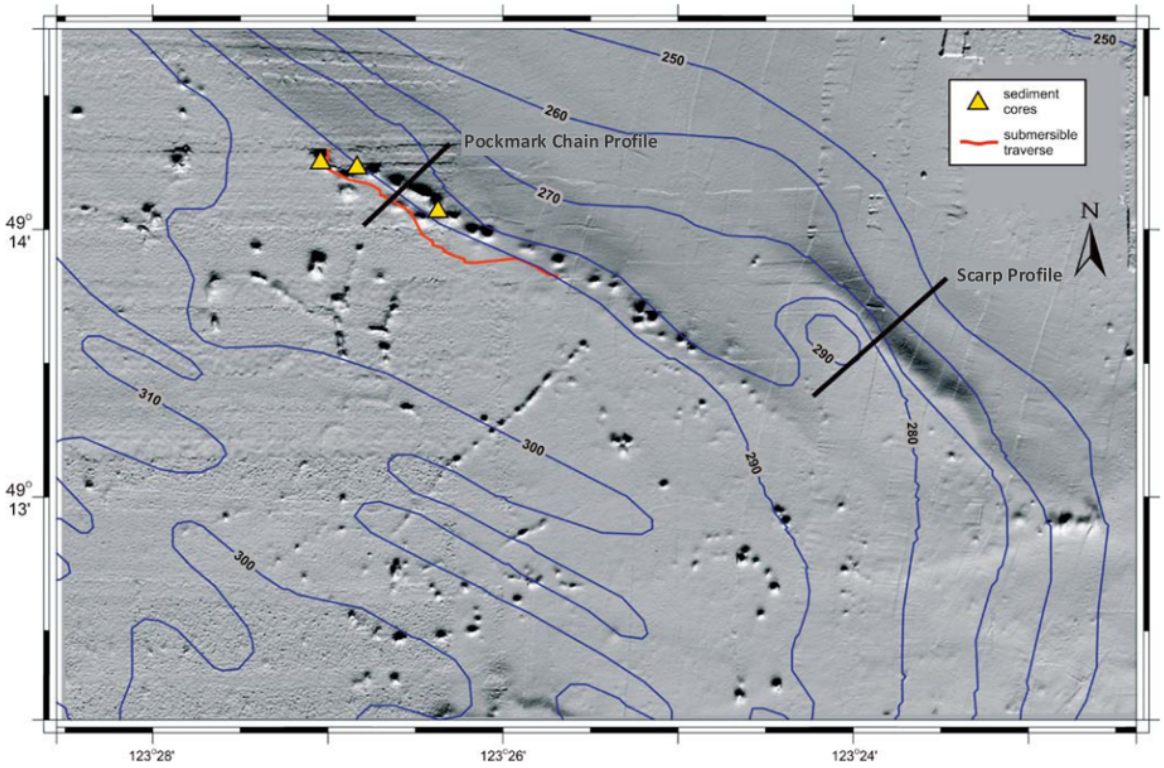


Figure 2.2.5: Seafloor relief and contours (blue; metres below sea level) showing a scarp and large pockmark chain (adapted from Barrie and Hill, 2004). Additional smaller pockmark chains and randomly oriented features are also present. Locations of follow-up seismic reflection profiles are indicated with thick black lines.

physical data. Following the identification of a suspected fault scarp and associated pockmark chain, seismic reflection lines were collected normal to each feature (Figure 2.2.6).

The eastern scarp of the Central Salish Sea/Fraser Delta fault is a 2.7 km long, NW-SE trending seafloor feature (Figure 2.2.5; Barrie and Hill, 2004). Seismic reflection interpretations show an apparent southwest-dipping normal fault that displaces Holocene and Pleistocene sediments with up to 50 m of apparent offset (Figure 2.2.6 A; Barrie and Hill, 2004). West of the fault scarp, Barrie and Hill (2004) identified a 4 km long, NW-SE trending linear pockmark chain situated at the base of a slope (Figure 2.2.5). Airgun seismic reflection data beneath the pockmark chain are ambiguous due to high acoustic turbidity (Figure 2.2.6 B). Nevertheless, the pockmark chain was interpreted as indicative of a fault due to its proximity to, and the unambiguity of faulting beneath, the eastern scarp (Barrie and Hill, 2004).

Barrie and Hill (2004) hypothesized that the scarp and pockmark chain may be part of a larger en-echelon fault system, but additional work to map and characterize the structures was beyond the scope of their study. Barrie and Hill (2004) provisionally dubbed the features the "Fraser Delta fault." To avoid confusion with the Fraser River Delta fault, another crustal fault located within the SoG (See Fraser River Delta Fault section below), the name Central Salish Sea fault or fault zone will be used in this thesis in place of the previous name. For further details, the reader is referred to Chapter 6, which details the process taken to rename the fault.

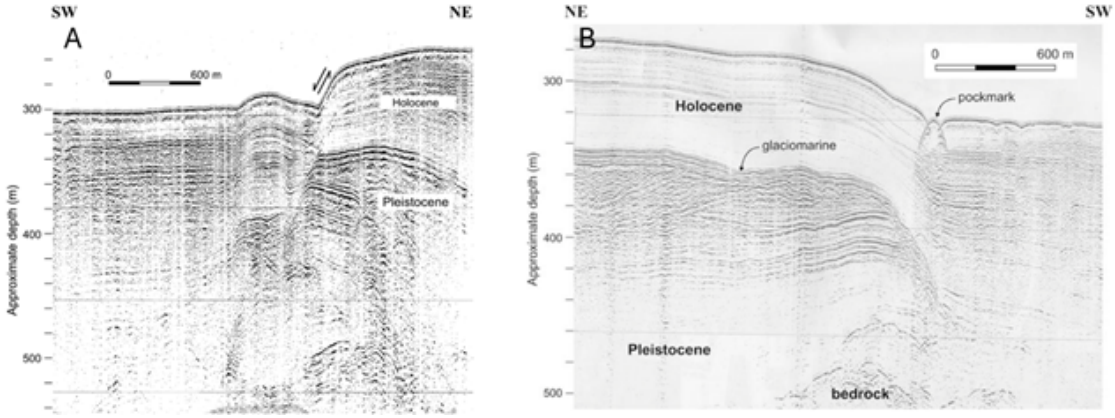


Figure 2.2.6: Airgun seismic reflection data over fault-related features (adapted from Barrie and Hill, 2004). Locations shown in Figure 2.2.5. A) Apparent offset of Holocene and Pleistocene strata beneath the seafloor scarp. B) Profile over the linear pockmark chain, showing a notable increase in acoustic turbidity southwest of the feature. Adapted from Barrie and Hill (2004).

2.2.2 Faults Adjacent to the Study Area

2.2.2.1 Fraser River Delta Fault

The Fraser River Delta fault (FRDF) was hypothesized by Greene et al. (2018) based on bathymetric evidence of slumping and a linear pockmark chain along the southern edge of the Fraser River Delta. Work on the FRDF was followed by Caston (2021), who utilized a suite of geophysical datasets to map and characterize the fault.

As mapped in Caston (2021), the FRDF is an approximately 72 km SE-NW trending reverse or right-lateral oblique reverse fault located in the southern SoG (Figure 2.2.1). The main section of the fault is approximately 41 km long and aligns well with a sizable aeromagnetic anomaly down the axis of the Strait, as well as relocated earthquake hypocentres and focal mechanisms from events recorded between 2001 and 2009 (Caston, 2021). To the north, an additional 31-km-long extension of the fault was mapped towards the central SoG (Figure 2.2.1); however, delineation of the fault further north into the central SoG was limited by strong magnetic interference from an underwater cable (Figure 2.2.3). Although not directly imaged with seismic reflection data, this extension was inferred from the presence of potentially associated features in shallow seismic reflection data and a second, lower-resolution aeromagnetic dataset (Caston, 2021). The fault merges with the Skipjack Island fault zone at its southern end.

2.2.2.2 Outer Islands Fault

The Outer Islands fault (OIF) lies along the western edge of the southern SoG parallel to and directly east of British Columbia's Gulf Islands (Figure 2.2.1). The structure was first identified in exploration reports and imaged in seismic reflection surveys conducted in 1968 (Machacek, 1970). In literature, the characterization of the OIF varies significantly. Early studies identify the fault as a northeast-dipping extensional fault that bounds the Georgia Basin, with evidence of Neogene activity (Machacek, 1970; England and Bustin, 1998). More recent research, however, identifies it as a southwest-dipping blind thrust fault (Dash et al., 2007; Polivka, 2013). Recent work by Huang et al. (in press), building on a forearc high formation model outlined by Menant et al. (2020), suggests that normal faulting along the OIF results from isostatic compensation in response to repeated tectonic underplating and associated

coastal uplift of Vancouver Island. However, this study does not explicitly address Holocene kinematics.

The OIF is often shown to extend to the seafloor with little to no Quaternary sediment coverage, limiting the ability to assess Quaternary activity using seismic reflection data (e.g., Figure 2.2.7). However, Polivka's (2013) interpretation of SHIPS seismic reflection data in the southern SoG presented no obvious evidence of Holocene activity in limited Holocene sediments along the fault. The OIF has been mapped within the southern SoG from Saturna Island northwards to Valdes Island based on bathymetry, seismic reflection, and seismic refraction data (England and Bustin, 1998; Dash et al., 2007; Polivka, 2013).

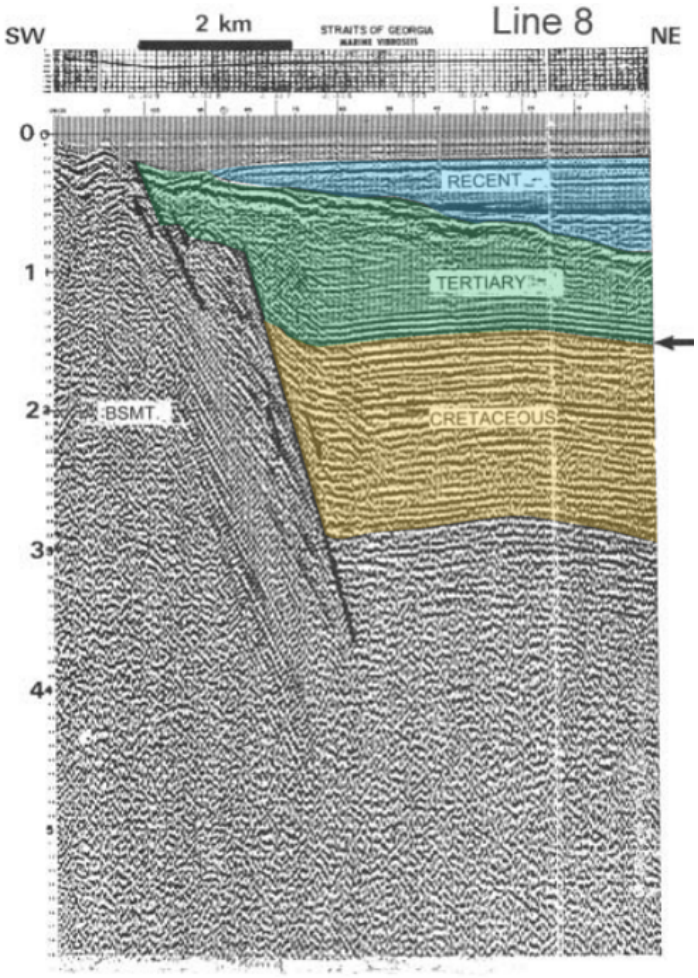


Figure 2.2.7: Seismic reflection data identifying the Outer Islands Fault. Modified from Figure 14 of England and Bustin (1998) to more clearly display boundaries between units. Cretaceous unit (Nanaimo Group sedimentary strata) is shown in yellow; Tertiary unit (non-marine sedimentary Huntingdon formation) is shown in green; Quaternary deposits are shown in blue. Note the lack of Quaternary sediment coverage over the fault, which prevents an assessment of Quaternary offsets or deformation at this location.

Chapter 3

Seismic Reflection Interpretation Framework

3.1 Theory

Seismic reflection is a widely used geophysical technique that provides high-resolution imaging of the Earth's subsurface. The method involves a controlled seismic source that generates a compressional wave (P-wave), which propagates into the subsurface (Figure 3.1.1 A). When the seismic wave encounters an interface between two media of different acoustic impedances, defined as the product of a medium's P-wave velocity (V_p) and its density (ρ), a portion of the wave is reflected, and the remainder is transmitted beyond the interface (e.g., Mosher and Simpkin, 1999). High acoustic impedance contrasts result in higher reflectivity at a given interface (Figure 3.1.1 B and C). This process generates a series of reflections from successive interfaces, which are detected by a receiver upon returning to the surface (Dondurur, 2018; Figure 3.1.1 A).

The recorded amplitudes and arrival times of the reflected waves are used to produce profiles representing acoustic impedance contrasts between subsurface layers. Prior to interpretation, raw seismic data must undergo a series of processing steps, including deconvolution and filtering to enhance resolution and reduce noise, common mid-point (CMP) stacking to resolve geometry, and migration to position the data accurately within the subsurface (i.e., time and depth migration) (Dondurur, 2018; Yilmaz, 2001). A comprehensive discussion of seismic reflection processing is beyond the scope of this chapter; however, interested readers are referred to relevant texts such as those by Yilmaz (2001) and Dondurur (2018) for further details.

Once processed, the resulting seismic data provide a profile of subsurface features, enabling structural and stratigraphic interpretation (Figure 3.1.1 B). The ease

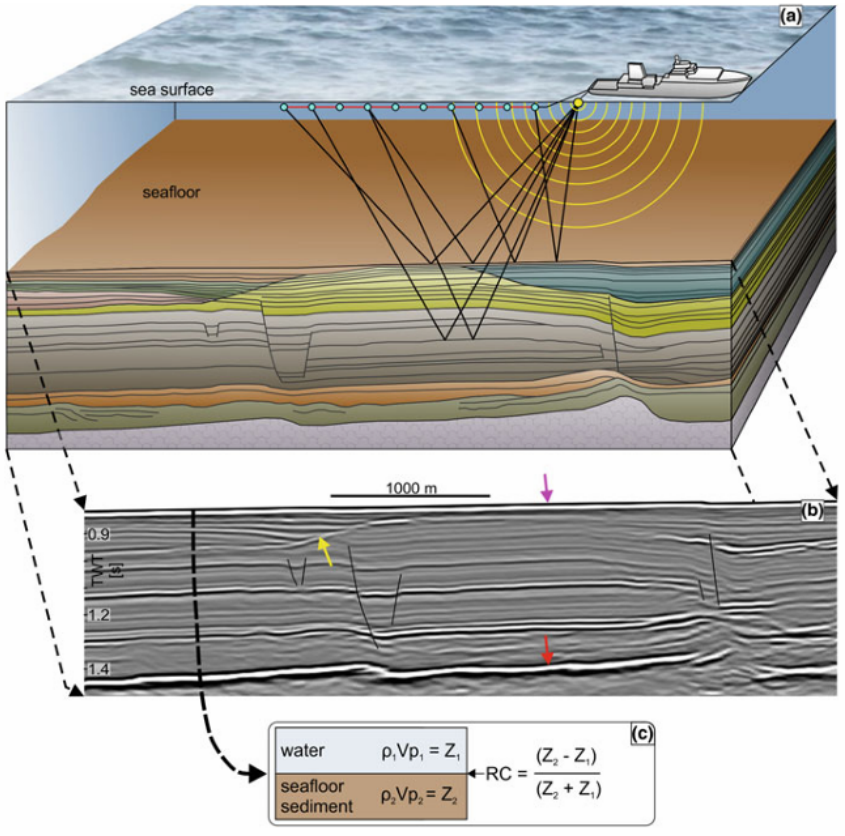


Figure 3.1.1: A) Schematic diagram of marine seismic reflection data acquisition. Hypothetical seismic ray paths are shown in black. Waves propagate from a seismic source towed behind a vessel (shown as a yellow dot). These waves reflect off the seafloor and subsequent layers, before returning to the surface where they are received by an array of hydrophones (shown as blue dots). B) Resultant seismic reflection profile. Black lines indicate interpreted faults, purple arrow indicates the seafloor reflection, red arrow indicates a high amplitude reflection off of a strong bedrock reflector, and the yellow arrow indicates an unconformity. C) A high contrast in acoustic impedance (Z) between seawater ($\rho_1 V_{p1}$=Z_1) and seafloor sediment ($\rho_2 V_{p2}$=Z_2), represented by the reflection coefficient (RC), results in the high amplitude seafloor reflection visible in B. From Crutchley and Kopp (2018).

of interpretation is closely tied to the resolution of the dataset, which depends on the frequency (f) band of the seismic source and depth (z). The generally accepted practical limit of vertical resolution is one-quarter of a wavelength (λ), $\lambda/4$, where λ can be determined by the quotient of a given seismic velocity divided by frequency (i.e., $v/f = \lambda$) (e.g., Dimmen et al., 2023; Misra and Mukherjee, 2018; Nanda, 2021). While horizontal resolution depends on multiple factors, including acquisition geometry and processing, a limit for horizontal resolution can be approximated by the Fresnel zone radius (r), the width of a swept planar area that produces a coherent reflection, where $r = \sqrt{z\lambda/2}$. Thus, systems with high frequencies (shorter wavelengths) provide higher resolutions. For example, a 3.5 kHz system would produce a high vertical resolution of tens of centimetres in sediments with a seismic velocity of $\sim$1540 m/s. However, there is an inherent trade-off between resolution and imaging depth in seismic reflection. The subsurface penetration of the seismic signal depends on the energy and frequency of a seismic source, with lower frequencies and longer wavelengths penetrating deeper into the subsurface (Dondurur, 2018). High-frequency signals attenuate quickly with depth, and therefore have limited subsurface penetration (Nanda, 2021). Additionally, all seismic signals experience a decrease in resolution with increasing depth, as attenuation results in diminished signal strength, preferentially affecting higher frequencies, as they inherently contain less energy (Nanda, 2021).

3.2 Fault Interpretation

The fault interpretations presented in this thesis were made using a multi-criterion, multi-record approach. This type of approach is critical for fault interpretation, as several fault indicators, such as terminated reflections and seismic discontinuities, are not exclusive to faulting and can result from other processes. In addition, gas and fluid conduits, which are not uncommon in the fluid-rich Holocene sediments of the Strait of Georgia, can superficially resemble faults in seismic reflection data (e.g., Marlow et al., 1996). However, while fluid conduits may coincide with faults in some cases, they can generally be differentiated from faults by their lack of lateral continuity. As a result, evidence of faulting must be correlated across multiple seismic records to rule out other causes.

This section provides a brief overview of fault indicators in seismic reflection data, aiming to provide a useful framework for fault interpretation. Representative images

have been selected from literature for their illustrative clarity. While the indicators described here are not exclusive to Quaternary faulting, fault interpretations in the following chapters of this thesis focus on Holocene- and Quaternary-active faults, by assessing the presence of fault criteria within post-glacial (approximately Holocene-age) and glacial (approximately Pleistocene-age) units. Seismic interpretations of note are presented in Chapters 4 and 5. Interpreted sections for all seismic lines analyzed for this body of work are presented in Appendix A. Eight fault indicators are considered, as outlined below.

1. **Offsets (Figure 3.2.1 A)**: Vertically offset packages of reflections are among the most common and visually distinct lines of evidence used to identify faults in seismic reflection data (e.g., Brandes et al., 2022). Once identified, interpreters can infer the sense of movement on the fault by analyzing the direction and magnitude of vertical displacement (e.g., Barrie and Hill, 2004; Misra and

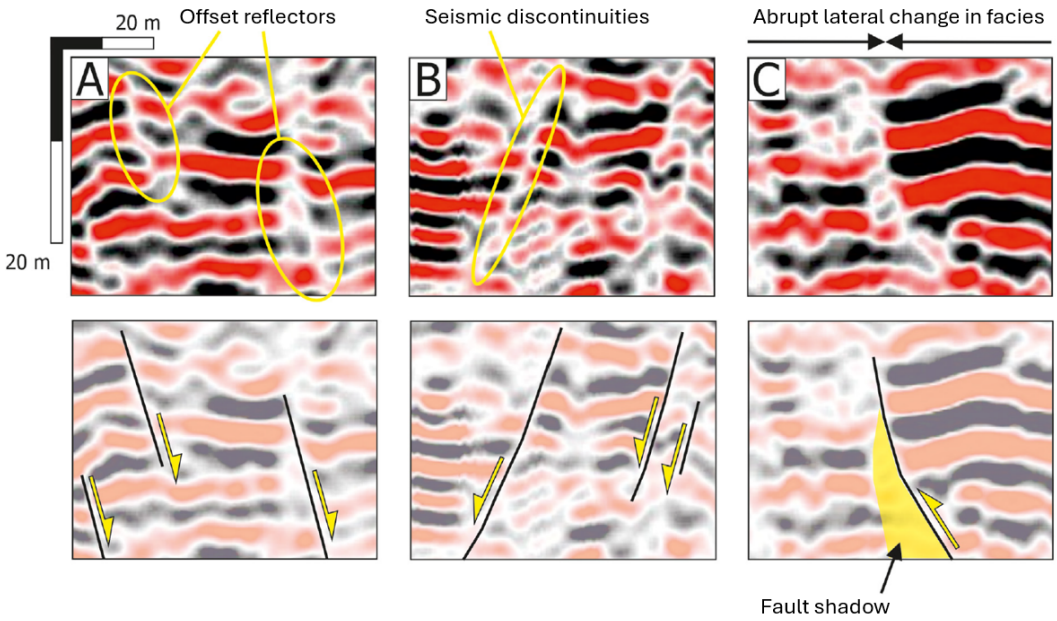


Figure 3.2.1: Examples of fault identification criteria in seismic reflection data (adapted from Brandes et al., 2022). Faults are delineated in the lower images with black lines. Yellow arrows show the sense of movement. A) Offset reflectors, shown with yellow circles, are used to identify the location of multiple faults. Given the downward displacement of hanging wall strata, the faults are interpreted as normal faults. B) Discontinuities, indicated with a yellow oval, imply the presence of a fault. C) Dimmed reflectors near bottom of the image are characteristic of fault shadow, labelled in the lower image in yellow. C also shows an abrupt change in seismic facies indicated with two black arrows.

Mukherjee, 2018). It is important to emphasize, however, that apparent offsets may not always represent true dip-slip displacement. Lateral (strike-slip) motion can result in apparent and variable offsets across seismic profiles, in which case, the observed displacement may not accurately reflect the actual displacement (e.g., Brandes et al., 2022).

2. **Discontinuities (Figure 3.2.1 B)**: When encountered laterally, brief breaks in reflectors – also known as seismic discontinuities - may indicate the presence of faults or fractures (Brandes et al., 2022; Misra and Mukherjee, 2018). Other geologic processes can create seismic discontinuities. For example, due to erosion and sediment transport, channelized slopes result in discontinuities, abrupt changes in seismic facies (see 5), or reflector truncations (see 6) (e.g., Eberli et al., 2004). Discontinuities are also common in low-quality data, where they may indicate poor signal quality (Nanda, 2021).

3. **Fault shadow (Figure 3.2.1 C)**: Ray bending, due to abrupt lateral velocity changes, often occurs across faults where facies with different physical properties are displaced relative to those on the other side (Fagin, 1996). This ray bending effect is known as fault shadow and results in slightly dimmed amplitudes on the footwall of a fault (e.g., Brandes et al., 2022). The fault shadow effect directly indicates the presence of a fault; however, it can be difficult to discern in noisy or low-resolution datasets.

4. **Fault plane reflections (Figure 3.2.2)**: Mineralization or fluid movement and accumulation along fault planes can result in planes being directly imaged, creating a visible reflection or bright spot where the fault is located (Misra and Mukherjee, 2018). Fault plane reflections are arc-shaped, steeply dipping reflectors and are occasionally referred to as 'illuminated faults' in literature (e.g., Dimmen et al., 2023).

5. **Abrupt change in seismic facies (Figure 3.2.1 C and 3.2.3)**: An abrupt lateral change in seismic units may indicate the presence of a fault and possible lateral displacement (e.g., Greene and Barrie, 2020). While a fault is one possible cause, abrupt lateral changes in seismic units can occur due to other geologic processes or artifacts (e.g., channelized slopes, see 2; shallow gas, Marlow et al., 1996).

6. **Reflector truncations (Figure 3.2.3)**: Reflector truncations occur when a reflector is suddenly cut off and does not reappear at an offset. Reflections may

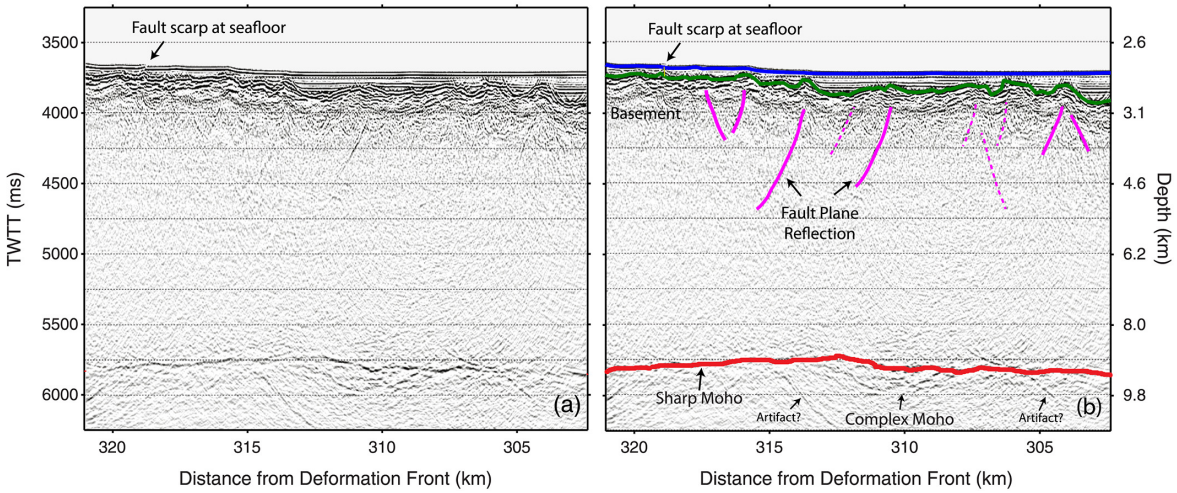


Figure 3.2.2: Uninterpreted (left) and interpreted (right) multichannel seismic reflection profiles (from Han et al., 2016). Fault plane reflections are shown in pink. Dashed lines indicate weak reflections. Blue and green lines indicate the seafloor and top of basement, respectively. The Moho is shown in red.

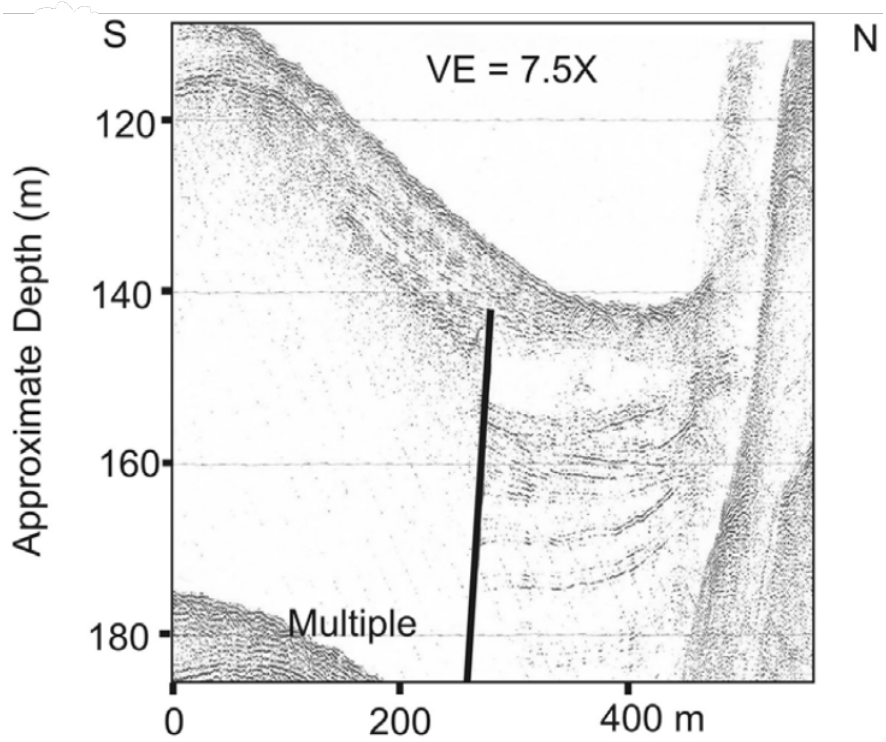


Figure 3.2.3: A fault, indicated with a black line, interpreted based on reflector truncations in a cross-bedded unit paired with an abrupt change in seismic facies from a well-layered, cross-bedded unit in the north contrasted with an acoustically transparent unit to the south (from Greene and Barrie, 2020).

terminate at a fault, and this criterion is particularly obvious when combined with an abrupt change in facies (e.g., Greene and Barrie, 2020). However, it's important to note that there are multiple reasons reflections could have truncation, including other geologic processes or errors in seismic data processing. For example, stacking - a common seismic processing technique which sums and averages multiple seismic traces to reduce noise - may erroneously cause reflectors to appear as if they terminate (Dondurdur, 2018; Misra and Mukherjee, 2018).

7. **Associated folding and deformation (Figure 3.2.4)**: Multiple types of folding are directly associated with faults and can be imaged in seismic reflection data. Fault drag, for example, a type of folding that occurs due to the bending of strata adjacent to a fault, is easily observed in seismic images and can occur on either reverse or normal faults (Grasemann et al., 2005). Fault-propagation folds and rollover folding are other examples of associated folding and deformation which are indicative of faults.

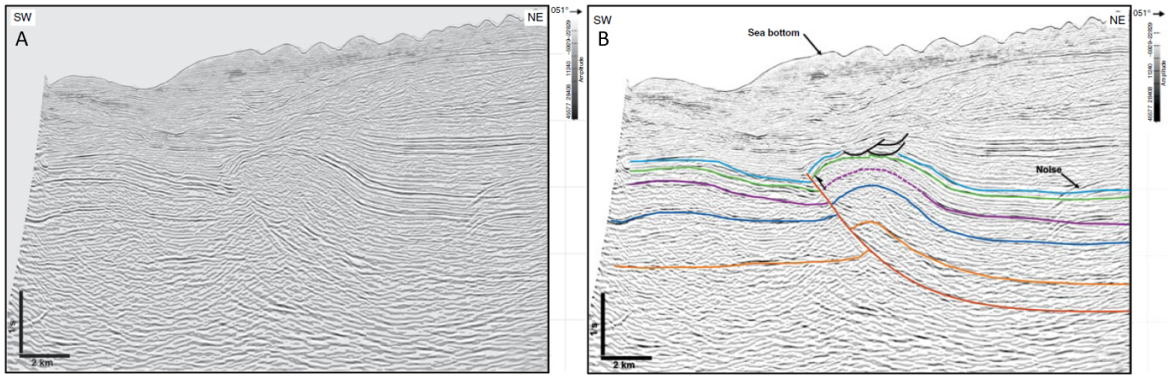


Figure 3.2.4: Uninterpreted (A) and interpreted (B) seismic profile of a fault and fault propagation fold (adapted from Misra, 2018). The fault is indicated with dark orange. Clearly offset and folded horizons are delineated in B.

8. **Abrupt changes in dip (Figure 3.2.5)**: Abruptly steepened dips, such as those seen over short monoclinal folds, can indicate the presence of a fault, particularly for small-scale faults where the total vertical displacement is close to the limit of vertical seismic resolution, i.e., $\lambda/4$ (Dimmen et al., 2023; Misra and Mukherjee, 2018). Changes in dip are, of course, not exclusive to faulting; in the absence of other fault indicators, the change in dip may be due to other geologic processes.

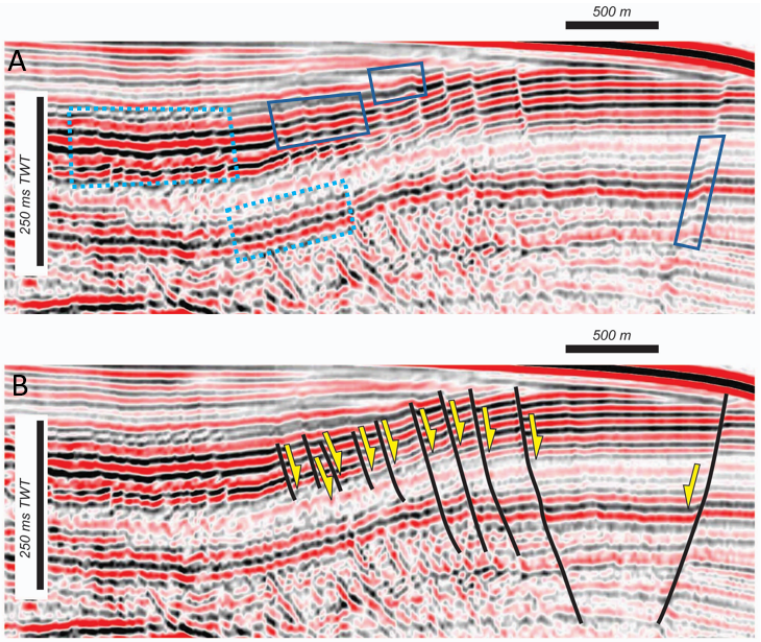


Figure 3.2.5: Uninterpreted (A) and interpreted (B) seismic profile illustrating a set of closely-spaced normal faults (modified from Butler, 2021). Short monoclinal folds can be seen throughout (e.g., dark blue boxes in A). Areas that may contain faults with spacing or offsets too small to resolve, apparent as successive small monoclinal folds, are highlighted with dotted light blue boxes in A. Interpreted faults are indicated in B.

3.3 Seismic Unit and Horizon Interpretation

The glacial history of the Strait of Georgia, and subsequent sedimentation at the Fraser River Delta, strongly influence the seismic units and interpreted horizons in the region's shallow subsurface (see Chapter 2.1.2). However, it is crucial to emphasize that seismic reflection data illustrate acoustic impedance contrasts between subsurface layers. Specific sediment and bedrock types, therefore, are not determined from seismic reflection data alone. Rather, interpretations of seismic units and horizons are based on seismic facies characteristics, such as reflection amplitude, continuity, and configuration (e.g., parallel, sub-parallel, chaotic). These units are correlated with ground-truth data, including sediment cores and grab samples, to assign a geologic understanding.

The seismic units in this study are consistent with previous work in the region (e.g., Hamilton, 1991; Mosher et al., 2000) and comprise three unconsolidated Quaternary units and a bedrock unit. These units have been well-documented in earlier

studies (e.g., Hamilton, 1991; Hart and Hamilton, 1993; Mosher and Hamilton, 1998), and a brief summary of their characteristics is provided below and in Figure 3.3.1.

3.3.1 Unit Descriptions

3.3.1.0.1 Upper post-glacial unit: A predominantly acoustically transparent unit. In previous studies, this unit has been interpreted as Holocene mud deposits originating from the Fraser River (Hamilton, 1991). In places, the unit presents faint, continuous, parallel internal reflections indicative of sediment stratification. The unit has local areas of high acoustic turbidity and brightened reflections, interpreted as evidence for subsurface fluids (Mosher and Hamilton, 1998). High levels of interstitial fluids scatter and attenuate seismic signals, resulting in zones of high acoustic turbidity ("gas masking") and isolated strong reflectors ("gas brightening") (Hart and Hamilton, 1993). Acoustic turbidity in the Strait of Georgia and Fraser prodelta region can obscure underlying structures, increasing uncertainty in seismic interpretations.

3.3.1.0.2 Lower post-glacial unit: Defined by horizontal, continuous reflections that represent sediment infilling accommodation space. The top of the unit is defined by a high-amplitude reflection. The unit does not appear to outcrop at the seafloor within the study area and is interpreted as a deglacial facies consisting of laminated and bedded silt (Mosher and Hamilton, 1998; Mosher et al., 2000). Hamilton (1991) interpreted this unit as glaciomarine turbidite sequences deposited during glacial retreat (Late Wisconsinan to Early Holocene), similar in character to ice recessional facies observed along other marine margins.

3.3.1.0.3 Glacial unit: Defined by an irregular top surface and high-amplitude internal reflections. Internal reflections vary considerably in orientation from horizontal and continuous to semi-chaotic. In previous work, this unit has been interpreted to be Pleistocene in age and composed of tills and glaciomarine sediments, as well as interglacial marine deposits which have been scoured and reworked by subsequent glaciations (Hamilton 1991; Mosher and Hamilton, 1998).

3.3.1.0.4 Bedrock unit: The acoustic basement. Shallow bedrock within the Strait of Georgia is largely composed of Jurassic, Cretaceous, and Paleogene rocks

of the Coast Plutonic Complex, Nanaimo Group, and Huntingdon Formation (Clague, 1998; England and Bustin, 1998; White and Clowes, 1984). The composition of the unit transitions across the strait from well-bedded marine sedimentary rocks of the Upper Cretaceous Nanaimo Group along the southwest edge of the strait to the granitic Coast Plutonic Complex in the north and northeast, and the overlying Paleogene Huntingdon Formation, composed of non-marine sedimentary rocks, to the east (Clague, 1998; England and Bustin, 1998; White and Clowes, 1984; Zelt et al., 2001).

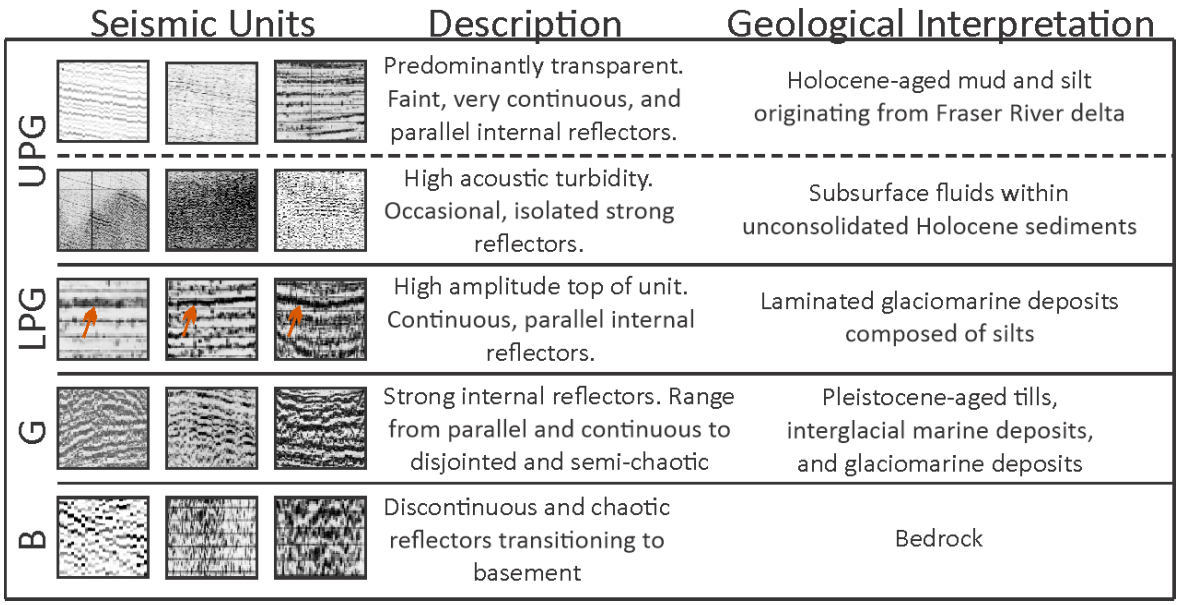


Figure 3.3.1: Simplified summary of seismic units with example images and geological interpretations. UPG: upper post-glacial, LPG: lower post-glacial (top of unit indicated with orange arrow), G: glacial, B: bedrock.

Chapter 4

Near-Surface Indicators of Active Faulting in the Central Strait of Georgia, Canada

4.1 Abstract

Understanding seismic hazard and associated risk in the central Strait of Georgia region of British Columbia requires identifying and mapping evidence of active faulting. To address this objective, >2200 line-kilometres of seismic reflection profiles are systematically interpreted. Seismic units are interpreted across all lines, and potential faults are assessed using a set of 8 criteria: reflection offsets, reflection discontinuities, abrupt lateral change in seismic units, reflection truncations, associated folding and deformation, abrupt changes in dip, fault shadow, and fault plane reflections. Evidence of active faulting is observed throughout the study area. While many indicators appear localized, others demonstrate lateral continuity along linear trends and consistency across multiple seismic reflection profiles. These seismic reflection interpretations enable the delineation of the Central Salish Sea fault, located 10 km offshore from Metro Vancouver. Although first identified two decades ago, the fault has not previously been mapped beyond its surface expression. The fault is traced with multiple criteria to a length of 12 km, with a possible extension up to a total length of 25 km. Evidence of active faulting is also observed in other regions of the study area, including beneath a seafloor scarp offshore Bowen Island and a seafloor lineament near Gabriola Island.

4.2 Introduction

4.2.1 Motivation and Objectives

The southwest coast of British Columbia, home to Canada's largest coastal population, is situated at the north end of the Cascadia subduction zone (Figure 4.2.1). With a population exceeding 3.5 million people (Statistics Canada, 2023), including urban centres like Metro Vancouver, Victoria, Nanaimo, and Sechelt, the region is particularly vulnerable to impacts from strong earthquake shaking. Three types of earthquakes occur within the region: subduction megathrust events at the interface between the Juan de Fuca and North America plates, intraslab events within the subducting Juan de Fuca plate, and shallow crustal events within the North America plate (Cassidy et al., 2000). Crustal earthquakes are notably the most numerous in the region's instrumental record (Rogers, 1998). Additionally, the three largest earthquakes recorded in southwest British Columbia and northwest Washington were crustal events, each with a magnitude of M_w ~7 or greater (Rogers and Hasegawa, 1978; Cassidy et al., 1988; Malone and Bor, 1979). Earthquakes on crustal faults occur at relatively shallow depths and can, therefore, result in significantly greater ground shaking and damage than deeper events of comparable magnitude. Despite the prominence of such earthquakes in southwest British Columbia, there is a lack of essential information about crustal events and their causative faults in the region.

Crustal faults can have recurrence intervals on the order of thousands of years and may not generate significant microseismicity, making them difficult to detect solely through seismic monitoring (e.g., Balfour et al., 2011). Potentially long recurrence intervals do not imply that such faults should be disregarded as sources of seismic hazard. For example, in 2023, two large-magnitude events (M_w 7.8 and M_w 7.6) occurred along the East Anatolian fault zone in Turkey just 9 hours apart, resulting in significant loss of life across 12 cities (Karabulut et al., 2023). Notably, the M_w 7.6 event occurred in a seismic gap with only one prior historical event, which occurred before the advent of instrumental seismic monitoring (Karabulut et al., 2023). Similarly, previously unknown crustal faults have resulted in significant economic impacts and fatalities, such as the Greendale fault in New Zealand, which ruptured in 2010 producing a M_w 7.1 earthquake and damaging aftershocks (Gledhill et al., 2011; Wood et al., 2016).

In order to enhance the understanding of seismic hazard in coastal British Columbia,

this study aims to assess seismic reflection data, primarily legacy data from the Geological Survey of Canada (GSC), for indicators of active faulting across the central Strait of Georgia (SoG) between the Canadian cities of Metro Vancouver, Nanaimo and Sechelt (Figure 4.2.1). The objectives of this study are to: 1) evaluate whether previously unrecognized geologically-recent (Holocene or Quaternary) faulting is present in the shallow subsurface, and 2) constrain the extent of associated fault structures, if present.

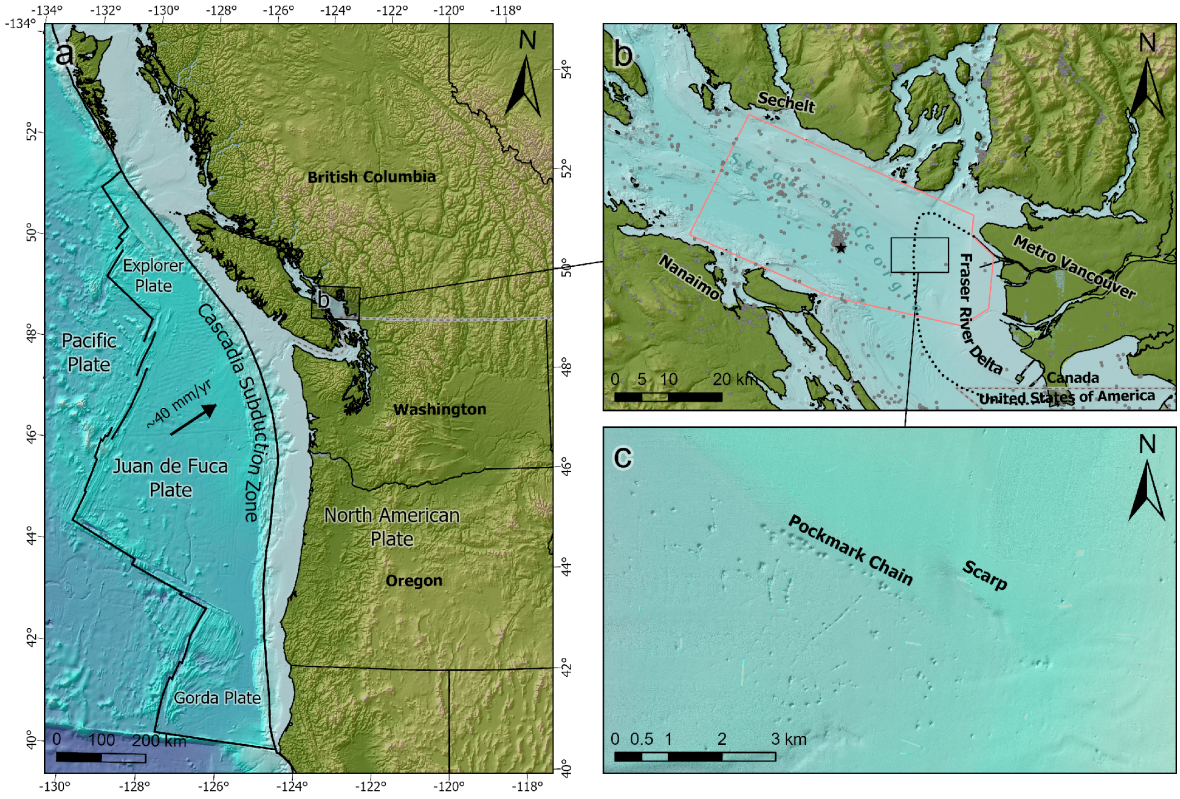


Figure 4.2.1: Tectonic setting in northern Cascadia. a) Overview of Cascadia subduction zone and Juan de Fuca plate motion with respect to North America (black arrow; DeMets et al., 2010). b) Study area within the SoG (red box) with crustal seismicity (grey dots; S and A grade events from Merrill et al., 2022) and epicentral location of the 1997 earthquake cluster (black star). Approximate extent of the Fraser River delta is shown with a black dotted line (La Croix et al., 2024). c) 5-m resolution multibeam bathymetry from 2000 detailing fault-related morphology first identified in Barrie and Hill (2004). Basemap created from Kung et al. (2023) and GEBCO (2020).

4.2.2 Geologic/Glacial Context

The central SOG is part of the Georgia Basin, a sedimentary and structural forearc basin that underlies parts of Vancouver Island, the SoG, and the adjacent mainland of southern British Columbia and northwest Washington. Bedrock is composed of Cretaceous to Late Eocene sedimentary rocks, overlain by thick sequences of unconsolidated Quaternary sediments (Hamilton, 1991; England and Bustin, 1998).

Canada's west coast has undergone a complex history of successive glaciations throughout the Pleistocene, which significantly influenced the basin's surface morphology and subsurface. During the late Wisconsinan glaciation (locally referred to as the Fraser glaciation, with ice cover in the SoG from ∼30 to 11 ka), ice flow was oriented down the axis of the SoG, southeastward at ∼100-110° from north (Clague and James, 2002; Barrie et al., 2005). This glacial activity eroded bedrock within the Georgia Basin into NW-SE oriented ridges and troughs (Clague et al., 1998). Successive glaciations deposited and reworked large amounts of sediment, resulting in deposition of glacial till, ice-marginal glaciomarine facies, and eventually ice-recessional glaciomarine turbidite sequences during rapid deglaciation (Barrie and Conway, 2002). Consequently, NW-SE oriented linear geomorphological features within the region may originate from either glacial and/or tectonic processes, leading to interpretation ambiguity.

Present-day sedimentation rates within the central SoG are largely governed by sediment input from the Fraser River, with sedimentation being dominated by sands and silts (Johannessen et al., 2003; La Croix et al., 2024). Coarser sediments, primarily sand, deposit near the delta front, while mud deposits form across the Prodelta (Hill et al., 2008). Sedimentation rates vary seasonally and with proximity to the Fraser River delta (Figure 4.2.1), ranging from 3 to 10 cm/yr (Hart et al., 1998).

4.2.3 Tectonic Context

Off the west coast of Vancouver Island, northeastward subduction of the Juan de Fuca plate beneath North America forms the Cascadia subduction zone (Figure 4.2.1 A; DeMets et al., 2010). The oblique relative plate motion contributes to northward migration of the Oregon and Washington forearc blocks (Wells et al., 1998). Further north, the rate of margin-parallel migration reduces due to decreasing obliquity, which results in strain accumulation within the upper plate in northwest Washington

and southwest British Columbia (Wells et al., 1998; Mazzotti et al., 2002; Finley et al., 2019). Global Navigation Satellite System (GNSS) observations indicate approximately 5 mm/yr of north-south-directed shortening in northwest Washington (Mazzotti et al., 2002). Rates of north-south shortening reduce to 0-2 mm/yr north of ∼48° (Mazzotti et al., 2002). Earlier models proposed that forearc shortening in northern Cascadia was bounded to the north by the Leech River – Devils Mountain fault, with the Coast Mountains serving as a rigid buttress (Wells et al., 1998; Johnson et al., 2001). More recent research on active faulting in southwestern British Columbia, however, has challenged this hypothesis and provided evidence for deformation farther north than previously suggested (e.g., Barrie and Hill, 2004; Caston, 2021; Greene et al., 2018; Kelsey et al., 2012; Lynch et al., 2023).

Crustal seismicity in the central SoG has been persistent in the instrumental record, consisting of low- to moderate- magnitude events (Figure 4.2.1 B). Notably, two moderate-sized crustal earthquake sequences were recorded in the region, one in 1975 and another in 1997 (Figure 4.2.1 B; Rogers, 1979; Cassidy et al., 2000). Both sequences had mainshocks of similar magnitude (M_L 4.9 in 1975 and M_W 4.6 in 1997) and similar location, approximately 30 km from both the cities of Nanaimo and Vancouver, British Columbia (Figure 4.2.1 B; Rogers, 1979; Cassidy et al., 2000). These events were felt as far as Seattle, Washington and southern Vancouver Island (Rogers, 1979; Cassidy et al., 2000).

4.2.4 Previous Work on Crustal Faults in the Central Strait of Georgia

Following the M_W 4.6 earthquake and aftershock sequence in June 1997 (Figure 4.2.1 B), targeted studies of seismicity (Cassidy et al., 2000), multibeam bathymetry (Barrie and Hill, 2004), and seismic reflection data (Mosher et al., 2000; Barrie and Hill, 2004) were conducted in the central SoG to map and characterize crustal faults in the region. Cassidy et al. (2000) used focal mechanism solutions from P-nodal and centroid moment tensors, combined with relocated hypocentre data, to delineate a northward-dipping east-west trending reverse fault responsible for the 1997 sequence. While this fault has not been linked to any surface or near-surface expression in the region, Mosher et al. (2000) identified a deformation zone and associated faults at depths of ∼1-3 km within bedrock approximately 3-5 km southwest of the 1997 event in multichannel seismic reflection data. This deformation zone reasonably aligns with the

projected fault plane of Cassidy et al. (2000); however, offsets within the deformation zones were interpreted as indicative of normal or listric normal faulting, contrasting with the reverse focal mechanisms of Cassidy et al. (2000) and the modern stress regime (Balfour et al., 2011). As the seismic profile did not traverse directly over the hypocentres of the 1997 events, a definitive correlation between these faults and the earthquake cluster could not be established (Mosher et al., 2000).

Approximately 13 km east of the 1997 earthquake sequence, Barrie and Hill (2004) identified a 2.7 km long scarp and 4.0 km long linear pockmark chain in the central SoG based on an analysis of multibeam bathymetry data (Figure 4.2.1 C). Based on two seismic reflection profiles, these features were subsequently interpreted as the surface expression of a Holocene-active crustal fault, extending over a combined distance of ∼4.6 km (Barrie and Hill, 2004). Previously referred to as the 'Fraser Delta' fault (Barrie and Hill, 2004), the name 'Central Salish Sea' fault (CSSF) is used hereafter to avoid confusion with the Fraser River Delta fault (Greene et al., 2018; Caston, 2021) located in the southern SoG.

4.3 Methods and Data

The study area for this work is a region of the central SoG located between the cities of Vancouver, Nanaimo, and Sechelt as indicated in Figure 4.2.1 B. As detailed below, a seismic reflection dataset supplemented by multibeam echosounder (MBES) and light detection and ranging (LiDAR) data are used to investigate evidence for active faulting in the central SoG.

IHS Kingdom Suite was used for interpretation of seismic reflection data, while Esri ArcGIS Pro was used for interpretation of multibeam bathymetry, backscatter, and LiDAR datasets. Legacy seismic reflection profiles were digitized using custom-written software produced at the Geological Survey of Canada (Courtney, 2013).

4.3.1 Seismic Reflection Dataset

The seismic reflection datasets analysed herein span 42 years of acquisition (1982 to 2024) and primarily comprise legacy paper seismic reflection records (1982-2003) collected using airgun, deep-tow boomer (Huntec DTS), and 3.5 kHz instruments. Ad-

ditional electric pulser sub-bottom profiler data collected over Sturgeon Bank and the Fraser River delta front, digital holdings, and a 3D airgun volume complete the dataset, as detailed below (Figure 4.3.1). Please see Appendix A for a complete collection of figures for all seismic reflection lines and interpretations. Most of the high-resolution, fully rectified scans of analogue data, as well as digital seismic reflection data, presented herein are publicly available through the Canadian National Marine Seismic Data Repository (a compiled .kmz of seismic lines is available via FTP). As of the time of writing, all seismic reflection data not presently available for public use have been uploaded to an internal staging space and will soon be accessible via FTP.

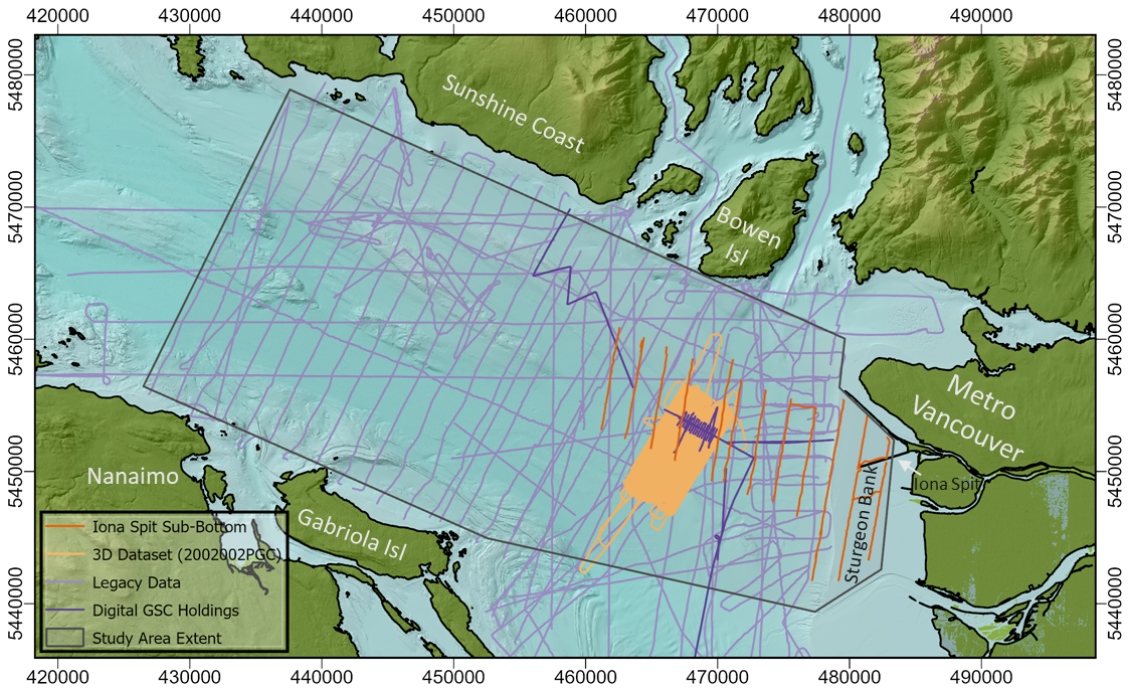


Figure 4.3.1: Map of ship track lines for all seismic reflection profiles. Dark purple, light and dark orange lines represent data collected digitally; light purple lines represent digitized analogue legacy data. Study area extent indicated with grey polygon.

4.3.1.1 Legacy Data and Geological Survey of Canada Holdings

The legacy seismic reflection dataset comprises 1760 line-kilometres of data acquired between 1982 and 2003 across the central SoG (Figure 4.3.1). These data were collected using a variety of instruments, including single-channel airgun, a deep tow boomer high resolution system (DTS; e.g., Huntec), and 3.5 kHz Compressed High Intensity Radiated Pulse (CHIRP). Numerous expeditions collected data from multiple instruments simultaneously (e.g., airgun and DTS, DTS and 3.5 kHz); data were sub-

sequently stored as physical paper records at the Geological Survey of Canada (GSC) – Pacific Geoscience Centre (PGC). Analogue paper copies were scanned, vectorized, rectified and georeferenced with cruise navigation coordinates, then converted into digital formats (JP2000 and SEG-Y) compatible with standard seismic interpretation software. Seismic reflection data collected by the GSC after the mid-2000's are in digital SEG-Y format. These include Huntec and 3.5 kHz CHIRP profiles collected between 2009 and 2023 (100 line-kilometres).

As the legacy dataset is composed of multiple smaller datasets from various cruises over a relatively long collection period, the data vary considerably in line orientation, instrumentation, resolution, and noise as outlined below:

3.5 kHz Compressed High Intensity Radiated Pulse Sub-Bottom Profiler

3.5 kHz CHIRP data comprise high-frequency, high-resolution profiles (e.g., vertical resolution ∼12.5-25 cm, Knudsen, n.d.; horizontal resolution near seafloor ∼50-70 cm) with low penetration (∼10-50 m). Due to high sedimentation rates in the central SoG (3-10 cm/yr; Hart et al., 1998), subbottom profiler data capture between ∼100 and 800 years of sedimentation. CHIRP systems provide excellent resolution for Holocene deformation where sediment stratification is present (see section 4.3.3.2); however, the system's limited penetration depth reduces its effectiveness in providing deeper subsurface information.

Huntec Deep-Tow System

Huntec DTS uses a high-energy boomer or sparker source (typically 800 Hz to 10 kHz; McKeown et al., 2014) and includes both an internal hydrophone and an external multi-element streamer. This results in increased subsurface penetration (up to 500 ms two-way-travel time, ∼375 m) but decreased resolution (vertical resolution ∼20-50 cm; horizontal resolution ∼60-100 cm near seafloor). However, the near-surface resolution of DTS data is substantially higher than the comparatively low-frequency airgun systems. For this study, interpretation was based primarily on data from the external streamer.

Airgun

Legacy airgun data comprise single-channel seismic profiles collected in the 1980's and 1990's (typically 1- and 5-cubic inch guns, 80 to 500 Hz bandwidth; Hart and Hamilton, 1993). These data provide deeper subsurface penetration than 3.5 kHz and Huntec DTS systems (1000 ms two-way-travel time; equivalent to ∼750 m) but

lower resolution (vertical resolution ∼0.75 to 5 m; horizontal resolution ∼1.25-3 m near seafloor).

4.3.1.2 Iona Spit Sub-Bottom Dataset

The Iona Spit dataset was collected from March 12 to 21, 2024, by Frontier Geosciences Inc. aboard a dinghy in shallow water depths (<5 m) and the Eion Mor, a 26-foot aluminum closed-cabin vessel, in deeper waters. Thirteen parallel sub-bottom acoustic profiling lines were collected, spaced approximately 2 km apart for a total of 126 line-kilometres. This dataset was collected to fill in gaps in the existing seismic reflection data coverage. Notably, data were collected over Sturgeon Bank, a shallow area of the Fraser River delta to the west of Richmond, British Columbia, which previously had no sub-bottom data coverage due to its shallow depth. Data were also collected across previously identified segments of the Central Salish Sea fault and to the northwest and southeast of these segments, in areas with no apparent surface expression of faulting.

Sub-bottom acoustic profiles were collected using an electric pulser system (250 Hz) and multi-element hydrophone array within a fluid-filled streamer (Vieira and Candy, 2024). The pulser was towed slightly below the surface, 10 m behind the vessel in shallow waters (< 5 m depth) and 20 m behind in deeper water. The resulting sub-bottom profiles were processed by Frontier Geosciences Inc. using the Seismic Unix reflection processing package (Vieira and Candy, 2024). Filtering was performed in multiple stages: a tapered bandpass filter was applied to attenuate frequencies below 40 Hz and above 600 Hz, followed by a notch filter to remove frequency-specific noise at 92 Hz and 120 Hz, attributed to outboard motor and electronic noise (Vieira and Hansen, personal communication, 2025). Trace normalization was performed using RMS amplitude normalization, and weighted trace averaging was applied using a five-trace window with weighted factors (0.2, 0.5, 1, 0.5, 0.2) to suppress localized noise (Vieira and Hansen, personal communication, 2025). Spike deconvolution was used to enhance reflection continuity and reduce multiples (Vieira and Hansen, personal communication, 2025). Finally, processed data were converted to SEG-Y format and georeferenced using shipboard GPS navigation tracks (Vieira and Candy, 2024). After receiving the data, attached navigation coordinates were converted from cm to m (UTM 10N) using tools developed at the GSC for interpretation in Kingdom Suite.

4.3.1.3 3D Seismic Dataset (2002002PGC)

Seismic data were collected on the Canadian Coast Guard Ship (CCGS) John P. Tully from May 21 to 26, 2002 as part of the Georgia Basin Geohazard Initiative at the GSC. The 3D dataset consists of 100 lines spaced 50 m apart, located over the linear pockmark chain and adjacent pockmark field (Riedel, 2002). For each line, single-channel airgun profiles and high-resolution DTS profiles (internal and external receivers) were collected concurrently. Profiles include ship turns in their recording, and turns were always acquired in starboard turn mode to avoid contact between the systems (Riedel, 2002). Seismic equipment was stopped when marine mammals were observed within 100 m of the vessel or if marine mammals observed further away appeared disturbed. As a result, multiple lines have areas with missing data (Riedel, 2002).

Data were viewed as individual 2D seismic profiles and interpreted using an 'under-sampled vertical profile' technique for 3D seismic volumes (e.g., similar to Workflow 5 in Robledo Carvajal et al., 2023): every 5th line was examined, and every 10th line was worked up with interpretations for each data type, for a total of 33 interpreted lines (240 line-kilometres).

4.3.2 Additional Data Sources

High-resolution (1, 2, and 5 m) MBES bathymetry and backscatter are used to compare subsurface fault evidence with seafloor morphology. These data were collected using a hull-mounted Kongsberg EM1002 in 2000 and Kongsberg EM710 in 2010, 2021, and 2023 aboard the vessels CCGS R.B. Young and CCGS Vector, respectively. MBES data collection was carried out by the Canadian Hydrographic Service (CHS) in cooperation with the GSC.

Gridded bathymetry data, derived from high-resolution (2 m) LiDAR surveys collected by CHS in 2021, are used to compare surface morphology with sub-bottom profiler data along the Fraser River delta front. Data were collected with a Leica Hawkeye 4X (HE4X) sensor on a Cessna 404 (N532NM) fixed-wing aircraft.

4.3.3 Seismic Interpretation Framework

4.3.3.1 Active Fault Interpretation Criteria

In this study, 'active' faulting is defined as that which has occurred during the Holocene or Quaternary. While the primary focus of this study requires the identification of Holocene-active faulting, interpretation is complicated by the properties of Holocene sediment within the central SoG. Across the study area, Holocene sedimentation largely consists of silts and muds (LaCroix et al., 2024). The upper post-glacial unit interpreted in this study (defined further below) is made up of Holocene silt-rich sediments and frequently presents as acoustically transparent or faintly stratified. As a result, the unit may not clearly demonstrate offset or deformation, nor may it effectively maintain post-rupture structure.

Therefore, a set of criteria is employed to identify evidence of Quaternary and Holocene-active faulting in shallow seismic reflection data. This includes: 1) reflection offsets, 2) reflection discontinuities, 3) fault shadow, 4) fault plane reflections, 5) abrupt lateral change in seismic units, 6) reflection truncations, 7) associated folding and deformation, and 8) abrupt changes in dip.

Many of these indicators (discontinuities, truncations, lateral change in seismic unit, folding and deformation, abrupt changes in dip) are not exclusive to a faulting origin. Instead, they may be indicative of other geologic processes (e.g., paleochannels: truncations, change in seismic unit and discontinuities; e.g., Eberli et al., 2004), in situ fluids (apparent offsets, truncations, change in seismic unit and discontinuities; e.g., Marlow et al., 1996), errors in seismic processing, or degradation of signal with depth. To minimize misinterpretation, a multi-criterion (requiring at least two fault indicators per profile), multi-record (confirming fault presence across at least two adjacent seismic lines) approach was implemented wherever possible.

The relative ages of fault indicators are interpreted based on which seismic unit they affect (i.e., Holocene-active fault evidence must occur within the upper and/or lower post-glacial units – see 4.3.3.2 Seismic Units). Thus, the analyses in this study do not account for blind faults, which may have been active within the Holocene but do not penetrate or disrupt younger overlying units.

4.3.3.2 Seismic Units

The seismic units in this chapter align with those described in detail in previous studies of the central Strait of Georgia (e.g., Hamilton, 1991; Hart and Hamilton, 1993; Mosher and Hamilton, 1998; Mosher et al., 2000). These include three unconsolidated Quaternary units and a bedrock unit; a concise summary of their characteristics is provided below.

Upper post-glacial unit: A predominantly acoustically transparent unit. In previous studies, this unit has been interpreted as Holocene mud deposits originating from the Fraser River (Hamilton, 1991). In places, the unit presents faint, continuous, parallel internal reflections indicative of sediment stratification. The unit has local areas of high acoustic turbidity and brightened reflections, interpreted as evidence for subsurface fluids (Mosher and Hamilton, 1998). High levels of interstitial fluids scatter and attenuate seismic signals, resulting in zones of high acoustic turbidity ("gas masking") and isolated high amplitude reflections ("gas brightening") (Hart and Hamilton, 1993). Acoustic turbidity in the Strait of Georgia and Fraser prodelta region can obscure underlying structures, limiting the effectiveness of shallowly penetrating seismic systems and increasing uncertainty in seismic interpretations.

Lower post-glacial unit: Defined by horizontal, continuous reflections infilling accommodation space. The top of the unit is defined by a high-amplitude reflection. The unit does not appear to outcrop at the seafloor within the study area and is interpreted as a deglacial facies consisting of laminated and bedded silt (Mosher and Hamilton, 1998; Mosher et al., 2000). Hamilton (1991) interpreted this unit as glaciomarine turbidite sequences deposited during glacial retreat (Late Wisconsinan to Early Holocene), similar in character to ice recessional facies observed along other marine margins.

Glacial unit: Defined by an irregular top surface and high-amplitude internal reflections. Internal reflections vary considerably in orientation from horizontal and continuous to semi-chaotic. In previous works, this unit has been interpreted to be Pleistocene in age and composed of tills and glaciomarine sediments, as well as interglacial marine deposits which were scoured and reworked by subsequent glaciations (Hamilton 1991; Mosher and Hamilton, 1998).

Bedrock unit: The acoustic basement. Shallow bedrock within the Strait of Georgia is largely composed of Jurassic, Cretaceous, and Paleogene rocks of the Coast Plutonic Complex, Nanaimo Group, and Huntingdon Formation (Clague, 1998; England

and Bustin, 1998; White and Clowes, 1984). The composition of this unit transitions across the Strait from well-bedded marine sedimentary rocks of the Upper Cretaceous Nanaimo Group along the southwest edge of the Strait to the granitic Coast Plutonic Complex in the north and northeast. To the east, the Paleogene Huntingdon Formation, composed of non-marine sedimentary rocks, overlies other bedrock units (Clague, 1998; England and Bustin, 1998; White and Clowes, 1984; Zelt et al., 2001).

4.3.4 Data and Methodological Considerations

The seismic interpretations herein rely primarily on shallow, high-resolution seismic reflection data as outlined above, which are subject to inherent limitations and characteristics that are important to consider prior to interpreting results. For example, the ability of seismic reflection data to penetrate the subsurface is constrained by source frequency, with lower frequencies and longer wavelengths being able to travel deeper into the subsurface (Dondurur, 2018). In this study, the maximum two-way-travel time across the dataset is 1000 ms (high-resolution airgun source), which corresponds to a maximum depth of ∼750-1000 m, assuming an average seismic velocity of 1500-2000 m/s. Consequently, structures such as the bedrock deformation zone identified by Mosher et al. (2000) at ∼1-3 km depth, located near the 1997 earthquake cluster in the central SoG, are beyond the resolution of this dataset.

The trade-off for limited subsurface penetration with higher frequency sources is increased vertical resolution at shallower depths of interest. Vertical resolution for seismic reflection data is primarily determined by the wavelength (λ) of the seismic wave generated by a seismic source, with higher frequencies, and therefore shorter wavelengths, producing higher resolutions (Mosher and Simpkin, 1999). Generally, $\lambda/4$ is regarded as the reasonable limit of vertical resolution (Nanda, 2021; Dimmen et al., 2023). For the high-resolution seismic reflection data in this study's dataset, this translates to approximately 1-6 m for airgun, 0.2-0.5 m for Huntec, and 0.125-0.25 m for 3.5 kHz data. Structures and sediment deformation at scales smaller than this will not be resolved. Horizontal resolution can be approximated by the width of the Fresnel zone ($r = \sqrt{z\lambda/2}$), which is dependent on both frequency and depth. In this dataset, it ranges from approximately 0.5-0.7 m (3.5 kHz), 0.6-1.0 m (Huntec DTS), and 1.25-3 m (airgun) at very shallow depths. It is noted, however, that horizontal resolution is also influenced by survey acquisition geometry and migration, so these values are considered simple approximations.

Finally, as high-frequency signals attenuate with depth, seismic resolution decreases and noise increases with depth across the dataset. As a result, identifying faults in areas with high noise introduces uncertainty, as reflections often present as discontinuous and chaotic at depth. In these cases, the discontinuity of the reflections – one of 8 criteria for faulting utilized in this study - does not necessarily indicate a fault but may instead be a consequence of poor signal quality (Nanda, 2021).

4.4 Results

Potential indicators of active faulting throughout the central SoG are identified and mapped, based principally on the interpretation of seismic reflection data (Figure 4.4.1). A simplified map showing interpreted and inferred faults is provided in Figure 4.4.2. For discussion, results are divided into five geographic subareas: 1) Fraser Prodelta, 2) Sturgeon Bank, 3) Point Grey Dredge Disposal Area, 4) Offshore NE Gabriola Island and Vicinity of the 1997 and 1975 Earthquake Clusters, and 5) Halibut Bank (Figure 4.4.3). A representative subset of interpreted seismic reflection lines is presented herein; all lines interpreted for this study are shown in Figure 4.3.1, with the complete dataset available in Appendix A.

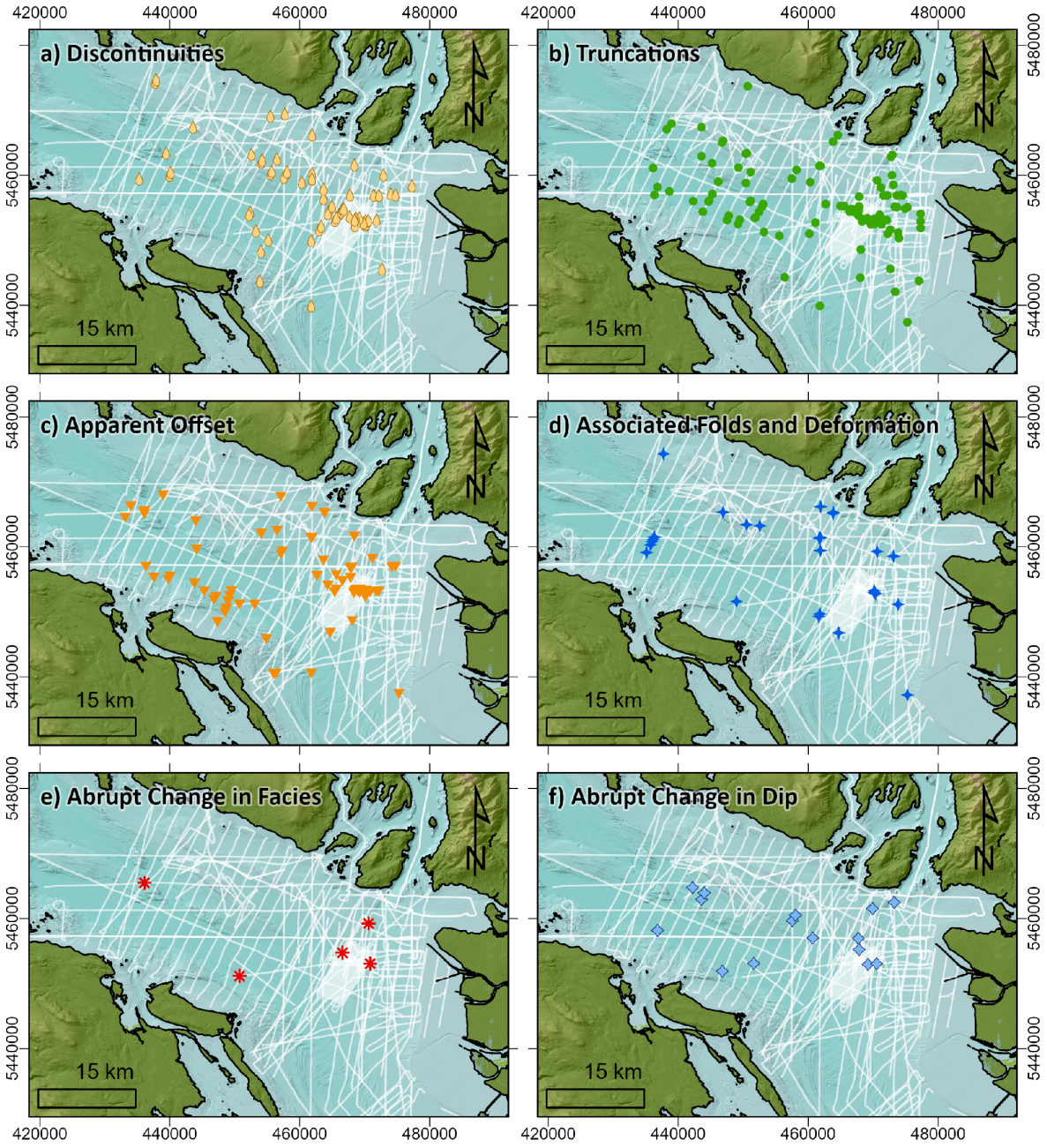


Figure 4.4.1: Spatial distribution of indicators of potential faults identified across the central SoG, categorized by fault criteria. A) Reflection discontinuities (yellow teardrops), B) reflection truncations (green circles), C) apparent reflection offsets (orange triangles), D) associated folds and deformation (deep blue four-point stars), E) abrupt change in seismic facies (red asterisks), F) abrupt change in dip (light blue diamonds). Seismic reflection profile locations are denoted by white lines.

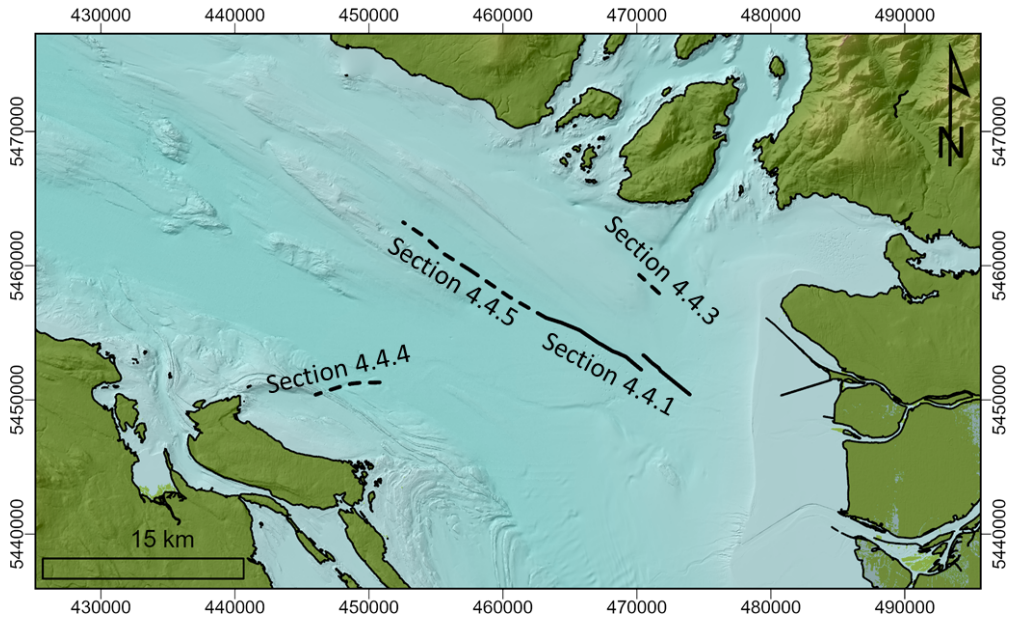


Figure 4.4.2: Simplified fault map based on seismic reflection and MBES interpretations. Inferred faults are indicated with dashed lines. References to relevant subsections for each segment are denoted within the figure.

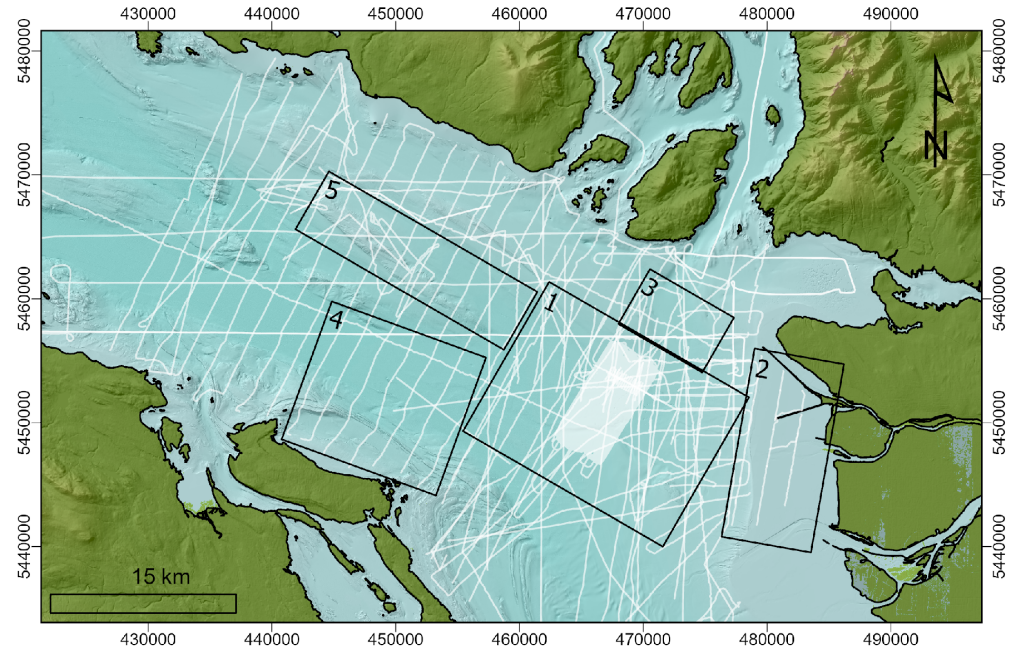


Figure 4.4.3: Map of subarea locations discussed in sections 4.4.1-4.4.5. 1) Fraser Prodelta, 2) Sturgeon Bank, 3) Point Grey Dredge Disposal Area, 4) Offshore NE Gabriola Island and Vicinity of the 1997 and 1975 Earthquake Clusters, 5) Halibut Bank.

4.4.1 Subarea 1: Fraser Prodelta

The Fraser Prodelta subarea (Figure 4.4.3) lies west of Vancouver and covers the area of active faulting previously identified by Barrie and Hill (2004), referred to herein as the CSSF. Locations for presented seismic reflection profiles are shown in Figure 4.4.4.

Subsurface data throughout are characterized by extensive acoustic turbidity and locally brightened reflections, indicating the presence of subsurface gases. Unfortunately, these features partially mask and limit seismic interpretation, particularly in shallow 3.5 kHz sub-bottom profiles (e.g., Figure 4.4.5). Subsurface evidence for fluids is consistent with the presence of seafloor pockmarks (fluid escape features) visible in multibeam bathymetry data (Figure 4.4.6). Potential faulting indicators for the CSSF were observed not only beneath the geomorphic features identified by Barrie and Hill (2004) but also in areas lacking any discernible surface expression, as detailed below.

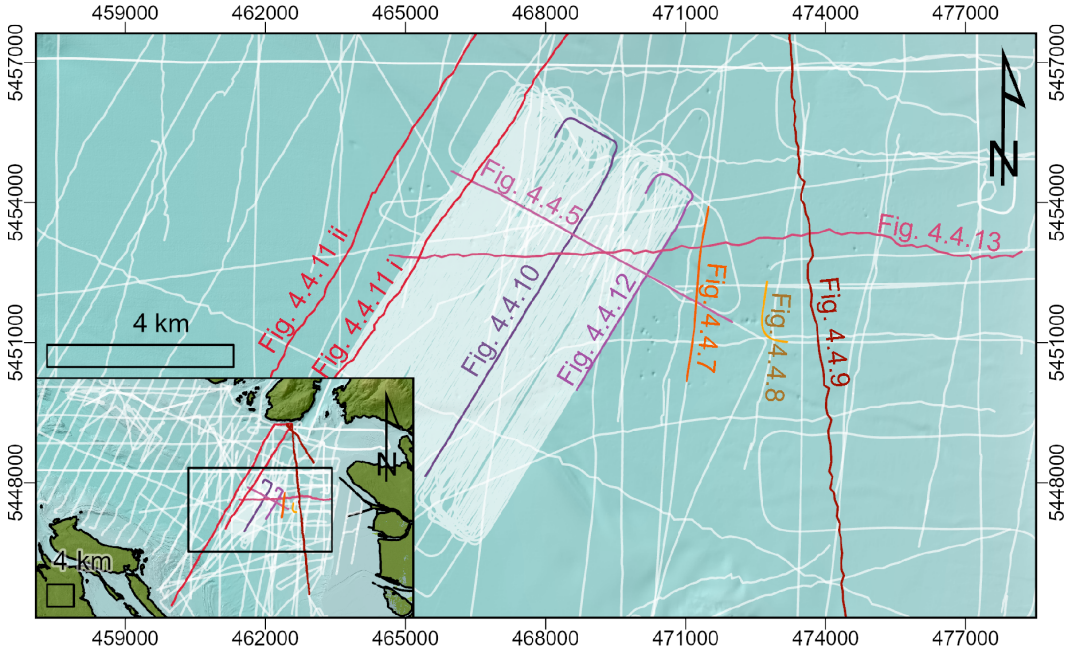


Figure 4.4.4: Fraser Prodelta subarea and seismic reflection data coverage (white lines). The locations of Figures 4.4.5 to 4.4.13 are indicated with coloured lines in the main map and inset.

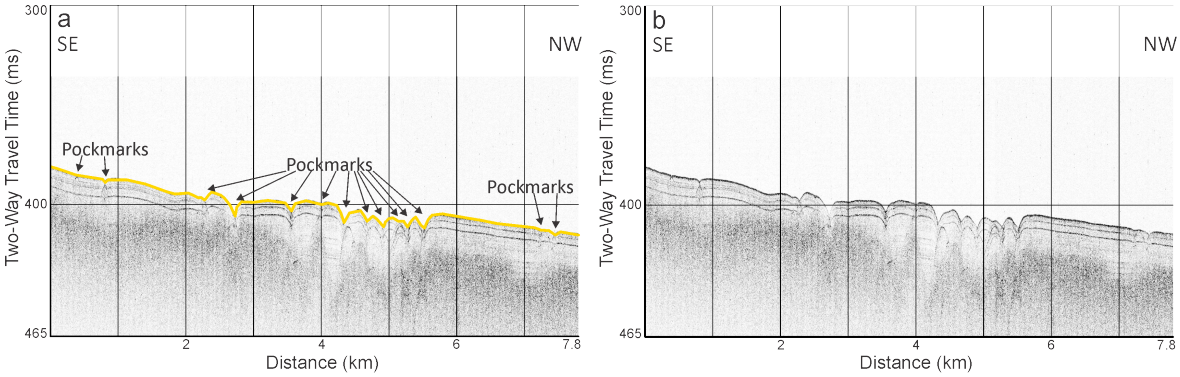


Figure 4.4.5: 3.5 kHz sub-bottom profile along the pockmark chain of the CSSF. Line 19 from cruise 2023004PGC. A) Interpreted profile showing upper post-glacial unit (horizon marked in yellow at seafloor) with significant acoustic turbidity and multiple pockmarks. B) Uninterpreted profile. See Figure 4.4.4 for location.

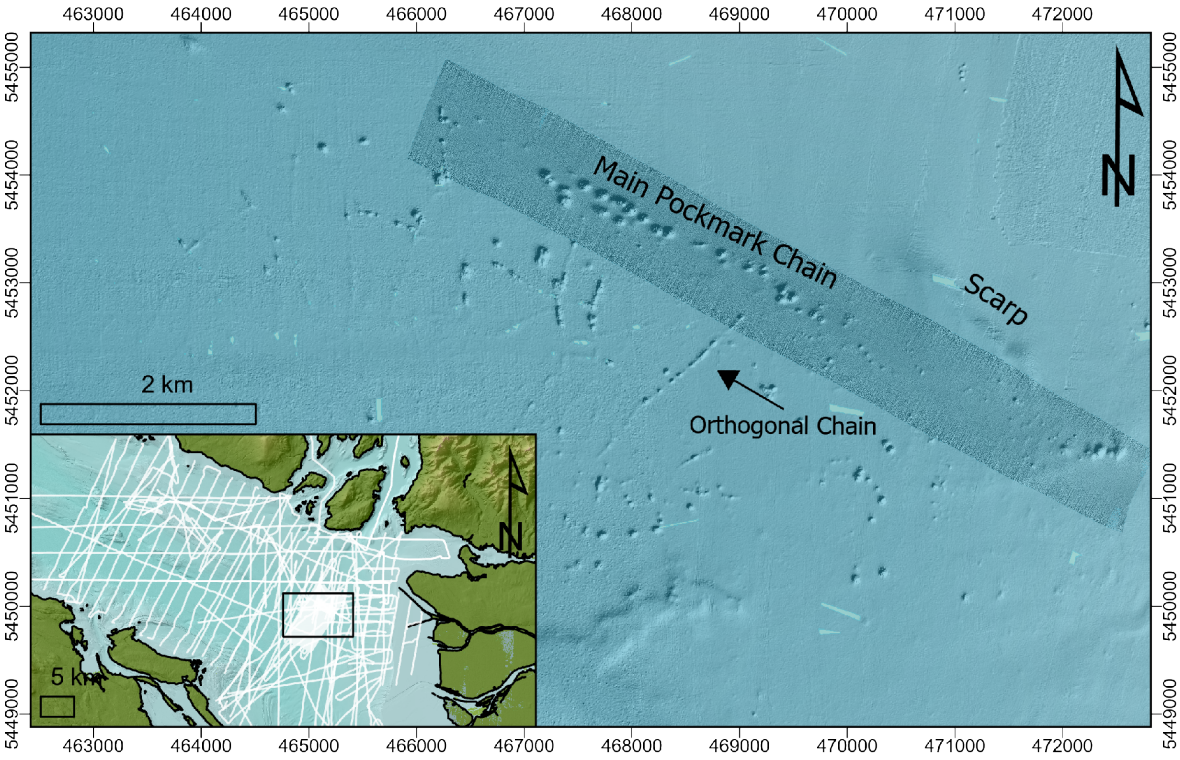


Figure 4.4.6: MBES data over the seafloor scarp, main pockmark chain and associated field. Line locations (white lines) and extent of main figure (black box) are shown in inset map.

4.4.1.1 Evidence for Faulting Beneath Escarpment

Six seismic reflection profiles cross the seafloor scarp identified by Barrie and Hill (2004). Directly beneath the scarp, a near-vertical, northwest-southeast trending linear

structure is interpreted (e.g., Figure 4.4.7). In Huntec DTS data, glacial reflections truncate beneath the base of the scarp (Figure 4.4.7). While truncations within the upper post-glacial unit are also noted, accurately distinguishing between reflection truncations and reflection offsets is limited due to the unit's faint internal reflections and the presence of significant acoustic turbidity. Nonetheless, deformation within the upper post-glacial unit remains apparent. Consistent with observations by Barrie and Hill (2004), acoustic turbidity and brightened reflections are visible across all profiles in the area, with an increase in acoustic turbidity across the fault contact at the base of the escarpment. Furthermore, truncated reflections continue for 3 km southeast of the scarp in adjacent seismic reflection profiles (e.g., Figure 4.4.8, Figure 4.4.9).

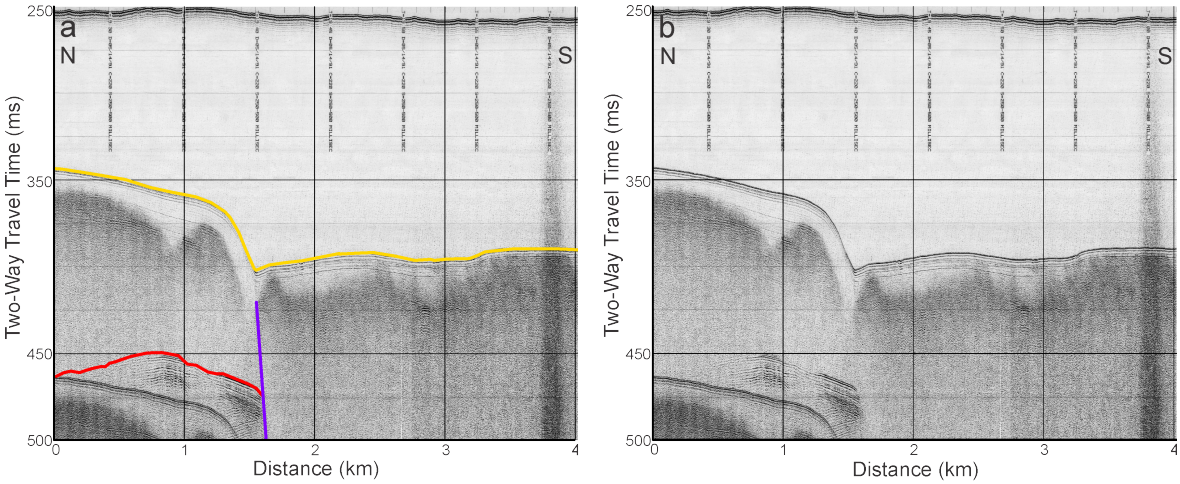


Figure 4.4.7: Huntec (external receiver) seismic reflection profile across the seafloor scarp. Line A5-B7 from cruise 91004PGC. A) Interpreted profile showing an inferred fault (purple) beneath the seafloor scarp. Tops of upper post-glacial and glacial units are shown in yellow and red, respectively. B) Uninterpreted profile. See Figure 4.4.4 for location.

4.4.1.2 Pockmark Chain

A fault zone is interpreted beneath the linear pockmark chain shown in Figure 4.4.6, based on the presence of seismic discontinuities, apparent offsets, reflection truncations, and abrupt changes in dip across 30 seismic profiles. Beneath the pockmark chain, 3.5 kHz CHIRP profiles show substantial acoustic turbidity, likely due to fluid-induced scattering, limiting the usefulness of such data in the area (e.g., Figure 4.4.5). From the 2002002PGC dataset, single-channel airgun and Huntec lines, oriented perpendicular to the pockmark chain, have increased subsurface penetration and are

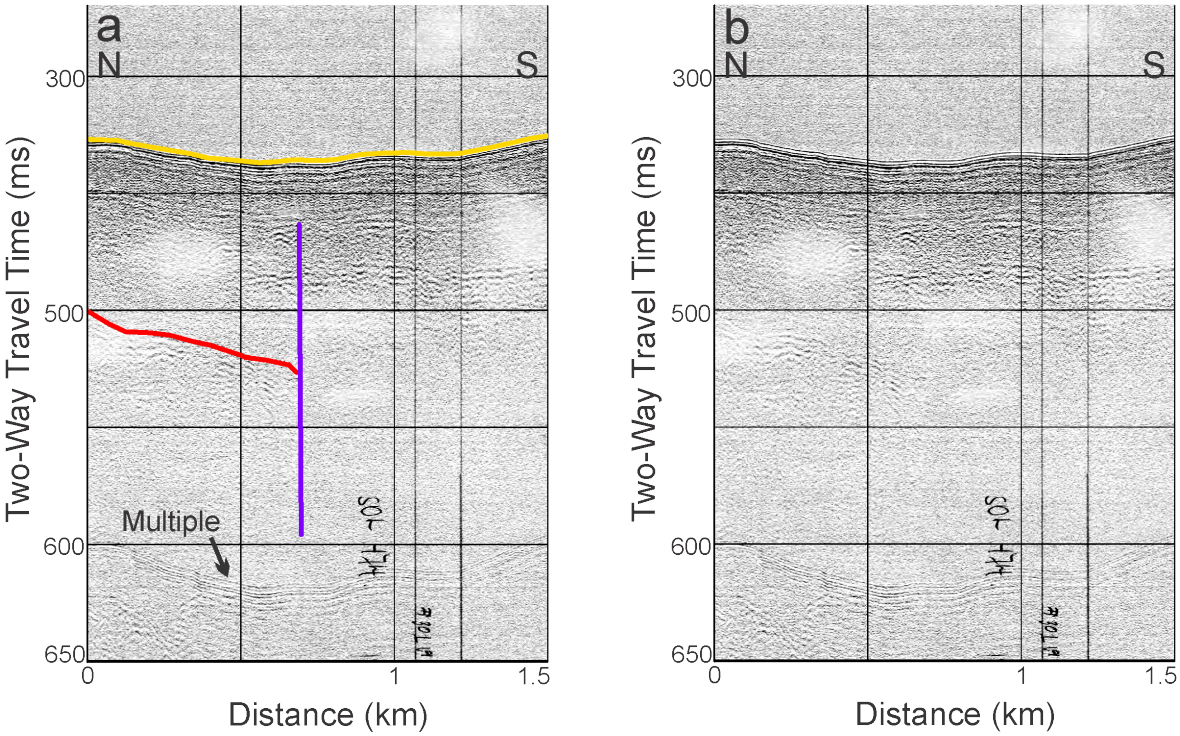


Figure 4.4.8: Airgun seismic reflection profile located approximately 2 km east of the scarp. Profile is from the transit between lines 473 and 474 from cruise 91008PGC; note the start of line 474 is hand-written on the profile as 'SOL 474'. A) Interpreted profile showing a possible fault (purple) based on reflection truncations. Tops of upper post-glacial and glacial units are shown in yellow and red, respectively. B) Uninterpreted profile. See Figure 4.4.4 for location.

comparatively less affected by acoustic turbidity. Within Huntec DTS data, reflection truncations of glacial and upper-post glacial units delineate a high-angle fault (Figure 4.4.10 A and B). Furthermore, single-channel airgun lines show the same feature in addition to deeper faults not resolved in the Huntec data (Figure 4.4.10 C and D). The high-angle fault visible in Huntec and airgun data is interpreted as the main strand of the fault zone.

The presence of a fault zone may be suggested by bathymetric evidence, as shown in Figure 4.4.6. MBES data also show smaller linear pockmark chains oriented approximately orthogonal to the main chain, which could indicate the presence of additional associated faults (Figure 4.4.6). However, direct evidence linking orthogonal chains to faults is limited. Mapping faults associated with pockmarks in the area is complicated by two factors: 1) seismic profiles run perpendicular to the main pockmark chain but are near parallel to other pockmark chains within the field, and 2) acoustic turbidity increases considerably over the pockmark field, substantially limiting penetration and

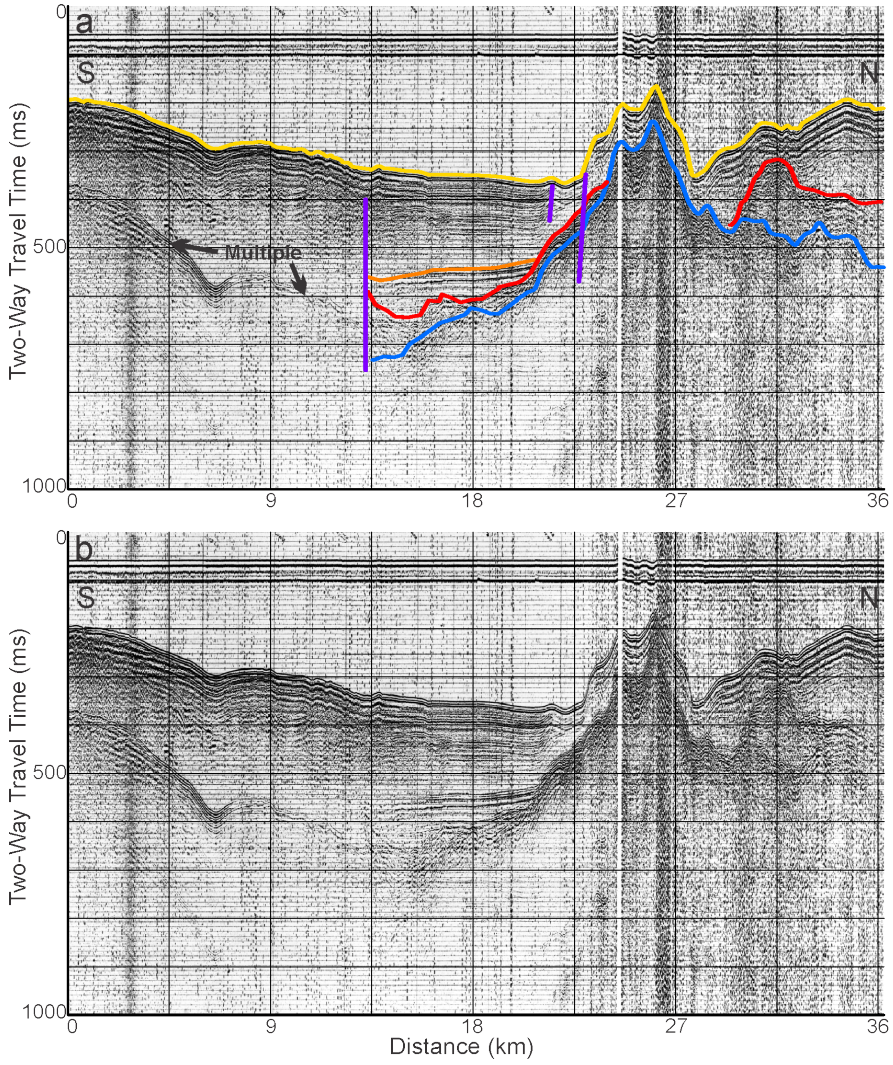


Figure 4.4.9: Airgun seismic reflection profile located approximately 3 km southeast of the scarp. Line Fraser Bowen from cruise 82003PGC. A) Interpreted profile showing an possible fault (purple) based on reflection truncations across multiple seismic units. Additional inferred faults are based on reflection discontinuities, truncations, and associated deformation. Horizon interpretations are shown in yellow (top of upper post-glacial), orange (top of lower post-glacial), red (top of glacial), and blue (top of bedrock). B) Uninterpreted profile. See Figure 4.4.4 for location.

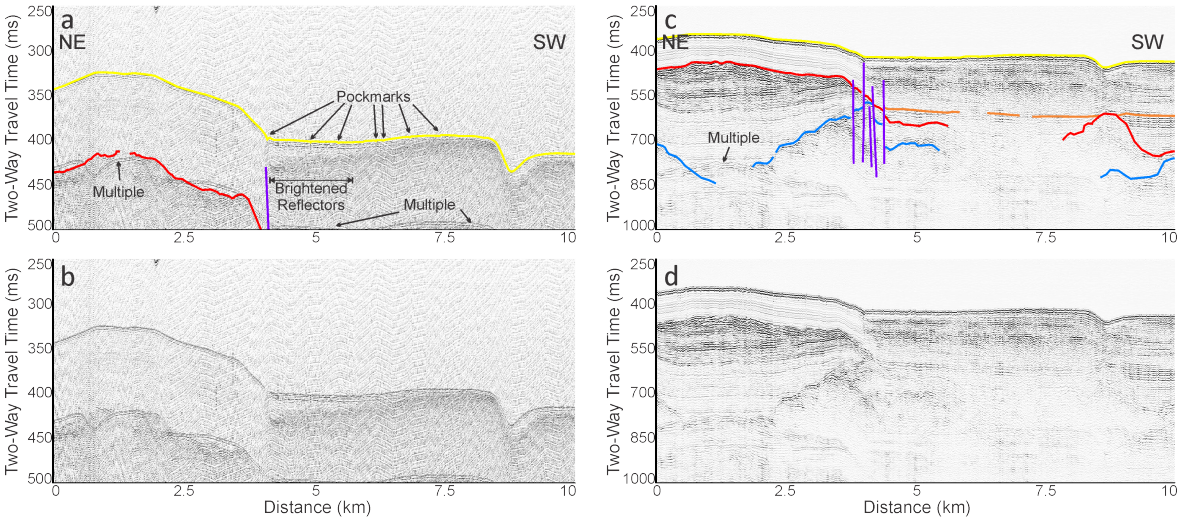


Figure 4.4.10: Huntec (A, B) and airgun (C, D) seismic reflection profiles crossing perpendicularly over the pockmark chain. Line 60 from cruise 2002002PGC. Horizon interpretations are shown in yellow (top of upper post-glacial), orange (top of lower post-glacial), red (top of glacial), and blue (top of bedrock). A) Interpreted Huntec profile showing an interpreted fault (purple). Pockmarks are evident on the seafloor, and acoustic turbidity increases southwest of the interpreted fault contact. Locally brightened reflections are indicated with a black double-pointed arrow. B) Uninterpreted Huntec profile. C) Interpreted airgun profile showing the same interpreted fault, as well as additional deeper faults not resolved in the Huntec profile (purple). Inferred faults are based on reflection discontinuities, truncations, and apparent offsets. Note increased signal degradation with depth beneath areas with high acoustic turbidity, which partially or fully obscures underlying units. D) Uninterpreted airgun profile. See Figure 4.4.4 for location.

therefore visibility of subsurface structures (e.g., Figure 4.4.10).

Northwest of the main pockmark chain, beyond any surface expression, indicators of active faulting - reflection discontinuities, truncations and apparent offsets - continue for an additional ∼4.5 km (e.g., Figure 4.4.11).

4.4.1.3 Relationship between Fault Traces - Interpreted Flower Structure

Two seismic reflection lines cross both the scarp and the linear pockmark chain, enabling investigation of a possible relationship between the two features (Figures 4.4.12 and 4.4.13). The interpretations in this study are consistent with the presence of a positive flower structure, visible in legacy airgun data (Figure 4.4.13). Higher-resolution Huntec DTS data between the two seafloor geomorphic features show Holocene

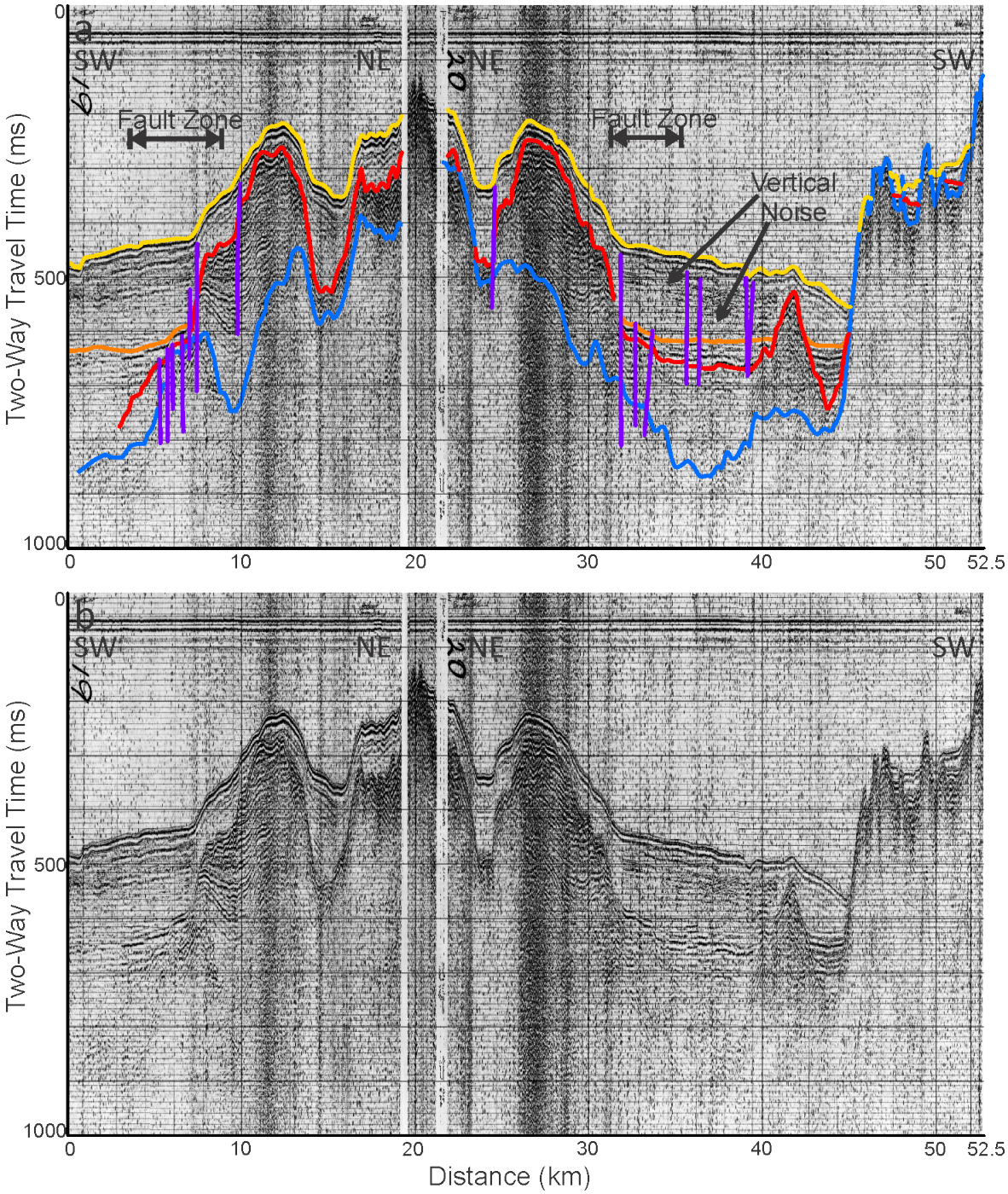


Figure 4.4.11: Airgun seismic reflection profiles located approximately 2.5-4.5 km west of the scarp. Lines 19 (east, i) and 20 (west, ii) from cruise 82003PGC. A) Profile showing interpreted faults (purple) associated with the proposed fault zone. Horizon interpretations are shown in yellow (top of upper post-glacial), orange (top of lower post-glacial), red (top of glacial), and blue (top of bedrock). B) Uninterpreted profile. See Figure 4.4.4 for location.

deformation and localized upward bending of the seafloor (Figure 4.4.12). These features are interpreted as evidence of a transpressional step-over, where compressional stress causes deformation between two en-echelon fault segments, resulting in localized uplift of the seabed (e.g., Woodcock and Rickards, 2003). Based on the spatial relationship between the fault traces (a left step), these observations are suggestive of right-lateral faulting, in contrast to left-lateral faulting, where extension and subsidence would be expected between the two features.

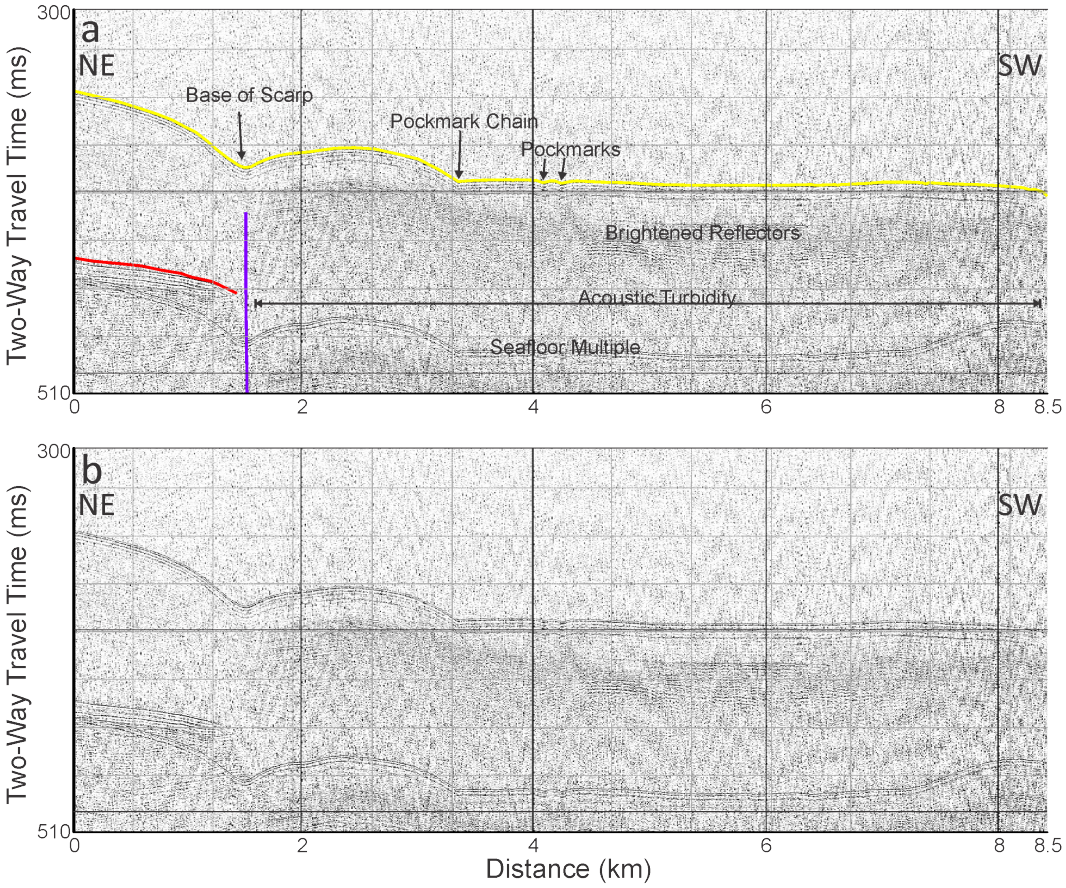


Figure 4.4.12: Huntec (external receiver) seismic reflection profile across the pockmark chain and seafloor scarp. Line 99 from cruise 2002002PGC. A) Interpreted profile showing an inferred fault (purple) beneath a seafloor scarp. The tops of upper post-glacial and glacial units are shown in yellow and red, respectively. Upper post-glacial deformation and upward bending of the seafloor is apparent between the scarp and pockmark chain. Note acoustic turbidity and local brightened reflections southwest of the inferred fault contact. B) Uninterpreted profile. See Figure 4.4.4 for location.

Based on the above analyses, the Central Salish Sea fault is interpreted to be longer than previously thought and may be a fault zone rather than single en-echelon strands. The Central Salish Sea fault zone is suggested to extend within the Fraser

Prodelta subarea to at least 12 km in combined length, significantly longer than the ~4 km length based on seafloor morphology (solid black lines, Figure 4.4.2; Barrie and Hill, 2004). See sections 4.4.2 and 4.4.5 for a discussion of possible further extensions of the fault toward the SE and NW directions, respectively.

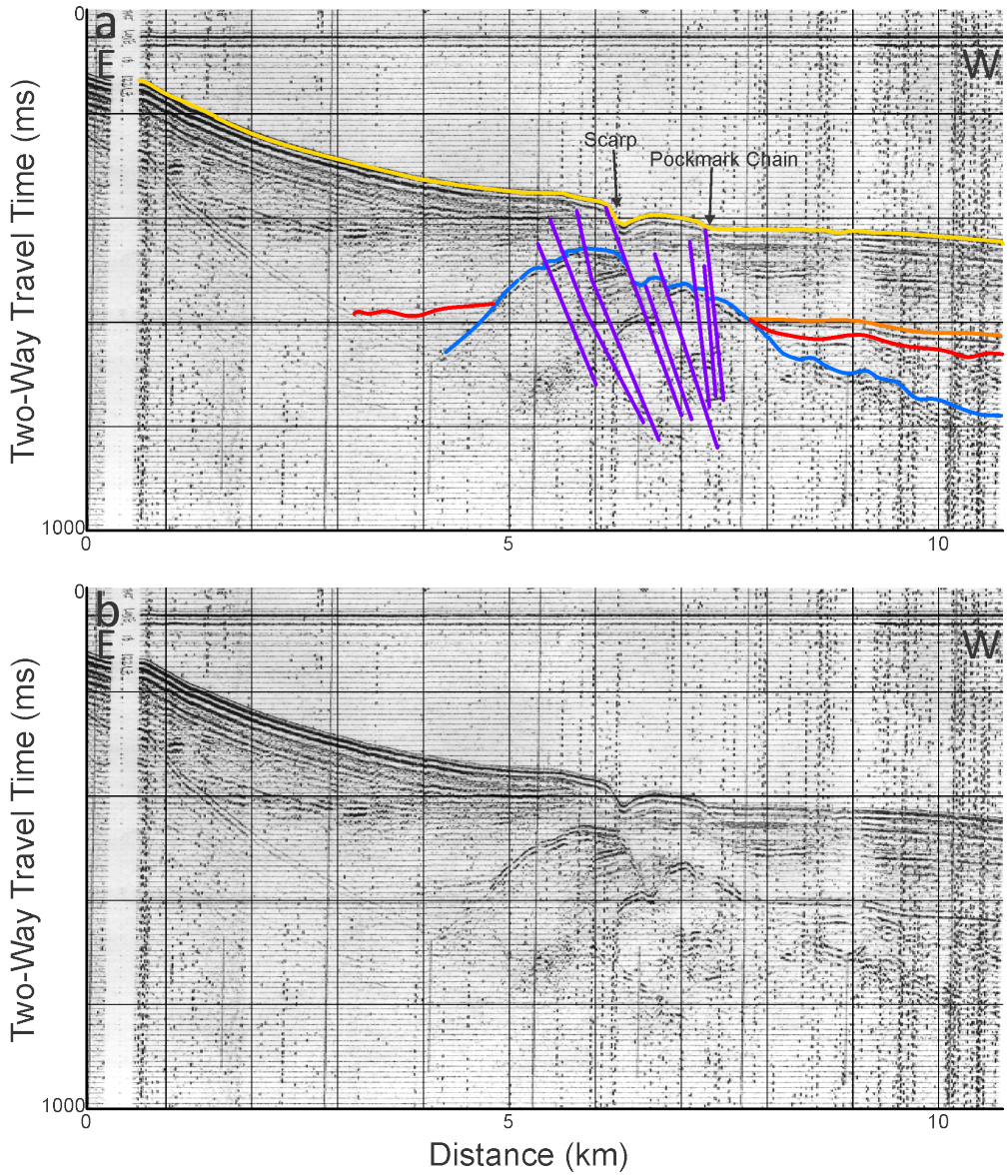


Figure 4.4.13: Airgun seismic reflection profile across the pockmark chain and seafloor scarp. Line 18 from cruise 83002PGC. A) Interpreted profile showing an inferred flower structure and faults (purple) between a scarp and a pockmark chain. The tops of upper post-glacial and glacial units are shown in yellow and red, respectively. Upper post-glacial deformation and upward bending of the seafloor is apparent between the scarp and the pockmark chain. B) Uninterpreted profile. See Figure 4.4.4 for location.

4.4.2 Subarea 2: Sturgeon Bank

The Sturgeon Bank subarea is located along strike from the Central Salish Sea fault mapped in subarea 1 (Figure 4.4.3). However, sub-bottom profiling data within the subarea (e.g., Figure 4.4.14) show only minor indicators of faulting, which are not conclusive on their own, nor are they vertically extensive. The indicators observed – primarily seismic discontinuities - are not unique to faulting and may be expected in a shallow delta environment characterized by mobile sediments and buried channels. Near-shore LiDAR data in the area show sediment bedforms, further indicative of dynamic sediment processes (Figure 4.4.14B). In sub-bottom data beneath bedforms,

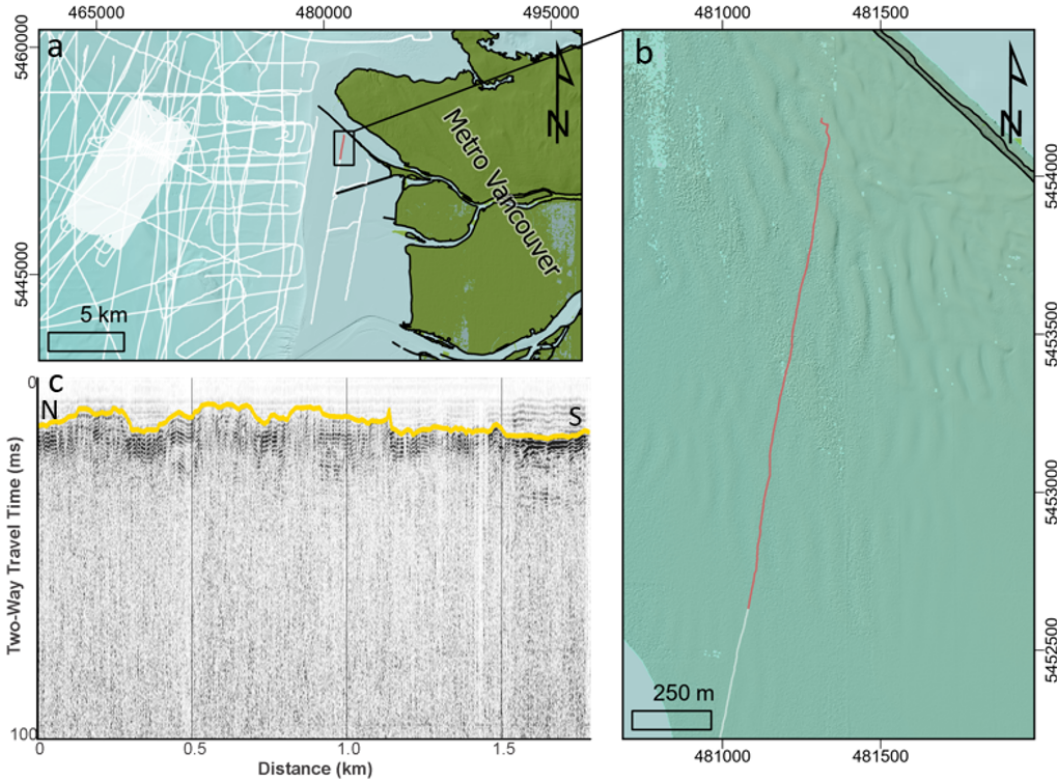


Figure 4.4.14: LiDAR and sub-bottom data along the Sturgeon Bank subarea. A) Regional map showing the location of profile C (red line), other seismic reflection profiles (white lines) and the extent of B. B) Zoomed view of LiDAR data collected offshore of Vancouver in 2021, with the location of profile C shown in red. Note the bedforms visible in surface morphology. C) Sub-bottom profile (Line U5) along the Sturgeon Bank subarea exhibiting gently inclined and variably dipping reflections in the upper ∼10 ms. Yellow marks the top of the upper post-glacial unit (seafloor). Line U5 is shown to represent the subarea, as it exhibits minimal noise and is in an area of complete LiDAR coverage. Data along strike of the CSSF are similar but lack full LiDAR coverage.

internal reflections are characterized by gently inclined and variably dipping reflections (Figure 4.4.14C). Discontinuities across the subarea appear associated with bedform structures and do not extend deeper into the subsurface. The shallow seismic discontinuities in this subarea are not interpreted as evidence of active faulting; instead, they are interpreted as evidence of sediment mobility apparent in both seismic reflection data and near-shore LiDAR. Other discontinuities are attributed to survey noise rather than geological features.

It is noted that seismic reflection data in this area comprise only sub-bottom profiler data, which, combined with the presence of coarser-grained sediments near the mouth of the Fraser River, results in significantly reduced subsurface penetration. While it is possible the Central Salish Sea fault extends into this subarea, it is not resolved in the available data.

4.4.3 Subarea 3: Point Grey Dredge Disposal Area

This subarea is named after the Point Grey marine disposal site, a dredge disposal site with a 1-nautical mile radius located ∼6 km offshore Vancouver, British Columbia (e.g., Pettigiani et al., 1997). MBES data reveal a variety of features, including (1) a scarp, (2) small, randomly oriented pockmarks, and (3) small chains of pockmarks, one of which aligns with a subtle seafloor lineament (Figure 4.4.15). These features may suggest subsurface processes; however, because dredge disposal areas are anthropogenically altered and exhibit irregular morphologies, interpreting seafloor geomorphology for evidence of faulting in this area is inherently uncertain. Seismic reflection data near the disposal site show reflection truncations and discontinuities within upper post-glacial units. The most vertically extensive feature in the subarea, observed in four intersecting profiles, extends from the upper-post glacial unit to bedrock and aligns with the small pockmark chain and subtle seafloor lineament (e.g., Figures 4.4.16 and 4.4.17). However, adjacent seismic reflection lines (locations shown in Figure 4.4.15 A) show no evidence for active faulting. Instead, the lack of lateral continuity supports the interpretation of this feature as a fluid conduit rather than a fault.

Approximately 2.6 km northwest of the disposal site and 5.5 km south of Bowen Island, along the edge of McCall Bank, lies a 1.8 km-long NW-SE trending seafloor scarp (Figure 4.4.15). Limited seismic reflection data exist over the feature, with

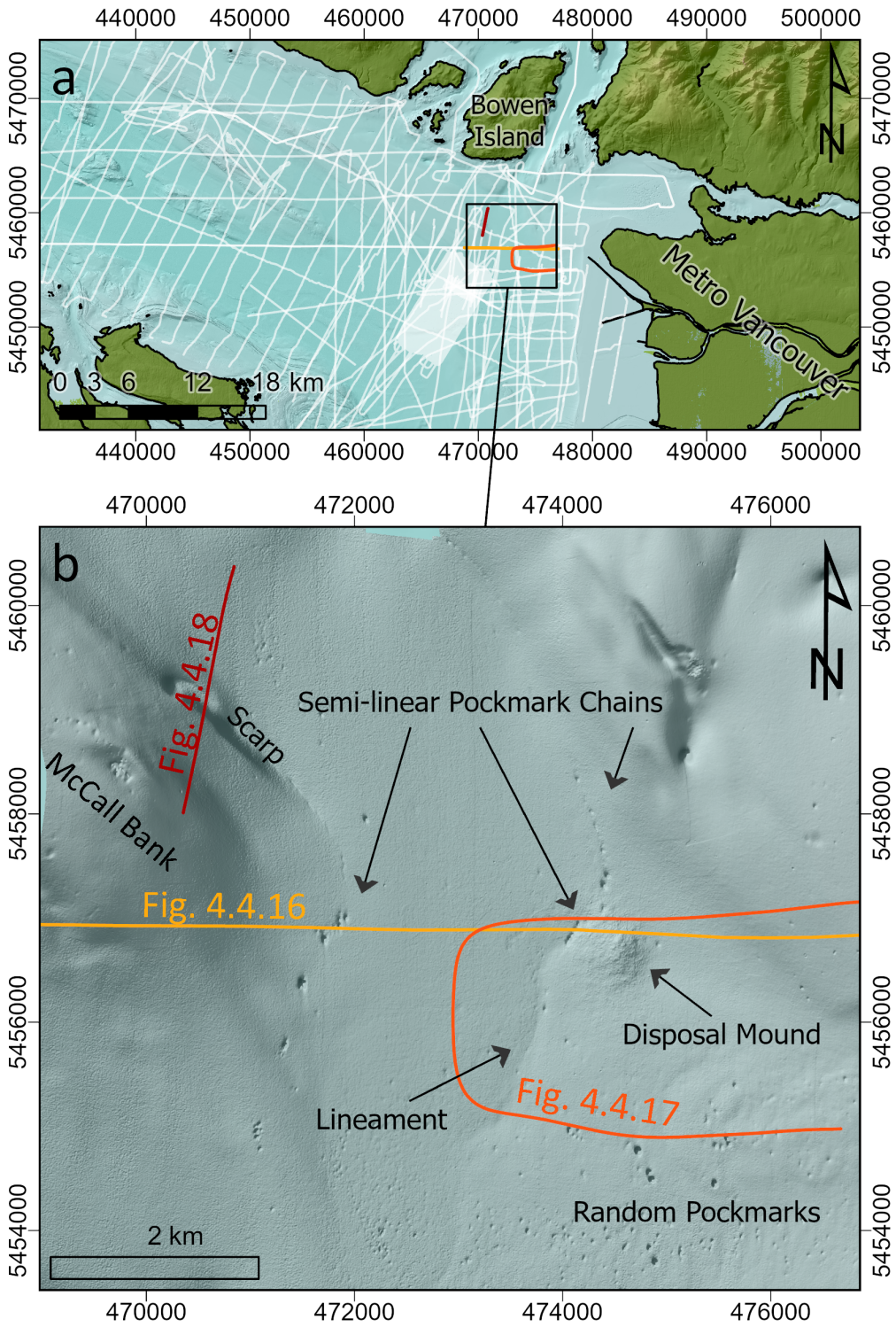


Figure 4.4.15: MBES data and line locations over the Point Grey Dredge Disposal Subarea. Profiles shown in subsequent figures are indicated with red, yellow, and orange lines. A) Overview map illustrating locations of all seismic profiles (white). B) Geomorphology of subarea, with key features indicated. Profiles shown in subsequent figures are delineated; other lines are omitted to avoid obscuring geomorphic features.

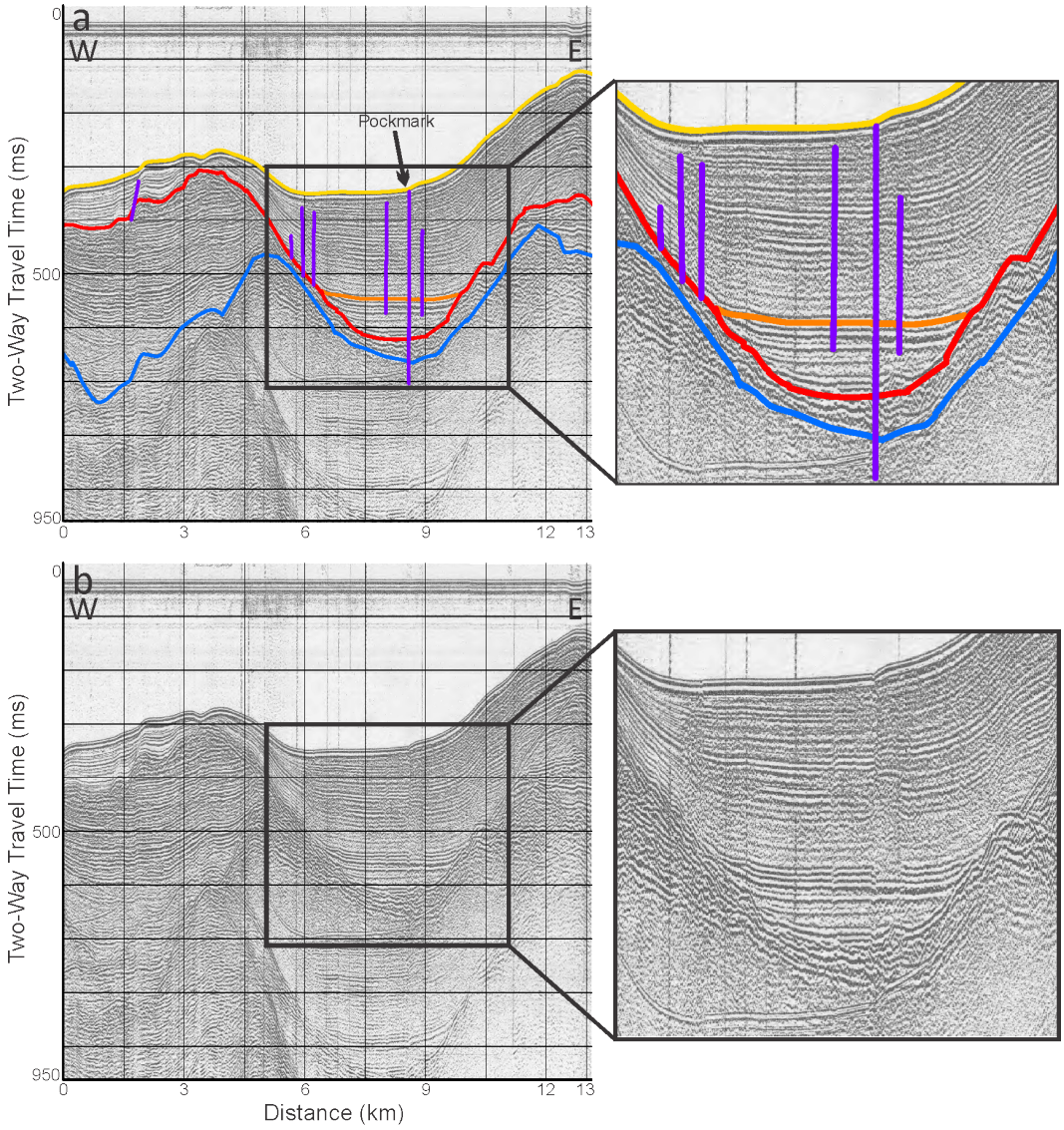


Figure 4.4.16: Airgun seismic reflection profile across a pockmark and lineament. This profile is from line 207 of cruise 89010PGC. A) Profile showing interpreted faults or fluid conduits (purple). Tops of upper post-glacial, lower post-glacial, glacial, and bedrock units are shown in yellow, orange, red, and blue, respectively. B) Uninterpreted profile. See Figure 4.4.15 for profile location.

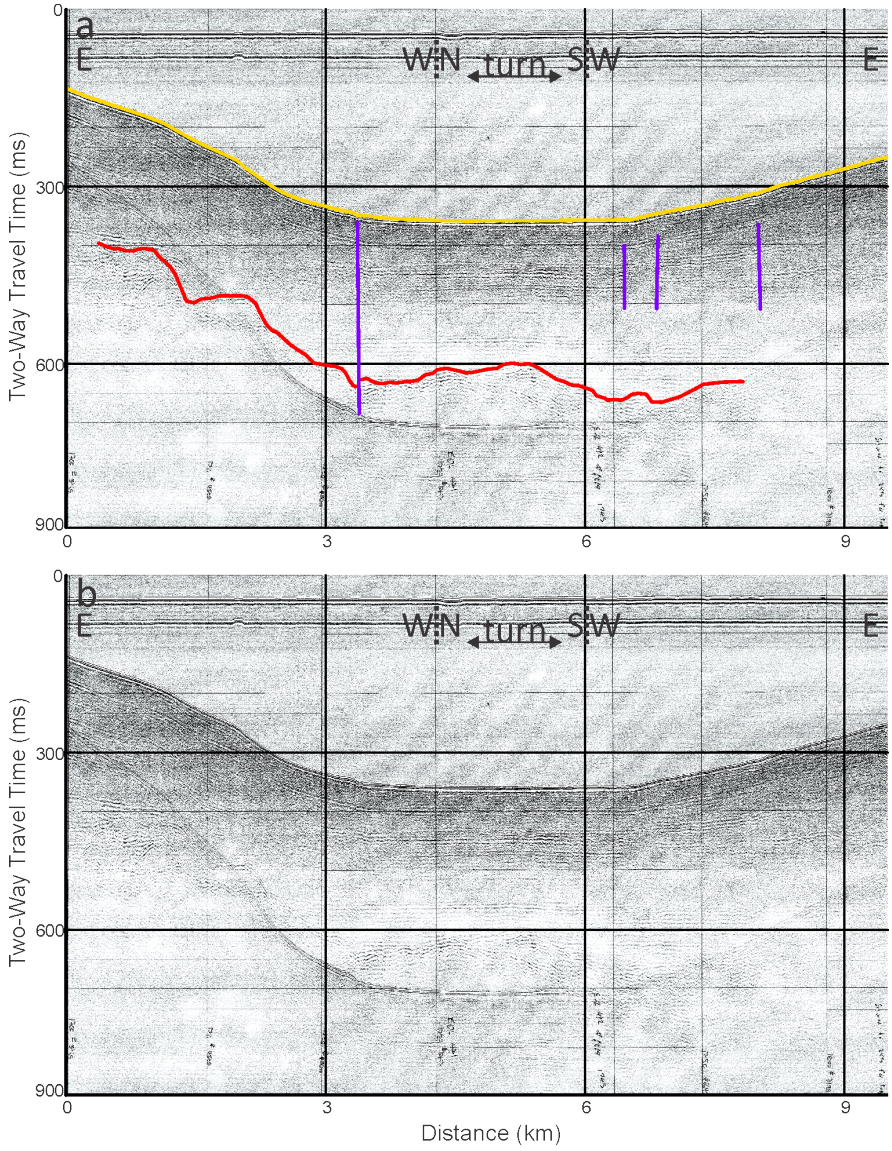


Figure 4.4.17: Airgun seismic reflection profile across pockmark and lineament. Line 471, 472 and turn from cruise 91008PGC. A) Interpreted profile showing inferred fluid conduits (purple). Tops of upper post-glacial and glacial units are indicated in yellow and red, respectively. B) Uninterpreted profile. See Figure 4.4.15 for profile location.

only one legacy Huntec profile being well-oriented to the feature (Figure 4.4.18). This profile shows faint internal upper post-glacial reflections that appear to be deformed at the base of the slope. Beneath the base, truncations of internal reflections are apparent; however, distinguishing between offsets and truncations is difficult due to deformation and faintness of internal reflections. Beneath the upper post-glacial unit, the glacial unit also exhibits truncation, with the unit not apparent on the northern side. Together, these observations suggest the presence of a near-vertical fault, which is inferred to be at least 1.8 km long based on the scarp's extent in MBES data (Figures 4.4.2 and 4.4.18).

Acoustic turbidity is observed north of the interpreted fault contact (Figure 4.4.18). In contrast, the southern side appears mostly gas-free. This is similar to observations along the CSSF (∼6 km to the south) in Huntec lines, where base-of-slope sediments show a notable increase in acoustic turbidity. The relationship between this inferred fault and the CSSF is not well understood. While the two structures are not oriented along strike (Figure 4.4.2), they share similar NW-SE trends. This similarity may indicate a larger, more extensive fault zone, though the exact structural relationship remains unclear.

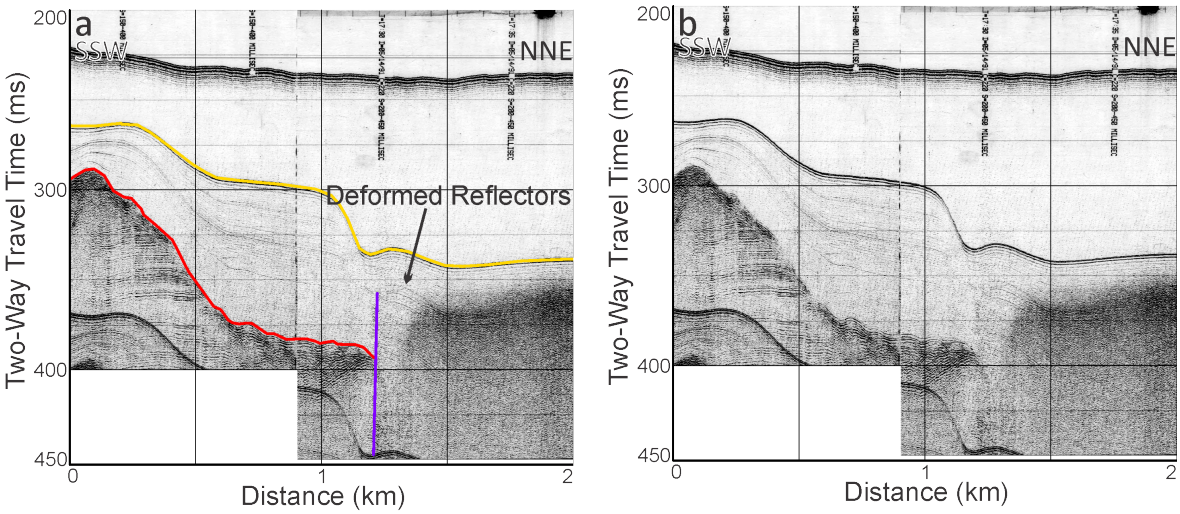


Figure 4.4.18: Huntec external seismic reflection profile across seafloor scarp. Line A7-B8 from cruise 91004PGCPGC. A) Interpreted profile showing a fault (purple) interpreted based on truncated upper post-glacial and glacial reflections, along with deformed upper post-glacial reflections. Tops of upper post-glacial and glacial units are shown in yellow and red, respectively. B) Uninterpreted profile. See Figure 4.4.15 for profile location.

4.4.4 Subarea 4: Offshore NE Gabriola Island and Vicinity of the 1997 and 1975 Earthquake Clusters

Approximately 7 km northeast of Gabriola Island and ∼3.5-4 km southwest of the SoG earthquake clusters, displacements of bedrock through upper post-glacial units are apparent (Figure 4.4.1), suggesting the presence of a fault with Holocene activity. This evidence is observed over two legacy airgun lines: Lines 25R (Figures 4.4.19 and 4.4.20) and 26 from cruise 82003PGC. High-resolution MBES data from the same area indicate laterally offset bedrock strata at the seafloor, and the apparent offsets visible in seismic reflection data align with a linear seafloor feature (Figures 4.4.19 B and 4.4.20). The trace of the inferred fault observed in both seismic and bathymetric data appears to be aligned with a fault mapped on Gabriola Island (Figure 4.4.19; Denny et al., 2007; Muller and Jeletzky, 1970).

Only minor evidence for Holocene deformation can be observed near the 1997 and 1975 earthquake epicentres. Line 25R from cruise 82003PGC, shows minor evidence of Holocene deformation, including discontinuous, truncated or abruptly dipping reflections within upper and lower post-glacial units near the 1997 and 1975 clusters (Figures 4.4.1, 4.4.19, and 4.4.20). However, this deformation does not appear to extend into underlying glacial or bedrock units. In contrast, the adjacent line 24, which passes directly over the 1997 mainshock epicentre, shows no significant evidence of Holocene- or Quaternary-active faulting in the area; however, it does exhibit reflection truncations, discontinuities, and minor offsets in lower post-glacial and glacial units approximately 3 km southwest of the 1997 epicentre (Figures 4.4.1, 4.4.19, and 4.4.21). Mosher et al. (2000) note that the events occurred on a ∼50° north-dipping east-west oriented plane at 3-4 km depth, meaning that any surficial evidence of the fault would be expected ∼1.7-3.4 km south of the 1975 and 1997 events.

Additional profiles across the SoG indicate minor Holocene deformation farther from the epicentral location. For example, Line 19-20 from the same cruise shows disturbed upper and lower post-glacial reflections at approximately 38 km along the profile (Figure 4.4.11, 7 km from epicentre). However, these disruptions do not extend into underlying glacial or bedrock units and cannot be conclusively linked to deeper structures.

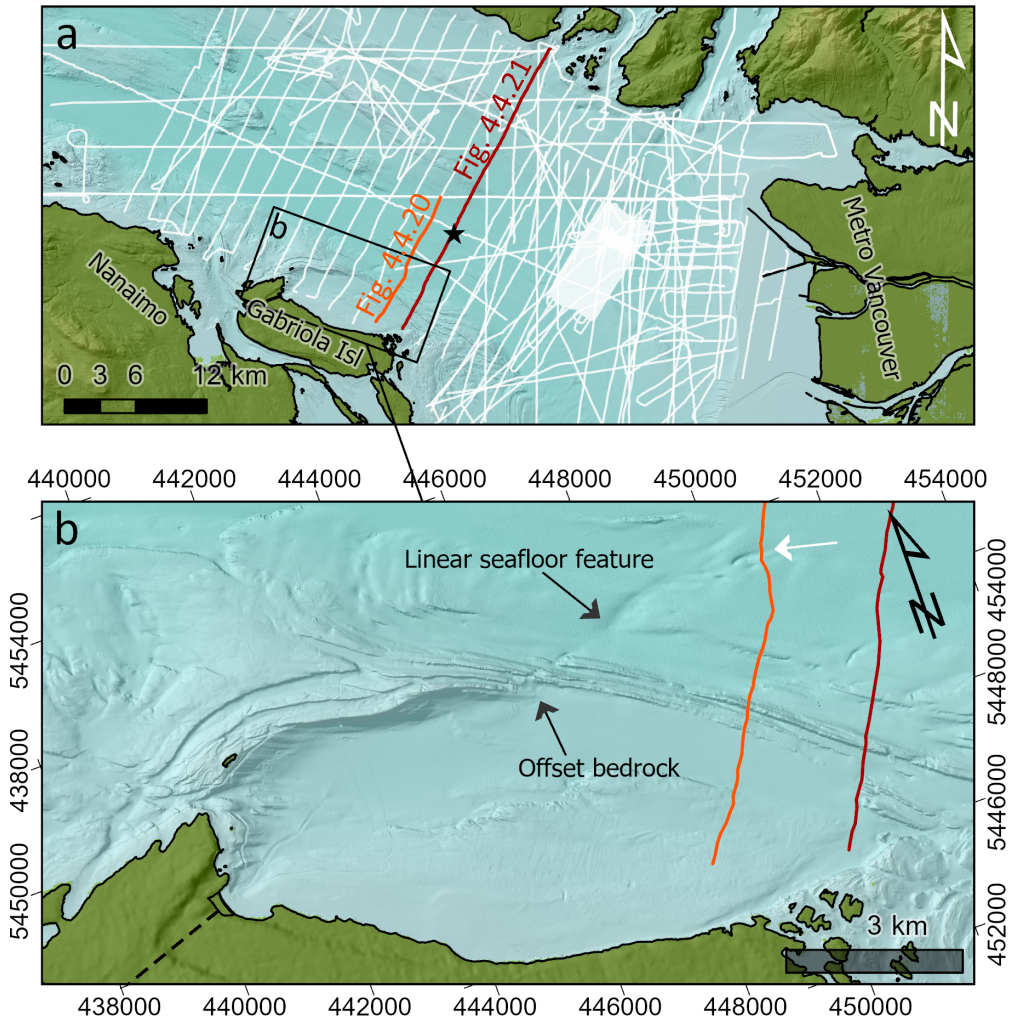


Figure 4.4.19: Map of MBES data and seismic reflection lines discussed in the text. A) Regional map showing seismic reflection lines (white) analysed for this study. Locations for Figures 4.4.20 (Line 25R, 82003PGC) and 4.4.21 (Line 24, 82003PGC) are shown in orange and red, respectively. The location of the 1997 mainshock is shown with a black star. B) Zoomed-in view of MBES data offshore Gabriola Island, highlighting seafloor geomorphology. Seismic reflection lines are omitted to enhance clarity of the seafloor, except for those shown in Figures 4.4.20 and 4.4.21 (orange and red, respectively). White arrow indicates the location of apparent offsets interpreted in seismic reflection data. Black dashed line illustrates the location of a mapped fault on Gabriola Island (from Denny et al., 2007; Muller and Jeletzky, 1970).

4.4.5 Subarea 5: Halibut Bank

Approximately 6.7 km northwest of the CSSF as mapped in the Fraser Prodelta subarea (Section 4.4.1), active fault indicators re-emerge along strike of the interpreted fault trace (Figures 4.4.1 and 4.4.2). For example, legacy line 24 from cruise 82003PGC

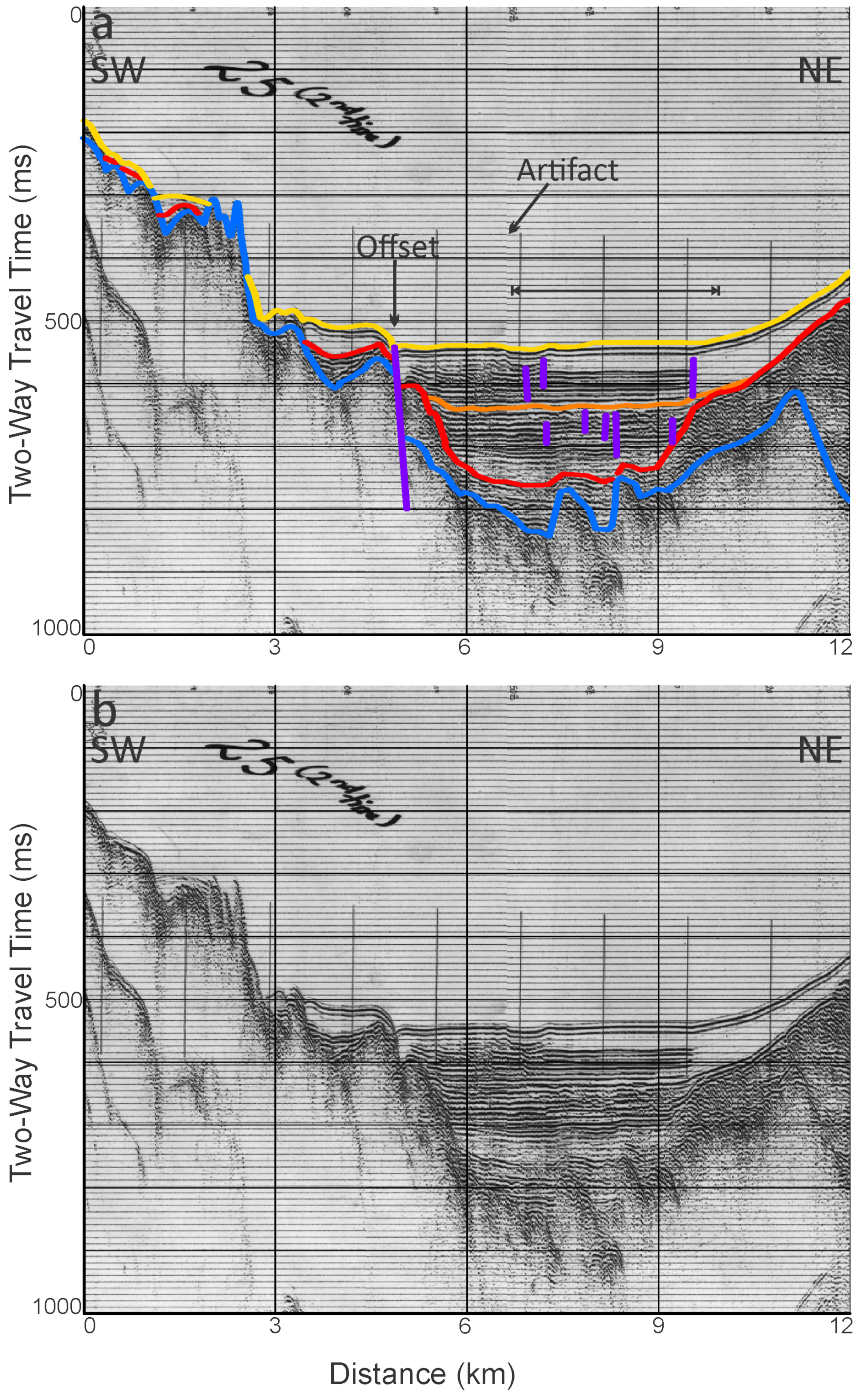


Figure 4.4.20: Airgun seismic reflection profile offshore Gabriola Island, zoomed to illustrate features mentioned in the text. Line 25R from cruise 82003PGC. A) Interpreted profile showing inferred faults (purple). The southwesternmost fault, located approximately 7 km from Gabriola Island, exhibits apparent offsets in upper post-glacial, glacial, and bedrock units (yellow, red, and blue, respectively). The top of the lower post-glacial unit is denoted in orange. A digitizing artifact, which creates false offsets, is marked with an arrow. The region near the 1997 earthquake cluster is indicated with a double-pointed arrow. B) Uninterpreted profile. See Figure 4.4.19 for location.

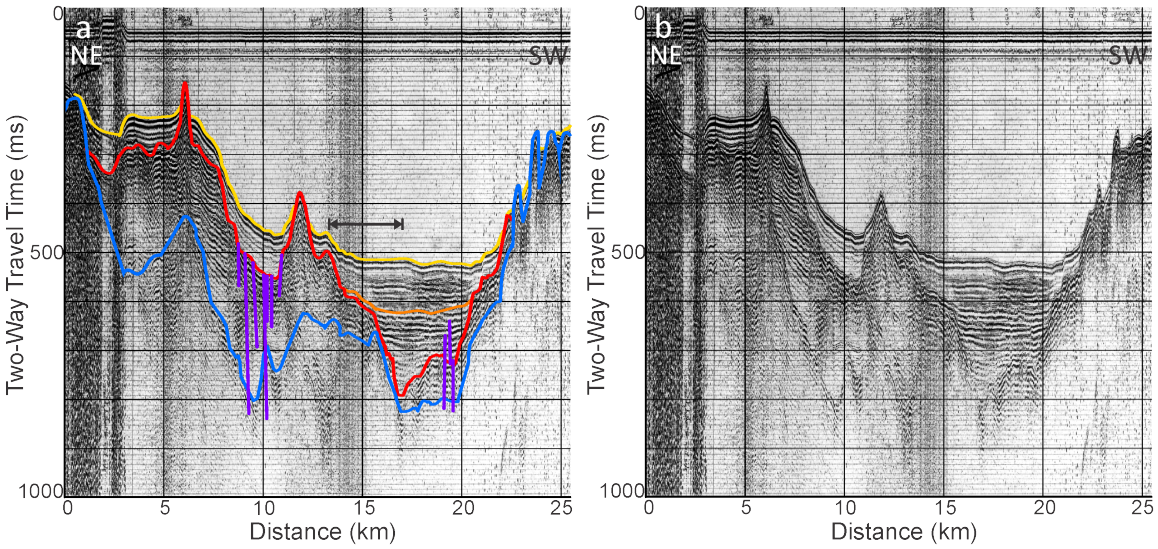


Figure 4.4.21: Airgun seismic reflection profile spanning the width of the SoG. Line 24 from cruise 82003PGC. A) Interpreted profile showing inferred faults (purple) along strike of the Central Salish Sea fault zone (left) and approximately 3 km SW of the 1997 SoG earthquake sequence (rightmost faults). Tops of upper post-glacial, lower post-glacial, glacial, and bedrock units are shown in yellow, orange, red, and blue, respectively. The region over the 1997 earthquake cluster is indicated with a double-pointed arrow. B) Uninterpreted profile. See Figure 4.4.19 for location.

(Figures 4.4.19 and 4.4.21) illustrates a set of fault indicators along strike, including reflection discontinuities, truncations, and offsets, paired with abruptly dipping reflections within the glacial unit. Adjacent lines to the northwest show reflection discontinuities and offsets in glacial units, along with discontinuities and associated deformation in upper post-glacial units (Figure 4.4.1). However, the interpretations along line 24 and adjacent lines exhibit lower confidence and increased ambiguity compared to those in the Fraser Prodelta subarea. Despite lower certainty, the spatial alignment of these indicators along strike of the Central Salish Sea fault is suggestive of a connection. Accordingly, a lower certainty, additional 6.7 to 12.8 km extension of the CSSF zone is inferred (Figure 4.4.2).

Further northwest of the inferred extension, approximately along strike but with a slight jog to the west, three locations exhibit minor fault indicators, including reflection truncations and non-horizontal reflections (i.e., minor deformation; Figure 4.4.1). However, extending the CSSF through these areas is uncertain for several reasons. These indicators are primarily confined to the glacial unit (i.e., not vertically extensive), and truncations and non-horizontal reflections are not uniquely indicative of faulting. Additionally, seismic lines over these locations contain significant noise that complicates

interpretation, and lines between them show no clear evidence of faulting. While these locations exhibit some characteristics of faulting, the evidence is insufficient to justify further extension of the CSSF.

4.5 Discussion

4.5.1 Study Limitations

The analyses presented in this study utilize shallow, high-resolution seismic reflection data. As a result, there are limitations which impact the results of this study. As discussed previously, deeper fault structures (greater than ∼1 km) are not resolvable, and structures with offsets smaller than the minimum vertical resolution cannot be distinguished (e.g., ∼1–6 m for airgun). Signal attenuation with depth also increases noise, reducing confidence in fault identification at greater depths.

The age of the data also introduces interpretation uncertainty. Many legacy seismic reflection profiles exhibit high levels of noise, which partially or completely obscure subsurface structures. Since the legacy dataset consists of scanned paper records, further processing to reduce noise is not possible. Moreover, most of the legacy dataset was collected after the 1975 earthquake cluster in the SoG but prior to the 1997 sequence. Thus, any near-surface deformation resulting from the latter sequence is not reflected in this dataset.

While a full characterization of the CSSF zone is beyond the scope of this Chapter, it is important to note that seismic profiles provide only limited information for fault characterizations, such as apparent vertical displacement and apparent dip. While strike-slip motion can be inferred, as suggested by the interpreted flower structure and seafloor deformation observed in this study, it cannot be characterized with 2D seismic data alone. Apparent vertical or dip-slip offsets in seismic profiles may also result from strike-slip motion, further complicating interpretation.

There is extensive data coverage over the central SoG, the result of decades of work by federal scientists and technicians (Figure 4.3.1). However, there are gaps in data coverage concerning two features of interest: the potential fault scarps identified near the Point Grey Dredge Disposal Area and offshore Gabriola Island. While additional analogue data exist over the fault scarp near the Point Grey Dredge Disposal

Area, they either have not been digitized or were not digitized at the time of this study. Further seismic reflection work near Gabriola Island is necessary to investigate the near-shore environment for additional evidence of faulting and possible connections to on-shore faults.

4.5.2 Hazard Implications

Based on set criteria, evidence for active faulting across the central SoG has been delineated. Many potential fault indicators do not delineate structures, while other evidence appears laterally extensive and consistent across multiple seismic reflection lines. There is sufficient evidence to at least partially map the here-named Central Salish Sea fault zone in the Fraser Prodelta area beyond its previously identified surface expression of ∼4.6 km (Barrie and Hill, 2004). The primary strand of the fault zone is mapped as two en-echelon NW-SE oriented faults linked by a positive flower structure. Linearly oriented pockmarks visible in MBES data could indicate additional associated faults; however, this interpretation remains uncertain, as structures beneath these features are not resolved due to unfavourable line orientations and significant acoustic turbidity.

Active fault evidence associated with the CSSF zone is traced laterally for at least 12 km, with an additional 6.7 to 12.8 km-long inferred extension. From this, a minimum combined fault trace length of ∼12 km is inferred and a maximum fault trace length of ∼25 km. In a scenario where the entire Central Salish Sea fault zone ruptures in a single event, the estimated magnitude, based on scaling relations outlined in Wesnousky (2008), is a magnitude ∼6.1 to 6.7. A rupture of this size has not been observed in the instrumental seismic record of the central SoG, and a full-fault rupture could result in considerable damage to nearby cities such as Metro Vancouver, Nanaimo, and Sechelt. Given the magnitude and lack of equivalent historical events, such an event would present a new and significant hazard that should be considered in future seismic hazard modelling.

The location of the CSSF zone, offshore of urban populations and near the Fraser River delta, may have significant implications for tsunami hazard. Previous studies of active faults in nearby northwest Washington suggest that an M ∼6 rupture could deform the seafloor and generate a tsunami (Kelsey et al., 2012). Locally dangerous waves can also result from slope failures triggered by ground shaking (Rabinovich et al., 2003; Christian et al., 1998). There is historical precedent for this in southwest

BC, including an M_s 7.3 earthquake beneath central Vancouver Island, which triggered multiple slope failures and generated waves capable of capsizing boats resulting in a fatality (Conway et al., 2013; Hodgson, 1946; Mosher et al., 2004; Rogers and Hasegawa, 1978). A vertical seafloor offset or sudden failure of the Fraser River delta due to a CSSF zone rupture could conceivably trigger a sizeable tsunami near multiple urban centres (e.g., Kelsey et al., 2012; Mosher, 2009; Rabinovich et al., 2003). Additional modelling is required to assess the full seismic hazard and tsunamigenic potential of the CSSF zone.

4.6 Conclusions

Through an analysis of >2200 line-km of seismic reflection data, indicators for active faulting across the central SoG have been identified and mapped. These interpretations delineate a submarine fault zone approximately 10 km west of Metro Vancouver, British Columbia, with evidence suggesting past Holocene rupture. The Central Salish Sea fault extends for at least 12 km, with an inferred length of up to 25 km. The fault trace becomes obscured beneath the Fraser River delta, precluding further delineation eastward towards Vancouver. As mapped, the inferred CSSFZ has the potential to generate an M ~6.1 to 6.7 earthquake if failing in a single rupture. This has significant seismic hazard implications for nearby population centres including Nanaimo, Metro Vancouver, and Sechelt. Additionally, one seismic reflection profile south of Bowen Island reveals active faulting evidence associated with a NW-SE oriented seafloor scarp. Offset bedrock and upper post-glacial units offshore NE Gabriola Island also suggest active faulting, aligned with a seafloor lineament and laterally offset bedrock observed in MBES data. Additional data are required to further map and characterize the features.

While upper and lower post-glacial units across the SoG exhibit localized deformation, the seismic reflection interpretations in this study do not reveal conclusive evidence of active faulting near the epicentral area of the 1975 and 1997 Strait of Georgia earthquake clusters. However, given that most data utilized were collected prior to 1997, deformation related to the latter events would not be adequately reflected in the dataset.

Chapter 5

Characterization of the Central Salish Sea Fault near Vancouver, Canada

5.1 Abstract

This study aims to evaluate the hazard and risk posed by the Central Salish Sea fault, a Holocene-active crustal fault located approximately 10 km offshore of Metro Vancouver, Canada. Three geohazards associated with the fault are considered: fault-strike seafloor pockmarks, earthquakes resulting from a potential full-fault rupture, and tsunamis.

Successive multibeam bathymetric surveys are used to quantify geomorphic change of fault-strike pockmarks over a 23-year period. Five pockmarks are newly imaged and cannot be attributed to increased survey resolution. The alignment of pockmarks along strike, combined with the observed changes in pockmark morphology over time, suggest that ongoing fluid migration along the fault may play a role in their formation. Based on the inferred development and observed deepening of existing pockmarks, the Central Salish Sea pockmark chain is interpreted as an active geohazard. For seismic hazard and risk modelling purposes, the Central Salish Sea fault is characterized as a 12- to 25-km-long right-lateral transpressional fault, dipping at 75° southwest and striking ∼123°. Assuming a simplified fault geometry, four scenarios are modelled, representing varying fault lengths (12 and 25 km) and rupture styles (oblique/reverse and strike-slip). Ground shaking during the most impactful of the modelled scenarios – a magnitude 6.7 daytime oblique or reverse rupture – is projected to result in 1300 deaths, 5600 buildings rendered uninhabitable, and $18.5 billion dollars (2019 CAD) in economic damage across southwestern British Columbia, Canada, due to building damage alone. The proximity of the Central Salish Sea fault to an area of known submarine slope instability, coupled with its characterization as a potential right-lateral transpressional fault, suggests that a rupture along the fault may be tsunamigenic.

Empirical relations are used to estimate tsunami runups resulting from seafloor tectonic offset during fault rupture. These estimated runups suggest that a magnitude 6.7 rupture could produce damaging waves affecting multiple coastal cities. Additional modelling is recommended to further assess the tsunami hazard of the fault.

5.2 Introduction

Southwest British Columbia is one of Canada's most seismically active regions, with a large coastal population exceeding 3.5 million (Statistics Canada, 2023) that places multiple communities at risk from earthquakes and associated geohazards. While the threat of a megathrust earthquake generated along the Cascadia subduction zone (CSZ) often dominates discussions, the destructive potential of shallower crustal earthquakes should not be overlooked. The danger posed by such earthquakes has been exemplified by multiple events globally. For example, an M_W 6.2 earthquake near Christchurch, New Zealand in 2011 killed 185 people and caused $40 billion in rebuilding costs (2015 NZD) (New Zealand Police, 2012; Wood et al., 2016). Likewise, an M_W 6.9 earthquake near Kobe, Japan in 1995 resulted in over 6000 deaths and the destruction of more than 170,000 buildings (Okimura et al., 1996). There is historical precedent for similar crustal earthquakes in southwest BC, including an M_S 7.3 event on central Vancouver Island in 1946, which caused extensive and well-documented damage but limited loss of life due to the sparse regional population at the time and its occurrence late on a Sunday morning, when many buildings, such as schools, were unoccupied (Figure 5.2.1; Hodgson, 1946; Rogers and Hasegawa, 1978).

Recent studies across southwest BC and northwest Washington, USA provide a growing body of evidence for Holocene activity on an extensive network of crustal faults (e.g., Caston, 2021; Greene et al., 2018; Harrichhausen et al., 2023; Kelsey et al., 2012; Morell et al., 2018). Notably, the Leech River – Devils Mountain fault, located near British Columbia's capital city of Victoria, has been interpreted as Holocene-active in multiple studies (Harrichhausen et al., 2021; Morell et al., 2017, 2018; Personius et al., 2014). The inclusion of the fault in seismic hazard models increases estimated peak ground acceleration in Victoria by up to 9% for a 2475-year return period (Kukovica et al., 2019). Modelling of seismic risk associated with a potential rupture along the Leech River – Devils Mountain fault projects an estimated 1000 deaths and $20 billion (CAD) in economic losses from building damage alone (Hobbs, 2022).

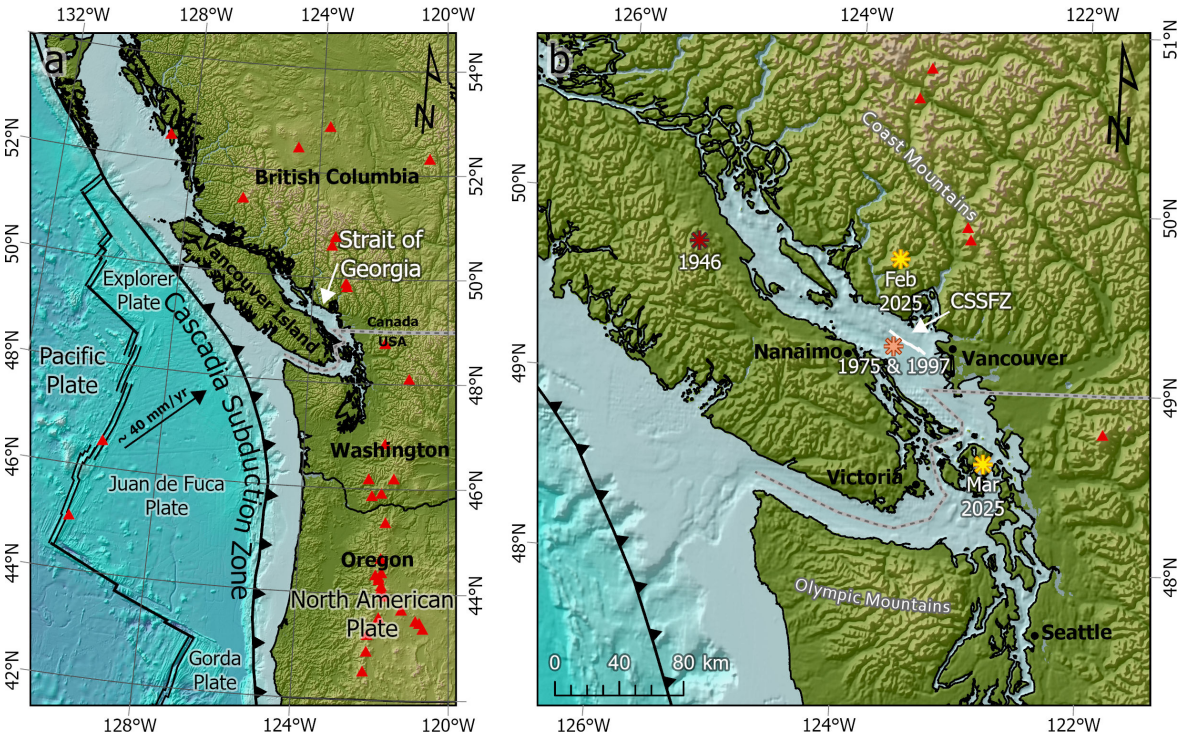


Figure 5.2.1: A) Tectonic setting of Cascadia. Plate motion with respect to North America is indicated with a black arrow (DeMets et al., 2010). Volcanoes are shown as red triangles. B) Regional map of southwest BC and northwest Washington. Locations for earthquakes discussed in text are shown as asterisks. CSSFZ: Central Salish Sea fault zone.

Chapter 4 detailed the use of seismic reflection data to delineate the extent of, and infer Holocene activity along, the Central Salish Sea fault zone (CSSFZ), a submarine fault zone located approximately 10 km offshore of Metro Vancouver, BC (Figure 5.2.1). In this chapter, the term CSSFZ is used to refer to this broader fault system. More specifically, the Central Salish Sea fault (CSSF) refers to the primary strands within this zone, interpreted as consisting of two en echelon segments. These definitions align with the fault zone and main strand interpretations defined in Chapter 4.

Based on empirical relationships between rupture length and magnitude (Wells and Coppersmith, 1994), the CSSFZ could produce earthquakes of magnitudes up to 6.3-6.7 should the entire mapped fault rupture. The proximity of the CSSFZ to population centres raises questions about associated hazards: could fault rupture substantially impact nearby communities, and if so, what is the scale of the risk? A primary goal of this chapter is to assess the hazard associated with the CSSF and to further constrain fault parameters by building upon the results presented in Chapter

4. Three hazards are addressed herein: seafloor pockmarks associated with the fault, which constitute a relatively minor geohazard with implications predominantly limited to seafloor infrastructure, as well as seismic hazard and tsunami hazard, both of which have the potential for considerably broader impacts. Given the proximity of the CSSFZ to major metropolitan population centres, this study also aims to model the seismic risk associated with a fault rupture, including consequences for human populations, buildings, and economic losses.

5.2.1 Tectonic Setting

The CSSFZ is located in the Strait of Georgia (SoG), BC along the northern Cascadia forearc. Regional tectonics are dominated by the CSZ, where the Juan de Fuca plate subducts northeastward beneath the North America plate at a rate of ∼40 mm/year (Figure 5.2.1A; DeMets et al., 2010). Southwest BC is susceptible to earthquakes from three sources: subduction megathrust events on the plate interface, intraslab events occurring within the subducted Juan de Fuca plate, and shallow earthquakes generated on crustal faults in the overlying North America Plate (e.g., Cassidy et al., 2000).

Along-strike variations in relative plate motion along the curved Cascadia margin result in differing deformation regimes across the forearc. Subduction obliquity is greatest in the south, which contributes to margin-parallel northward migration of the Oregon and Washington forearc blocks (Wells et al., 1998). Forearc migration rates reduce as obliquity decreases in the northern portion of the subduction zone. Margin-parallel shortening rates of ∼5 mm/yr have been determined from Global Navigation Satellite System (GNSS) data between 46.5°N and 48°N, with north-south shortening decreasing significantly north of the Olympic Mountains (Mazzotti et al., 2002). GNSS data indicate opposite senses of rotation within the forearc north and south of the Olympic Mountains, consistent with oroclinal bending around a NE-trending hinge axis through the Olympic Mountains (Finley et al., 2019). Oroclinal bending is thought to be accommodated by flexural slip on the orocline limbs (Finley et al., 2019), consistent with the mainly oblique right-lateral and left-lateral faulting observed north and south of the Olympic mountains, respectively (e.g., Harrichhausen et al., 2021; Personius et al., 2014). Early models identified the Leech River – Devils Mountain fault as the northern boundary of forearc shortening in Cascadia, based upon the idea that the Coast Mountains of British Columbia act as a backstop (Wells et al., 1998; Johnson et

al., 2001). However, recent studies of Holocene-active faulting in southwest BC indicate that deformation extends farther north than previously known, reaching at least as far as central Vancouver Island (e.g., Caston, 2021; Douglas et al., 2022; Greene et al., 2018; Kelsey et al., 2012; Lynch et al., 2023).

The SoG has hosted persistent low- to moderate-magnitude crustal seismicity at least since the onset of instrumental recording on Canada's west coast. Within the last 50 years, two shallow (3-4 km) moderate-magnitude earthquake sequences have occurred approximately 30 km from Metro Vancouver and Nanaimo, BC (Figure 5.2.1B). The two sequences, occurring in 1975 and 1997, had mainshocks of similar magnitude (M∼5) which were felt as far as Seattle, Washington, and southern Vancouver Island (Rogers, 1979; Cassidy et al., 2000). While the CSSFZ is not thought to be responsible for these sequences, they emphasize that seismic events are not historically unprecedented within the SoG. As mentioned previously, the CSSFZ could be capable of generating earthquakes up to magnitude 6.7, should a full rupture occur in a single event.

Recent seismic activity further highlights ongoing crustal seismicity surrounding the SoG. In early 2025, two considerable earthquakes occurred: one on February 21 in the Sunshine Coast (M_w 4.7, approximately 45 km north of the CSSFZ; Natural Resources Canada, 2025a), and another on March 3 near the San Juan Islands (M_w 4.1, approximately 80 km southeast; Natural Resources Canada, 2025b). Both events were felt across southwest BC, although no damage was reported (Natural Resources Canada, 2025a; 2025b).

5.2.2 Previous Studies

Barrie and Hill (2004) collected multibeam bathymetry data and interpreted two seismic reflection lines over a suspected fault-related scarp and a linear pockmark chain. Results revealed deformation of Holocene reflections and apparent offset of Holocene, Quaternary and bedrock units beneath the seafloor scarp; however, seismic reflection interpretations beneath the pockmark chain were ambiguous and the chain's formation mechanism could not be definitively linked to subsurface faulting (Barrie and Hill, 2004).

Building on earlier research, seismic reflection data were analysed for potential indicators of active faulting across the central SoG (Chapter 4), allowing for the CSSFZ

to be mapped beyond its surface expression. Chapter 4 suggests that the CSSFZ extends northwestward from the Fraser River prodelta for at least 12 km, with a possible extension bringing the total length to 25 km (Figure 5.2.1B). As first hypothesized by Barrie and Hill (2004), the primary strand of the fault is interpreted to comprise two en echelon segments which are connected via a positive flower structure. The reader is referred to Chapter 4.4 for a more thorough discussion of seismic reflection interpretations.

5.2.3 Linear Pockmark Chains and Their Relationship to Subsurface Faults

Pockmarks are seafloor depressions that form when subsurface fluids escape into the water column through venting and displace surrounding fine-grained sediments (Cathles et al., 2010). Pockmarks can occur in isolation, small groups, random fields, or linear chains, and their formation process can be short-lived, episodic or continuous (Hovland and Judd, 1988; Pilcher and Argent, 2007). Pockmarks are considered geohazards (e.g., Hovland et al., 2002; Cathles et al., 2010; Marsset et al., 2010; Cox et al., 2020; Riera et al., 2022). Active venting from seafloor pockmarks can lead to sediment incompetence and seafloor instability; both venting and localized incompetence are hazards for marine infrastructure such as pipelines and telecommunication cables (Hovland and Judd, 1988; Hovland et al., 2002). Thus, the characterization of seafloor pockmarks provides critical information for infrastructure planning.

Morphologically similar linear pockmark chains can form through multiple mechanisms, including iceberg scouring (e.g., Hovland and Judd, 1988; Fader 1991), anthropogenic activity (e.g., Hovland and Judd, 1988; Fader 1991), slope instability (e.g., Pilcher and Argent, 2007), faulting (e.g., Acosta et al., 2001; Pilcher and Argent, 2007), and buried turbidite channels (e.g, Gay et al., 2006; Ho et al., 2018). Another plausible mechanism involves lateral migration of gas along upper permeable beds. When these beds are juxtaposed laterally against an impermeable unit such as bedrock or glacial till, gas may be forced upward to the seafloor, potentially producing linear chains of pockmarks along the boundary. This process is conceptually consistent with known gas migration behaviors (e.g., Hovland and Judd, 1988), although documentation of this specific mechanism and associated chains appears limited.

The presence of a linear pockmark chain alone is not sufficient to confirm sub-

surface faulting; however, such features can serve as potential indicators for underlying structures when considered in conjunction with geophysical data and local context. Several of the mechanisms mentioned above are unlikely to have caused the CSSFZ pockmark chain. For example, there are no present-day icebergs in the Strait of Georgia, and with sedimentation rates of 3-10 cm/yr (Hart et al., 1998), early Holocene iceberg scours would not be preserved. Although the pockmark chain is located on the distal prodelta of the Fraser River, downslope of an area of slope instability (Hill et al., 2008; Stacey, 2014; Rafiei et al., 2023), the orientation and proximity of the chain to the slope instability, along with the low slope of the area surrounding the pockmarks, make slope instability an unlikely cause. There is no reported anthropogenic seafloor activity at this location, although the pockmark chain lies approximately 4 km southwest of the boundary of the Point Grey dredge disposal site, where linear dredge spoils have been observed beyond the designated boundary (e.g., Pettigiani et al., 1997; Mosher et al., 1997).

Previous studies have shown associations between linear pockmark chains and faults (e.g., Acosta et al., 2001; Barrie et al., 2005; Pilcher and Argent, 2007; Zhang et al., 2020). Pilcher and Argent (2007) define fault-related pockmarks based on their formation mechanism. Fault-strike pockmarks form when a fault plane acts as a fluid migration pathway resulting in a linear chain of pockmarks along the fault's surface trace (e.g., Pilcher and Argent, 2007, Acosta et al., 2001). On the other hand, fault hanging wall pockmarks form from extensional faulting that creates an offset of fluid-charged layers and locally reduced overburden pressures, leading to vertical fluid migration through unconsolidated sediments in the hanging wall and the formation of a linear pockmark chain offset from the fault trace (Pilcher and Argent, 2007). Based on seismic reflection interpretations of the CSSF and the distribution of pockmarks along its trace, the pockmark chain associated with the CSSFZ can be classified as a fault-strike chain (Chapter 4).

5.3 Data and Methods

5.3.1 Multibeam Bathymetry and Water Column Data

High-resolution (1, 2, and 5 m) multibeam echosounder (MBES) bathymetry rasters are used to identify fault-related pockmarks and analyze changes in seafloor

morphology over time. Differences between raster datasets were calculated using ESRI ArcGIS Pro software and simple custom Python scripts (via ArcPy) to automate raster subtraction. Datasets were collected in 2000, 2010, 2021, and 2023 using a hull-mounted Kongsberg EM1002 (in 2000) and Kongsberg EM710 (2010-2023) aboard the vessels CCGS RB Young and CCGS Vector, respectively. MBES data were acquired by the Canadian Hydrographic Service in partnership with the Geological Survey of Canada.

Acoustic water column datasets were collected in 2013, 2019, 2021, and 2023, using a Kongsberg EA600 and EA640 aboard the vessels CCGS J.P. Tully and CCGS Vector. Raw data processing and interpretations were conducted using Fledermaus FMMidwater 7.9.4. Raw files were processed into Generic Water Column files, compatible with FMMidwater.

Fluid venting can be interpreted from water column data based on characteristic high reflectivity and flare shapes extending from the seafloor: elongated ribbon-shaped or compact droplet-shaped plumes (e.g., Kehew et al., 2023). Files were assessed for potential flares originating from seafloor pockmarks. All water column data were assessed in R-stack and fan views within FMMidwater.

5.3.2 Seismic Hazard and Risk Calculations

Deterministic seismic hazard and risk scenario calculations were performed with the OpenQuake Engine for a set of hypothetical rupture scenarios along the CSSF. Seismic hazard and risk calculations follow the methodology established by the Canadian Seismic Risk Model (CanSRM1) and were run through modified OpenQuake scripts (Hobbs et al., 2023; https://github.com/OpenDRR/). Multiple input datasets, including gridded shear wave velocity data (Allen and Wald, 2009), a Canadian exposure model (Journeay et al., 2022), Canadian-specific fragility and vulnerability functions (Hobbs et al., 2023), ground motion logic trees from the Canadian Seismic Hazard Model (Kolaj et al., 2020), and user-specified rupture parameters (see Appendix B) are required to run the scripts.

Scenario calculations provide estimates for probable ground shaking, building damage, human consequences and financial losses due to building damage. These scenarios represent a range of plausible ruptures of the CSSF which may occur based on interpretations of presently available data; however, it is important to stress that the scenarios are purely hypothetical and do not represent real events or forecasts.

Modelled results account only for damage resultant from mainshock ground shaking and do not account for secondary perils (e.g., tsunami, slope failure, fire), business interruptions and indirect losses, aftershocks, or damage to linear infrastructure such as roads and highways.

A simplified fault rupture model was employed, requiring inputs for fault trace coordinates, dip, rake, hypocentre location, and upper and lower seismogenic depths. Spatial analyses of modelled results were carried out with QGIS 3.10, further processing (e.g., generating plots from tabular data) were performed with Python, and visualizations were completed with ArcGIS Pro. Seismic hazard results for peak ground acceleration (PGA) were rasterized to a resolution of 3.3 km, equal to the distance between gridded shear wave velocity sites. PGA values were then converted to the Modified Mercalli Index based on empirical relationships outlined in Worden et al. (2012) using simple Python scripts. Modelled results for human consequences, building damage, and economic losses were joined with available census subdivision data (Statistics Canada, 2021) to further analyze the spatial distribution of seismic risk.

5.4 Results and Discussion

5.4.1 Seafloor Pockmarks

5.4.1.1 Pockmark Morphology and Venting

The morphology of the pockmark chain associated with the CSSF was assessed using MBES data collected in 2023. Seventy-nine pockmarks were identified, with the main chain comprising sixty-eight features (Figure 5.4.1). The remaining eleven pockmarks are located off the northwest and southeast ends of the main chain. An additional six features imaged along the chain are too small to be classified as pockmarks with high certainty. Along the pockmark chain, features range in shape from circular (length-to-width ratio = 1.0-1.5) to elliptical (length-to-width ratio = 1.5-2). The pockmarks range in size from 25 to 200 m wide and from 1 to 25 m deep. Seventy percent of pockmarks in the dataset can be classified as 'normal' circular pockmarks based on their size and shape (Hovland et al., 2002; Chen et al., 2015).

Difference analyses comparing the 2000 and 2023 datasets reveal five pockmarks that were unresolved in the initial MBES survey (Figure 5.4.1 C). These features range

in width from 25 to 40 m and have depths that are 1-2.85 m greater than the same seafloor location in the 2000 dataset. As the newly imaged features are much wider than the 5-meter resolution of the initial dataset, they cannot be attributed to enhanced survey resolution. Instead, these features are interpreted as having developed since the initial survey in 2000. Three of the newly developed pockmarks are situated on the northwest end of the linear chain and extend the chain by ~750 m along the trace of the CSSF. The alignment and continued development of pockmarks along the CSSF suggest that ongoing fluid migration along the fault could play a role in their formation. Analyses of all available MBES datasets (Figure 5.4.1) indicate that existing pockmarks

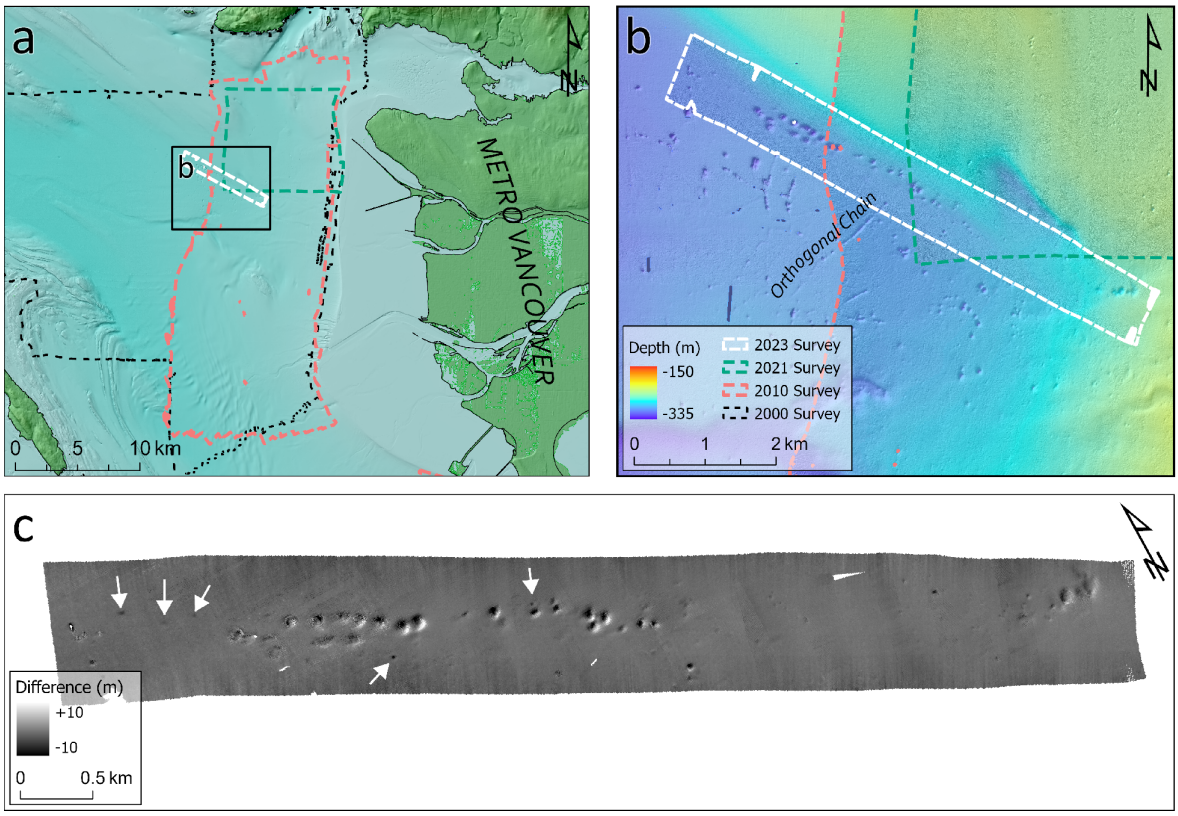


Figure 5.4.1: MBES survey extents are indicated with white, green, red, and black dashed lines for the 2023, 2021, 2010 and 2000 datasets, respectively. A) Location map, indicating the location of panel B with respect to Metro Vancouver. Basemap modified from Kung et al. (2023). B) Multibeam bathymetry datasets over the linear pockmark chain. The extent of the original survey, collected in 2000, covers the entirety of the subfigure, whereas the 2010 and 2021 surveys lack data for the northwestern part of the pockmark chain. C) Difference map, calculated from the 2023 and 2000 datasets. Features interpreted as new pockmarks having developed since the 2000 survey are indicated with white arrows. Map extent matches the extent of the 2023 survey, indicated in panels A and B.

are deepening at their centres, while sediment deposition occurs on their southeastern flanks. No evidence of active fluid venting was observed over seafloor pockmarks along the main pockmark chain in the assessed water column data.

A smaller additional linear pockmark chain lies to the south of, and approximately orthogonal to, the main pockmark chain, along with numerous randomly oriented pockmarks (Figure 5.4.1 B). This secondary chain is 1.9 km long and consists of at least 10 pockmarks which are 35 to 76 m in width and up to 9 m deep. Multiple pockmarks within this smaller chain appear to have converged into a single, continuous elongated feature. Seismic reflection profiles in the area do not cross the SW-NE-oriented chain at orientations that would enable examination of the subsurface beneath the chain (see Section 4.4.1). Thus, its relation to the main strand and its formation mechanism cannot be constrained.

5.4.1.2 Hazards Associated with Pockmarks

Despite the lack of observed venting in this study, the development of new pockmark features, combined with an observed deepening of existing features in an area of high sedimentation (La Croix et al., 2024), indicates likely active venting along the linear pockmark chain. Offshore Vancouver Island, fluid venting has been shown to be highly temporal and affected by tides, with increased emissions strongly correlating with decreasing water pressure (Römer et al., 2016). The lack of observed fluid venting in this study could indicate inactivity; alternatively, it could be indicative of intermittent venting due to tidal modulation.

Active linear pockmark chains can be associated with subsurface geohazards such as faults, as is interpreted in this study, and can serve as indicators of such structures when combined with additional geophysical data (e.g., Acosta, 2001; Pilcher and Argent, 2007; Zhang et al., 2020). Additionally, the relationship between pockmark venting and earthquakes has been studied in other regions globally. Increases in venting have been observed prior to and during sizeable ($M > 5$) earthquakes (e.g., Field and Jennings, 1987; Hasiotis et al., 1996; Soter, 1999; Fakiris et al., 2023). On Vancouver Island, several craters resulting from 'sand blows' (water geysers expelling sand and muddy sediments) were observed on beaches following the 1946 M_W 7.3 earthquake (Hodgson, 1946). Hovland et al. (2002) suggest the need for ongoing monitoring of pockmarks in areas of high seismic risk. However, no known studies exist for offshore regions of the Salish Sea, and no such correlations have been observed in nearby waters,

such as offshore Vancouver Island (Lapham et al., 2013; Römer et al., 2016). Active venting prior to and during earthquake events would likely not explain the observed deepening and the development of new features along the main chain, as no sizeable earthquakes attributable to the CSSFZ were recorded within the timeframe of the datasets in this study.

Beyond associations with other hazards, active pockmarks can be a geohazard on their own. Pockmark venting can lead to sediment incompetence and seafloor instability, which can damage seafloor infrastructure such as pipelines and telecommunication cables (Hovland et al., 2002). While the associated hazard is minor compared to a fault rupture, pockmarks constitute an inferred-active, localized hazard associated with the CSSFZ, for which potential risk should be considered during future seafloor infrastructure planning.

5.4.2 Fault Characterization and Input Parameters

Potential indicators for active faulting across the central Strait of Georgia study area have been systematically mapped from seismic reflection data (Chapter 4). The focus within this chapter is on further constraining the CSSF to inform seismic hazard and risk calculations. A characterization of the CSSF, including lateral extent, strike and dip were estimated from these seismic reflection data interpretations (Chapter 4 and Appendix A). Additional parameters, such as constraints for rake and hypocentre depth are more difficult to determine with the available data, yet remain key parameters needed for hazard and risk calculations.

5.4.2.1 Lateral Extent, Strike, and Dip

The lateral extent of the CSSF is shown in Figure 5.4.2, based on interpretations of seismic reflection data outlined in Chapter 4. The fault is composed of two en echelon segments oriented NW-SE, with local variations along its length; it has a net strike of $\sim$123°. Indicators for Holocene-active faulting are traced for at least 12 km (solid black lines in Figure 5.4.2; Chapter 4). Additional observed fault indicators within Quaternary-aged units extend the CSSF (dashed line, Figure 5.4.2) at least 6.7 km and possibly up to 12.8 km. Thus, hazard and risk scenarios consider two lengths: a 'short scenario' representing a magnitude 6.3 earthquake along a 12-km-long fault and a 'long scenario' representing a magnitude 6.7 earthquake along a 25-km-long fault.

Seismic reflection data suggest the presence of a 2-3 km wide fault zone, rather than a singular fault near the pockmark chain (Chapter 4); however, for the hazard and risk calculations described in 5.4.3, a combined rupture of the two main en echelon segments (CSSF) is considered. The CSSF fault is modelled as a single, continuous plane with a simple geometry, assuming a full-length rupture and neglecting any additional faults that may exist within a broader fault zone. It is emphasized that the fault trace shown in Figure 5.4.2 should be taken as indicative of the CSSFZ, not definitive linear segments.

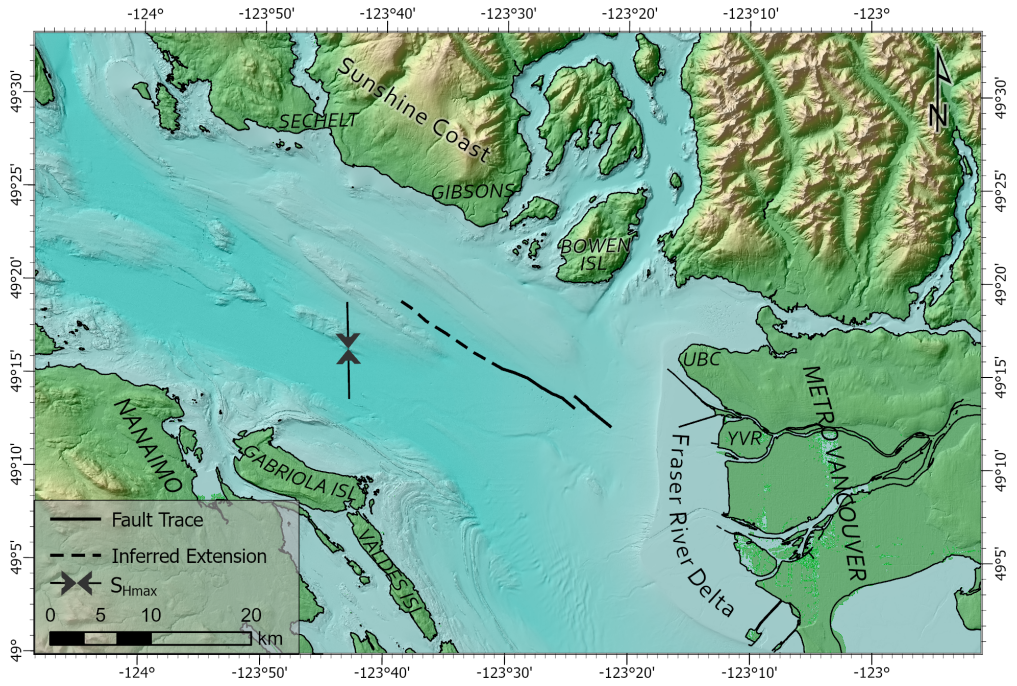


Figure 5.4.2: Simplified extent of the CSSF based on interpretations of active fault indicators in Chapter 4. Fault segment traces are shown with solid black lines. The fault's inferred extension to the northwest is shown with a dashed black line. Orientation of local maximum horizontal compressive stress is shown with black arrows (Balfour et al., 2011). Basemap modified from Kung et al. (2023). YVR: Vancouver International Airport; UBC: University of British Columbia campus.

The dip of the CSSF is constrained from seismic reflection lines, with measured values ranging from 61° to 89° SW; an average dip of 75° SW is applied for these calculations with an uncertainty of $\sim \pm 10°$. To enable estimation of fault dip, two-way travel time (TWT) was converted to depth using an average seismic velocity of 1540 m/s for saturated unconsolidated sediment units (e.g., Tóth et al., 2014). As the seismic reflection data used in this study image the shallow subsurface (up to 1000 ms, ~750 m), fault dip at depth remains unknown. Thus, a uniform dip extending to

depth is assumed.

Uncertainty in measured dip is higher in many legacy airgun data, which tend to exhibit lower signal-to-noise ratios. To minimize uncertainty in dip estimates, values were only calculated for seismic reflection lines oriented orthogonal to the fault and were not calculated for lines with high interpretational uncertainty. An additional source of uncertainty stems from the conversion of TWTs to depth through the application of a constant seismic velocity across Holocene and Quaternary units. Seismic velocities, however, are not constant and vary depending on factors such as composition, the presence of subsurface fluids, and depth/compaction, introducing additional uncertainty. To explore the impact of seismic velocity on the estimated depths, a range of reasonable velocities higher (e.g., 1800 m/s; Dash et al., 2007) and lower (e.g., 1450 m/s; Schumann et al., 2014) than the assumed constant value were tested. Results did not vary significantly, with the resultant dips predominantly insensitive to the velocity within the inferred dip uncertainty of $\pm 10^{o}$.

5.4.2.2 Faulting Mechanism and Rake

Seismic reflection data present inherent limitations in the determination of the style of fault rupture. Since the data are profiles of the subsurface, vertical displacements can be estimated; however, strike-slip motion can only be inferred from indirect evidence and cannot be quantified from 2D seismic reflection data. Additionally, apparent vertical offsets observed in seismic reflection profiles may arise from lateral displacements. Further, there are no recorded earthquakes, and consequently, no focal mechanisms or derived S_{Hmax} orientations, attributable to the CSSFZ which could help constrain rupture style. Consequently, a plausible faulting mechanism is constrained by comparing the nearby S_{Hmax} orientation with the fault orientation and dip direction. This value serves as an estimate to inform the hazard and risk calculations in this study.

The local S_{Hmax} direction in the central SoG is 178^{o}, as determined through a formal inversion of 12 focal mechanisms (Figure 5.4.2; Balfour et al., 2011). This orientation is $\sim 55^{o}$ clockwise of the net strike of the CSSF, suggesting that the fault may accommodate oblique right-lateral slip with a reverse component. It is important to note that this estimate refers to the net strike of the fault and does not take into account relays or changes to strike along its length. In addition, this estimate only accounts for the main strands of the fault, and does not consider any additional faults

that may exist within a broader fault zone (see Chapter 4).

Seismic reflection interpretations, including a positive flower structure, localized Holocene deformation, and upward bending of the seabed between en echelon fault segments, support an oblique right-lateral slip sense (Section 4.4.1). Oblique right-lateral faulting is consistent with previous studies of active faults in nearby locations, such as the southern Salish Sea and southern Vancouver Island, which predominantly exhibit right-lateral and oblique right-lateral faulting (e.g., Caston, 2021; Harrichhausen et al., 2021; Harrichhausen et al., 2023; Kelsey et al., 2012).

5.4.2.3 Seismogenic Depth

In the absence of instrumentally recorded seismicity directly associated with the CSSFZ, regional seismicity data are used to estimate a plausible hypocentre depth and lower seismogenic depth. Figure 5.4.3 depicts a depth histogram of the relocated earthquake catalog of Merrill et al. (2022) for events within the study area, considering only highly ranked events (S and A) and all others discarded. Earthquakes occur through the range of 0-30 km, with an average depth of 11 km. For the fault model used in subsequent hazard and risk calculations, 11 km is used as the hypocentre depth. To minimize the effect of outliers, the 95th percentile cut-off for the distribution, equal to 17 km, is used as an estimate for lower seismogenic depth (e.g., Magistrale, 2002; Rolandone et al., 2004; Zuza and Cao, 2020), such that earthquake scenarios are assumed to involve rupture from the seafloor to 17 km depth.

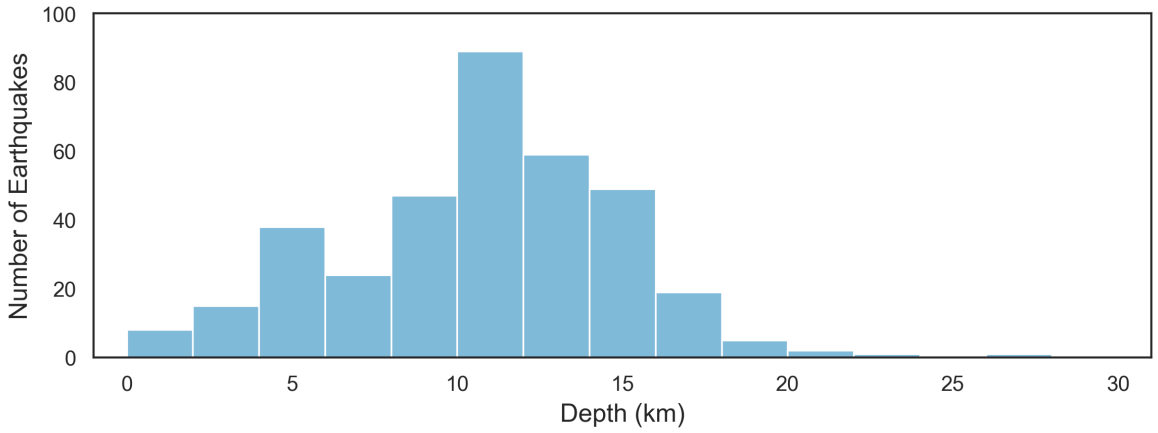


Figure 5.4.3: Distribution of earthquake events by depth in the central Strait of Georgia study area. Seismicity data from the REST catalogue (Merrill et al., 2022).

5.4.3 Seismic Hazard and Risk

Four scenarios were modelled, representing different rupture styles and varying fault lengths. While oblique right-lateral faulting is considered likely as discussed above, a singular likely rake cannot be constrained. As such, scenarios were selected to encompass a range of possibilities, including right-lateral strike-slip, oblique, and reverse ruptures. However, the ground motion prediction equations utilized in Canada's Seismic Hazard Model do not differentiate between pure reverse slip (rake = 90°) and oblique slip (e.g., rake = 135°), resulting in reverse and oblique scenarios generating equivalent results (Abrahamson et al., 2014; Boore et al., 2014; Campbell and Bozorgnia, 2014; Chiou and Youngs, 2014). Consequently, the models include long and short ruptures involving oblique/reverse slip (rake = 90-150°) or pure strike slip (rake = 180°). Input parameters for all models are summarized in Table 5.4.1. OpenQuake inputs, including ruptures and model initializations, are given in Appendix B.

Average ground motion fields for all scenarios are presented in Figure 5.4.4. Modelled results indicate that Metro Vancouver and Gibsons, BC experience the strongest ground motion as a result of a CSSF rupture, regardless of size or mechanism. Additional areas which experience moderate to strong shaking (MMI = 5-7) include Nanaimo, the Sunshine Coast, Gabriola Island and Valdes Island (Figure 5.4.4). The highest value for peak ground acceleration (PGA) across all scenarios is an estimated 0.34 g, located at the University of British Columbia (UBC) campus in Metro Vancouver.

Table 5.4.1: Summary of input parameters for all modelled fault rupture scenarios.

Scenario	Length (km)	Rake (°)	Dip (°)	Dip Direction	Rupture Type	M_w	Hypocentre Depth (km)
Short Strike-Slip	12	180	75	SW	Strike-Slip	6.3	11
Short Oblique /Reverse	12	110	75	SW	Reverse / Oblique	6.3	11
Long Strike-Slip	25	180	75	SW	Strike-Slip	6.7	11
Long Oblique /Reverse	25	110	75	SW	Reverse / Oblique	6.7	11

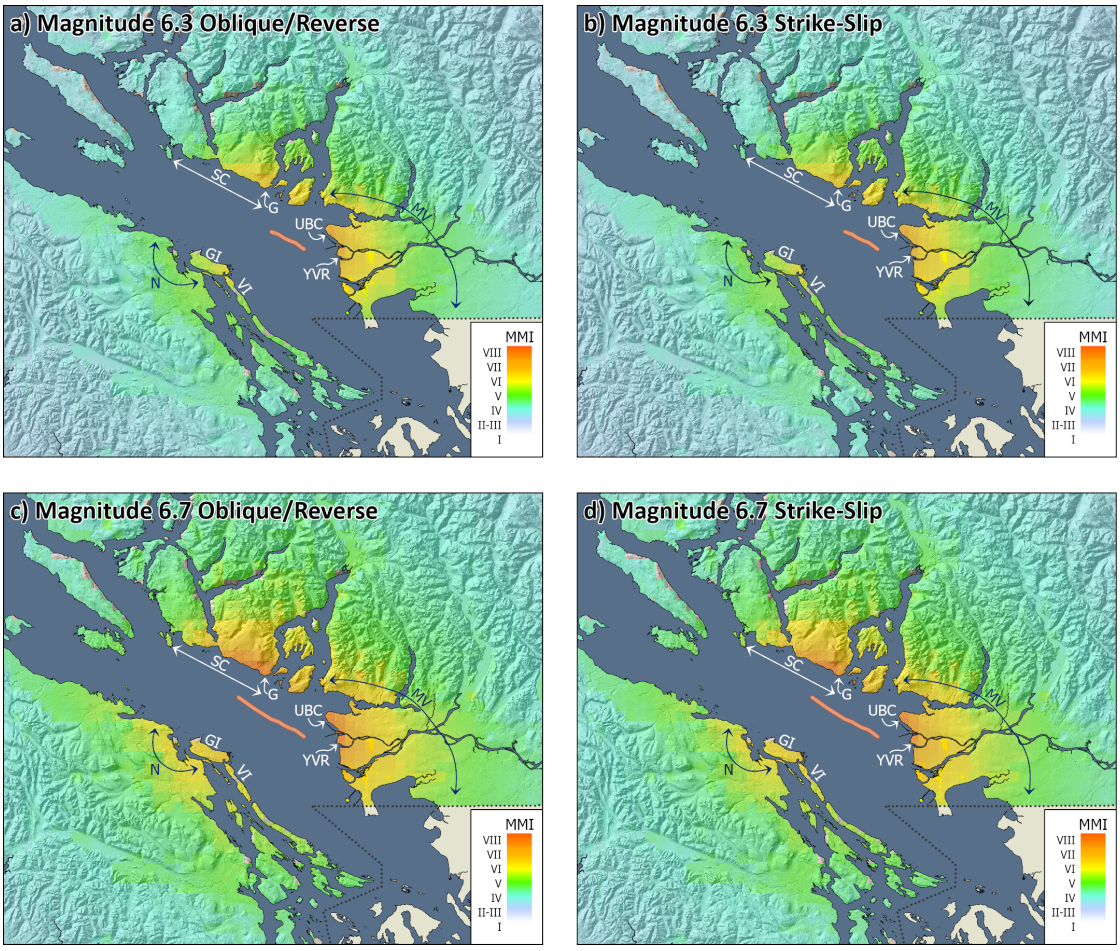


Figure 5.4.4: Seismic hazard maps for each daytime CSSF rupture scenario. Ground shaking values were converted to the MMI scale from mean PGA based on empirical relationships outlined in Worden et al. (2012). Canada-US border is shown with a dotted black line. Simplified fault traces for each scenario are indicated with an orange line. Seismic hazard results were not calculated for areas outside of Canada. Areas beyond the map extent are expected to experience MMI values of 0-IV, corresponding to no to light perceived shaking and no expected damage. G: Gibsons; GI: Gabriola Island; MV: Metro Vancouver; N: Nanaimo; SC: Sunshine Coast; UBC: University of British Columbia Campus; V: Valdes Island; YVR: Vancouver International Airport.

Modelled average economic losses, building damage, and human consequences offer insight into the impact of a potential fault rupture. A summary of estimated casualties, damage, disrupted residents, and losses for all scenarios is provided in Table 5.4.2. Among the modelled scenarios, the magnitude 6.7 oblique/reverse event would have the greatest impact on local populations. In this scenario, an estimated 1300 deaths, 650 life-threatening injuries, 5600 buildings classified as completely damaged ("red-tagged"), and $18.5 billion (2019 CAD) in economic losses are projected. These values assume a daytime rupture, occurring between 9 am and 5 pm, when many are

Table 5.4.2: Key results for seismic hazard and risk for CSSF scenarios.[1]

Scenario	Deaths	Life-Threatening Injuries	Residents Disrupted after 90 Days	Red-Tagged Buildings	Total Losses (2019 CAD, Billions)
M 6.3 Strike-Slip	680	330	113,000	2800	$10.8
M 6.3 Oblique /Reverse	690	340	115,000	2900	$11.1
M 6.7 Strike-Slip	1260	630	235,000	5400	$17.7
M 6.7 Oblique /Reverse	1300	650	243,000	5600	$18.5

assumed to be at work or school (FEMA, 2024). Definitions for key impacts are based on those outlined by FEMA (2024): "deaths" are defined as immediate deaths and mortal injuries and do not account for additional deaths resulting from any untreated life-threatening injuries; "life-threatening injuries" are defined as all injuries that are an immediate, life-threatening condition if not treated properly and expeditiously; "red-tagged buildings" are defined as buildings in a complete damage state, which are considered permanently uninhabitable, and may be collapsed, or be in imminent danger of collapse; and "disrupted residents" are defined as occupants living in a damaged building after a given time period.

To illustrate the spatial distribution of affected communities across the range of scenarios, results for the least and most impactful modelled events - the magnitude 6.3 strike-slip and magnitude 6.7 oblique/reverse scenarios, respectively - are mapped by census subdivision in Figure 5.4.5. These results indicate that census subdivisions within Metro Vancouver, Nanaimo, Sechelt, and the Gulf Islands may experience higher impacts than other coastal BC communities. This is especially true for Vancouver, which across all scenarios experiences the highest estimated damage, casualties, and economic losses. Estimates for hospital demand, defined as the number of people with life-threatening or non-life-threatening injuries requiring hospitalization after an earthquake, suggest that multiple census subdivisions within Metro Vancouver could be affected. In Vancouver, hospital demand is projected to be 1990 people in the most severe modelled scenario and 1120 people in the least severe (Figure 5.4.6). Nanaimo, located on Vancouver Island, is also within the top ten census subdivisions in terms of hospital demand, with an estimated 140 and 50 people hospitalized in the most and

[1]Scenarios assume a daytime rupture. Total losses are given in Canadian dollars as of 2019. Values <2,000 rounded to nearest 10; 2,000–10,000 to nearest 100; >10,000 to 3 significant figures.

least severe scenarios, respectively. Major hospitals projected to be affected include, but are not limited to, Vancouver General Hospital, St Paul's Hospital, Lion's Gate Hospital, Nanaimo Regional General Hospital and the UBC Hospital.

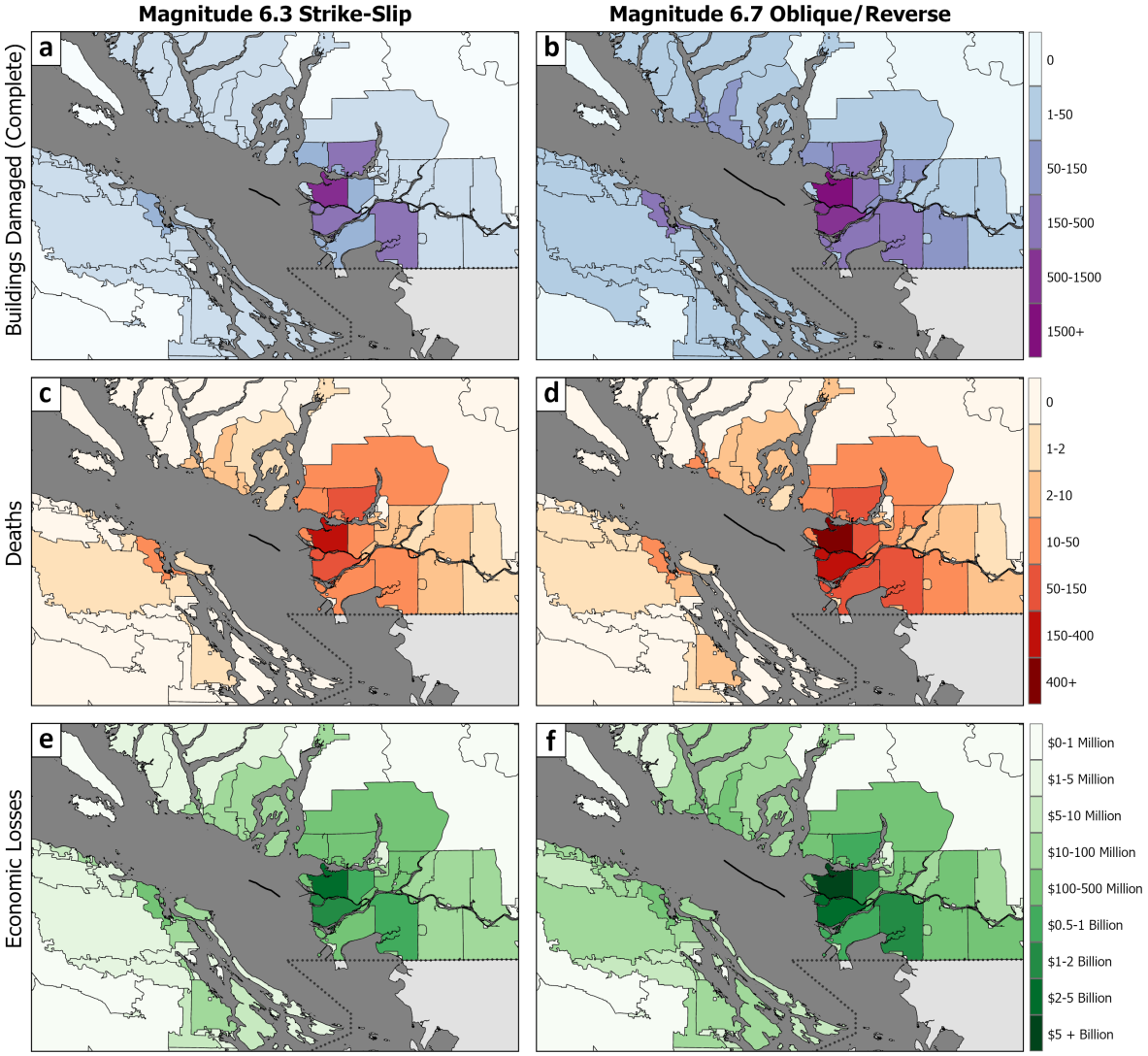


Figure 5.4.5: Modelled results summarized by census subdivision for the most (right panels; b, d, f) and least (left panels; a, c, e) impactful modelled daytime scenarios. For all panels, a simplified fault trace is denoted with a black line, and the Canada-US border is shown with a dotted line. A and B: Number of buildings in a state of complete damage. C and D: Estimated deaths. E and F: Estimated economic losses. Dollar values are in Canadian currency as of 2019.

The results outlined above account only for the direct impacts of shaking during a mainshock event and do not account for secondary effects such as liquefaction, slope failures, tsunamis, aftershocks, or fires. Additionally, they do not account for damage to linear infrastructure (e.g., roads, seafloor telecommunication cables, airport runways,

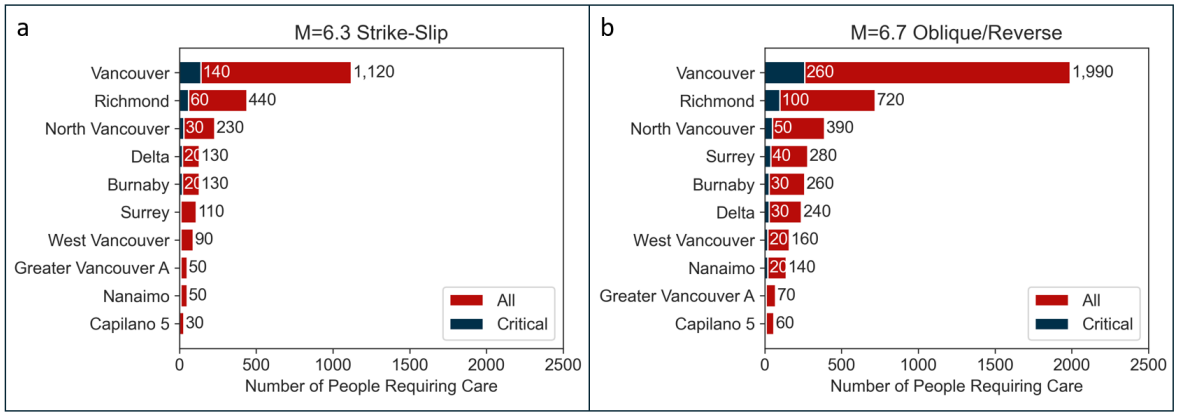


Figure 5.4.6: Estimated hospital demand for the 10 most impacted census subdivisions. Results are summarized for the magnitude 6.3 strike-slip and magnitude 6.7 oblique/reverse daytime scenarios. Note that Greater Vancouver A corresponds to the UBC campus. Values are rounded to the closest ten.

water pipelines, etc.), which could lead to further, unquantified impacts. For example, the modelled hazard scenarios suggest that the Vancouver International Airport (YVR) could experience a mean PGA up to 0.30 g. Past earthquakes of similar magnitudes have resulted in varying degrees of damage to airport runways due to ground shaking. In 2007, an M_W 6.7 earthquake on Japan's Noto Peninsula resulted in multiple runway cracks (Hata et al., 2012). In contrast, the 2010 M_W 7.1 Darfield earthquake in New Zealand resulted in only minor structural and non-structural (e.g., broken windows) damage, with no damage to the airport's linear infrastructure or fueling facilities (Tang, 2016). For this event, recorded ground motions reached ~0.30 g at the closest airport (Tang, 2016), the same level modelled for YVR in this study.

Secondary hazards and damage to linear infrastructure can contribute substantially to fatalities. Eighteen percent of fatalities resulting from the 2024 M_W 7.5 Noto Peninsula earthquake resulted from secondary hazards (7% from landslides, 3% from fires, 1% from tsunami, and 7% unspecified; Suppasri et al., 2024). For the same event, fourteen percent of deaths occurred due to exposure and hypothermia, attributed in large part to severely damaged roads, which prevented timely rescues (Suppasri et al., 2024). During the 2011 Canterbury sequence in New Zealand, in which 185 fatalities occurred due to a M_W 6.2 earthquake, five fatalities were attributed to rockfall (~3% of total fatalities) and hundreds of houses were damaged by slope failures (Potter et al., 2015; Dellow et al., 2011).

It is prudent to discuss recurrence rates with these hazard and risk results in mind. Although interpretations of seismic reflection data indicate possible Holocene

activity along the CSSFZ (Chapter 4), the recurrence rate of large earthquakes on the fault is unknown and cannot be determined with presently available data. Typically, recurrence rates for terrestrial faults are estimated through paleoseismic studies, such as trenching to date past ruptures (e.g., Morell et al., 2018; Harrichhausen et al., 2023). However, this approach is not feasible for submarine faults. While estimates of Holocene offset along submarine faults can offer some constraints on recurrence, vertical offsets along the CSSFZ are inconsistent, likely reflecting a degree of strike-slip motion. The hazard and risk calculations presented herein represent plausible ruptures of the fault yet may not be representative of actual future events. The results should be interpreted cautiously; nevertheless, they are noteworthy enough to warrant consideration and suggest that a rupture could have measurable consequences for coastal British Columbia, particularly areas of Metro Vancouver and Nanaimo. Given the potential for serious impacts, incorporating the CSSFZ into Canada's National Seismic Hazard Model could help ensure that local building codes adequately address the risks posed to coastal British Columbian communities.

5.4.4 Implications for Tsunami Hazard

Tsunami hazard associated with crustal faults can arise from both seafloor tectonic offsets and from shaking-induced submarine/coastal slope failures. Both are pertinent for the CSSFZ, as its proximity to the Fraser River delta and multiple urban centres may present substantial implications for tsunami hazard.

5.4.4.1 Shaking-Induced Slope Failures

Considering the proximity of the CSSFZ to the Fraser River delta – an area of known slope instability and ongoing geohazard research (Hill et al., 2008; Stacey, 2014; Rafiei et al., 2023) – it is worthwhile to discuss the tsunamigenic implications of shaking-induced submarine/coastal slope failures within the central SoG. Numerical modelling of hypothetical submarine slope failures along the delta front simulated wave crests of 2-18 m for a large (7 x 3 km^2; 0.75 km^3) failure and 0.8-8.5 m for a small (4 x 2.6 km^2; 0.23 km^3) failure (Rabinovich et al., 2003). Previous crustal earthquakes in coastal British Columbia have produced locally dangerous waves from shaking-induced slope failures. Notably, an M_S 7.3 crustal earthquake, which occurred beneath central Vancouver Island in 1946, showed no discernible seafloor offset yet triggered multiple

onshore and submarine slope failures and generated large local waves capable of capsizing boats (Conway et al., 2013; Hodgson, 1946; Mosher et al., 2004; Rogers and Hasegawa, 1978). One drowning death occurred in Canada as a result (Rogers and Hasegawa, 1978).

5.4.4.2 Seafloor Tectonic Offset

The CSSF exhibits evidence of past Holocene surface rupture through 1) a fault scarp visible in MBES data and 2) seafloor and near-surface Holocene deformation detectible in seismic reflection data (Chapter 4). Although no confirmed tsunami deposits have been reported around the central Strait of Georgia (e.g., Goff et al., 2020), nor any known deposits which may be associated with the CSSFZ, previous studies have detailed paleoseismic evidence for tsunami deposits from crustal faults in the Salish Sea (e.g., Williams and Hutchinson, 2000; Kelsey et al., 2012). Kelsey et al. (2012), based on interpretations of a probable tsunami deposit, coincident with vertical coseismic displacement, in the southern Strait of Georgia, suggest that an M∼6 earthquake along a submarine crustal fault could deform the seafloor and be tsunamigenic. Seafloor displacements in scenario ruptures were modelled by Caston (2021).

Additional work, beyond the scope of this study, is required to properly model the tsunamigenic potential of a rupture along the CSSFZ. However, potential tsunami runup (the elevation reached by seawater during a tsunami) resultant from reverse seafloor tectonic offset can be estimated through empirical relationships as defined by Abe (1995). For coastlines up to a limiting distance D_L from an earthquake source,

$$log_{10}H_L = 0.5M_W - 3.3 \tag{5.1}$$

where H_L is the limiting runup. For coastlines at a distance (D) greater than D_L,

$$log_{10}H_r = M_W - log_{10}D - 5.55 \tag{5.2}$$

where H_r is the local mean runup. The limiting distance D_L is determined by

$$log_{10}D_L = 0.5M_W - 2.25 \tag{5.3}$$

Notably, D_L is equal to 8 km for M_W 6.3 and 13 km for M_W 6.7 events. Limiting

local maximum runups and local maximum runups ($2H_L$ and $2H_r$, respectively) can be calculated by multiplying the resultant mean runup values by 2.

Table 5.4.3 presents calculated local mean and local maximum runups for UBC campus, Gibsons, Sechelt, and Nanaimo for M_W 6.3 and M_W 6.7 events. Distances are set as the minimum distance from the coast to the CSSFZ. The values in Table 5.4.3 account for seafloor offset alone, and do not quantify tsunami runup generated from shaking-induced slope failures; they also do not account for topography, bathymetry, source parameters, or currents. Strike-slip or oblique ruptures, which involve less vertical seafloor displacement than reverse ruptures, can be expected to generate lower tsunami runups.

Table 5.4.3: Calculated local mean and maximum tsunami runups for select locations near the central SoG for two CSSF rupture scenarios.[2]

Magnitude	Runup Type	UBC Campus	Gibsons	Sechelt	Nanaimo
M_W 6.3	Local mean runup (H_r)	0.6 m	0.5 m	0.3 m	0.25 m
	Local max runup ($2H_r$)	1.2 m	1.0 m	0.6 m	0.5 m
M_W 6.7	Local mean runup (H_r)	1.1 m = H_L	1.1 m = H_L	0.8 m	0.6 m
	Local max runup ($2H_r$)	2.2 m = $2H_L$	2.2 m = $2H_L$	1.6 m	1.2 m

Damage and inundation tend to occur for runups as low as 1.5-2.0 m (Whitmore et al., 2008). Thus, tsunami runups of 1.5 m can be used as an estimated threshold for damaging coastal waves (e.g., Leonard et al., 2012). It's important to note, however, that more limited damage and casualties may occur for runups below 1.5 m due to strong currents (e.g., Whitmore et al., 2008). Along the west coast of North America, there have been reports of damage to moorings and boats for runups as low as 0.5 m, and drownings or near drownings have been reported for runups between 0.6 and 0.8 m (Whitmore et al., 2008).

In the M_W 6.3 scenario, no coastal locations are expected to meet or exceed the 1.5 m runup threshold. However, some locations may experience runups between 0.5 and 1.2 m, which could have minor impacts (e.g., Gibsons and UBC Campus). In the M_W 6.7 scenario, local maximum runups exceed 1.5 m, which could result in more severe flooding and damages (e.g., UBC, Gibsons, Sechelt, Table 5.4.3). Using Equation 2, it can be determined that coastal sites up to 19 km from an earthquake source experience local maximum runups of at least 1.5 m. For a CSSF rupture,

[2]Calculations based on empirical relations from Abe (1995) assuming a reverse rupture.

this could encompass multiple population centres in southwest BC including Gibsons, Bowen Island, Sechelt, Gabriola Island and parts of Metro Vancouver (Figure 5.4.7). Leonard et al. (2012) define tsunami runups of 3 m or greater as having significant damage potential, resulting in major, geographically extensive damage. Neither an M_W 6.3 nor an M_W 6.7 CSSF rupture are expected to produce runups of this magnitude due to seafloor offset.

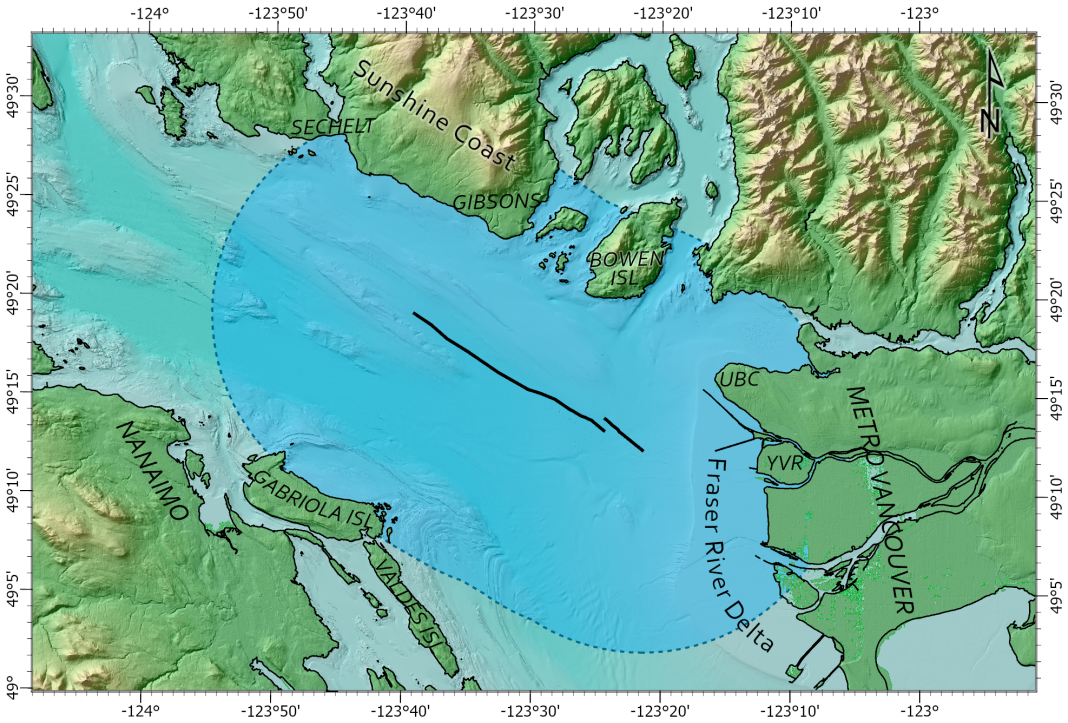


Figure 5.4.7: Zone for potentially damaging tsunami waves, based on empirical relations from Abe (1995) assuming an M_W 6.7 event. Areas within the blue polygon may experience a local maximum runup of $\geq$1.5 m. Fault trace is shown as a black line. Basemap modified from Kung et al. (2023).

5.5 Conclusions

Within this chapter, the CSSFZ was assessed for its potential impacts in terms of pockmark formation and earthquake shaking. Consideration was also given to tsunamigenic potential from seafloor displacement and shaking-induced slope failure. Intermittent seafloor venting and localized seafloor incompetence along the CSSFZ's linear pockmark chain are inferred from the development of new pockmarks observed over a period of 23 years. Newly imaged pockmarks range in size from 25 to 40 m in width,

and extend the length of the pockmark chain by approximately 750 m to a total length of 4.6 km.

The CSSF is characterized for seismic hazard and risk modelling purposes as a 12-25 km long, right-lateral oblique fault, dipping at 75° to the southwest, which may be capable of producing a shallow, magnitude 6.3 to 6.7 earthquake near populated areas of BC. Fault ruptures were modelled for four scenarios, representing variations in rupture length and rake. Modelled results estimate up to 1300 deaths, 5600 buildings rendered uninhabitable, and 18.5 billion dollars in economic damage, with the strongest impacts being felt in the City of Vancouver. The CSSFZ has additional implications for tsunami hazard. Based on its characterization herein and its geographic location, a fault rupture could conceivably result in seafloor displacement or failure of the Fraser River delta, an area of slope instability. Empirical equations were used to estimate tsunami runups resulting from seafloor displacement for magnitude 6.3 and 6.7 ruptures. The calculations suggest that a magnitude 6.7 rupture could generate damaging waves affecting multiple populated coastal areas of BC. These results warrant future tsunami modelling to better assess potential impacts for nearby communities and coastal assets.

Chapter 6

Process and Rationale for Fault Renaming

6.1 Indigenous Name Usage in Geoscience Publications

Increasingly, geoscience publications are incorporating Indigenous languages to name features, structures, and stratigraphy in Canada. For example, the X̲EOLX̲ELE~~K~~-Elk Lake fault near Victoria, British Columbia primarily uses the SENĆOŦEN name for Elk Lake used by the W̱SÁNEĆ peoples (Harrichhausen et al., 2023). This name was suggested to researchers by Simon Smith Jr, a W̱SÁNEĆ cultural observer for excavation on the fault, and then adopted as the fault's published name (Finley, personal communication, 2024). This is a positive example of attempting to incorporate Indigenous language. However, even in cases where Indigenous connections to the land are considered in naming, there is a lack of documentation on how names were chosen and if Indigenous communities were approached for their direct input.

In addition to incorporating Indigenous perspectives in names for newly published features, there have been efforts in recent years to rename features. Unfortunately, many examples of such name changes within geoscience were justified by the former names being culturally offensive, archaic, or inappropriate (Hadlari et al., 2020; MacNaughton et al., 2022). One such example is the Husky Lakes fault zone, which was renamed due to the previous name, 'Eskimo Lakes fault zone', being culturally offensive (Hadlari et al., 2020). A second example is the abandonment of the name 'Maori Bottom' in New Zealand, which referred to an unconformity and an underlying brown-coloured greywacke sandstone conglomerate, in favour of the name Maniototo Conglomerate (Youngson et al., 1998). MacNaughton et al. (2020), in their application to revise the North American Stratigraphic code to encourage the use of Indigenous

language and address culturally inappropriate names, note that the 'Maori Bottom' example was "the single published example [of renaming a culturally insensitive stratigraphic name] of which we are aware." These efforts align with broader renaming initiatives in Canada, where numerous place names have been changed to better reflect Indigenous languages and remove colonial or inappropriate terminology. For instance, the name Haida Gwaii replaced Queen Charlotte Islands in 2010, and the community of Ulukhaktok, NWT, was renamed from Holman in 2006. Within a Canadian geoscience context, only one instance of renaming – the example by Hadlari et al. (2020) above – could be found in the review for this thesis chapter.

Although both examples given here abandoned an older name, neither of these examples document Indigenous participation in renaming. Instead, the Husky Lakes fault zone was renamed after the English name for a geographic feature (the Husky Lakes), and the name Maniototo Conglomerate was chosen because it was the first published name given to the strata (Hadlari et al., 2020; Youngson et al., 1998).

6.2 Central Salish Sea Fault

Previous chapters in this thesis discuss a crustal fault located in the central Strait of Georgia, referred to previously as the Fraser Delta fault (Barrie and Hill, 2004). Also in the Strait of Georgia is the Fraser River Delta fault, another crustal fault interpreted to be Holocene-active (Greene et al., 2018; Caston, 2021). Given the name and location similarities between the Fraser River Delta fault and the Fraser Delta fault, the Fraser Delta fault was given an interim name - the Central Salish Sea fault - to avoid confusion within this thesis.

In choosing a new name for this fault, cultural sensitivity and historical context were key considerations. Acknowledging and recognizing the impacts of the geoscience community's history of colonial naming practices, the importance of Indigenous participation was prioritized. This decision was motivated by the Truth and Reconciliation Commission of Canada's Calls to Action (Truth and Reconciliation Commission of Canada, 2015) and the 10 Calls to Action for Natural Scientists (Wong et al., 2020). Wong et al.'s (2020) Call 6 is particularly pertinent: "To decolonize the landscape, we call on natural scientists to incorporate Indigenous place names as permitted." Indigenous traditions and language offer unique, often overlooked, perspectives on landscapes, geohazards and the real, significant impacts of seismic events on communities over time.

The following section serves to document the approach taken for Indigenous engagement during this process, with full disclosure that time constraints for this thesis prevented a proper renaming of the fault to incorporate Indigenous language and perspectives. While the interim name (Central Salish Sea fault) does not reflect Indigenous language, the section below is included for transparency and in hopes that these efforts may help or inform similar endeavours in the future.

6.2.1 Engaging Indigenous Communities and Interim Renaming

With an overarching goal of working with local Indigenous communities to incorporate their perspectives into a renaming process, first and foremost we considered which First Nations to consult. The marine environment has long been shared among many Nations, and a rupture from a possible fault in the central Strait of Georgia could impact multiple communities. As such, an initial contact list of Indigenous communities was obtained through the Aboriginal and Treaty Rights Information System. Preliminary seismic hazard modelling was used to help identify additional communities which may have previously experienced moderate to strong shaking from a Central Salish Sea fault rupture. Twelve Nations were identified through this process to be contacted. A letter, which outlined the renaming project and invited collaboration, was sent out to each (see 6.2.2). Throughout this process, guidance was sought from Natural Resources Canada's Indigenous Relations Network. Discussions began in May 2024, with letters being sent out that summer, allowing for an overall timeline of approximately one year.

Responses were varied but generally positive about the concept of renaming the fault. Some indicated a lack of capacity to participate at present, while others posed follow-up questions for discussion. Responses, more broadly, cautioned that further engagement would take longer than the available timeline. This is important to highlight: this work is deeply important, and meaningful engagement requires early consideration, flexibility and an understanding that such discussions cannot and should not be rushed. Indigenous communities face high demands on their time, capacity and resources, and processes such as these must not occur on a strictly academic timeline. Similar projects going forward would benefit from an earlier start and a more accommodating timeframe.

Unfortunately, therefore, time constraints for this project prevented a meaningful renaming of the fault to incorporate Indigenous language and perspectives. Taking this into consideration, an interim name, chosen for its geographic descriptiveness and its avoidance of colonial names, was adopted for use in this thesis. The 'Central Salish Sea fault' name should not be considered final; revisiting the renaming process remains an open possibility, should there be interest and capacity in the future.

6.2.2 Initial Letter to Nations

Hi,

My name is Anna. I am a master's student at the University of Victoria and a research affiliate at the Geological Survey of Canada. My research focuses on geologic structures in the Salish Sea known as "crustal faults."

I am reaching out to gauge interest in collaboratively renaming the "Fraser Delta fault", shown in the attached map, as the fault has a name that is very similar to another nearby fault. These names are used to incorporate faults into public safety considerations, as well as in scientific publications, at conferences, and may occasionally get used in the news if there are earthquakes nearby.

The "Fraser Delta fault" may have caused earthquakes that produced moderate to very strong perceived ground shaking in your community over the last 10,000 years. For clarity, while this fault can cause strong local shaking every few thousand years, crustal faults are not the cause of 'The Big One' (subduction zone earthquakes), and there's no immediate cause for alarm regarding these features.

I understand that many communities have long-standing traditions related to earthquakes and ground shaking, and I would love to incorporate those in the naming process, if there is interest and if deemed appropriate. We are reaching out to each Nation that may have experienced moderate or strong shaking from this feature during the last few thousand years with this invitation to participate.

If your Nation is interested in participating, **please get in touch with me at apodhoro@uvic.ca before October 1st.** I am also more than happy to answer any questions or provide additional information in the meantime. Your perspectives matter greatly, and your input would be immensely valued.

Thank you very much. I look forward to hearing from you soon.

Best regards,
Anna

Anna Podhorodeski
M.Sc. Student (Geophysics and Marine Geoscience) | School of Earth and Ocean Sciences | University of Victoria
Research Affiliate | Geological Survey of Canada – Pacific | Natural Resources Canada
apodhoro@uvic.ca | anna.podhorodeski@NRCan-RNCan.gc.ca

I acknowledge with respect the Lekwungen peoples on whose traditional territory the university stands and the Songhees, Esquimalt and WSÁNEĆ peoples whose historical relationships with the land continue to this day.

Chapter 7

Conclusions

7.1 Summary

This study was conducted to assess the potential presence of previously unrecognized Holocene-active faults in the central Strait of Georgia (SoG), and to evaluate the hazard and risk associated with these structures. Over approximately 2200 km of seismic reflection data, this research utilized an objective set of criteria to interpret evidence of active faulting across the central SoG. As noted in previous chapters, many non-unique fault criteria appear in isolation and do not delineate structures; however, others are consistent and laterally extensive across numerous seismic reflection lines. These analyses provided sufficient evidence to map and characterize the Central Salish Sea fault zone (CSSFZ; referred to in previous works as the Fraser Delta fault) beyond its previously recognized extent. Based on constraints in seismic reflection profiles interpreted within this thesis, the main strand of the CSSFZ is characterized as two en echelon fault segments which extend 12-25 km in combined length. The main strand is assigned an average dip of $\sim$75^{o} southwest and strike of $\sim$123^{o} for modelling purposes. Based on a comparison of the local S_{Hmax} direction with fault orientation and dip, the CSSFZ is presumed to accommodate oblique right-lateral slip with a reverse component. Mapping of the CSSFZ further southeast was limited by thick sediments and shallow subsurface penetration of coastal sub-bottom surveys; limited, non-unique fault criteria are present northwest of the mapped CSSFZ but are considered insufficient to justify further extension.

The findings presented in this study have demonstrated hazard implications for communities surrounding the SoG (Chapters 4 and 5). To address the overarching concern of a potential fault rupture, seismic hazard and risk modelling was conducted for various rupture lengths and styles. The modelled scenarios are deterministic, and results do not address the probability of a CSSFZ rupture; its slip rate and the recurrence interval of large earthquakes remain unknown. The results of the modelling

suggest that a 12- to 25-km-long fault rupture during daytime could lead to an estimated 680 to 1300 deaths, 2800 to 5600 buildings damaged beyond repair, and $10.8 to $18.5 billion dollars (2019 CAD) in direct economic losses. These outcomes provide a baseline assessment for a CSSFZ rupture, upon which secondary hazards (e.g., aftershocks, fires, liquefaction) and damage to critical infrastructure are expected to lead to additional, as-of-yet unquantified damage and casualties. The CSSFZ's characterization as a right-lateral oblique fault, combined with its proximity to areas of submarine slope instability, raise concerns that a CSSFZ rupture may be tsunamigenic. As a preliminary assessment for tsunami hazard, tsunami runups for hypothetical M_W 6.3 and M_W 6.7 earthquakes were calculated based on empirical relationships. These calculations indicate that an M_W 6.7 rupture could produce damaging coastal waves affecting multiple communities in British Columbia. Finally, the pockmark chain located along the CSSFZ shows signs of active venting and constitutes an ongoing, albeit localized, geohazard for marine infrastructure.

7.2 Recommendations for Future Work

7.2.1 Hazard and Risk Assessment

As previously mentioned, the CSSFZ is mapped based on active faulting indicators in seismic reflection data. While the recurrence rate of large earthquakes remains unknown (see Chapter 2.2.2), seismic hazard and risk modelling shows that a full-length rupture of the fault could lead to significant damage and losses. It is therefore recommended that the CSSFZ be incorporated into future seismic hazard and risk assessments.

The risk assessment presented in Chapter 5 does not account for damage to critical infrastructure, including linear infrastructure (e.g., roads, telecommunication cables, pipelines) or facilities (e.g., hospitals, emergency response centres). Additionally, secondary effects such as fire, liquefaction, landslides, and aftershocks were not considered, despite their potential to further compound damage, casualties, and economic losses. Further modelling efforts should aim to incorporate the potential impacts of damaged infrastructure and secondary effects to better constrain the risk associated with a CSSFZ rupture.

Given that the models presented in Chapter 5 are deterministic, the probability

of fault rupture remains unaccounted for. For example, while deterministic modelling of seismic risk for the Leech River – Devils Mountain fault near Victoria, BC projects ∼1000 deaths and $20 billion in economic losses from building damage (Hobbs, 2022), the incorporation of the fault into Canada's 6th Generation Seismic Hazard Model results in only a modest and local increase in hazard for Victoria, due in large part to high seismic hazard already accounted for (Halchuk et al., 2019). A key question is whether incorporating the CSSFZ into probabilistic seismic hazard and risk models would meaningfully increase local or regional hazard or the probability of fatality or building collapse over any given timeframe.

Improvements could also be made to the fault geometry used in the modelled scenarios. This study assumes a full-length rupture of the CSSF with a simple, continuous, and planar fault geometry. While this approach provides a baseline estimate for seismic hazard and risk, it does not account for complexities such as the en echelon nature of the two main fault segments of the CSSFZ or varying dip across the fault's length or downdip width. The models also assume a uniform rupture from the seafloor to 17 km depth. While incorporating more complex geometries, including segmentation, variable dips, and non-uniform ruptures, may not substantially alter hazard and risk estimates at broader scales, these refinements would enhance the precision of future assessments and support more realistic modelling.

The tsunami runup calculations in Chapter 5 suggest that an M_W 6.7 earthquake could result in potentially damaging coastal waves for communities within 19 km of the CSSFZ, warranting further modelling. It is also conceivable that a shaking-induced submarine slope failure along the Fraser River delta could result in a damaging tsunami (e.g., Rabinovich et al., 2003). Detailed modelling of a range of rupture scenarios to quantify tsunami hazard and risk would be beneficial to better understand the implications for a submarine fault rupture within the central SoG.

7.2.2 Estimates of Fault Recurrence / Slip Rate

Recurrence intervals and/or slip rates are key parameters required for probabilistic seismic hazard and risk modelling, yet are unknown from this study. Due to several compounding factors, estimating a recurrence interval or slip rate for the CSSFZ has significant challenges, and many conventional methods used for terrestrial and marine faults may not be feasible:

1. A primary obstacle is that the CSSFZ is entirely submarine. As a result, paleoseismic trenching to constrain a rupture history, which has been successfully applied to several Quaternary-active faults in southwest BC and Washington State (e.g., Personius et al., 2014; Morell, 2018; Harrichhausen et al., 2021; Harrichhausen et al., 2023), is not an option for the CSSFZ.

2. Previous studies further south in the Salish Sea have successfully used cores and ^{14}C dating to constrain ages of offset Quaternary sediments near potentially active faults (e.g., Greene et al., 2018; Greene and Barrie, 2020). However, a similar study along the CSSFZ would likely be limited by high sedimentation rates (∼3-10 cm per year; Hart et al., 1998) and a lack of distinct stratification or structure within the upper post-glacial unit (e.g., Chapter 4). Holocene sediment cover further south in the Salish Sea is significantly thinner than in the central SoG; Greene and Barrie (2020) describe datable materials encountered at depths of 30 cm and 122 cm, yielding ^{14}C ages of ∼8400 ka BP and ∼9390 ka BP, respectively. From an extrapolation of sedimentation rates, equivalent depths along the CSSFZ would capture only between 3 and 40 years of sedimentation. This age range is well within the instrumental seismic record, which contains no seismicity attributable to the CSSFZ (see Chapter 5). Additionally, gravity cores previously collected along the CSSFZ show no discernable strata or structure, consisting entirely of fine-grained, bioturbated, dark grey mud (Barrie and Hill, 2004). Piston cores, which are able to penetrate deeper than gravity cores, are typically able to recover up to ∼9 - 12 m of sediment on the Fraser Delta prodelta (Barrie and Stacey, personal communication, 2025). Given the thickness of upper post-glacial sediments (e.g., Chapters 2 and 4), a core of this length collected along the CSSFZ would likely consist primarily of structureless silty mud, representing only a few hundred years of deposition.

   A potential alternative to dating offset strata could be dating deformed strata. Seismic reflection interpretations indicate deformed internal reflectors within upper post-glacial units along the CSSFZ. These deformed reflectors are shallower than visibly offset reflectors (Chapter 4) and may serve as more feasible coring targets. If datable material can be recovered, these units could potentially constrain minimum dates for Holocene deformation. However, they would not yield conclusive dates for past ruptures. Similar to the limitation above for dating offset strata, given the high sedimentation rates and lack of clear stratigraphy or structure in previously collected cores, it is uncertain whether meaningful age

constraints could be obtained via this method.

3. Estimating slip from seismic reflection data is further complicated by inconsistent vertical offsets along the length of the CSSFZ, consistent with its interpretation as an oblique-slip fault (Chapters 4 and 5). Due to a lack of consistent cumulative offset, any estimates of slip from seismic reflection data alone would be unreliable.

Given these limitations, future research may be more effective if directed toward other aspects of the CSSFZ and faulting in the central SoG (i.e., the recommendations on modelling and surveying herein).

7.2.3 Additional Data Analysis for Marine Faults

The methods outlined in previous chapters primarily use seismic reflection data; however, there are multiple types of data that can aid in mapping and constraining faults. For example, in the central Strait of Georgia, the Geological Survey of Canada provides publicly available aeromagnetic data with resolutions of 200 m and 1 km (Miles and Oneschuk, 2016). Additionally, marine magnetic data, if it does not already exist, could be collected during future expeditions to provide a higher-resolution, more targeted, complementary dataset. Both marine and aeromagnetic data have been instrumental in delineating crustal faults in the southern Strait of Georgia (e.g., Kelsey et al., 2014; Caston, 2021). Integrating the seismic interpretations presented in this thesis with these additional datasets could potentially enable further mapping of known faults and/or the delineation of presently unknown structures, including blind faults, which would not be imaged in shallow seismic reflection data.

7.2.4 Sub-bottom Surveying and Coastal Studies

The seismic reflection interpretations outlined in Chapter 4 reveal a possible fault beneath a seafloor scarp north of the Central Salish Sea Fault and south of Bowen Island (Figures 4.4.15 and 4.4.18). At present, only an obliquely oriented Huntec line exists over this feature. Given the scarp's orientation and subsurface active fault indicators (such as reflector truncations and deformation), both of which resemble the surface and subsurface expression of the Central Salish Sea fault scarp, acquiring additional sub-bottom lines would be prudent. These data would aid in 1) confirming whether or

not the feature is an active fault, 2) delineating its extent, and 3) exploring its possible relationship to the Central Salish Sea fault zone.

Similarly, the seismic reflection interpretations in previous chapters indicate apparent active faulting in two seismic lines offshore Gabriola Island. The faulting indicators align with a seafloor lineament and offset bedrock, visible in multibeam bathymetry, which trend towards the island (Figure 4.4.19). However, the available data do not provide enough information to further constrain the fault, and there is a lack of sub-bottom data closer to Gabriola Island. Additional sub-bottom surveys would provide clarity on the offshore fault extent. If warranted, investigations of nearshore, intertidal, and terrestrial environments could help establish potential connections between offshore and onshore fault segments in this area (e.g., Kelsey et al., 2012; Barrie et al., 2021a). Such studies, which combine offshore and terrestrial research, are a missing component for many crustal fault studies across the Pacific Northwest. Addressing these gaps in future work would significantly enhance the understanding of crustal tectonics, seismic hazard and tsunami hazard in the region.

Furthermore, the extent of active faulting north of the study area in this thesis, and more broadly in the northern Cascadia forearc, remains unknown. Sub-bottom and analogue seismic reflection data coverage extend past the present study area's boundaries towards Texada Island and farther north. One possible avenue for further research would be analysing these and other geophysical data to identify evidence for presently unrecognized structures. Given evidence for active faulting offshore of Cape Lazo (Barrie et al., 2021b; Douglas et al., 2022), it would be justified to investigate whether similar structures exist between Cape Lazo and the study area for this thesis. Therefore, expanding similar studies northwards could provide insights into the broader extent of forearc faulting in the region.

7.2.5 Additional Seismic Reflection Data Collection

While the future collection of sub-bottom profiling data remains practical, present permitting requirements significantly limit the ability to obtain lower frequency seismic reflection data in the SoG. One potential alternative may be distributed acoustic sensing (DAS), which repurposes existing fibre optic cables. The feasibility of such a technique within the SoG is worth assessing, as recent studies have successfully used DAS to passively image fault zones with high resolution (e.g., Atterholt et al., 2022;

Xiao et al., 2025). Within the SoG, Connected Coast operates a fibre optic cable that runs from Vancouver to Gabriola Island (Connected Coast, 2025). As mapped, the cable crosses 2 km northwest and along strike of the scarp near Bowen Island and runs over the inferred extension of the CSSFZ. In addition, Canadian nautical charts indicate that 6 seafloor power cables cross areas of interest, including the western segment of the CSSFZ, its extension, and the scarp south of Bowen Island (Canadian Hydrographic Service, n.d.). While these are not explicitly fibre optic cables, modern seafloor power cables can include embedded optical fibres suitable for DAS (e.g., Williams et al., 2023); their presence within these specific cables and their suitability would need to be confirmed. If any of the above-mentioned cables contain suitable dark optical fibres, DAS could be utilized for passive subsurface imaging as an alternative to presently restricted active seismic reflection imaging.

Should active seismic reflection surveying become feasible in the future, I make the following suggestions:

1. The above suggestions on sub-bottom surveying would be enhanced by incorporating additional seismic reflection data collection, particularly Huntec DTS and high-resolution airgun data.

2. Shallow seismic reflection data can only image faults that exhibit surface rupture or near-surface expressions. Deeper faults, such as the Fraser River Delta fault mapped by Caston (2021) immediately south of this study's area of interest, cannot be resolved with shallow seismic data. The interpretations of high-resolution airgun data (1000 ms TWT) presented in this thesis do not contain convincing evidence of the Fraser River Delta fault within the Central SoG. Thus, deeper seismic reflection data could be utilized to investigate the potential extent of the Fraser River Delta fault into the central SoG.

3. Similarly, the trace of the Central Salish Sea fault is obscured beneath thick Fraser River Delta sediments and could not be imaged with coastal sub-bottom surveys. However, deeper seismic reflection data may be able to better image the fault and provide more clarity on its eastward extent towards Metro Vancouver.

4. The seismic reflection data available for this study in proximity to the epicentre of the 1997 SoG earthquake cluster were collected before the 1997 events occurred. Consequently, any potential near-surface sediment deformation resulting from this event would not be captured within these data. Although Mosher

et al. (2000) conducted subsequent multichannel seismic reflection studies over the epicentral region, their data lack the resolution needed to identify potential near-surface deformation. The collection of additional high-resolution DTS or airgun data could enable the determination of whether or not near-surface deformation occurred and an assessment of its extent, if present. Furthermore, deeper seismic reflection profiles would be required to further map the nearby bedrock deformation zone identified by Mosher et al. (2000).

Bibliography

Abe, K. (1995). Estimate of tsunami run-up heights from earthquake magnitudes. In Y. Tsuchiya & N. Shuto (Eds.), *Tsunami: progress in prediction, disaster prevention and warning, Advances in Technological Hazards Research* (Vol. 4, pp. 21–35). Springer, Dordrecht. https://doi.org/10.1007/978-94-015-8565-1_2

Abrahamson, N. A., Silva, W. J., & Kamai, R. (2014). Summary of the ASK14 ground motion relation for active crustal regions. *Earthquake Spectra*, *30*(3), 1025–1055. https://doi.org/10.1193/070913EQS198M

Acosta, J., Munoz, A., Herranz, P., Palomo, C., Ballesteros, M., Vaquero, M., & Uchupi, E. (2001). Pockmarks in the Ibiza Channel and Western end of the Balearic Promontory (Western Mediterranean) revealed by multibeam mapping. *Geo-Marine Letters*, *21*(3), 123–130. https://doi.org/10.1007/s003670100074

Allen, T. I., & Wald, D. J. (2009). On the use of high-resolution topographic data as a proxy for seismic site conditions (VS30). *Bulletin of the Seismological Society of America*, *99*(2 A), 935–943. https://doi.org/10.1785/0120080255

Atterholt, J., Zhan, Z., & Yang, Y. (2022). Fault zone imaging with distributed acoustic sensing: Body-to-surface wave scattering. *Journal of Geophysical Research: Solid Earth, 127, e2022JB025052.* https://doi.org/10.1029/2022JB025052

Atwater, B. F., Tuttle, M.P., Schweig, E., Rubin, C.M., Yamaguchi, D.K., & Hemphill-Haley, E. (2004). Earthquake recurrence inferred from paleoseismology. In Rose, J., Gillespie, A.R., Porter, S.C., & Atwater B.F. (Eds), *The Quaternary Period of the United States: Developments in Quaternary Science 1*, Elsevier, Amsterdam-New York, 331–350.

Balfour, N. J., Cassidy, J. F., Dosso, S. E., & Mazzotti, S. (2011). Mapping crustal stress and strain in southwest British Columbia. *Journal of Geophysical Research*, *116*, 3314. https://doi.org/10.1029/2010JB008003ï

Barrie, J. V., & Conway, K. W. (2002). Rapid sea-level change and coastal evolution on the Pacific margin of Canada. *Sedimentary Geology*, *150*, 171–183.

Barrie, J. V., & Hill, P. R. (2004). Holocene faulting on a tectonic margin: Georgia Basin, British Columbia, Canada. *Geo-Marine Letters, 24(2),* 86–96. https://doi.org/10.1007/s00367-003-0166-6

Barrie, J. V., Hill, P., Conway, K., Iwanowska, K., & Picard, K. (2005). Environmental Marine Geoscience 4: Georgia Basin: Seabed Features and Marine Geohazards. *Geoscience Canada*, *32*(4), 145–156.

Barrie, J.V., Molloy, B., and Douglas, K., (2021a). *Preliminary assessment of active faulting in the Victoria/Esquimalt region of British Columbia.* Geological Survey of Canada Open File 8774. https://doi.org/10.4095/328132

Barrie, J. V., Douglas, K., & Molloy, B. (2021b). *Geological hazards off Cape Lazo, eastern Vancouver Island.* Geological Survey of Canada Open File 8773. https://doi.org/10.4095/328131

Blais-Stevens, A., Rogers, G. C., & Clague, J. J. (2011). A revised earthquake chronology for the last 4,000 years inferred from varve-bounded debris-flow deposits beneath an inlet near Victoria, British Columbia. *Bulletin of the Seismological Society of America*, *101*(1), 1–12. https://doi.org/10.1785/0120090360

Boore, D. M., Stewart, J. P., Seyhan, E., & Atkinson, G. M. (2014). NGA-West2 equations for predicting PGA, PGV, and 5% damped PSA for shallow crustal earthquakes. *Earthquake Spectra*, *30*(3), 1057–1085. https://doi.org/10.1193/070113EQS184M

Brandes, C., Polom, U., Winsemann, J., & Sandersen, P.B.E. (2022). The near-surface structure in the area of the Børglum Fault, sorgenfrei-tornquist zone, Northern Denmark: Implications for fault kinematics, timing of fault activity and fault control on Tunnel Valley Formation. *Quaternary Science Reviews, v. 289.* doi: 10.1016/j.quascirev.2022.107619.

Butler, R. (2021, February 1). Closely spaced normal faults - imaging issues. Virtual Seismic Atlas. https://web.archive.org/web/20210725072504/https://seismicatlas.org/entity?id=feb7aaca-ef53-4ba2-8ada-0c063a3cf93b

Campbell, K. W., & Bozorgnia, Y. (2014). NGA-West2 ground motion model for the average horizontal components of PGA, PGV, and 5% damped linear acceleration response spectra. *Earthquake Spectra*, *30*(3), 1087–1114. https://doi.org/10.1193/062913EQS175M

Canadian Hydrographic Service. (n.d.). *Canadian Coast Guard e-Navigation Cartographic Tool.* https://e-navigation.canada.ca/interactive-map. Accessed Mar. 30, 2025

Cassidy, J. F., Ellis, R. M., & Rogers, G. C. (1988). The 1918 and 1957 Vancouver Island earthquakes. *Bulletin of the Seismological Society of America*, *78*(2), 617–635.

Cassidy, J. F., Rogers, G. C., & Waldhauser, F. (2000). Characterization of Active Faulting Beneath the Strait of Georgia, British Columbia. *Bulletin of the Seismological Society of America*, *90*(5), 1188–1199. http://pubs.geoscienceworld.org/ssa/bssa/article-pdf/90/5/1188/3581638/1188.pdf

Caston, M. (2021). Tsunamigenic Potential of Crustal Faults in the Southern Strait of Georgia and Boundary Bay [Master's Thesis, University of Victoria].

Cathles, L. M., Su, Z., & Chen, D. (2010). The physics of gas chimney and pockmark formation, with implications for assessment of seafloor hazards and gas sequestration. *Marine and Petroleum Geology*, *27*(1), 82–91. https://doi.org/10.1016/j.marpetgeo.2009.09.010

Chen, J., Song, H., Guan, Y., Yang, S., Pinheiro, L. M., Bai, Y., Liu, B., & Geng, M. (2015). Morphologies, classification and genesis of pockmarks, mud volcanoes and associated fluid escape features in the northern Zhongjiannan Basin, South China Sea. *Deep-Sea Research Part II: Topical Studies in Oceanography*, *122*, 106–117. https://doi.org/10.1016/j.dsr2.2015.11.007

Chiou, B. S. J., & Youngs, R. R. (2014). Update of the Chiou and Youngs NGA model for the average horizontal component of peak ground motion and response spectra. *Earthquake Spectra*, *30*(3), 1117–1153. https://doi.org/10.1193/072813EQS219M

Christian, H.A., Mosher, D.C., Barrie, J.V., Hunter, J.A., & Luternauer, J.L. (1998). Seabed instability on the Fraser River delta. In Clague, J. J., Luternauer, J. L., & Mosher, D. C. (Eds). *Geology and natural hazards of the Fraser River Delta, British Columbia*. Geological Survey of Canada Bulletin 525, p. 217-230.

Clague, J.J. (1998) Geological setting of the Fraser River delta. In Clague, J. J., Luternauer, J. L., & Mosher, D. C. (Eds.), *Geology and natural hazards of the Fraser River Delta, British Columbia*. Geological Survey of Canada Bulletin 525.

Clague, J. J., & James, T. S. (2002). History and isostatic effects of the last ice sheet in southern British Columbia. In *Quaternary Science Reviews* (Vol. 21).

Connected Coast. (2025). *Build Status Map*. https://connectedcoast.ca/map/build-status-map/. Accessed Mar. 30, 2025.

Conway, K. W., Kung, R. B., Barrie, J. V, Hill, P. R., & Lintern, D. G. (2013). A preliminary assessment of the occurrence of submarine slope failures in coastal British Columbia by analysis of swath multibeam bathymetric data collected 2001-2011. *Geological Survey of Canada Open File 3748.* https://doi.org/10.4095/292370

Courtney, R. C. (2013). Canada GEESE 2: Visualization of Integrated Marine Geoscience Data for Canadian and Proximal Waters. *Geoscience Canada*, *40*(2), 141–148. https://doi.org/10.12789/GEOCANJ.2013.40.0010

Cox, D. R., Knutz, P. C., Calvin Campbell, D., Hopper, J. R., Newton, A. M. W., Huuse, M., & Gohl, K. (2020). Geohazard detection using 3D seismic data to enhance offshore scientific drilling site selection. *Scientific Drilling*, *28*, 1–27. https://doi.org/10.5194/SD-28-1-2020

Crutchley, G.J., & Kopp, H. (2018). Reflection and Refraction Seismic Methods. In Micallef, A., Krasterl, S., & Savini, A. (Eds). *Submarine Geomorphology*. Springer Geology, p. 43-62.

Dash, R. K., Spence, G. D., Riedel, M., Hyndman, R. D., & Brocher, T. M. (2007).

Upper-crustal structure beneath the SoG, Southwest British Columbia. *Geophysical Journal International*, *170*(2), 800–812. https://doi.org/10.1111/j.1365-246X.2007.03455.x

Dellow, G., Yetton, M., Massey, C., Archibald, G., Barrell, D. J. A., Bell, D., Bruce, Z., Campbell, A., Davies, T., de Pascale, G., Easton, M., Forsyth, P. J., Gibbons, C., Glassey, P., Grant, H., Green, R., Hancox, G., Jongens, R., Kingsbury, P., ... Walsh, I. (2011). Landslides caused by the 22 February 2011 Christchurch earthquake and management of landslide risk in the immediate aftermath. *Bulletin of the New Zealand Society for Earthquake Engineering*, *44*(4). http://data.gns.cri.nz/af/

DeMets, C., Gordon, R. G., & Argus, D. F. (2010). Geologically current plate motions. *Geophysical Journal International*, *181*(1), 1–80. https://doi.org/10.1111/j.1365-246X.2009.04491.x

Dimmen, V., Rotevatn, A., & Lecomte, I. (2023). Imaging of small-scale faults in seismic reflection data: Insights from seismic modelling of faults in outcrop. *Marine and Petroleum Geology, v. 147, p. 105980.* doi: 10.1016/j.marpetgeo.2022.105980.

Douglas, K., Barrie, J. V., Dill, T., Fralic, T., & Koshure, N. (2022). *2021004PGC cruise report: mapping Salish Sea marine geohazards, British Columbia*. Geological Survey of Canada Open File 8865. https://doi.org/10.4095/329621

Dondurur, D. (2018) *Acquisition and processing of Marine Seismic Data*, Elsevier, Amsterdam, Netherlands, p. 1-36, 171-210, 459-492.

Eberli, G.P., Anselmetti, F.S., Betzler, C., Van Konijnenburg, J.H., & Bernoulli, D. (2004). Carbonate platform to basin transitions on seismic data and in outcrops: Great Bahama Bank and the Maiella Platform margin, Italy: Seismic Imaging of Carbonate Reservoirs and Systems. *American Association of Petroleum Geologists Bulletin Memoir, v. 81, p. 207-250.*

England, T. D. J., & Bustin, R. M. (1998). Architecture of the Georgia Basin southwestern British Columbia. *Bulletin of Canadian Oil Petrology*, *46*(2), 288–320.

Fader, G. (1991). Gas-related sedimentary features from the eastern Canadian continental shelf. *Continental Shelf Research*, *11*(8–10), 1123–1153.

Fagin, S. (1996). The fault shadow problem: Its nature and elimination. *The Leading Edge, v. 15, no. 9, p. 1005–1013, doi: 10.1190/1.1437403.*

Fakiris, E., Papatheodorou, G., Christodoulou, D., Roumelioti, Z., Sokos, E., Geraga, M., Giannakopoulos, V., Dimas, X., & Ferentinos, G. (2023). Using Distributed Temperature Sensing for Long-Term Monitoring of Pockmark Activity in the Gulf of Patras (Greece): Data Processing Hints and Preliminary Findings. *Sensors (Basel, Switzerland)*, *23*(20). https://doi.org/10.3390/s23208520

FEMA, (2024). Hazus Earthquake Model User Guidance, Hazus 6.1. Technical Report, Federal Emergency Management Agency. Available at: https://www.fema.gov/sites

/default/files/documents/fema-hazus-6.1-earthquake-model-user-guidance.pdf. Accessed February 2, 2025.

Field, M. E., & Jennings, A. E. (1987). Seafloor gas seeps triggered by a northern California earthquake. *Marine Geology*, *77*(1–2), 39–51. https://doi.org/10.1016/0025-3227(87)90082-X

Finley, T., Morell, K., Leonard, L., Regalla, C., Johnston, S. T., & Zhang, W. (2019). Ongoing oroclinal bending in the Cascadia forearc and its relation to concave-outboard plate margin geometry. *Geology*, *47*(2), 155–158. https://doi.org/10.1130/G45473.1

Gay, A., Lopez, M., Cochonat, P., Séranne, M., Levaché, D., & Sermondadaz, G. (2006). Isolated seafloor pockmarks linked to BSRs, fluid chimneys, polygonal faults and stacked Oligocene-Miocene turbiditic palaeochannels in the Lower Congo Basin. *Marine Geology*, *226*(1–2), 25–40. https://doi.org/10.1016/j.margeo.2005.09.018

GEBCO. (2020). General Bathymetric Chart of the Oceans Gridded Bathymetry Data. https://www.gebco.net/data_and_products/gridded_bathymetry_data/

Gledhill, K., Ristau, J., Reyners, M., Fry, B., & Holden, C. (2011). The Darfield (Canterbury, New Zealand) Mw 7.1 Earthquake of September 2010: A Preliminary Seismological Report. *Seismological Research Letters, 82*(3), 378–386. https://doi.org/10.1785/GSSRL.82.3.378

Goff, J., Bobrowsky, P., Huntley, D., Sawai, Y., & Tanagawa, K. (2020). Palaeotsunamis along Canada's Pacific coast. *Quaternary Science Reviews*, *237*. https://doi.org/10.1016/j.quascirev.2020.106309

Grasemann, B., Martel, S., & Passchier, C. (2005). Reverse and normal drag along a fault. *Journal of Structural Geology, 27*(6)*, p. 999–1010.* doi: 10.1016/j.jsg.2005.04.006.

Greene, H. G., Barrie, J. V., & Todd, B. J. (2018). The Skipjack Island fault zone: An active transcurrent structure within the upper plate of the Cascadia subduction complex. *Sedimentary Geology*, *378*, 61–79. https://doi.org/10.1016/j.sedgeo.2018.05.005

Greene, H. G., & Barrie, J. V. (2020). Faulting within the San Juan–southern Gulf Islands Archipelagos, upper plate deformation of the Cascadia subduction complex. *Geological Society Special Publication*, *505*(1), 169–191. https://doi.org/10.1144/SP505-2019-125

Hadlari, T., Millar, R. A., & Lane, L. S. (2020). The Eskimo Lakes Fault Zone renamed Husky Lakes Fault Zone, Tuktoyaktuk Peninsula, Northwest Territories. Geological Survey of Canada, Open File 8740. https://doi.org/10.4095/326948

Halchuk, S., Allen, T., Adams, J., & Onur, T. (2019). Contribution of the Leech River Valley-Devil's Mountain Fault System to Seismic Hazard in Victoria, B.C. *12th*

Canadian Conference on Earthquake Engineering.

Hamilton, T. S. (1991). Seismic stratigraphy of unconsolidated sediments in the central Strait of Georgia: Hornby Island to Roberts Bank. *Geological Survey of Canada, Open File 2350.*

Han, S., Carbotte, S. M., Canales, J. P., Nedimovic, M. R., Carton, H., Gibson, J. C., & Horning, G. W. (2016). Seismic reflection imaging of the Juan de Fuca plate from ridge to trench: New constraints on the distribution of faulting and evolution of the crust prior to subduction. *Journal of Geophysical Research: Solid Earth*, *121*(3), 1849–1872. https://doi.org/10.1002/2015JB012416

Harrichhausen, N., Morell, K. D., Regalla, C., Bennett, S. E. K., Leonard, L. J., Lynch, E. M., & Nissen, E. (2021). Paleoseismic trenching reveals late quaternary kinematics of the Leech River fault: Implications for forearc strain accumulation in northern Cascadia. *Bulletin of the Seismological Society of America*, *111*(2), 1110–1138. https://doi.org/10.1785/0120200204

Harrichhausen, N., Finley, T., Morell, K. D., Regalla, C., Bennett, S. E. K., Leonard, L. J., Nissen, E., McLeod, E., Lynch, E. M., Salomon, G., & Sethanant, I. (2023). Discovery of an Active Forearc Fault in an Urban Region: Holocene Rupture on the XEOLXELEK-Elk Lake Fault, Victoria, British Columbia, Canada. *Tectonics*, *42*(12). https://doi.org/10.1029/2023TC008170

Hart, B. S., & Hamilton, T. S. (1993). High-resolution acoustic mapping of shallow gas in unconsolidated sediments beneath the strait of Georgia, British Columbia. *Geo-Marine Letters*, *13*, 49–55.

Hart, B. S., Hamilton, T. S., & Barrie, J. V. (1998). Sedimentation rates and patterns on a deep-water delta (Fraser Delta, Canada): integration of high-resolution seismic stratigraphy, core lithofacies, and 137 Cs fallout stratigraphy. *Journal Of Sedimentary Research,* 68(4), 556-568.

Hasiotis, T., Papatheodorou, G., Kastanos, N., & Ferentinos, G. (1996). A pockmark field in the Patras Gulf (Greece) and its activation during the 14/7/93 seismic event. *Marine Geology*, *130*, 333–344.

Hata, Y., Ichii, K., & Nozu, A. (2012). Three-dimensional non-linear FEM analysis of a seismic induced crack at an airport runway. *Soil Dynamics and Earthquake Engineering*, *42*, 105–118. https://doi.org/10.1016/J.SOILDYN.2012.06.009

Hill, P. R., Conway, K., Lintern, D. G., Meulé, S., Picard, K., & Barrie, J. V. (2008). Sedimentary processes and sediment dispersal in the southern Strait of Georgia, BC, Canada. *Marine Environmental Research*, *66*. https://doi.org/10.1016/j. marenvres.2008.09.003

Ho, S., Imbert, P., Hovland, M., Wetzel, A., Blouet, J. P., & Carruthers, D. (2018). Downslope-shifting pockmarks: interplay between hydrocarbon leakage, sedimentations, currents and slope's topography. *International Journal of Earth Sciences*,

107(8), 2907–2929. https://doi.org/10.1007/s00531-018-1635-5

Hobbs, T. E. (2022). A selection of earthquake scenarios for government planning purposes in 2021. *Geological Survey of Canada Open File 8853*. https://doi.org/10.4095/329397ma

Hobbs, T.E., Van Ulden, J., Rotheram, D., Chow, W., LeSueur, P., Journeay, J.M., Ulmi, M., Ulmi, D., Fok, A., Van de Valk, J., Hastings, N., Herring, J., Wong, T., Evans, P., & Safaie, S. (2022). *RiskProfiler*, Geological Survey of Canada. www.RiskProfiler.ca. Accessed March 31, 2025.

Hobbs, T. E., Journeay, J. M., Rao, A. S., Kolaj, M., Martins, L., LeSueur, P., Simionato, M., Silva, V., Pagani, M., Johnson, K., Rotheram, D., & Chow, W. (2023). A national seismic risk model for Canada: Methodology and scientific basis. *Earthquake Spectra*, *39*(3), 1410–1434. https://doi.org/10.1177/87552930231173446

Hodgson, E. A. (1946). British Columbia earthquake June 23, 1946. *Journal of the Royal Astronomical Society of Canada*, *40*(8), 285–319.

Hovland, M., Gardner, J. v., & Judd, A. G. (2002). The significance of pockmarks to understanding fluid flow processes and geohazards. *Geofluids*, *2*(2), 127–136.

Hovland, M., & Judd, A. (1988). *Seabed Pockmarks and Seepages: Impact on Geology, Biology, and the Marine Environment*. Graham and Trotman Limited.

Huang, C., Dashtgard, S. E., Gibson, H. D., & Calvert, A. J. (In press.). *The Origin of Forearc Depressions*. https://doi.org/10.31223/X5J98H

Hutchinson, I., James, T. S., Clague, J. J., Barrie, J. V., & Conway, K. W. (2004). Reconstruction of late Quaternary sea-level change in southwestern British Columbia from sediments in isolation basins. *Boreas*, *33*(3), 183–194. https://doi.org/10.1111/J. 1502-3885.2004.TB01140.X

Hyndman, R. D., Mazzotti, S., Weichert, D., & Rogers, G. C. (2003). Frequency of large crustal earthquakes in Puget Sound–Southern Georgia Strait predicted from geodetic and geological deformation rates. *Journal of Geophysical Research: Solid Earth*, *108*(B1). https://doi.org/10.1029/2001jb001710

Johannessen, S. C., Macdonald, R. W., & Paton, D. W. (2003). A sediment and organic carbon budget for the greater Strait of Georgia. *Estuarine, Coastal and Shelf Science*, *56*(3–4), 845–860. https://doi.org/10.1016/S0272-7714(02)00303-7

Johnson, S., Dadisman, S., Mosher, D., Blakely, R., & Childs, J. (2001). *Active Tectonics of the Devils Mountain Fault and Related Structures, Northern Puget Lowland and Eastern Strait of Juan de Fuca Region, Pacific Northwest*. http://minerals.er.usgs.gov/minerals/

Journeay, M., LeSueur, P., Chow, W., & Wagner, C. L. (2022). *Physical exposure to natural hazards in Canada*. https://doi.org/10.4095/330012

Karabulut, H., Güvercin, S. E., Hollingsworth, J., & Konca, A. Ö. (2023). Long silence on the East Anatolian Fault Zone (Southern Turkey) ends with devastating double earthquakes (6 February 2023) over a seismic gap: implications for the seismic potential in the Eastern Mediterranean region. *Journal of the Geological Society*, *180*(3). https://doi.org/10.1144/jgs2023-021

Kehew, J., Douglas, K., Riedel, M., Klaucke, I., Norgard, T., du Preez, C., Li, Z., & Stacey, C. (2023). Swiftsure Bank water column survey SO294, offshore British Columbia. *Geological Survey of Canada Open File 8943*. https://doi.org/10.4095/331402

Kelsey, H. M., Sherrod, B. L., Blakely, R. J., & Haugerud, R. A. (2012). Holocene faulting in the Bellingham forearc basin: Upper-plate deformation at the northern end of the Cascadia subduction zone. *Journal of Geophysical Research: Solid Earth*, *117*(3). https://doi.org/10.1029/2011JB008816

Knudsen. (n.d.). *Technical Information - D101-05550-Rev1.7*. Retrieved November 10, 2024, from https://knudseneng.com/files/manuals/pinger/D101-05550-Rev1.7.pdf.

Kolaj, M., Halchuk, S., Adams, J., & Allen, T. I. (2020). *Sixth Generation Seismic Hazard Model of Canada: input files to produce values proposed for the 2020 National Building Code of Canada*. https://doi.org/10.4095/327322

Kukovica, J., Ghofrani, H., Molnar, S., & Assatourians, K. (2019). Probabilistic Seismic Hazard Analysis of Victoria, British Columbia: Considering an Active Fault Zone in the Nearby Leech River Valley. *Bulletin of the Seismological Society of America*, *109*(5), 2050–2062. https://doi.org/10.1785/0120180330

Kung, R., Douglas, K., & Stacey, C. D. (2023). *Canada west coast topo-bathymetric digital elevation model, British Columbia*. https://doi.org/10.4095/331539

LaCroix, A. D., Dashtgard, S. E., Hill, P. R., Ayranci, K., & Clague, J. J. (2024). The Holocene to modern Fraser River Delta, Canada: geological history, processes, deposits, natural hazards, and coastal management. *Canadian Journal of Earth Sciences*. https://doi.org/10.1139/cjes-2024-0041

Lapham, L., Wilson, R., Riedel, M., Paull, C. K., & Holmes, M. E. (2013). Temporal variability of in situ methane concentrations in gas hydrate-bearing sediments near Bullseye Vent, Northern Cascadia Margin. *Geochemistry, Geophysics, Geosystems*, *14*(7), 2445–2459. https://doi.org/10.1002/ggge.20167

Leonard, L. J., Rogers, G. C., & Mazzotti, S. (2012). A preliminary tsunami hazard assessment of the Canadian Coastline. *Geological Survey of Canada Open File 7201*. https://doi.org/10.4095/292067

Lynch, E. M., Regalla, C. A., Morell, K. D., Harrichhausen, N., & Leonard, L. J. (2023). *Late Pleistocene to Holocene transtension in the northern Cascadia forearc: Evidence from surface ruptures along the Beaufort Range fault*. [Manuscript submitted for publication]. *ESS Open Archive*. https://doi.org/10.22541/essoar.168614686

.67638260/v1

Machacek, V. (1970). *Geophysical Report of the Georgia Straits 1968 Project, British Columbia, Canada; Seismic Survey conducted in the Georgia Straits Ariea in December 1968 by Geophysical Service Incorporated for Texaco Exploration Company.* [Report].

MacNaughton, R. B., Dafoe, L. T., & Haggart, J. W. (2022). North American Commission on Stratigraphic Nomenclature Note 72 – Application for Revisions to the North American Stratigraphic Code to Address Culturally Offensive or Inappropriate Unit Names and to Encourage the Use of Indigenous Place Names. *Stratigraphy,* 19(3), 187–200. https://doi.org/10.29041/strat.19.3.03

Magistrale, H. (2002). Relative contributions of crustal temperature and composition to controlling the depth of earthquakes in Southern California. *Geophysical Research Letters*, *29*(10), 87–1. https://doi.org/10.1029/2001GL014375

Malone, S. D., & Bor, S.S. (1979). Attenuation patterns in the Pacific Northwest based on intensity data and the location of the 1872 North Cascades earthquake. *Bulletin of the Seismological Society of America*, *69*(2), 531–546. http://pubs.geoscienceworld.org/ssa/bssa/article-pdf/69/2/531/5321777/bssa0690020531.pdf

Marlow, M.S., Hart, P.E., Carlson, P.R., Childs, J.R., Mann, D.M., Anima, R.J., & Kayen, R.E. (1996). Misinterpretation of lateral acoustic variations on high-resolution seismic reflection profiles as fault offsets of Holocene bay mud beneath the southern part of San Francisco Bay, California. *Marine and Petroleum Geology, 13(3)*, 341-348.

Marsset, T., Marsset, B., Ker, S., Thomas, Y., & le Gall, Y. (2010). High and very high resolution deep-towed seismic system: Performance and examples from deep water Geohazard studies. *Deep Sea Research Part I: Oceanographic Research Papers*, *57*(4), 628–637. https://doi.org/10.1016/J.DSR.2010.01.001

Mazzotti, S., Dragert, H., Hyndman, R. D., Miller, M. M., & Henton, J. A. (2002). GPS deformation in a region of high crustal seismicity: N. Cascadia forearc. *Earth and Planetary Science Letters*, *198*, 41–48. www.elsevier.com/locate/epsl

McKeown, D. L., Simpkin, P. G., Fader, G. B. J., Parrott, R. & Mosher, D. C. (2014). The Huntec deep tow seismic system: a revolution in high resolution profiling. In Nettleship, D. N., Gordon, D. C., Lewis, C. F. M. & Latremouille, M. P. (eds.), *Voyage of Discovery: Fifty years of marine research at Canada's Bedford Institute of Oceanography*, 269-273. BIO Oceans Association.

Menant, A., Angiboust, S., Gerya, T., Lacassin, R., Simoes, M., & Grandin, R. (2020). Transient stripping of subducting slabs controls periodic forearc uplift. *Nature Communications*, *11*(1). https://doi.org/10.1038/s41467-020-15580-7

Merrill, R. J., Bostock, M. G., Peacock, S. M., Schaeffer, A. J., & Roecker, S. W. (2022). Complex Structure in the Nootka Fault Zone Revealed by Double-Difference To-

mography and a New Earthquake Catalog. *Geochemistry, Geophysics, Geosystems*, *23*(2). https://doi.org/10.1029/2021GC010205

Miles, W. F. & Oneschuk, D. (2016). *Magnetic anomaly map, Canada.* Geological Survey of Canada Open File 7799. https://doi.org/10.4095/297337

Misra, A.A. (2018). Fault Propagation Folds in the Active North Ecuador–South Colombia Margin. In Misra, A. A. & Mukherjee, S. (2018). *Atlas of Structural Geological Interpretation from Seismic Images.* Wiley Blackwell, Oxford, p. 151-153.

Misra, A. A. & Mukherjee, S. (2018). *Atlas of Structural Geological Interpretation from Seismic Images.* Wiley Blackwell, Oxford, p. 1-26, 257-261.

Morell, K. D., Regalla, C., Leonard, L. J., Amos, C., & Levson, V. (2017). Quaternary Rupture of a Crustal Fault beneath Victoria, British Columbia, Canada. *GSA Today*, *27*(3–4), p. 4–10. https://doi.org/10.1130/GSATG291A.1

Morell, K. D., Regalla, C., Amos, C., Bennett, S., Leonard, L., Graham, A., Reedy, T., Levson, V., & Telka, A. (2018). Holocene Surface Rupture History of an Active Forearc Fault Redefines Seismic Hazard in Southwestern British Columbia, Canada. *Geophysical Research Letters*, *45*(21), 11,605-11,611. https://doi.org/10.1029/2018GL078711

Mosher, D.C. (2009). Submarine landslides and consequent tsunamis in Canada. *Geoscience Canada, 26*, p. 179-190.

Mosher, D. C., Cassidy, J. F., Lowe, C., Mi, Y., Hyndman, R. D., Rogers, G. C., & Fisher, M. (2000). Neotectonics in the SoG : first tentative correlation of seismicity with shallow geological structure in southwestern British Columbia. *Current Research* (2000-A22). Geological Survey of Canada.

Mosher, D.C., Currie, R.G., & Sullivan, D. (1997). Monitoring of ocean disposal using side-scan mosaicing. *The Leading Edge, Society of Exploration Geophysicists, November issue,* p. 1667-1669.

Mosher, D.C., & Hamilton, T.S. (1998). Morphology, structure and stratigraphy of the offshore Fraser delta and adjacent Strait of Georgia. In Clague, J. J., Luternauer, J. L., & Mosher, D. C. (Eds). *Geology and natural hazards of the Fraser River Delta, British Columbia.* Geological Survey of Canada Bulletin 525, p. 147-160.

Mosher, D.C , Monahan, P.A., Barrie, J.V., and Courtney, R.C. (2004). Coastal Submarine Failures in the Strait of Georgia, British Columbia: Landslides of the 1946 Vancouver Island Earthquake. *Journal of Coastal Research, 20, p. 277-291.*

Mosher, D.C., & Simpkin, P.G. (1999). Environmental Marine Geoscience 1. Status and Trends of Marine High-Resolution Seismic Reflection Profiling: Data Acquisition. *Geoscience Canada, v. 26, no. 4, p. 174–188.* https://journals.lib.unb.ca/index.php/GC/article/view/4024/4538

Muller, J. E., & Jeletzky, J. A. (1970). Geology of the upper Cretaceous Nanaimo Group, Vancouver Island and Gulf Islands, British Columbia. *Paper 69-25, Geological Survey of Canada.*

Nanda, N. C. (2021). *Seismic Data Interpretation and Evaluation for Hydrocarbon Exploration and Production: A Practitioner's Guide Second Edition*. Springer International Publishing, New York, NY, p. 25-45, 83–100, 243-257. http://www.springer.com/series/15228

Natural Resources Canada. (2025a). *Earthquake Details (2025-02-21)*. https://www.earthquakescanada.nrcan.gc.ca/recent/2025/20250221.2126/index-en.php. Accessed Mar 25, 2025.

Natural Resources Canada. (2025b). *Earthquake Details (2025-03-03)*. https://www.earthquakescanada.nrcan.gc.ca/recent/2025/20250303.1302/index-en.php. Accessed Mar 25, 2025.

New Zealand Police. (2012). *List of deceased*. https://www.police.govt.nz/news/major-events/previous-major-events/christchurch-earthquake/list-deceased. Accessed Feb 20, 2025.

Okimura, T., Takada, S., & Koid, T. H. (1996). Outline of the great Hanshin earthquake, Japan 1995. *Natural Hazards*, *14*(1), 39–71. https://doi.org/10.1007/BF00229911/METRICS

Personius, S. F., Briggs, R. W., Nelson, A. R., Schermer, E. R., Zebulon Maharrey, J., Sherrod, B. L., Spaulding, S. A., & Bradley, L. A. (2014). Holocene earthquakes and right-lateral slip on the left-lateral Darrington-Devils Mountain fault zone, northern Puget Sound, Washington. *Geosphere*, *10*(6), 1482–1500. https://doi.org/10.1130/GES01067.1

Pettigiani, E., Hodgins, D. O., & Tinis, S. E. (1997). Point Grey Disposal Site Monitoring Program: September 24 - October 29, 1996. [Report]. https://publications.gc.ca/collections/collection_2021/eccc/en37/En37-496-1997-eng.pdf

Pilcher, R., & Argent, J. (2007). Mega-pockmarks and linear pockmark trains on the West African continental margin. *Marine Geology*, *244*(1–4), 15–32. https://doi.org/10.1016/j.margeo.2007.05.002

Polivka, P. M. (2013). *Tectonics of the Georgia Basin, northwest Washington State, USA, and southwest British Columbia, Canada* [Master's Thesis, University of Washington].

Potter, S. H., Becker, J. S., Johnston, D. M., & Rossiter, K. P. (2015). An overview of the impacts of the 2010-2011 Canterbury earthquakes. *International Journal of Disaster Risk Reduction*, *14*, 6–14. https://doi.org/10.1016/J.IJDRR.2015.01.014

Rabinovich, A. B., Thomson, R. E., Bornhold, B. D., Fine, I. v, & Kulikov, E. A. (2003). Numerical Modelling of Tsunamis Generated by Hypothetical Landslides

in the Strait of Georgia, British Columbia. *Pure and Applied Geophysics*. 160.

Rafiei, A., Rahman, M. S., & Gabr, M. A. (2023). Evaluation of wave-induced instability of nearly saturated sandy slopes under partially undrained condition: A case study of landslide in Fraser River delta front. *Computers and Geotechnics*, *159*, 105496. https://doi.org/10.1016/J.COMPGEO.2023.105496

Riera, R., Paumard, V., de Gail, M., Saqab, M. M., Lebrec, U., Lang, S. C., & Lane, A. (2022). Origin of seafloor pockmarks overlying submarine landslides: Insights from semi-automated mapping of 3D seismic horizons (North West Shelf, Australia). *Marine and Petroleum Geology*, *136*, 105453. https://doi.org/10.1016/J.MARPETGEO.2021.105453

Riedel, M. (2002). *Report on Cruise PGC02002 on C.G.G. J.P. Tully, Georgia Basin Geohazards Initiative Mapping of Near Surface Active Faults*.

Robledo Carvajal, F., Butler, R. W. H., & Bond, C. E. (2023). Mapping faults in 3D seismic data – why the method matters. *Journal of Structural Geology*, *177*. https://doi.org/10.1016/j.jsg.2023.104976

Rockwell, T. K., Lindvall, S., Herzberg, M., Murbach, D., Dawson, T., & Berger, G. (2000). Paleoseismology of the Johnson Valley, Kickapoo, and Homestead Valley Faults: Clustering of Earthquakes in the Eastern California Shear Zone. *Bulletin of the Seismological Society of America*, *90*, 1200–1236.

Rogers, G.C. (1979). Earthquake fault plane solutions near Vancouver Island. *Canadian Journal of Earth Sciences*, *16*, 523–531.

Rogers, G.C. (1998). Earthquake and earthquake hazard in the Vancouver area. In Clague, J. J., Luternauer, J. L., & Mosher, D. C. (Eds.), *Geology and natural hazards of the Fraser River Delta, British Columbia*. Geological Survey of Canada Bulletin 525.

Rogers, G. C., & Hasegawa, H. S. (1978). A second look at the British Columbia earthquake of June 23, 1946. *Bulletin of the Seismological Society of America*, *68*(3), 653–675. http://pubs.geoscienceworld.org/ssa/bssa/article-pdf/68/3/653/5321226/bssa0680030653.pdf

Rolandone, F., Bürgmann, R., & Nadeau, R. M. (2004). The evolution of the seismic-aseismic transition during the earthquake cycle: Constraints from the time-dependent depth distribution of aftershocks. *Geophysical Research Letters*, *31*(L23610). https://doi.org/10.1029/2004GL021379

Römer, M., Riedel, M., Scherwath, M., Heesemann, M., & Spence, G. D. (2016). Tidally controlled gas bubble emissions: A comprehensive study using long-term monitoring data from the NEPTUNE cabled observatory offshore Vancouver Island. *Geochemistry, Geophysics, Geosystems*, *17*(9), 3797–3814. https://doi.org/10.1002/2016GC006528

Schumann, K., Stipp, M., Behrmann, J. H., Klaeschen, D., & Schulte-Kortnack, D.

(2014). P and S wave velocity measurements of water-rich sediments from the Nankai Trough, Japan. *Journal of Geophysical Research: Solid Earth*, *119*(2), 787–805. https://doi.org/10.1002/2013JB010290

Stacey, C. D. (2014). *Frequency and initiation mechanisms of submarine slides on the Fraser Delta front.* [Master's Thesis, University of Victoria].

Statistics Canada. (2021). 2021 Census - Boundary files [Shapefile]. https://www12.statcan.gc.ca/census-recensement/2021/geo/sip-pis/boundary-limites/index2021-eng.cfm?year=21. Accessed February 2, 2025.

Statistics Canada. (2023). Census Profile, 2021 Census of Population. [Table]. *Statistics Canada Catalogue 98-316-X2021001.* https://www12.statcan.gc.ca/census-recensement/2021/dp-pd/prof/index.cfm?Lang=E. Accessed March 21, 2025.

Soter, S. (1999). Macroscopic seismic anomalies and submarine pockmarks in the Corinth–Patras rift, Greece. *Tectonophysics*, *308*(1–2), 275–290. https://doi.org/10.1016/S0040-1951(99)00090-6

Suppasri, A., Kitamura, M., Alexander, D., Seto, S., & Imamura, F. (2024). The 2024 Noto Peninsula earthquake: Preliminary observations and lessons to be learned. *International Journal of Disaster Risk Reduction*, *110*, 104611. https://doi.org/10.1016/J.IJDRR.2024.104611

Tang, A. (Ed.). (2016). Chapter 10: Airport. In Tang, A. (Ed.), *Christchurch, New Zealand, Earthquakes of 2010 and 2011, Lifeline Performance* (TCLEE Monograph No. 41). American Society of Civil Engineers. https://doi.org/10.1061/9780784414217.ch10

Tõth, Z., Spiess, V., Mogollõn, J. M., & Jensen, J. B. (2014). Estimating the free gas content in Baltic Sea sediments using compressional wave velocity from marine seismic data. *Journal of Geophysical Research: Solid Earth*, *119*(12), 8577–8593. https://doi.org/10.1002/2014JB010989

Truth and Reconciliation Commission of Canada (2015). Truth and Reconciliation Commission of Canada: Calls to Action. Accessed January 31, 2025, https://nctr.ca/records/reports/#trc-reports

Vargas, G., Klinger, Y., Rockwell, T., Forman, S., Rebolledo, S., Baize, S., Lacassin, R., & Armijo, R. (2014). Probing large intraplate earthquakes at the west flank of the Andes. *Geology*, 42. https://doi.org/10.1130/G35741.1ï

Vieira, L. C., & Candy, P. G. (2024). *Sub-bottom acoustic profiling surveying report – Iona Spit, BC.* [Report].

Wells, D. L., & Coppersmith, K. J. (1994). New Empirical Relationships among Magnitude, Rupture Length, Rupture Width, Rupture Area, and Surface Displacement. *Bulletin of the Seismological Society of America* 84(4).

Wells, R., Weaver, C., & Blakely, R. (1998). Fore-arc migration in Cascadia and its

neotectonic significance. *Geology*, *26*(8), 759–762.

Wesnousky, S. G. (2008). Displacement and Geometrical Characteristics of Earthquake Surface Ruptures: Issues and Implications for Seismic-Hazard Analysis and the Process of Earthquake Rupture. *Bulletin of the Seismological Society of America*, *98*(4), 1609–1632. https://doi.org/10.1785/0120070111

White, D., & Clowes, R. M. (1984). Seismic investigation of the Coast Plutonic Complex – Insular Belt boundary beneath the Strait of Georgia. *Canadian Journal of Earth Sciences*, *21*, 1033–1049.

Whitmore, P., Benz, H., Bolton, M., Crawford, G., Dengler, L., Fryer, G., Goltz, J., Hansen, R., Kryzanowski, K., Malone, S., Oppenheimer, D., Petty, E., Rogers, G., & Wilson, J. (2008). NOAA/West Coast and Alaska Tsunami Warning Center Pacific Ocean response criteria. *Science of Tsunami Hazards*, *27*(2), 1.

Williams, H., & Hutchinson, I. (2000). Stratigraphic and Microfossil Evidence for Late Holocene Tsunamis at Swantown Marsh, Whidbey Island, Washington. *Quaternary Research*, *54*(2), 218–227. https://doi.org/https://doi.org/10.1006/qres.2000.2162

Williams, E. F., Ugalde, A., Martins, H. F., Becerril, C. E., Callies, J., Claret, M., Fernandez-Ruiz, M. R., Gonzalez-Herraez, M., Martin-Lopez, S., Pelegri, J. L., Winters, K. B., & Zhan, Z. (2023). Fiber-Optic Observations of Internal Waves and Tides. *Journal of Geophysical Research: Oceans*, *128*(9). https://doi.org/10.1029/2023JC019980

Wong, C., Ballegooyen, K., Ignace, L., Johnson, M. J., & Swanson, H. (2020). Towards reconciliation: 10 Calls to Action to natural scientists working in Canada. *Facets,* 5(1), 769–783. https://doi.org/10.1139/facets-2020-0005

Wood, A., Noy, I., & Parker, M. (2016). The Canterbury rebuild five years on from the Christchurch earthquake. *Reserve Bank of New Zealand Bulletin*, *79*(3).

Woodcock, N. H., & Rickards, B. (2003). Transpressive duplex and flower structure: Dent Fault System, NW England. *Journal of Structural Geology*, *25*(12), 1981–1992. https://doi.org/10.1016/S0191-8141(03)00057-9

Worden, C. B., Gerstenberger, M. C., Rhoades, D. A., & Wald, D. J. (2012). Probabilistic relationships between ground-motion parameters and modified mercalli intensity in California. *Bulletin of the Seismological Society of America*, *102*(1), 204–221. https://doi.org/10.1785/0120110156

Xiao, H., Zhang, S., Moss, R., and Zhan, Z. (2025). Imaging Underwater Faults and Tracking Whales with Optical Fiber Sensing. *Seismological Research Letters 96, p. 678–690.* doi: 10.1785/ 0220240359.

Yilmaz, Ö. (2001). *Seismic data analysis: processing, inversion, and interpretation of seismic data* (2nd ed.). Society of Exploration Geophysicists.

Youngson, J. H., Craw, D., Landis, C. A., & Schmitt, K. R. (1998). Redefinition and

interpretation of late Miocene-Pleistocene terrestrial stratigraphy, Central Otago, New Zealand. *New Zealand Journal of Geology and Geophysics*, 41(1), 51–68. https://doi.org/10.1080/00288306.1998.9514790

Zhang, K., Guan, Y., Song, H., Fan, W., Li, H., Kuang, Y., & Geng, M. (2020). A preliminary study on morphology and genesis of giant and mega pockmarks near Andu Seamount, Nansha Region (South China Sea). *Marine Geophysical Research*, *41*(1). https://doi.org/10.1007/s11001-020-09404-y

Zelt, B. C., Ellis, R. M., Zelt, C. A., Hyndman, R. D., Lowe, C., Spence, G. D., & Fisher, M. A. (2001). Three-dimensional crustal velocity structure beneath the Strait of Georgia, British Columbia. *Geophysical Journal International*, *144*, 695–712. https://academic.oup.com/gji/article/144/3/695/614792

Zuza, A. V., & Cao, W. (2020). Seismogenic thickness of California: Implications for thermal structure and seismic hazard. *Tectonophysics*, *782–783*, 228426. https://doi.org/10.1016/J.TECTO.2020.228426

Appendix A

Interpretations of Seismic Reflection Data

A.1 Preliminary Information

This appendix contains seismic reflection profiles used for this thesis. Profiles are presented with and without interpretation, labelled a and b, respectively. For more information on the data and the employed seismic reflection interpretation framework, the reader is referred to Chapter 3 and the Methods section of Chapter 4. IHS Kingdom Suite and custom-written applications produced at the Geological Survey of Canada were used to interpret and digitize seismic reflection data.

Those hoping to access these data for their own research, or who would like to view high-resolution copies of uninterpreted profiles and complementary datasets, are referred to a compiled Google Earth .kmz file available via FTP at `https://ftp.maps.canada.ca/pub/nrcan_rncan/raster/marine_geoscience/NRCAN%20Windows%2010%20Software/KMLS/NRCanMarineDataHoldings.kmz`. Alternatively, an FTP repository, organized by cruise ID, is available at `https://ftp.maps.canada.ca/pub/nrcan_rncan/raster/marine_geoscience/Seismic_Reflection_Scanned/`. Both resources are maintained intermittently by Natural Resources Canada. As of the time of writing, seismic reflection data not currently available through these public resources have been uploaded to an internal staging space and are intended to be made publicly accessible in the near future. Requests for data can be directed to Kevin Desroches at Natural Resources Canada (kevin.desroches@NRCan-RNCan.gc.ca).

The following colour scheme is applied to all seismic interpretations for faults and the tops of units:

- Faults and/or fluid conduits, purple
- Bedrock horizons, blue
- Glacial horizons, red

- Lower-post glacial horizons, orange
- Upper-post glacial horizons, yellow

A.2 Data and Interpretations

A.2.1 Cruise ID 82003PGC

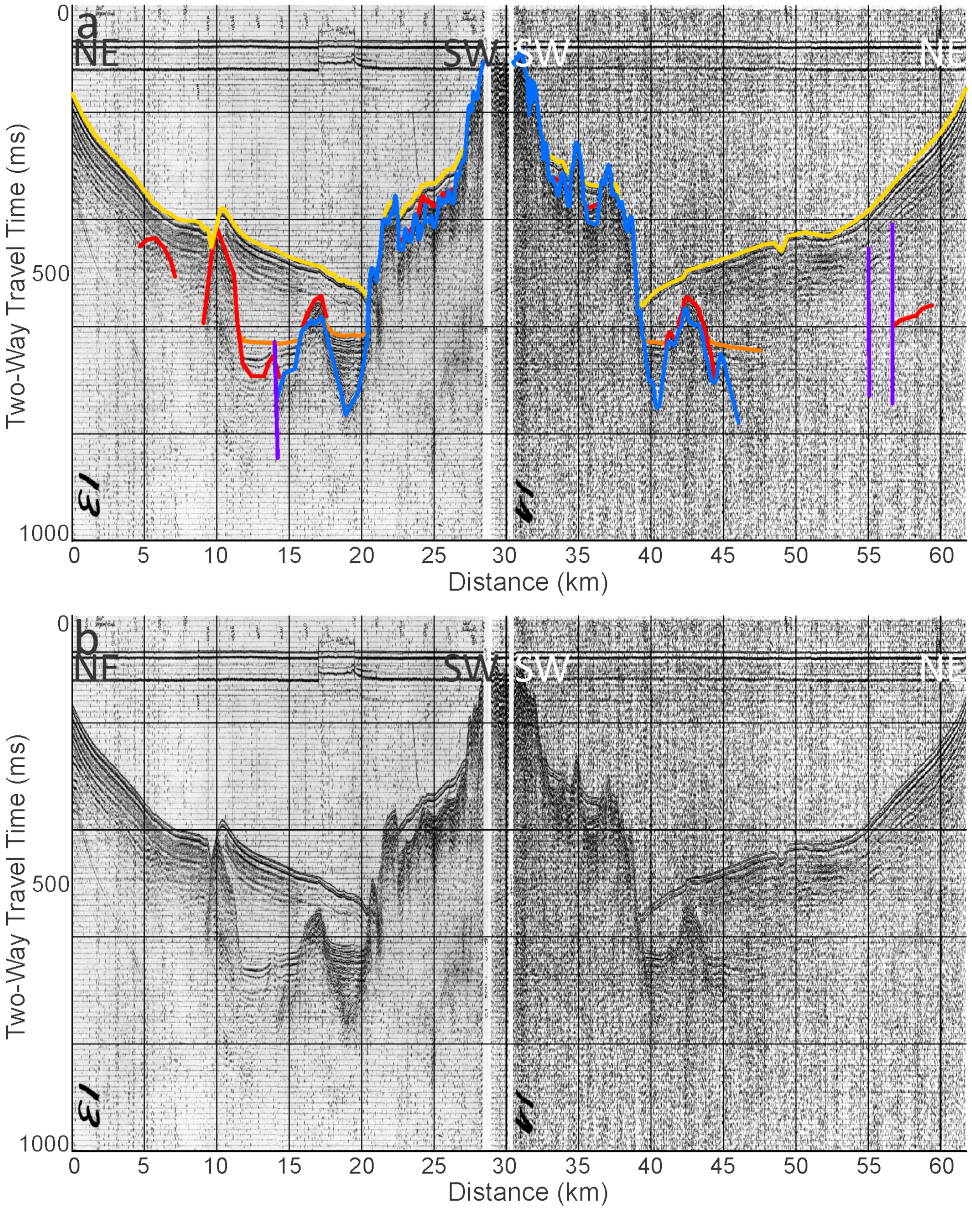


Figure A.2.1: Lines 13 and 14, cruise 82003PGC

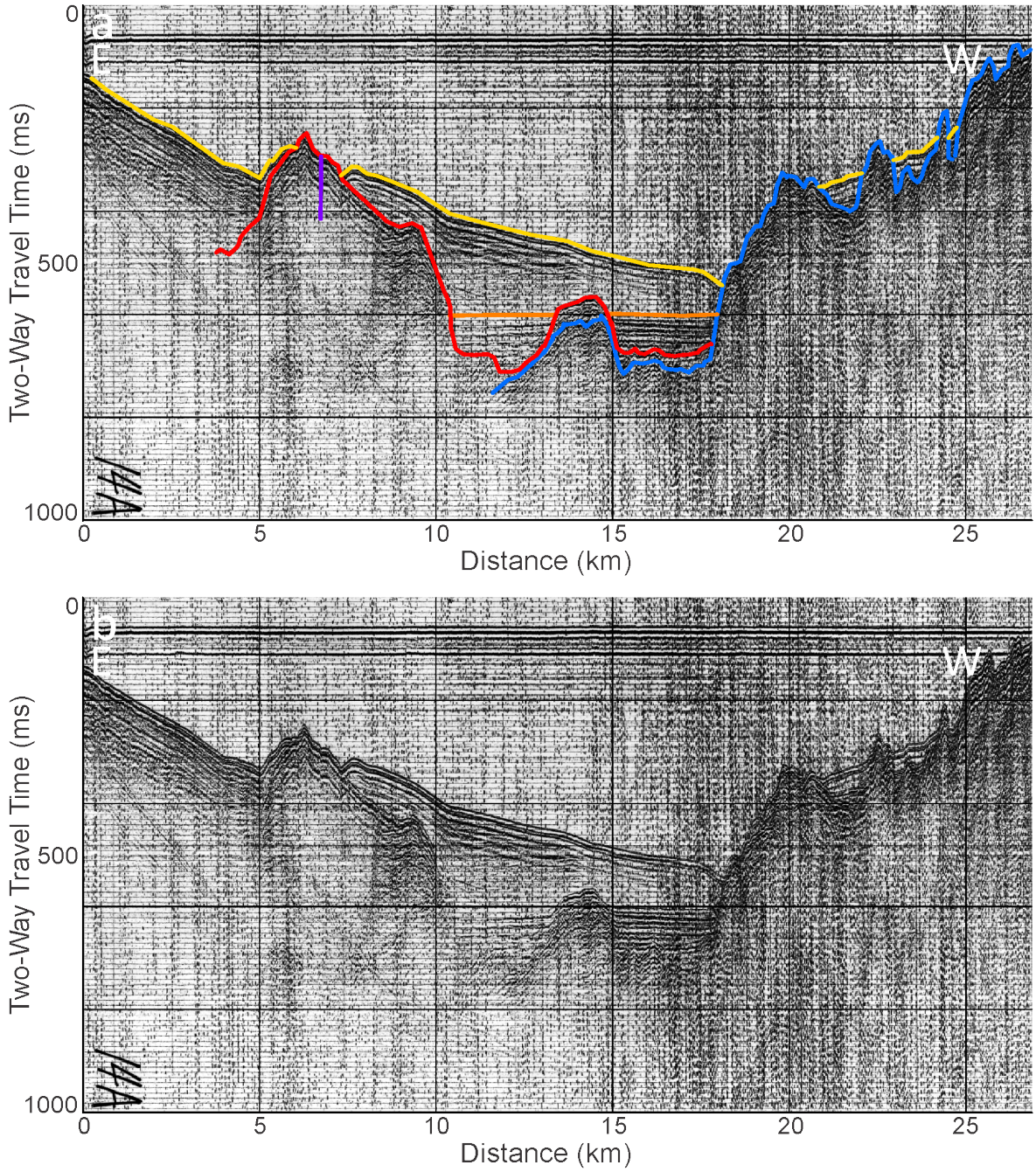


Figure A.2.2: Line 14 A, cruise 82003PGC

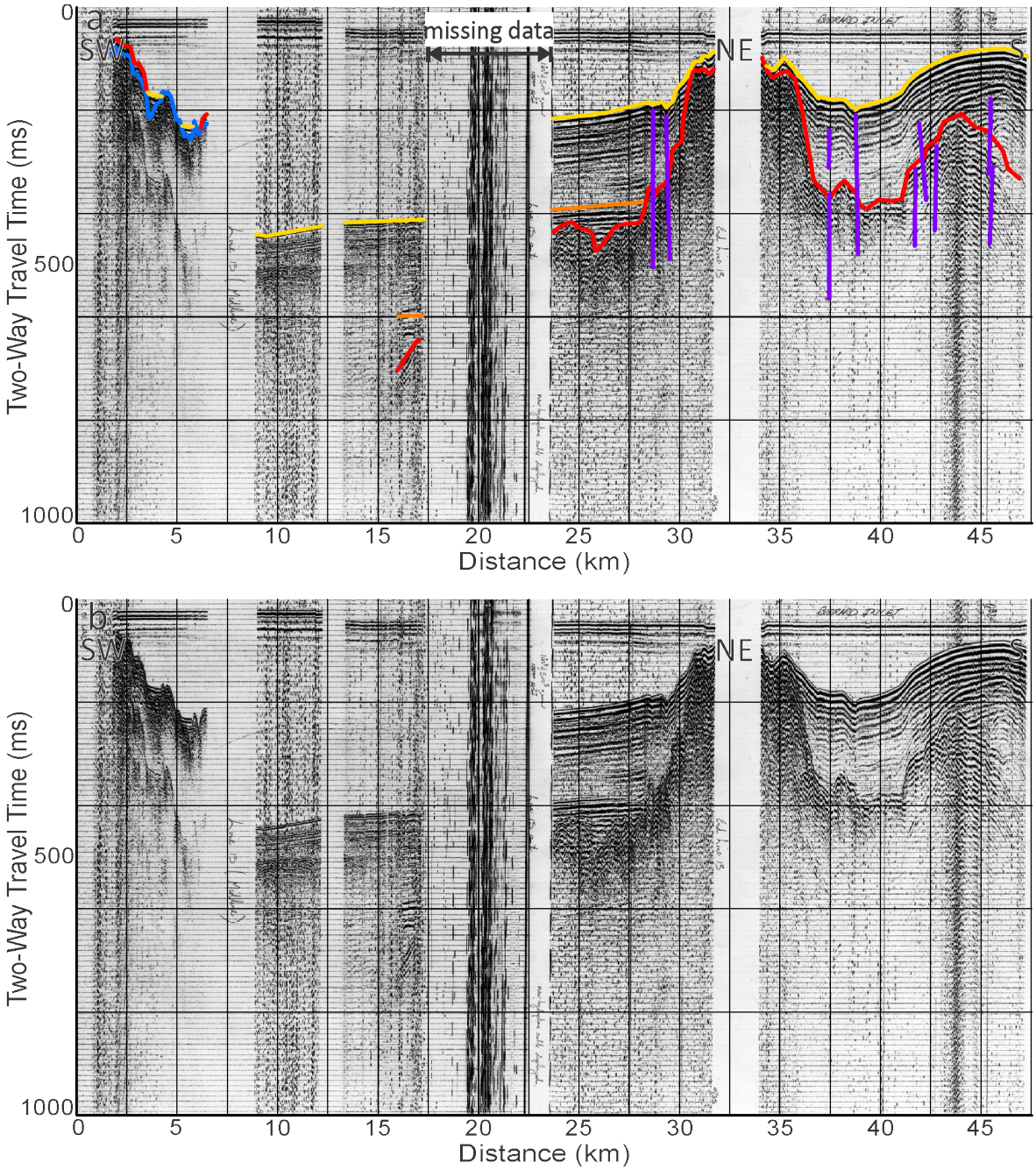


Figure A.2.3: Line 15, cruise 82003PGC. Excluded from results due to discrepancies between the seafloor reflector in profile and seafloor relief in MBES data, suspected navigation and/or georeferencing errors.

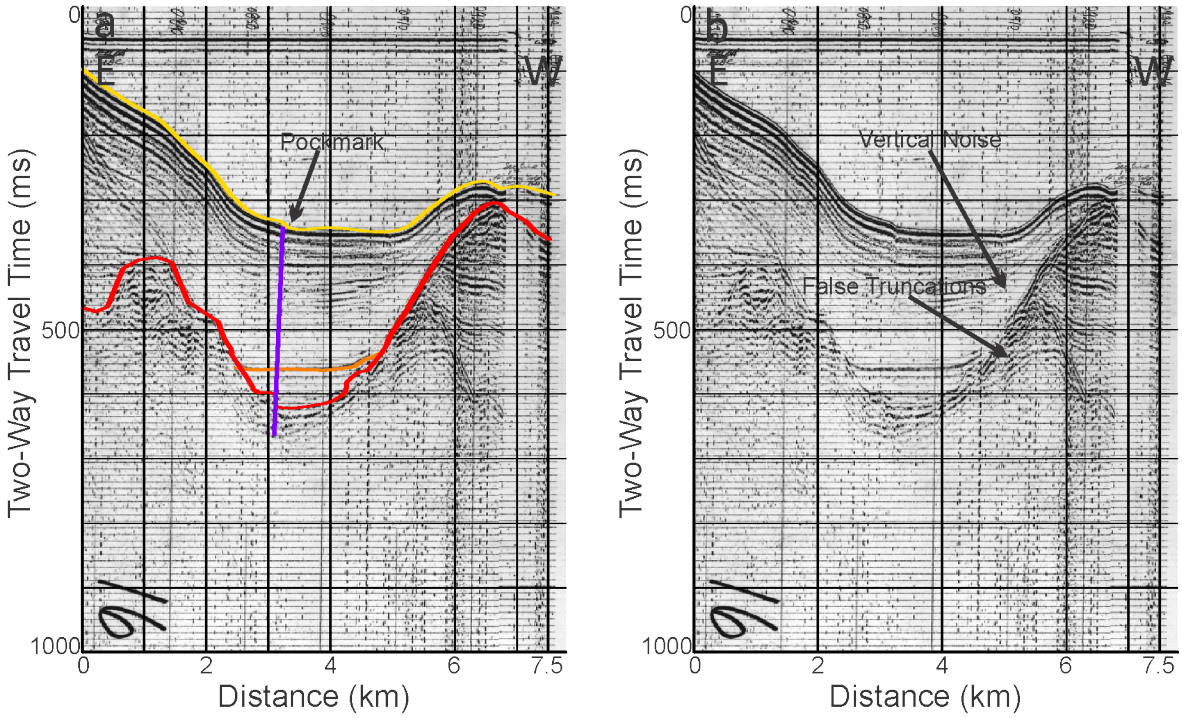


Figure A.2.4: Line 16, cruise 82003PGC

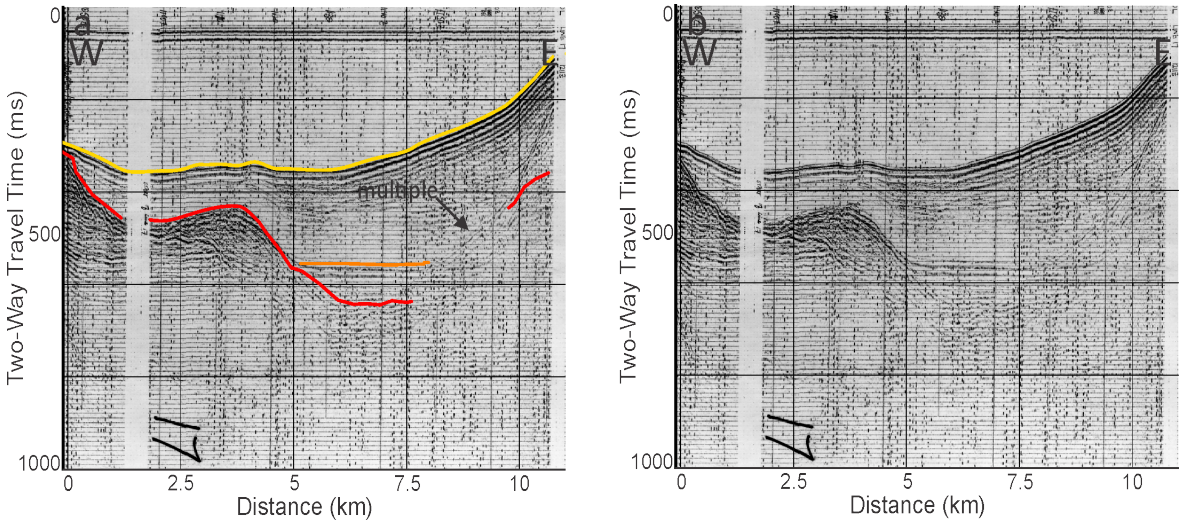


Figure A.2.5: Line 17, cruise 82003PGC

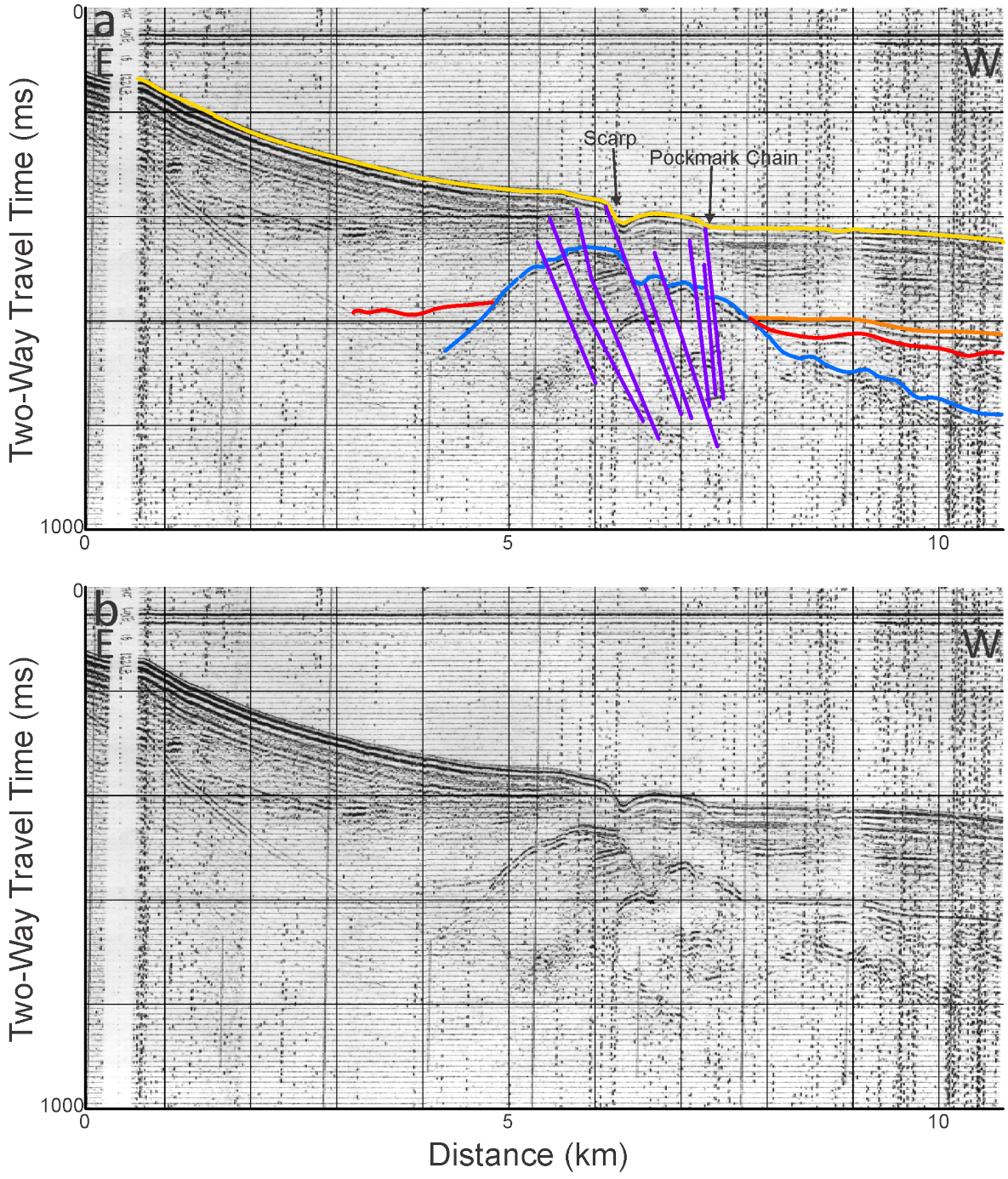


Figure A.2.6: Line 18, cruise 82003PGC

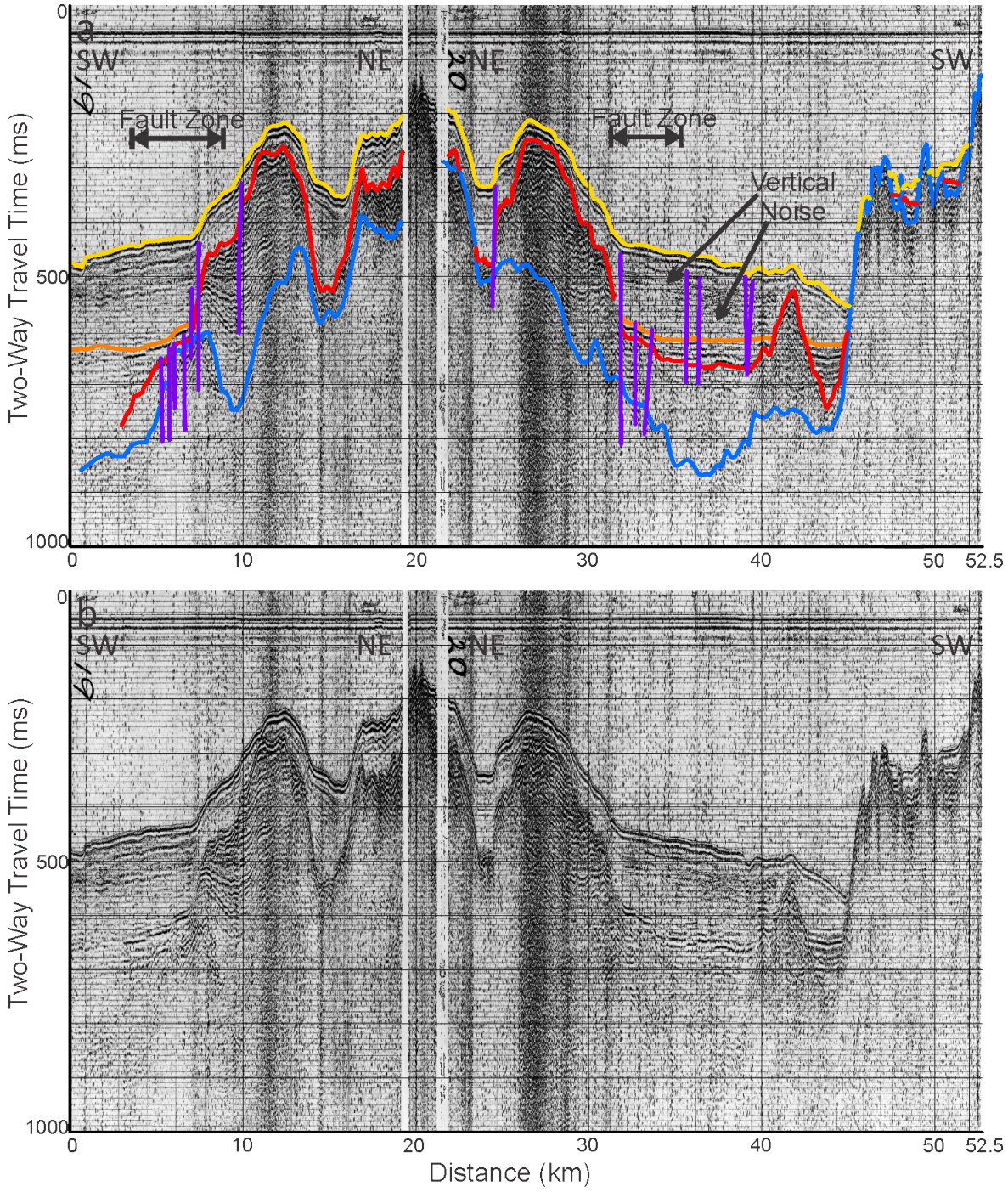


Figure A.2.7: Lines 19 and 20, cruise 82003PGC

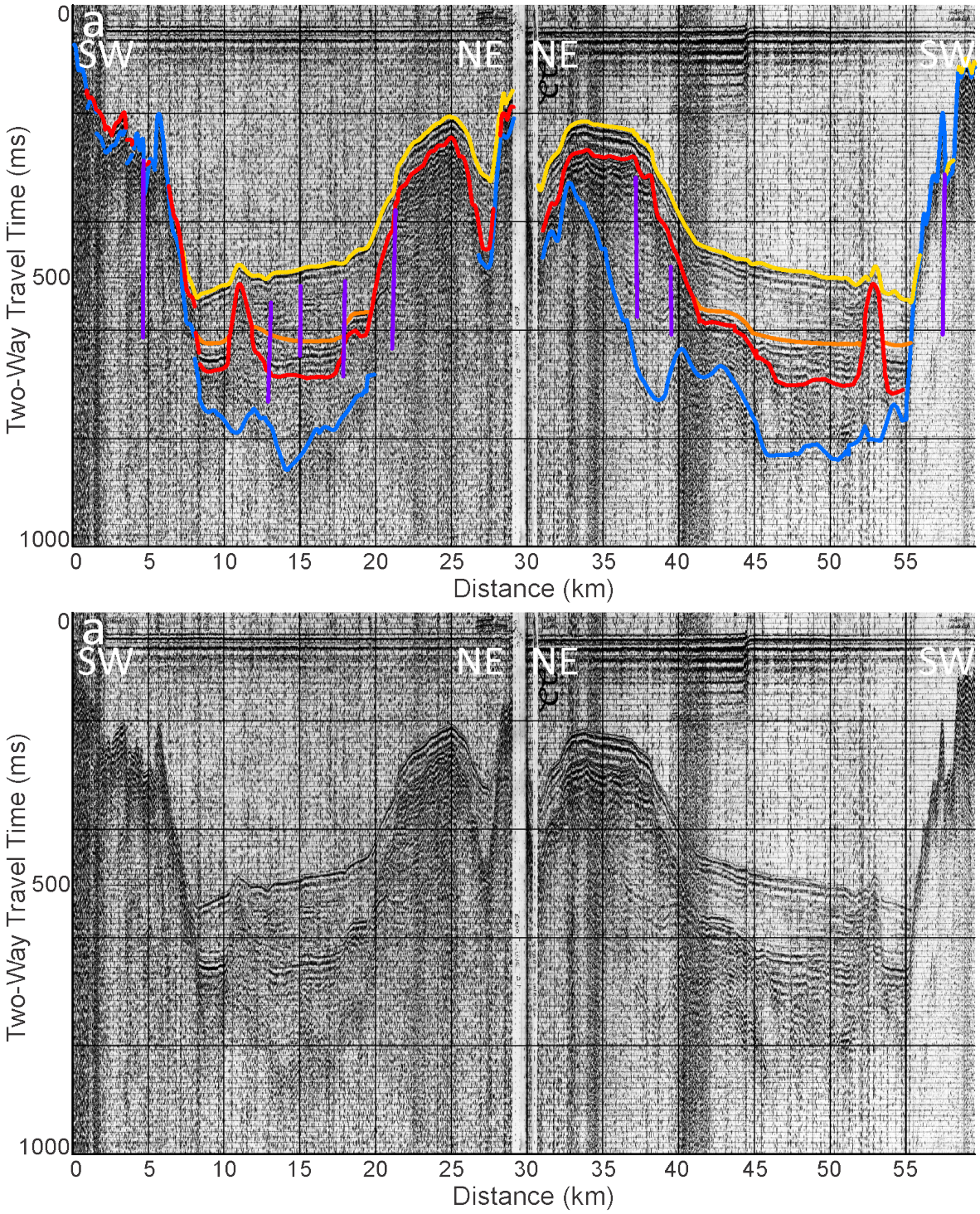


Figure A.2.8: Lines 21 and 22, cruise 82003PGC

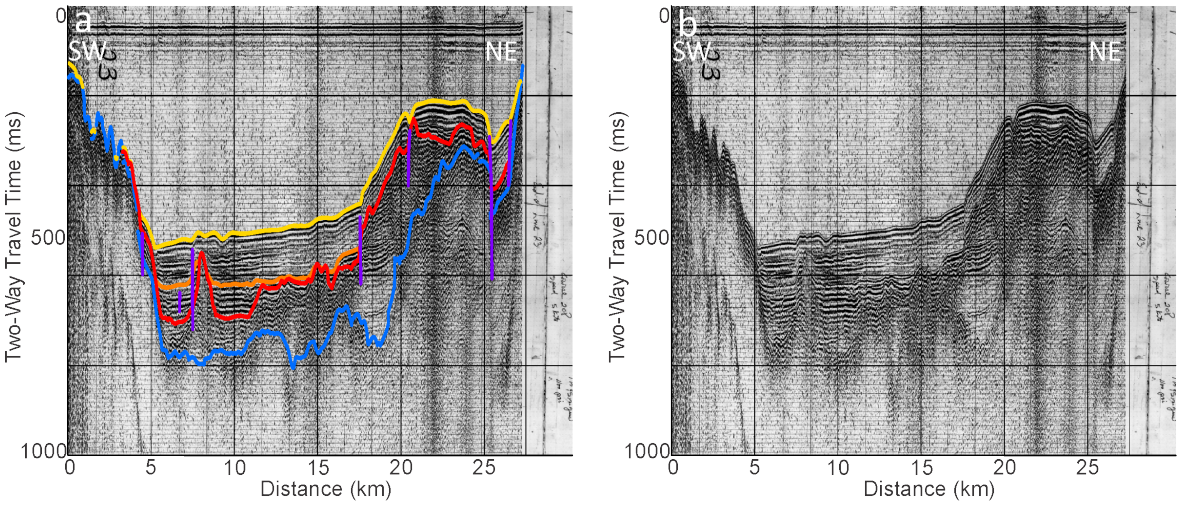


Figure A.2.9: Line 23, cruise 82003PGC

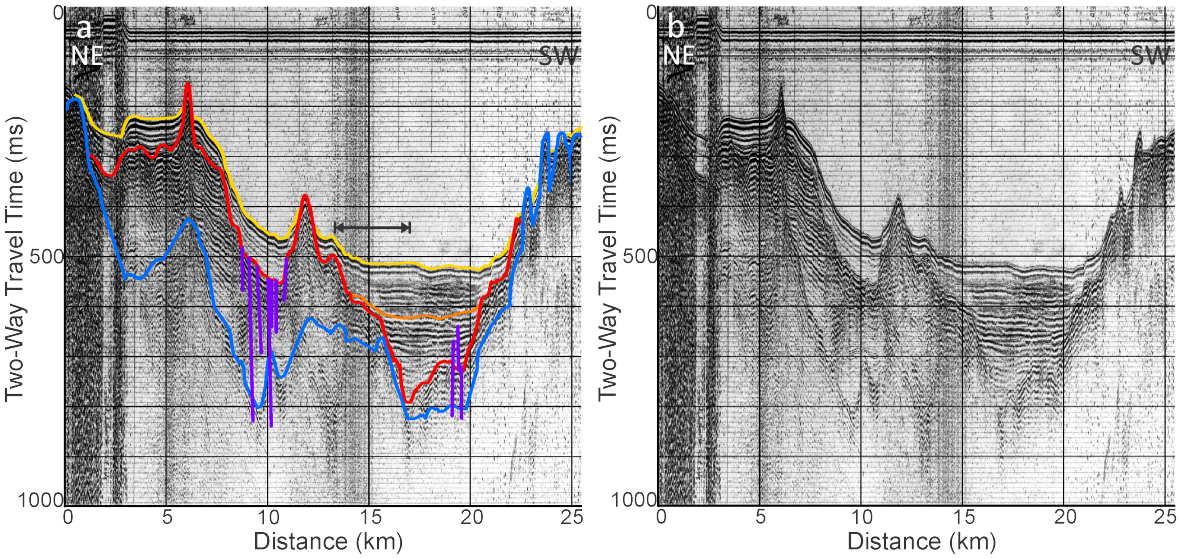


Figure A.2.10: Line 24, cruise 82003PGC

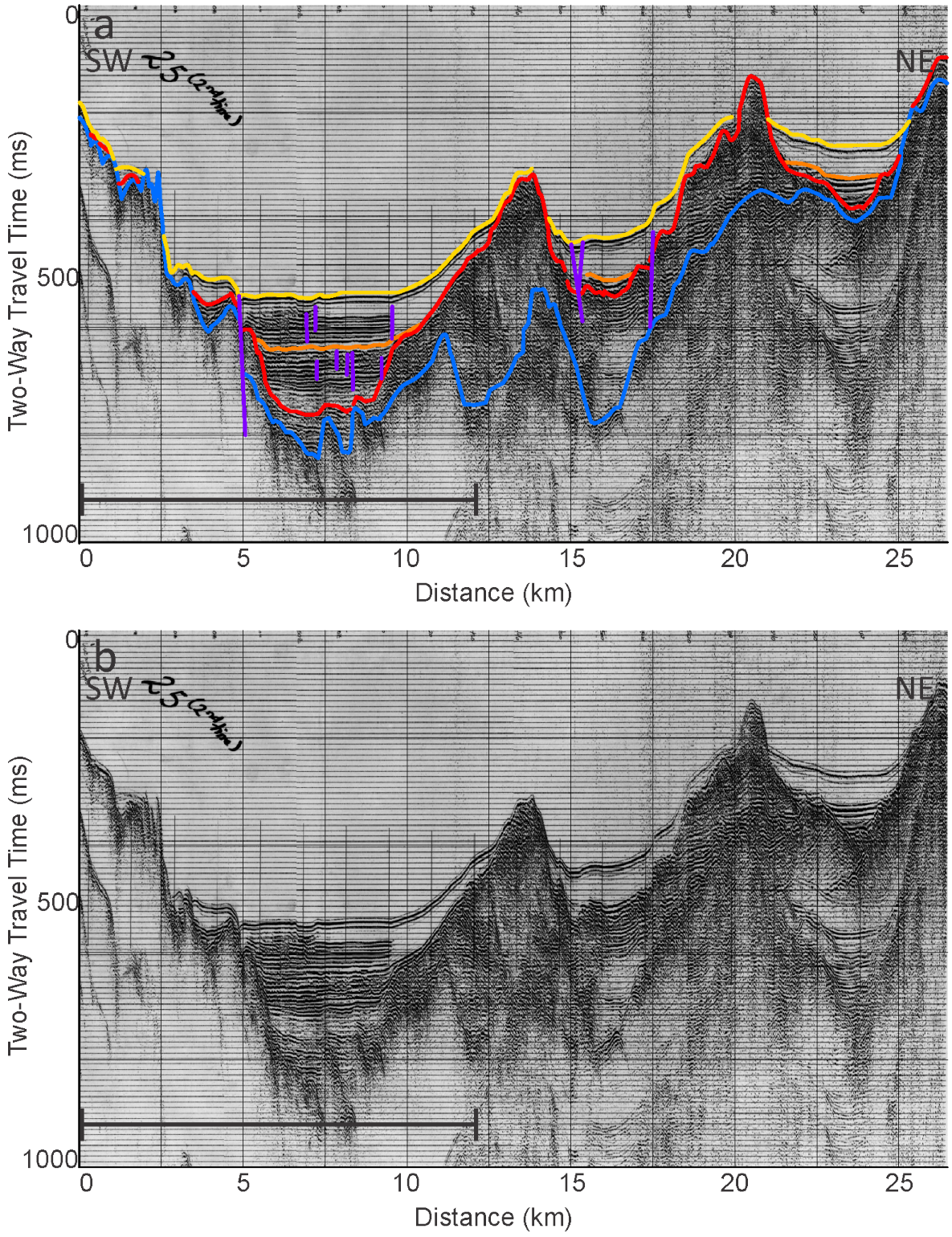


Figure A.2.11: Line 25R, cruise 82003PGC. Black line indicates the extent of detailed profile shown in Figure A.2.12.

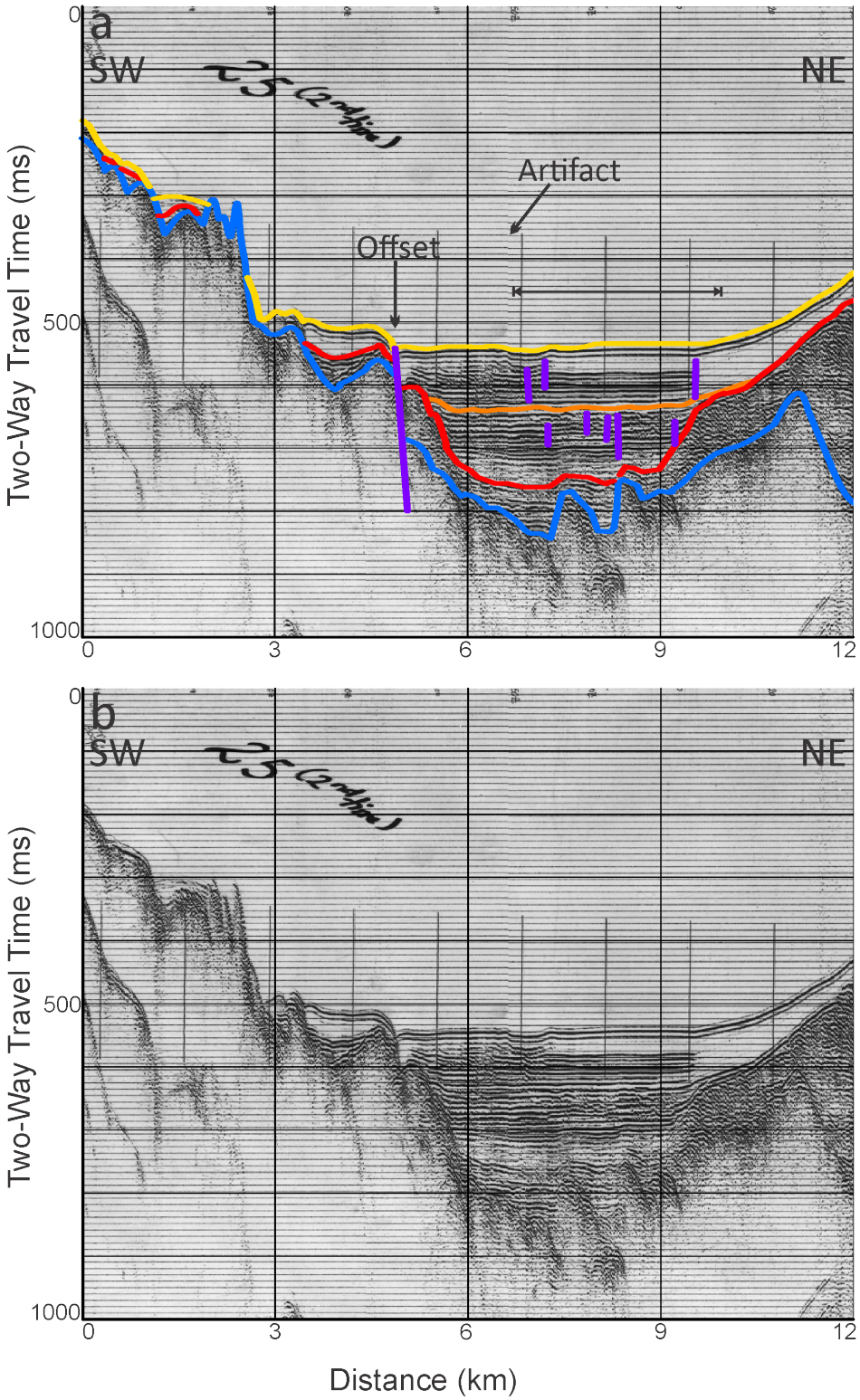


Figure A.2.12: Magnified profile of line 25R near Gabriola Island and the 1975/1997 Strait of Georgia earthquake clusters.

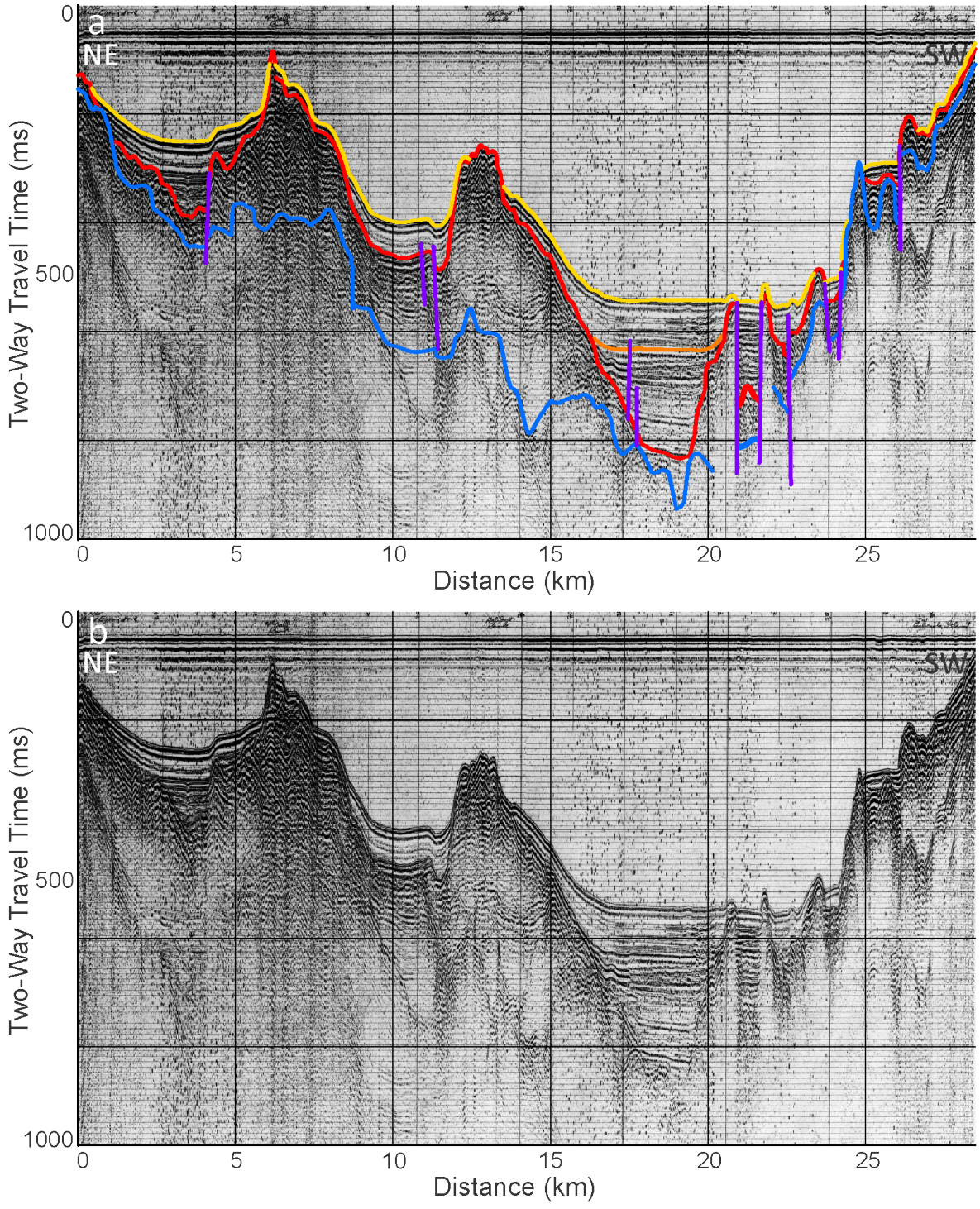


Figure A.2.13: Line 26, cruise 82003PGC

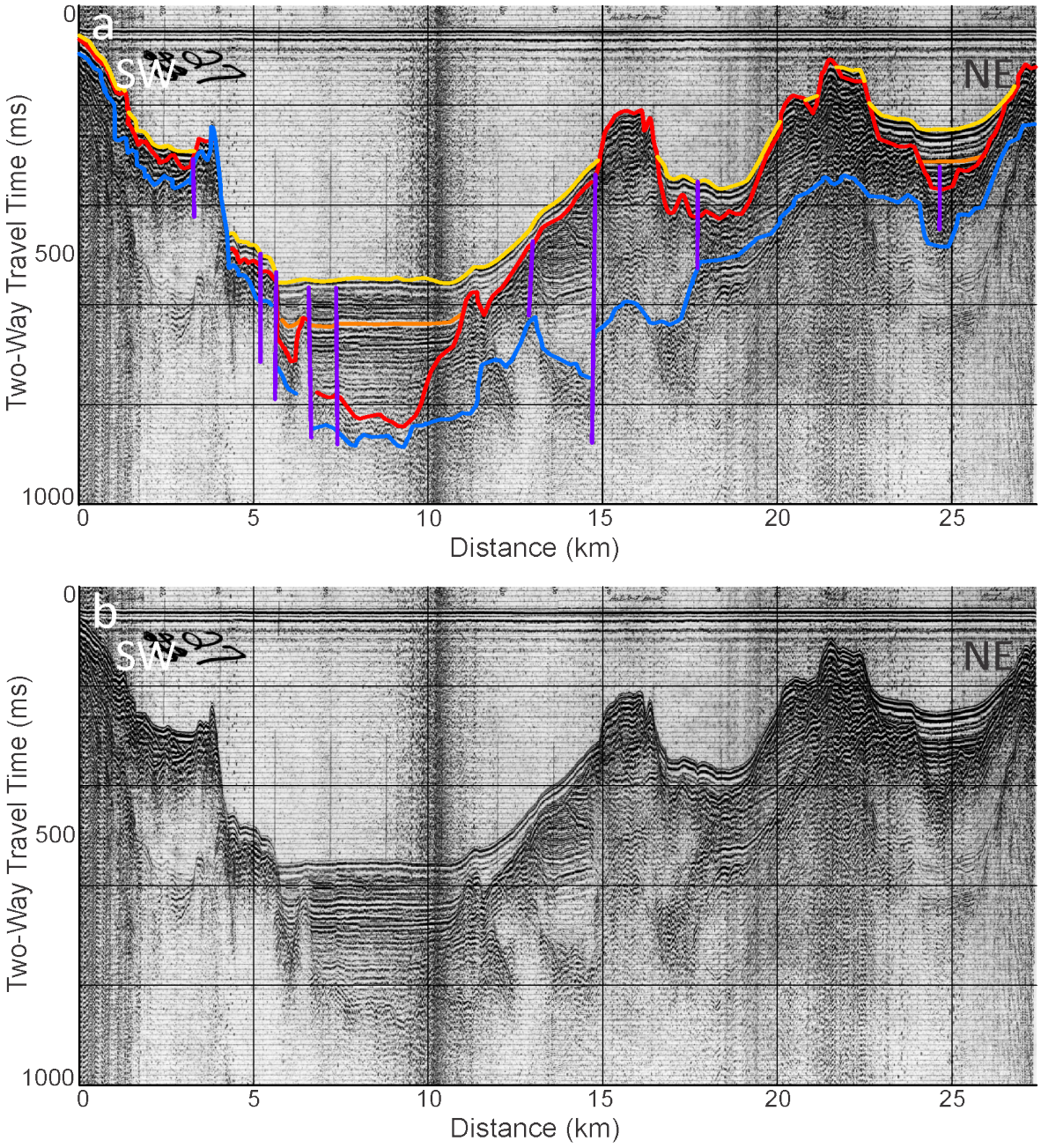


Figure A.2.14: Line 27, cruise 82003PGC

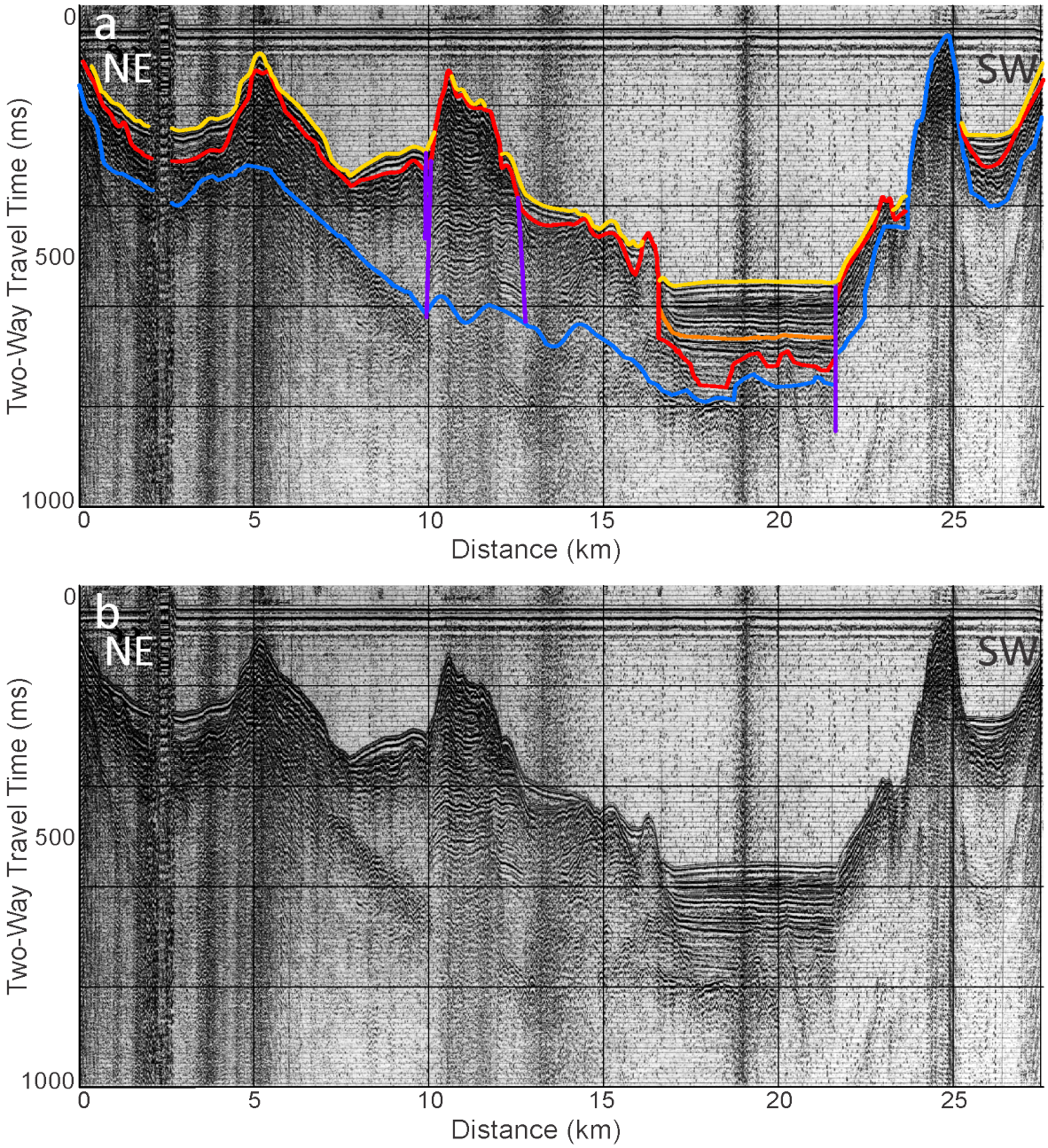


Figure A.2.15: Line 28, cruise 82003PGC

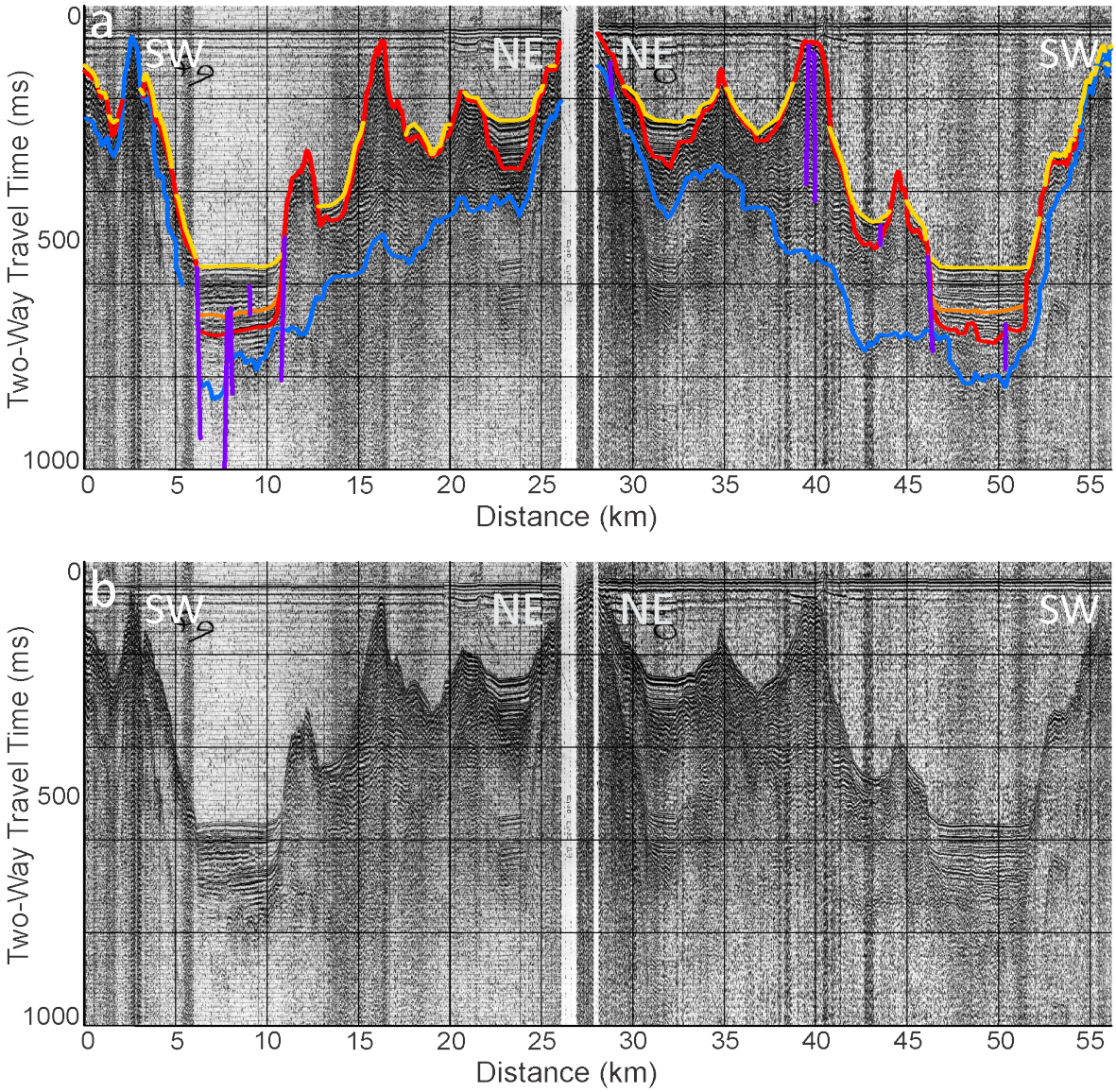


Figure A.2.16: Lines 29 and 30, cruise 82003PGC

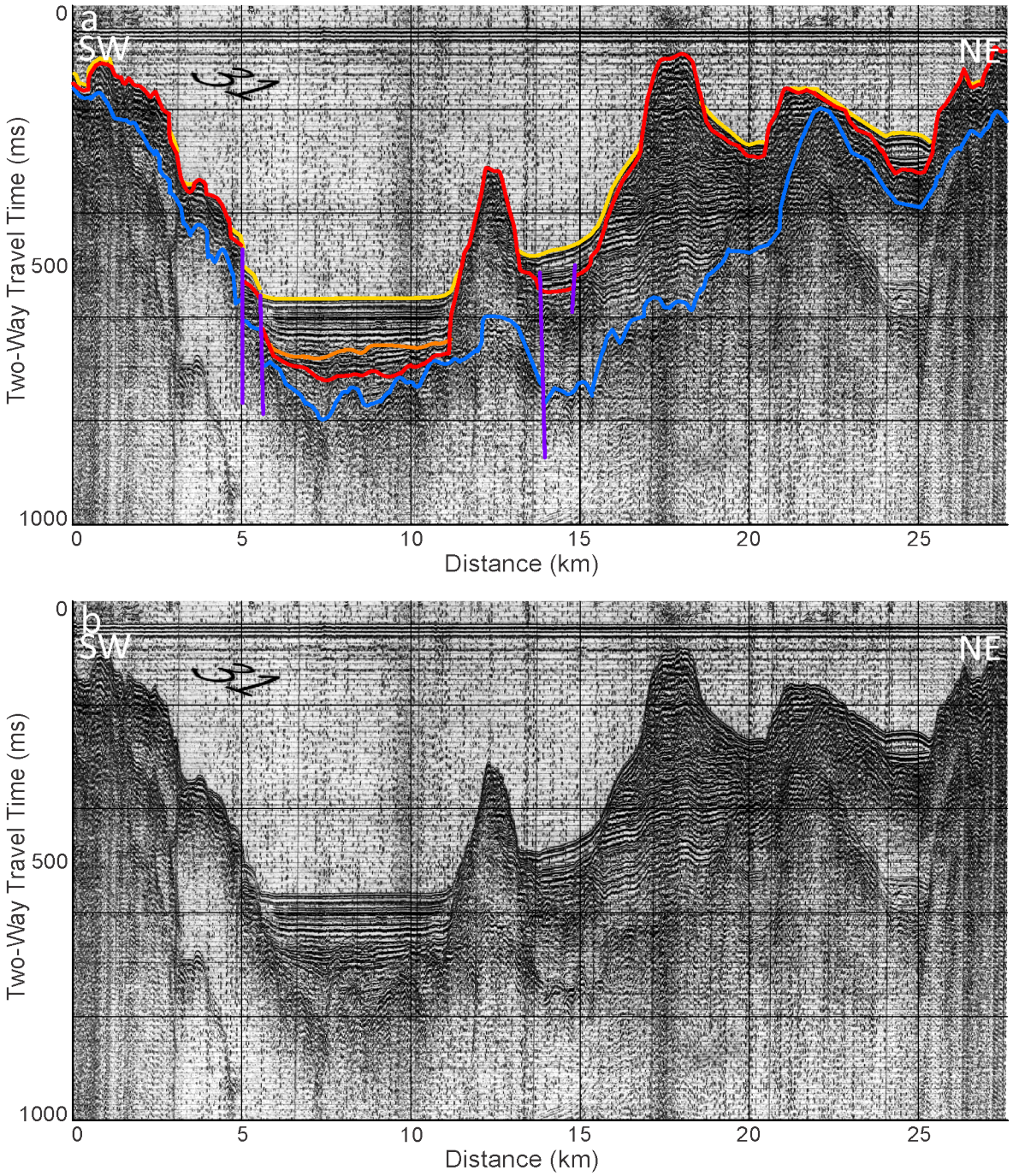


Figure A.2.17: Line 31, cruise 82003PGC

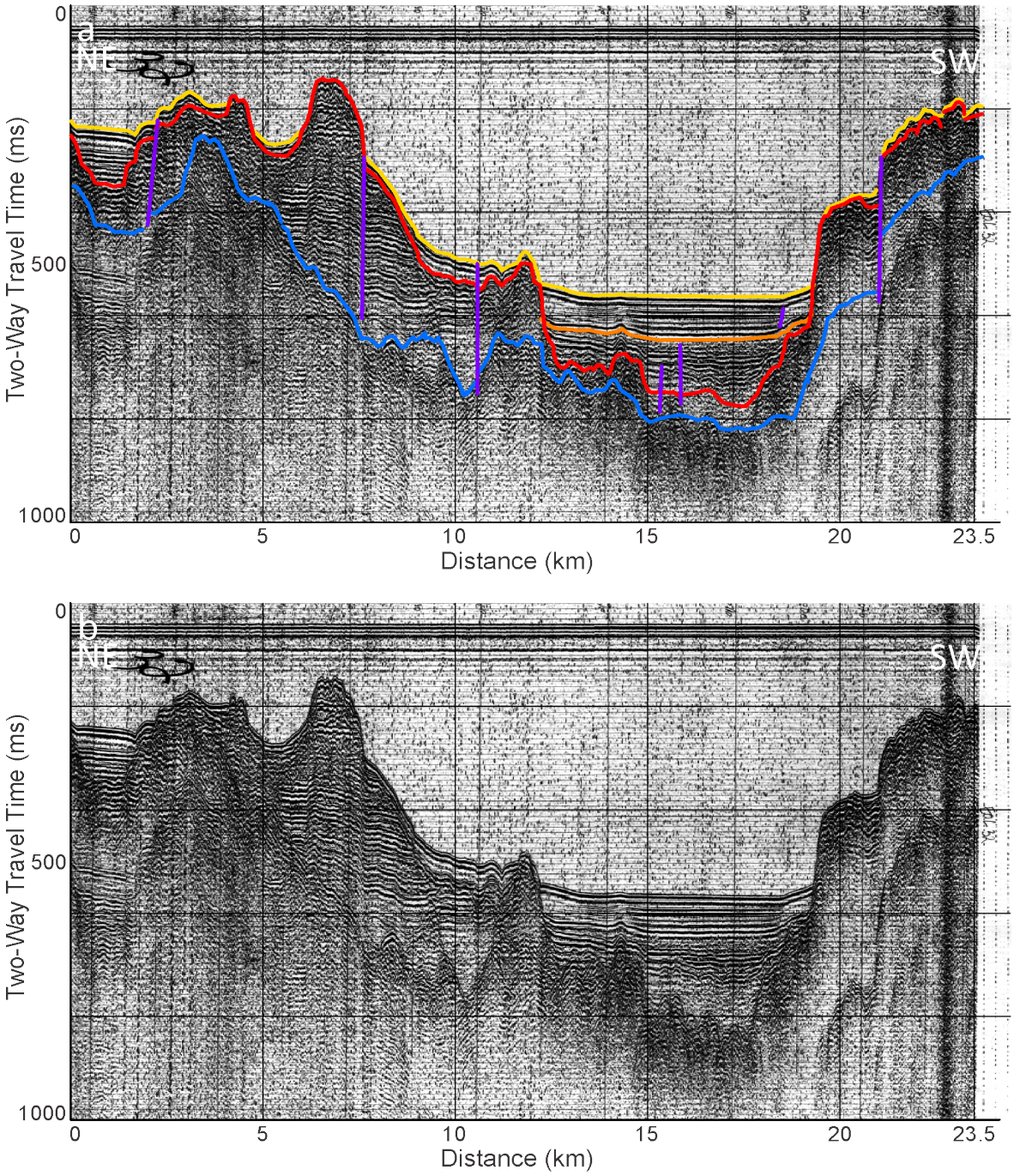


Figure A.2.18: Line 32, cruise 82003PGC

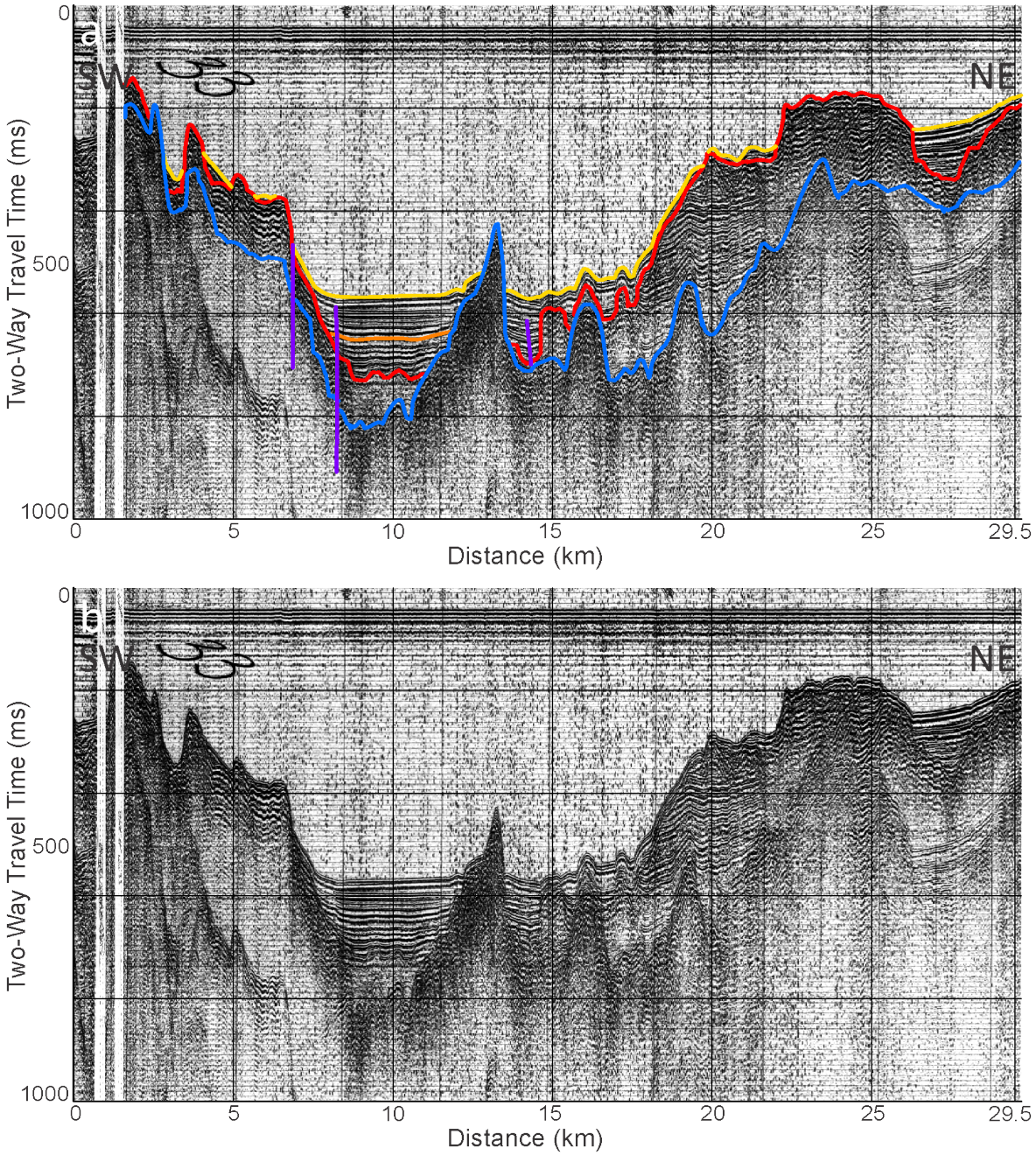


Figure A.2.19: Line 33, cruise 82003PGC

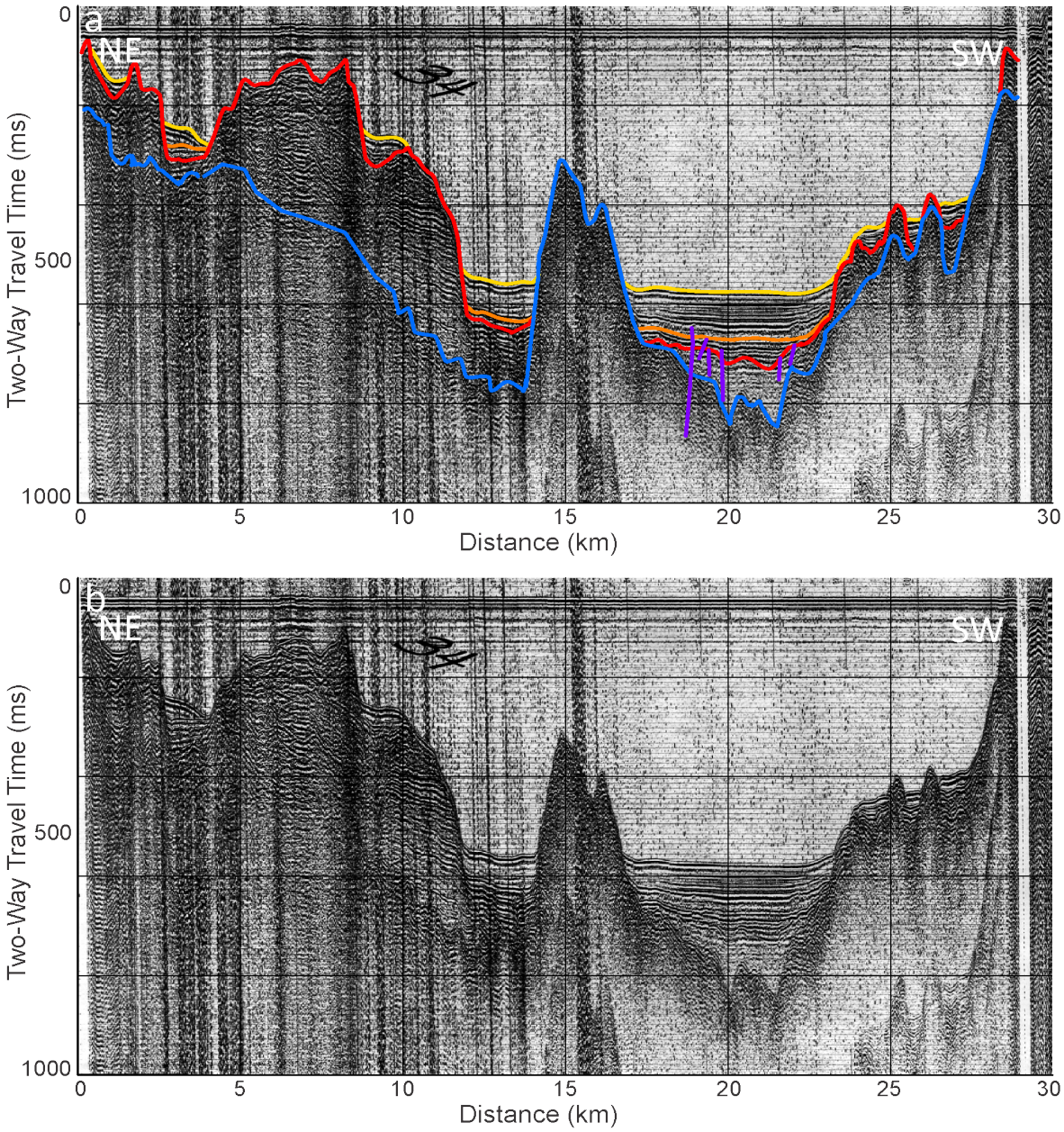


Figure A.2.20: Line 34, cruise 82003PGC

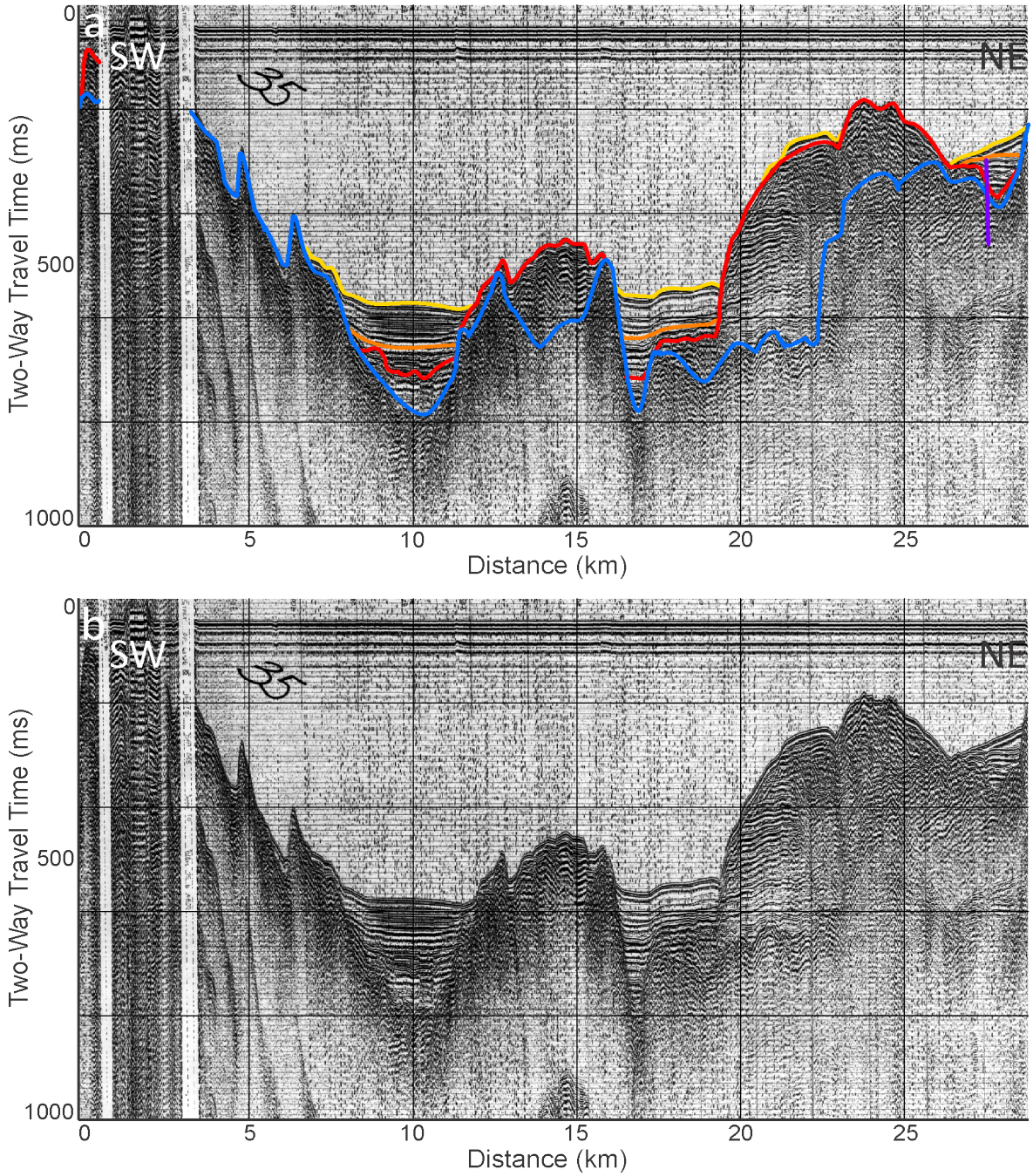


Figure A.2.21: Line 35, cruise 82003PGC

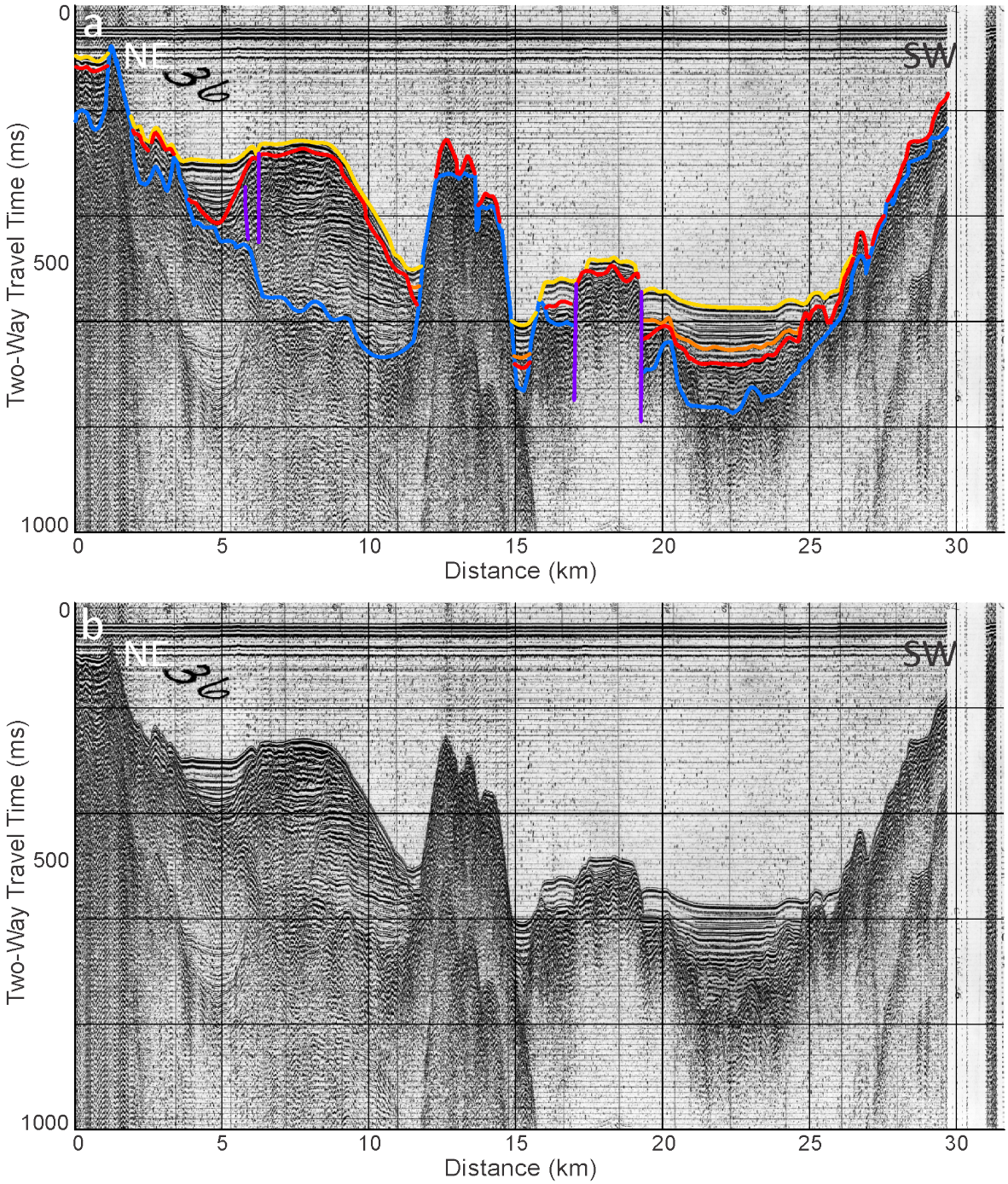


Figure A.2.22: Line 36, cruise 82003PGC

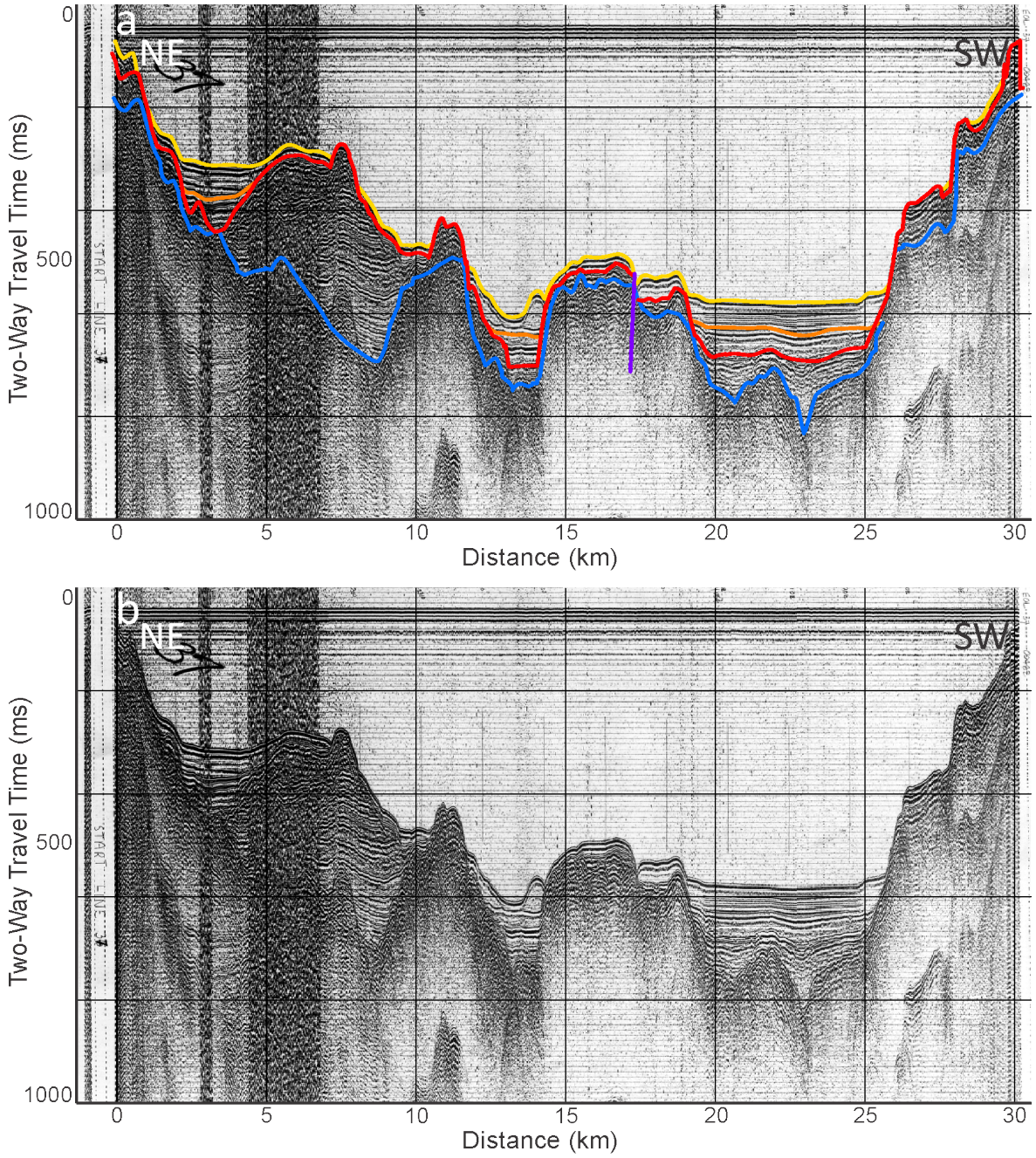


Figure A.2.23: Line 37, cruise 82003PGC

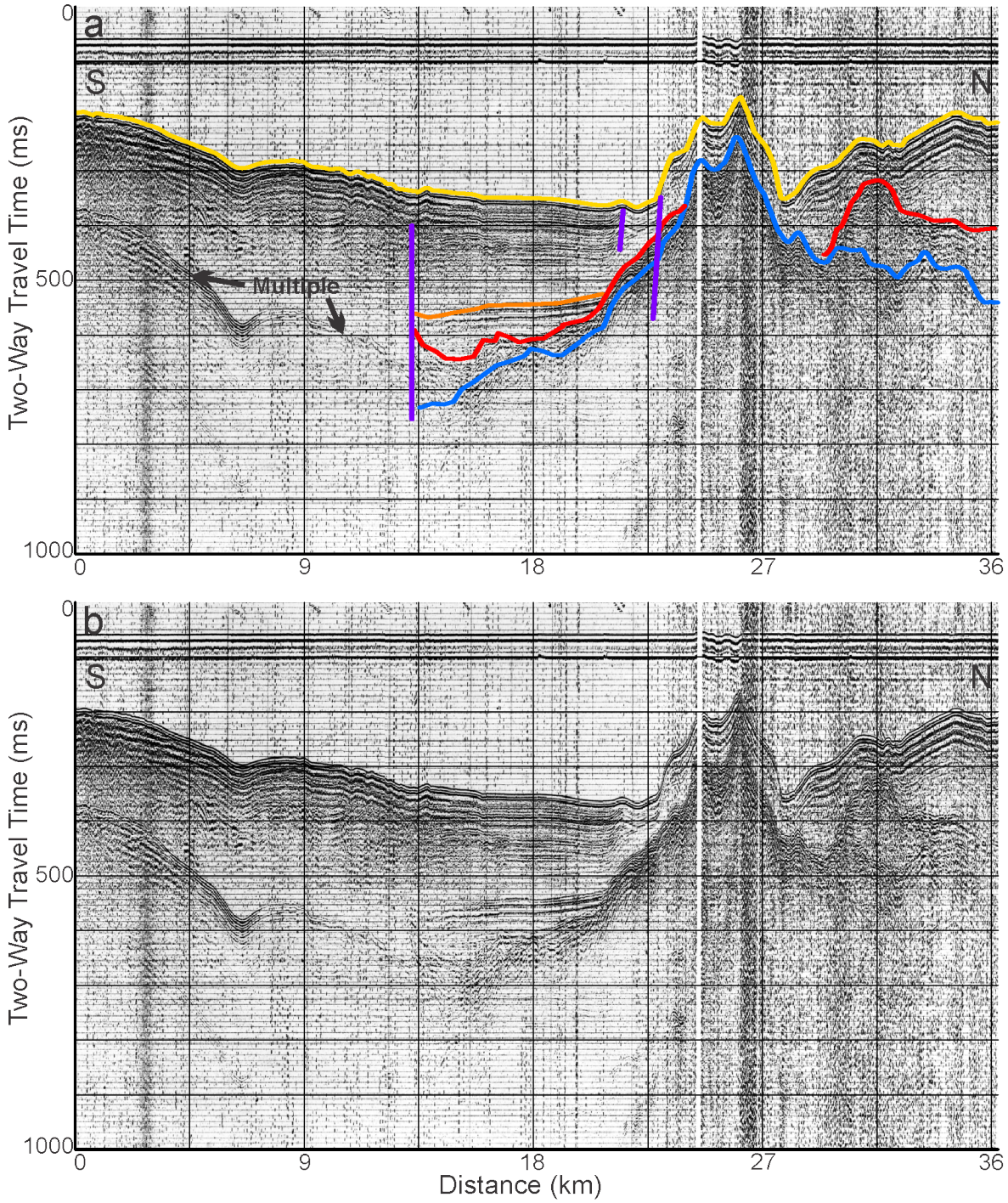


Figure A.2.24: Line Fraser Bowen, cruise 82003PGC

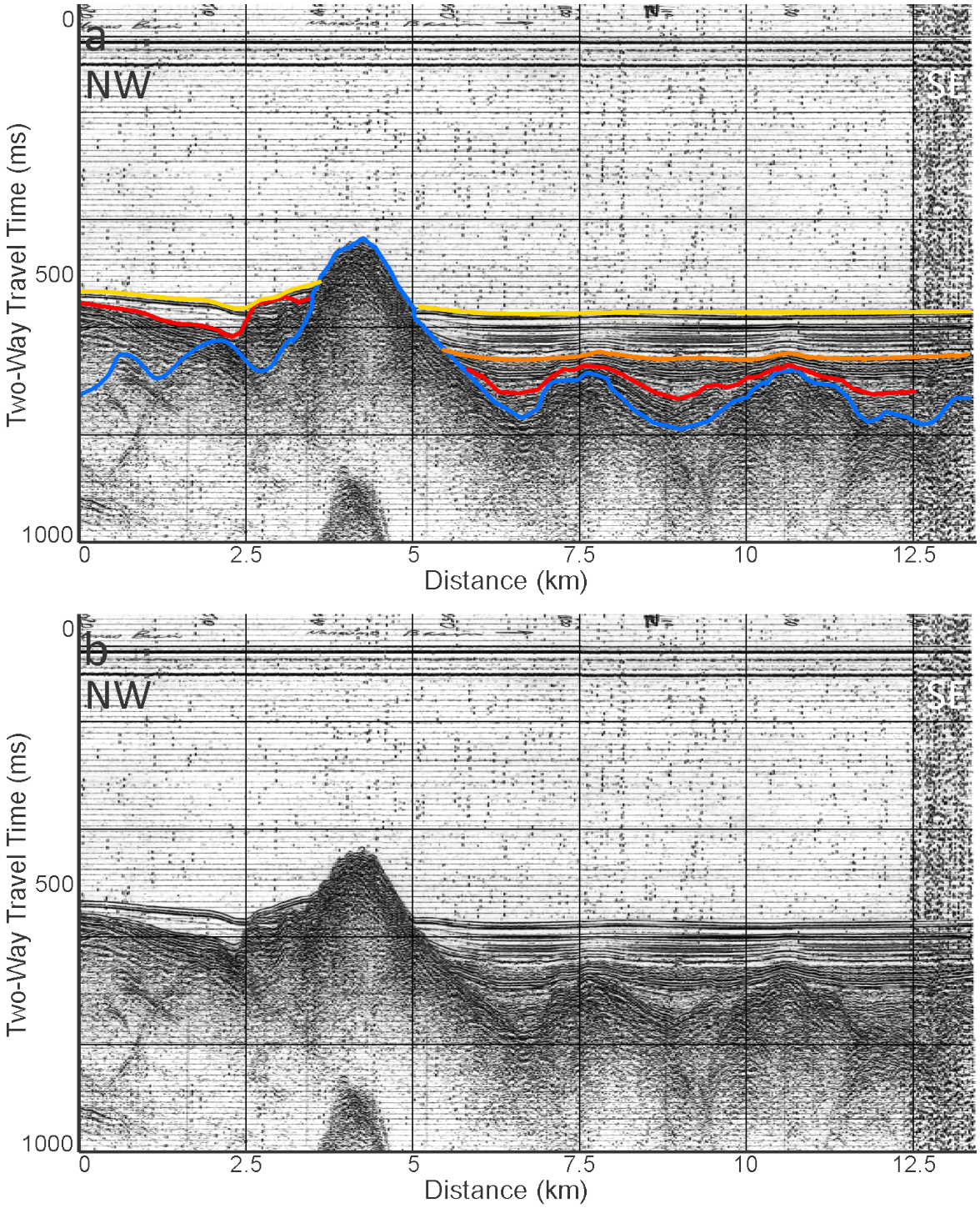


Figure A.2.25: Line Gabriola (Part 1), cruise 82003PGC. Line has been cropped to match study area; full line extends further northwest.

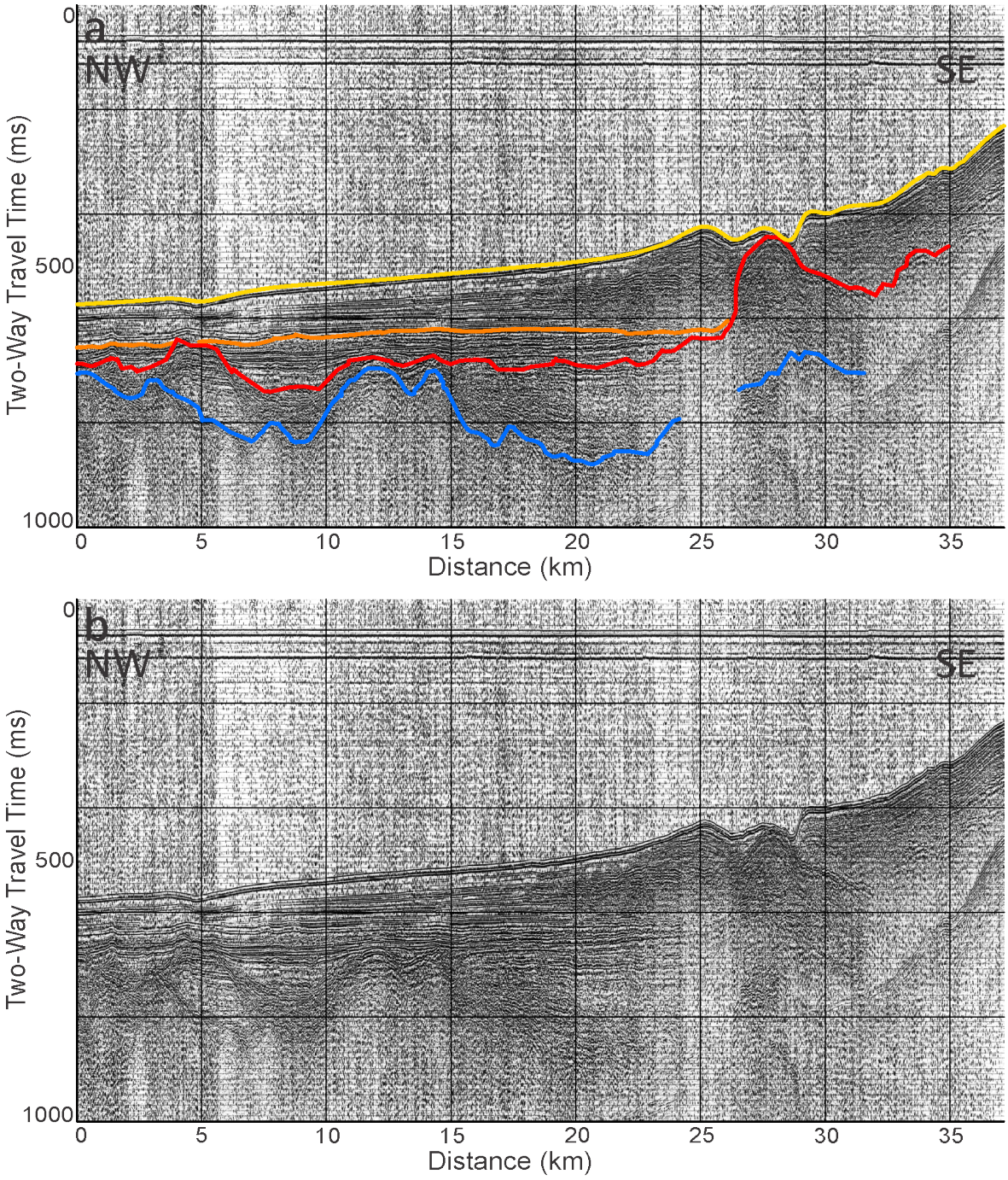


Figure A.2.26: Line Gabriola (Part 2), cruise 82003PGC

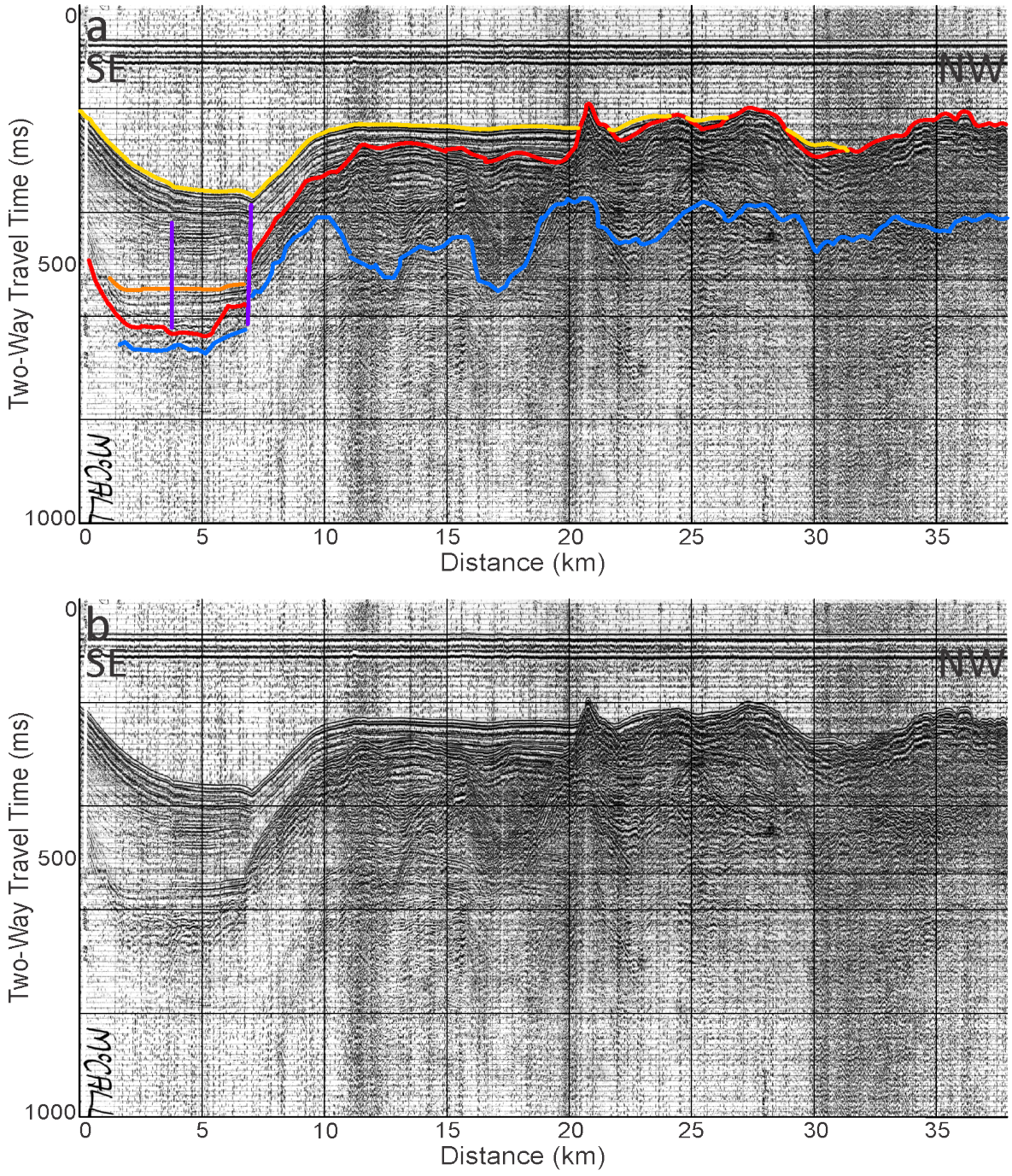


Figure A.2.27: Line McCall, cruise 82003PGC

A.2.2 Cruise ID 86008PGC

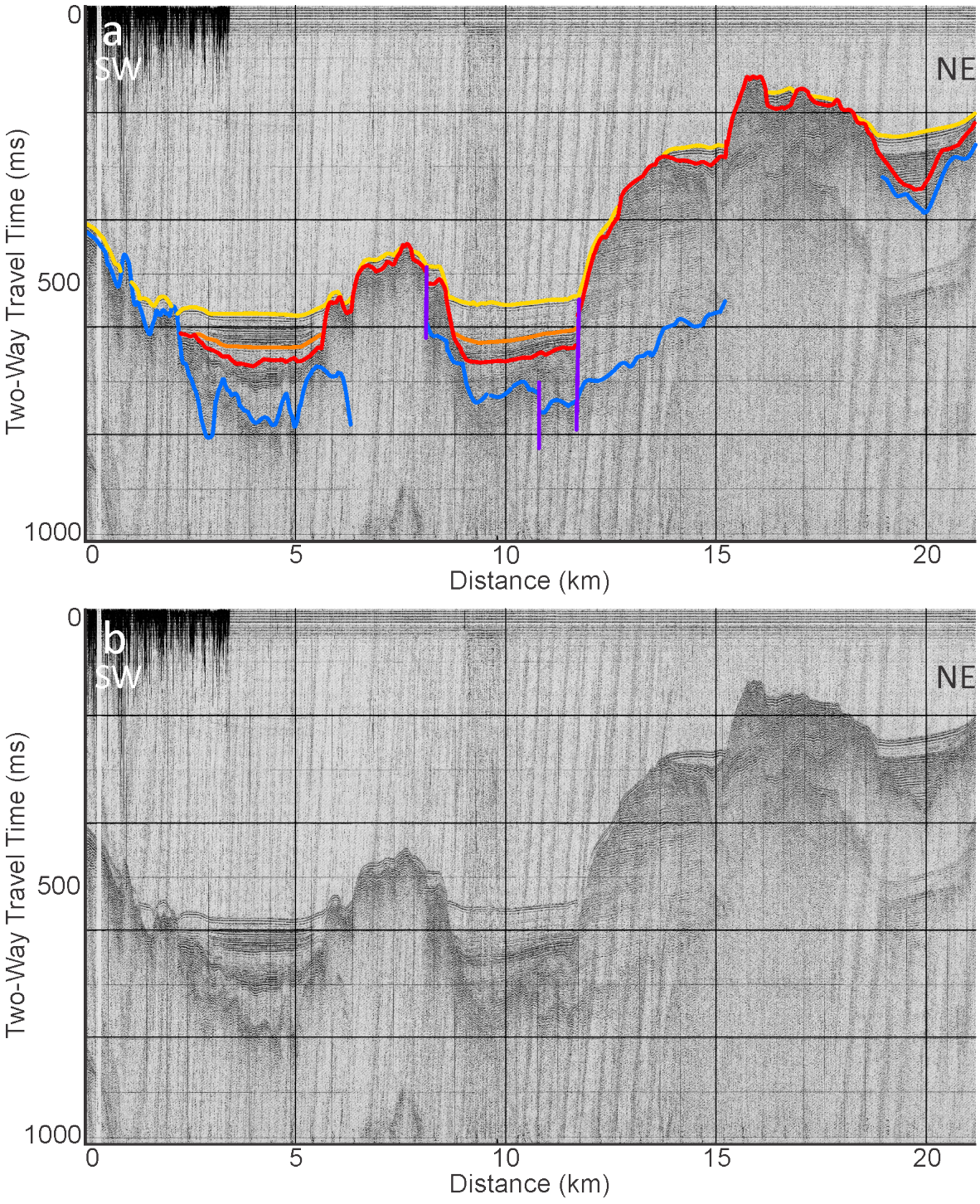


Figure A.2.28: Line 25, cruise 86008PGC

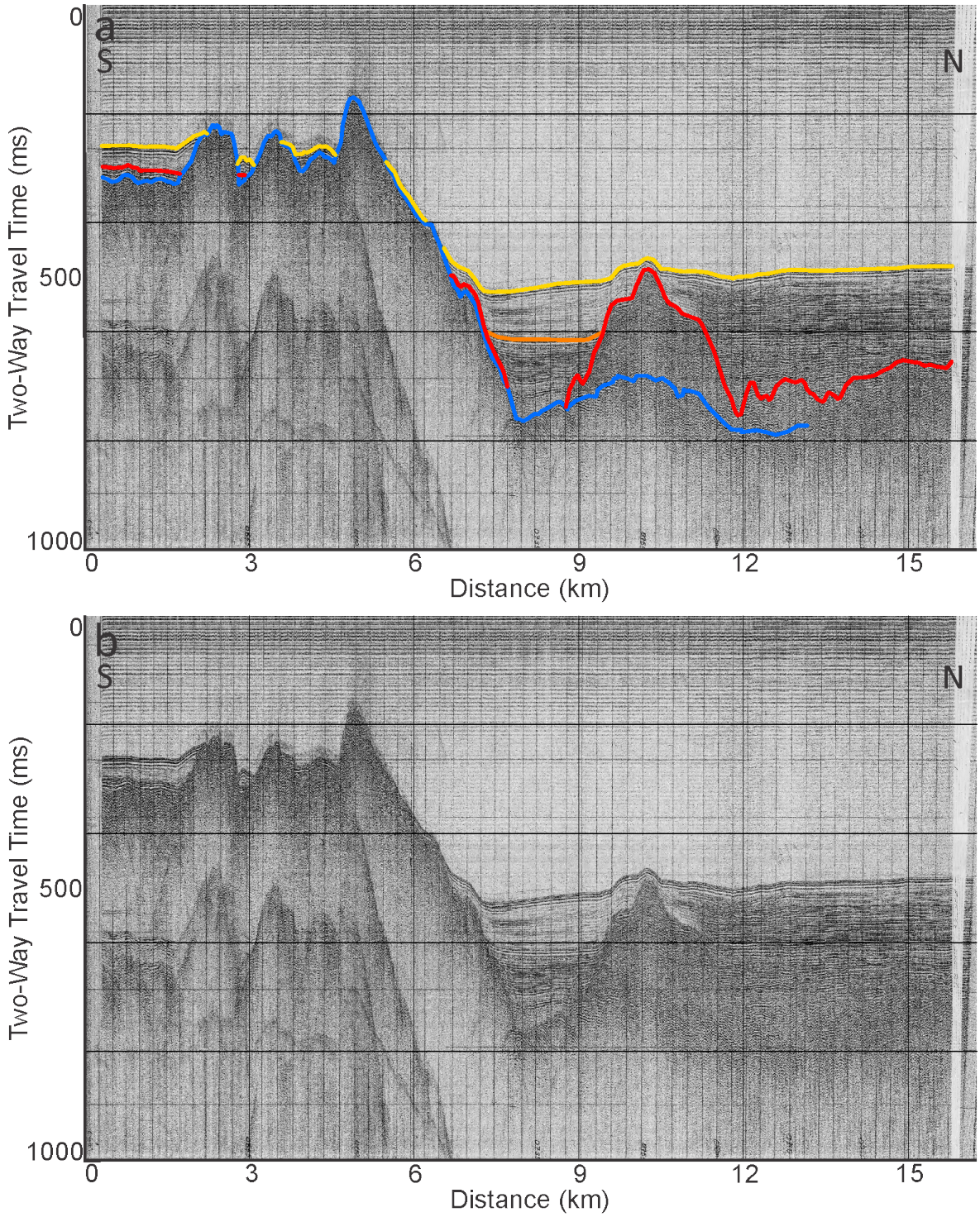


Figure A.2.29: Line 36, cruise 86008PGC

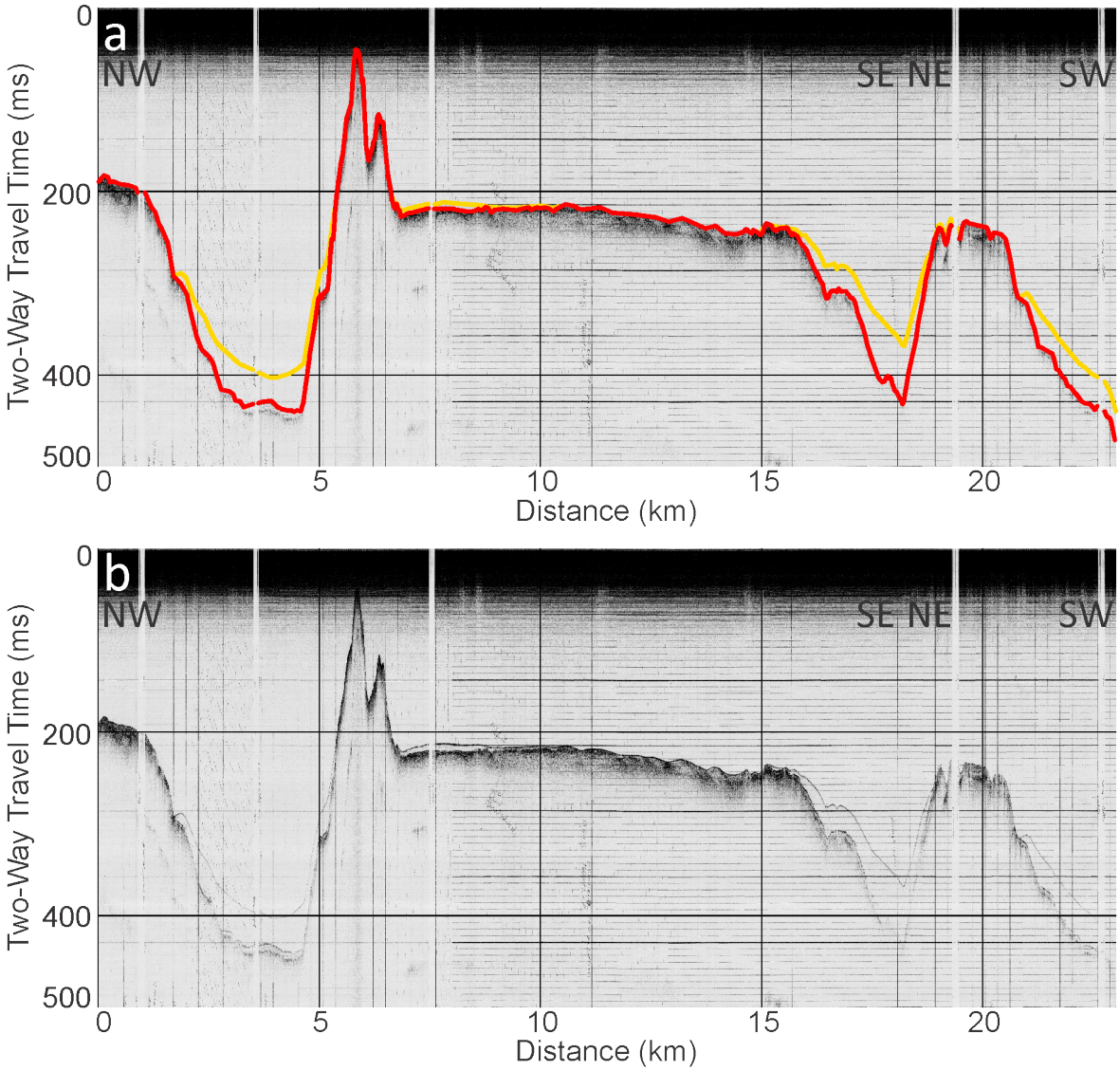


Figure A.2.30: Lines 41-49 (Part 1), cruise 86008PGC

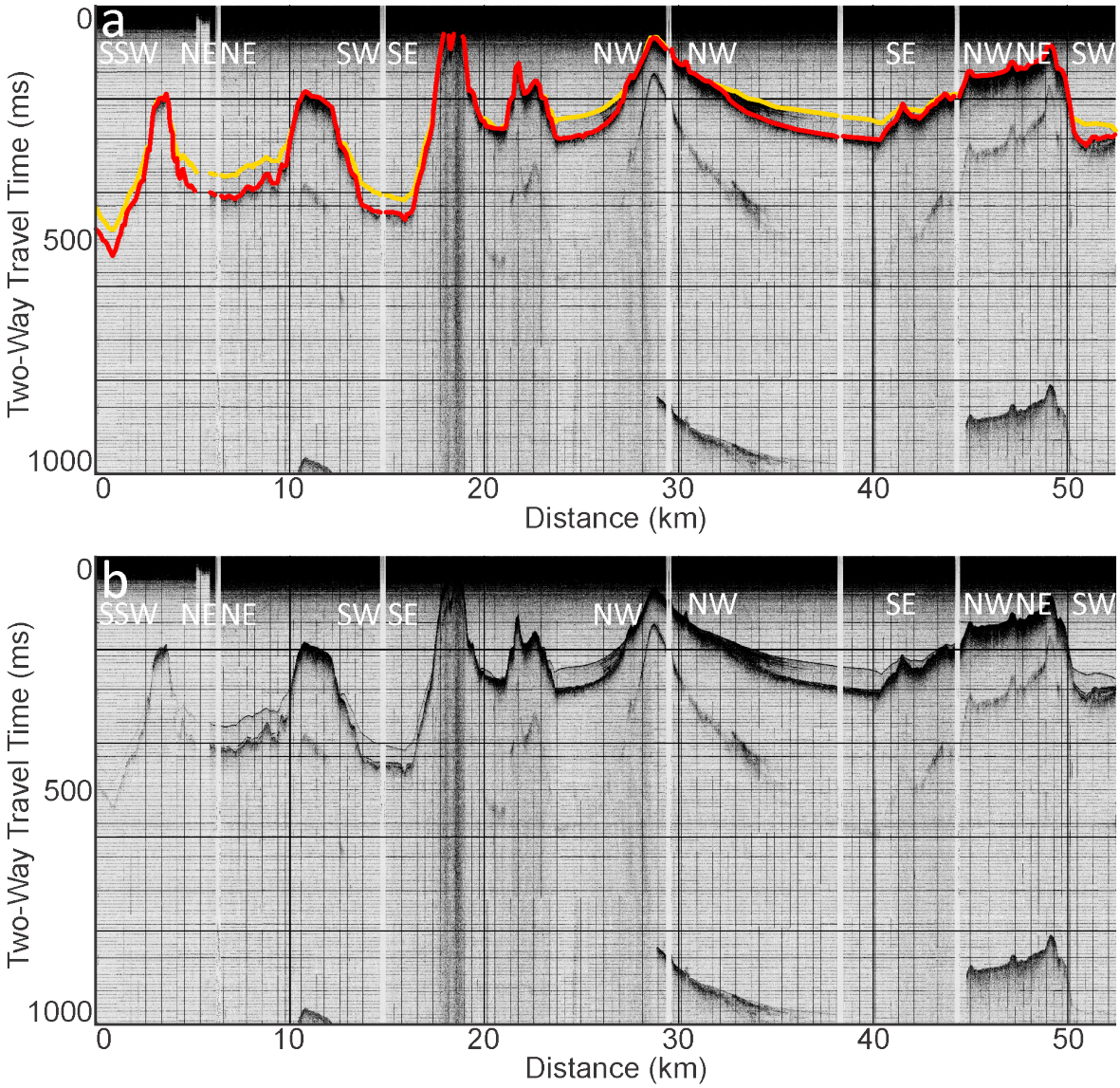


Figure A.2.31: Lines 41-49 (Part 2), cruise 86008PGC

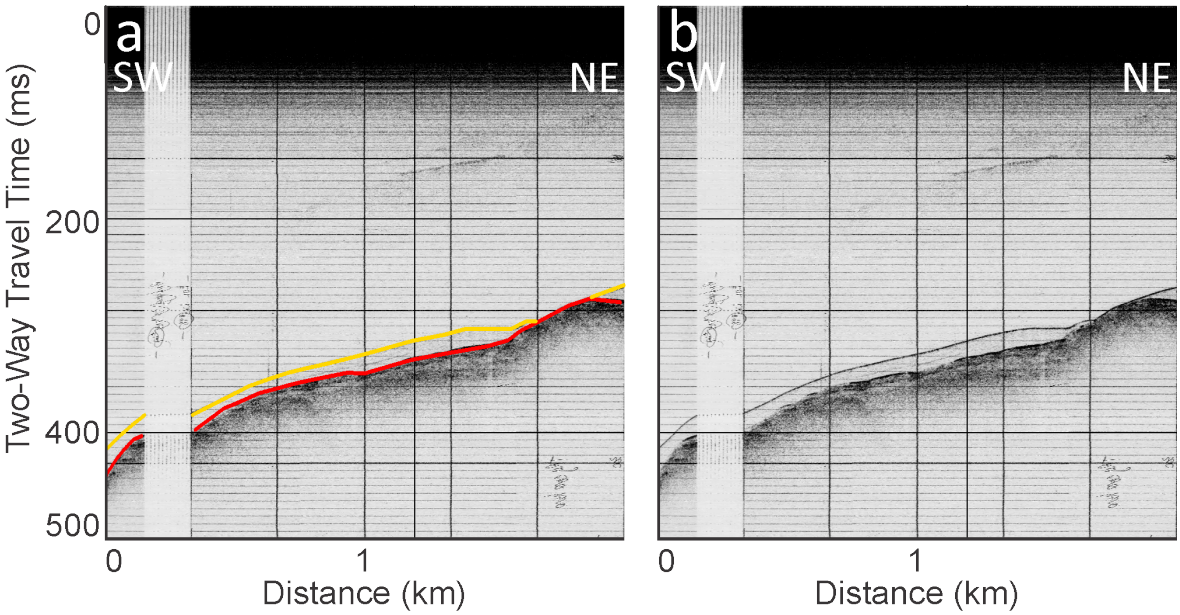


Figure A.2.32: Lines 41-49 (Part 3), cruise 86008PGC

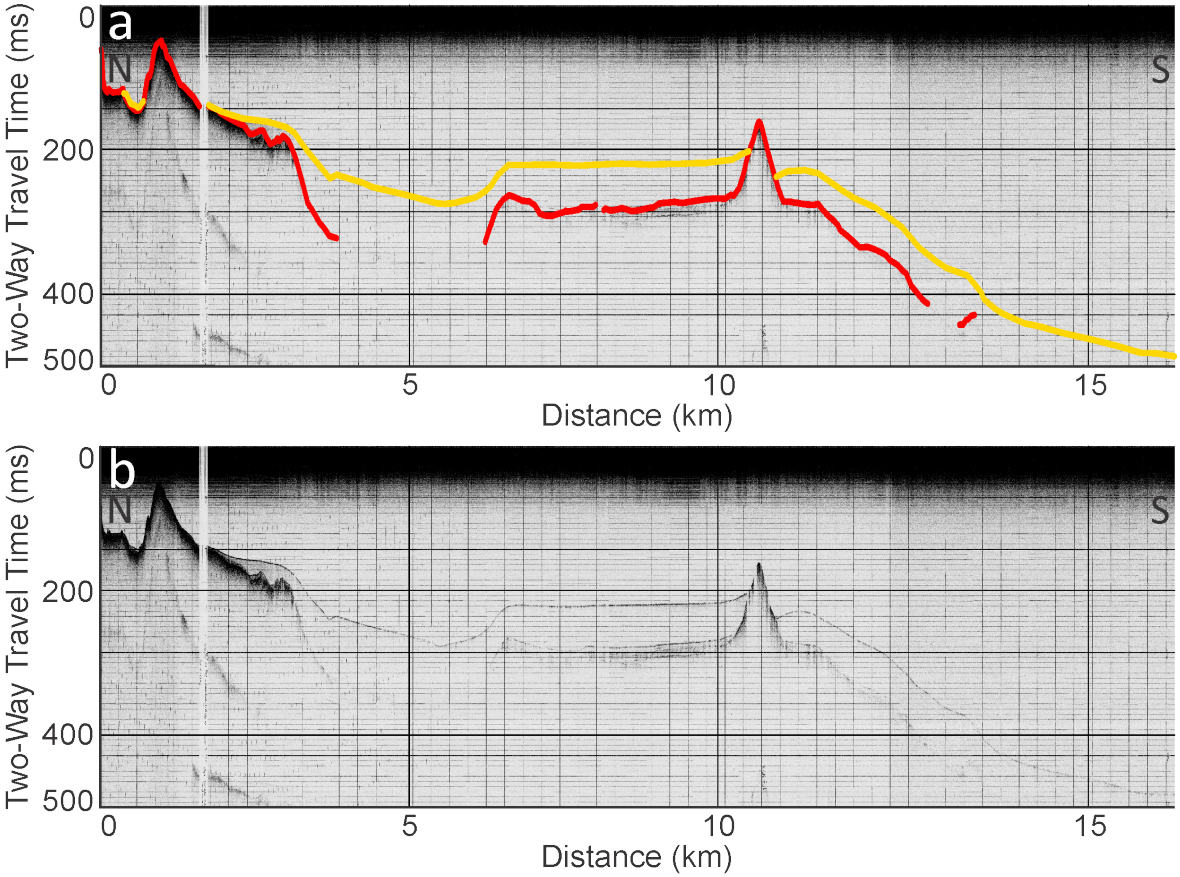


Figure A.2.33: Lines 41-49 (Part 4), cruise 86008PGC

A.2.3 Cruise ID 89010PGC

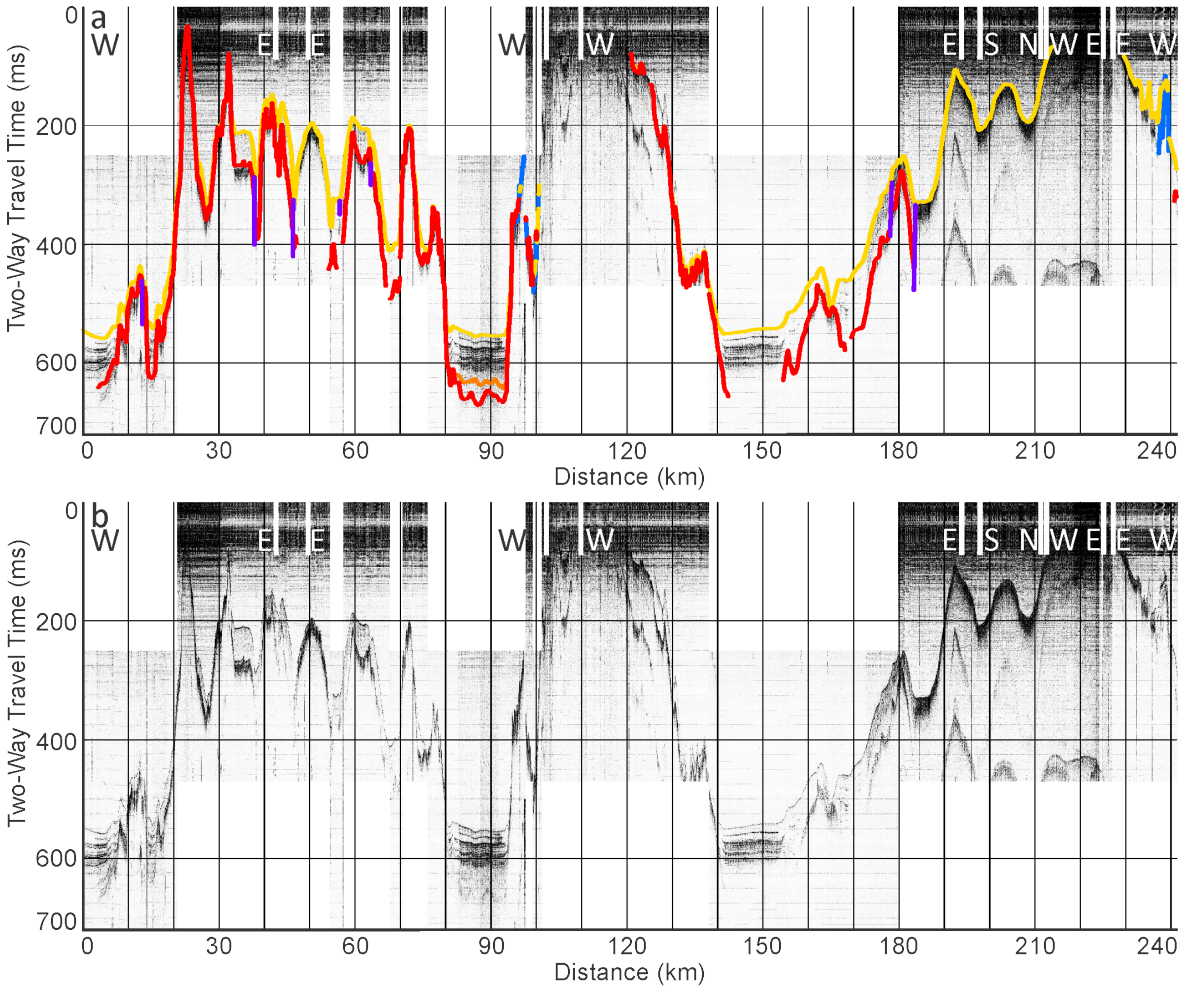


Figure A.2.34: Profile 151-743 (Section 1), cruise 89010PGC. Profile cropped to study area; full profile originates in the Strait of Georgia (Section 1), extends into Howe Sound, returns to the central Strait of Georgia (subsequent figure; Section 2), and continues further south.Thick vertical lines along top of profile indicate locations of turns and transits between straight sections.

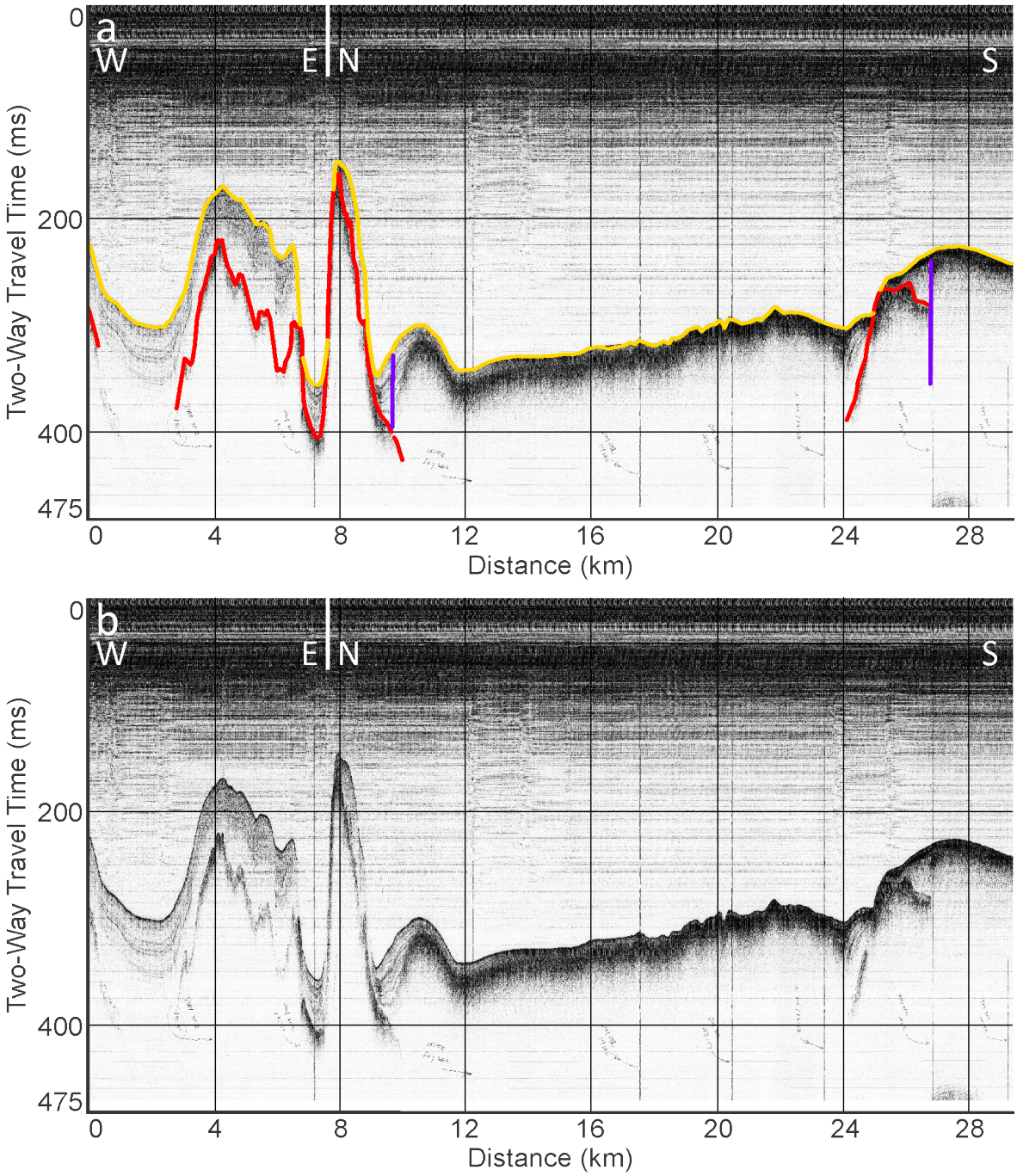


Figure A.2.35: Line 151-743 (Section 2), cruise 89010PGC. Profile cropped to study area; full profile originates in the Strait of Georgia (previous figure; Section 1), extends into Howe Sound, returns to the central Strait of Georgia (Section 2), and continues further south. Thick vertical lines along top of profile indicate locations of turns and transits between straight sections.

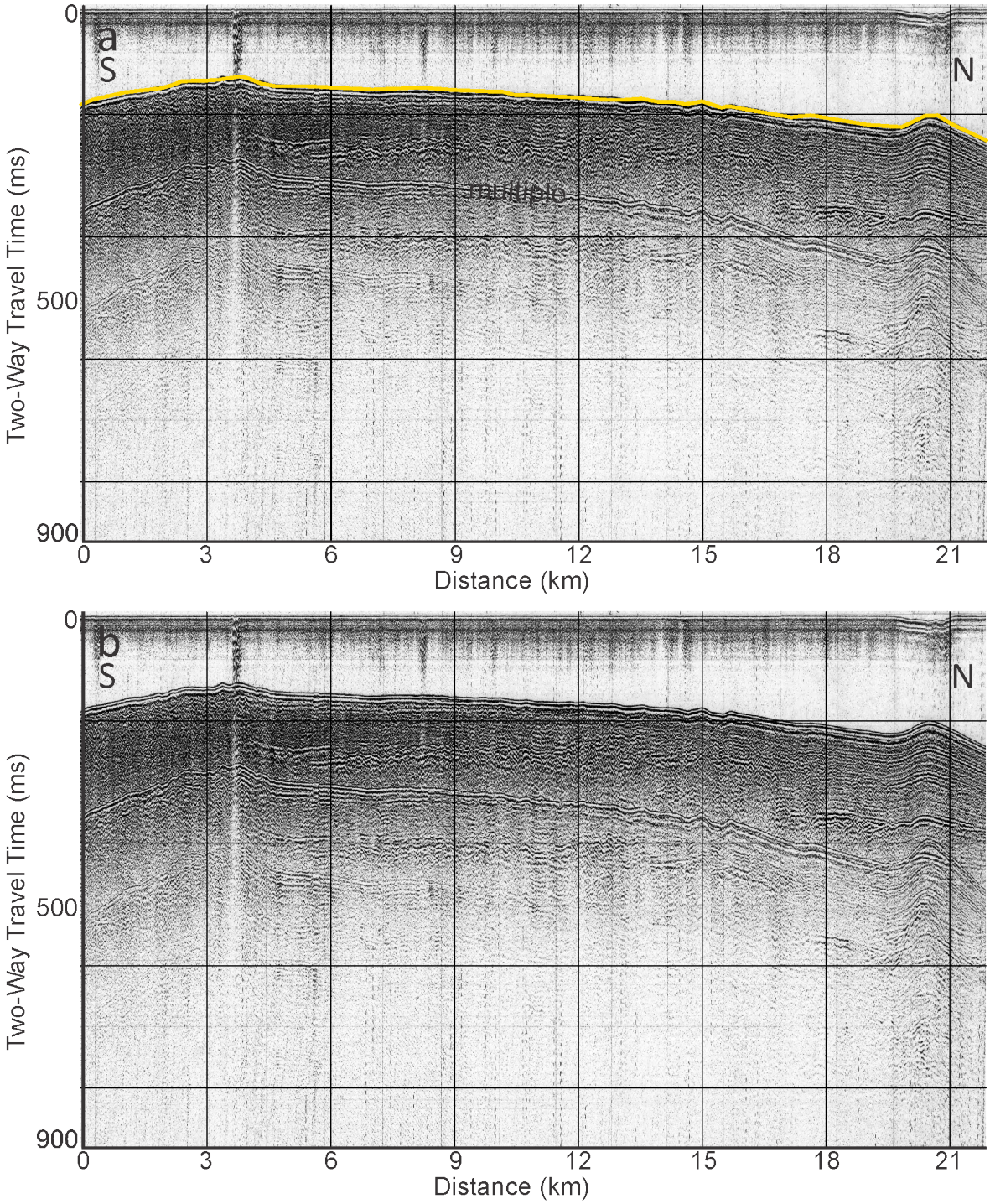


Figure A.2.36: Line 126, cruise 89010PGC. Line located along Fraser River delta slope; Reflector truncations and discontinuities are interpreted as heavily reworked delta sediments. Profile is cropped to study area; full profile extends further south.

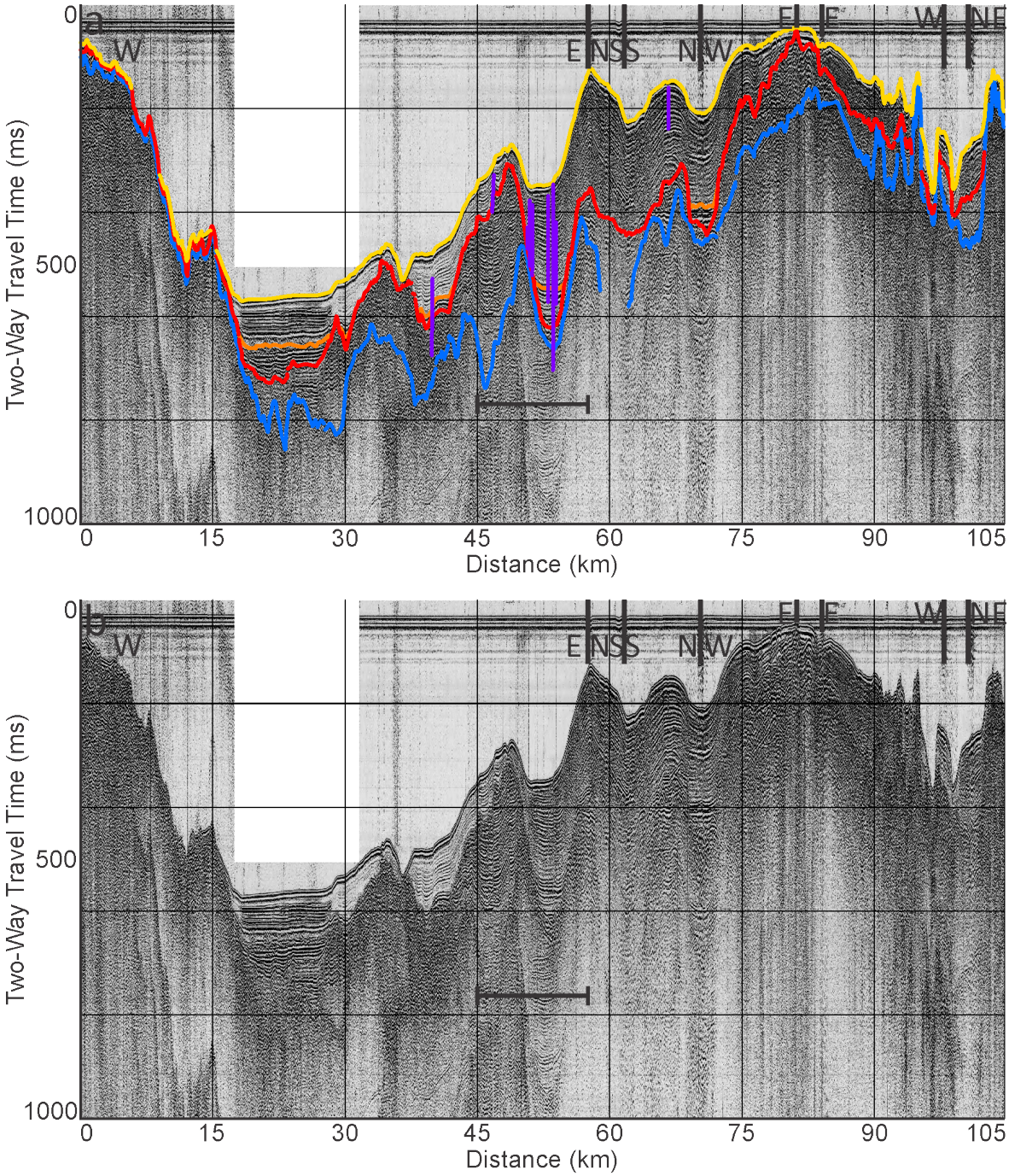


Figure A.2.37: Line 207, cruise 89010PGC. Thick vertical lines along top of profile indicate locations of line turns and transits between straight sections. Black horizontal double-ended line indicates the extent of detailed profile shown in Figure A.2.38. Profile is cropped to study area; full profile extends NE into Howe Sound.

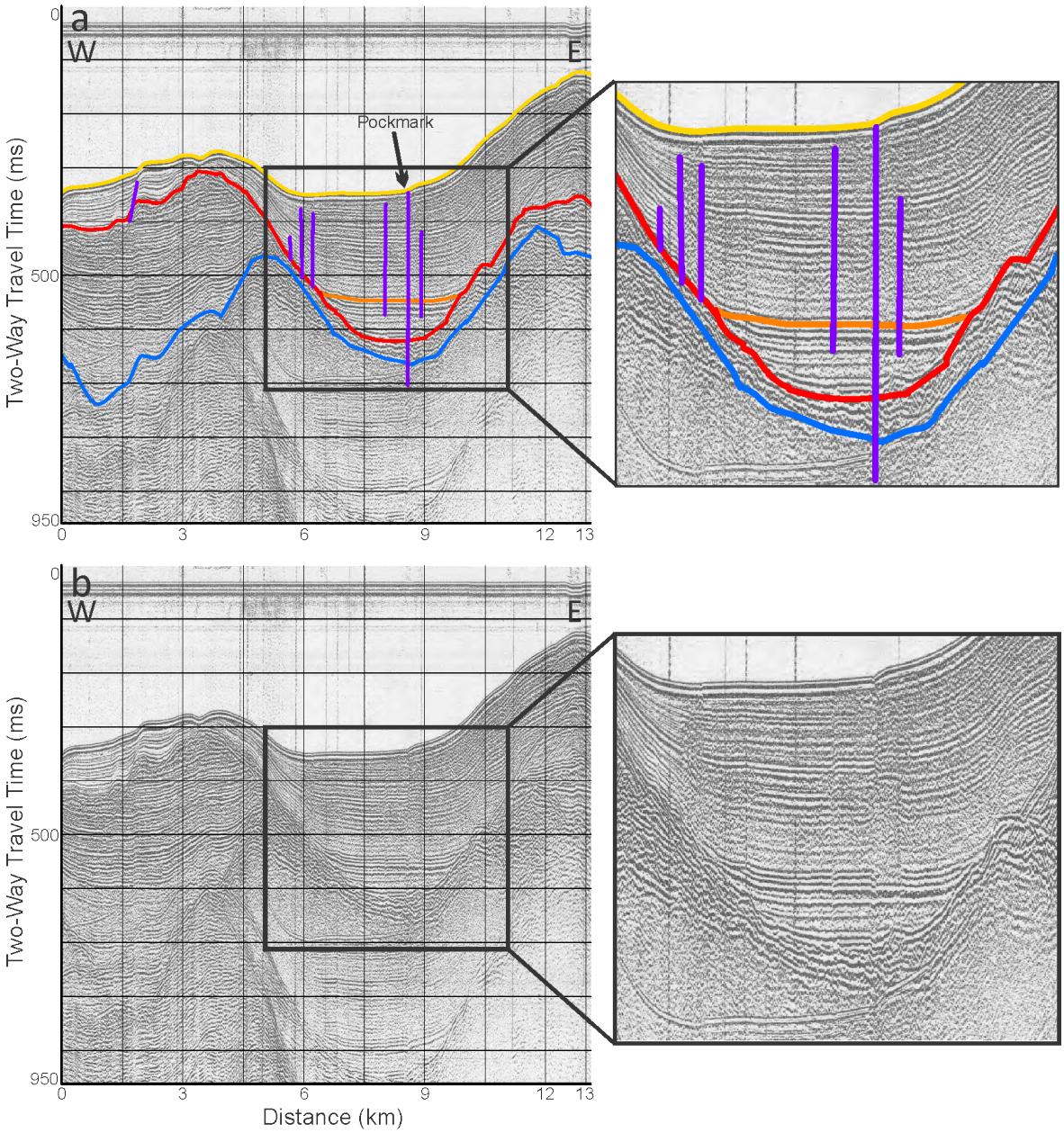


Figure A.2.38: Magnified profile of line 207, cruise 89010PGC

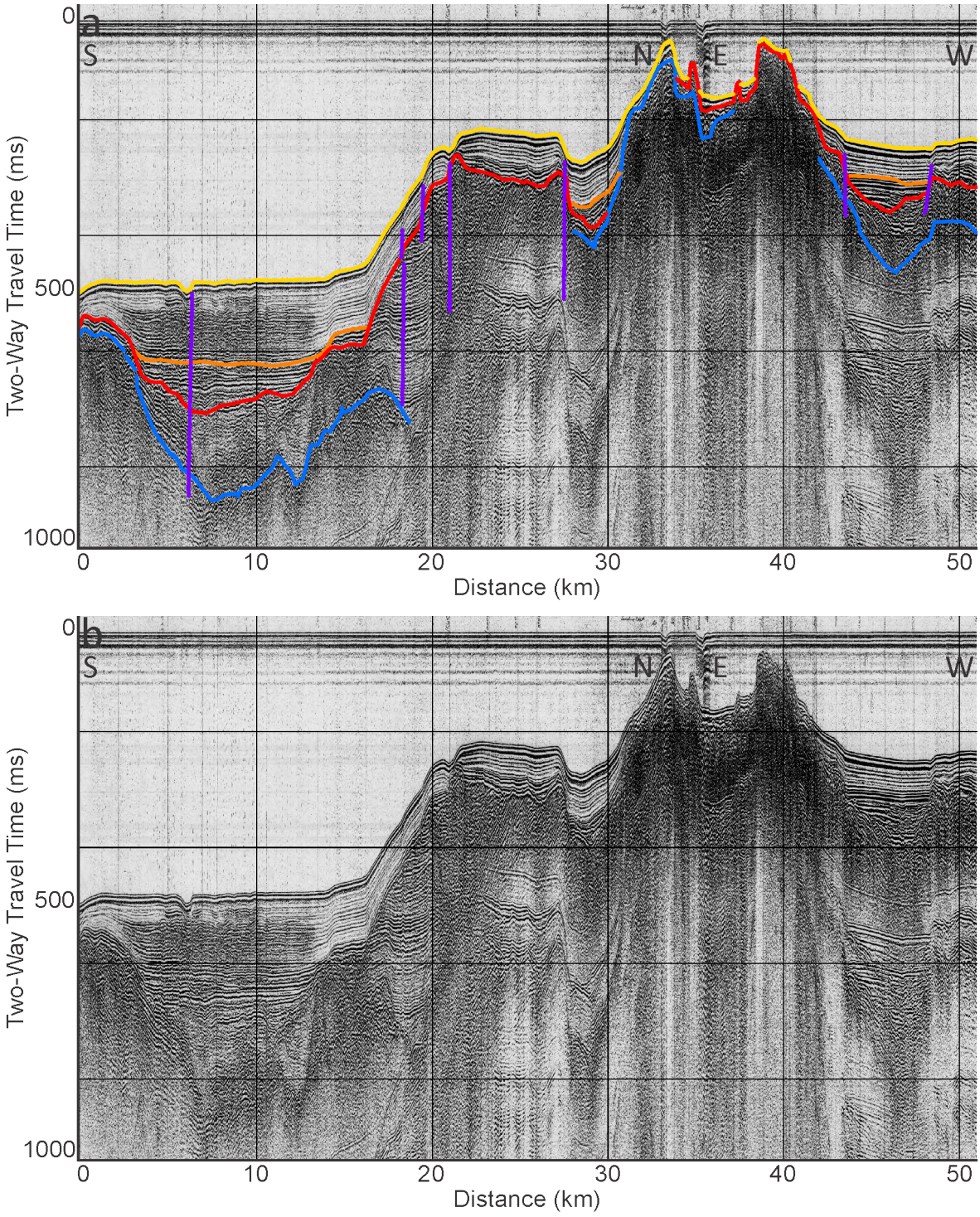


Figure A.2.39: Line 221, cruise 89010PGC. Profile is cropped to study area; full profile continues further south and further west.

A.2.4 Cruise ID 91004PGC

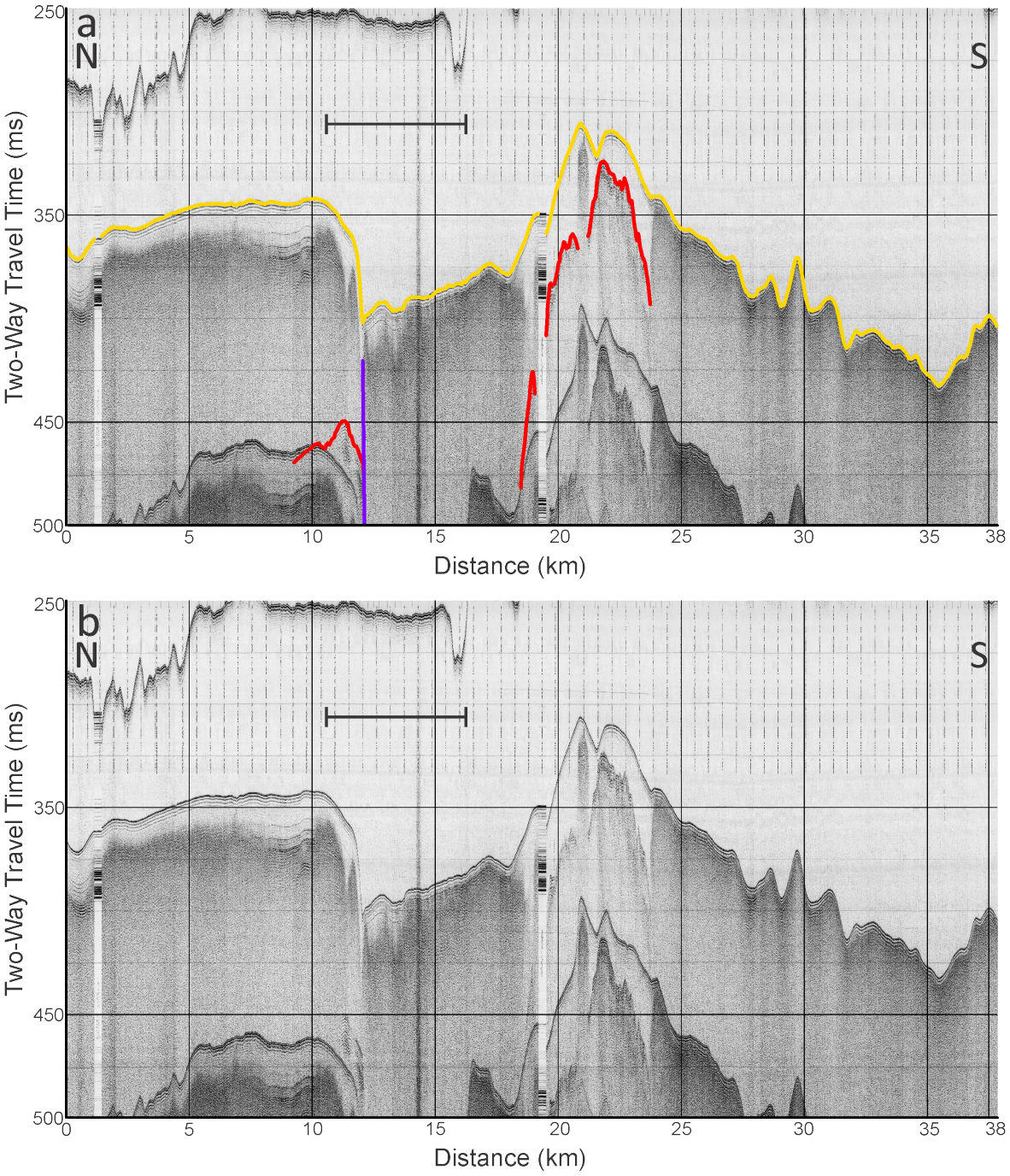


Figure A.2.40: Line A5-B7, cruise 91004PGC. Line is cropped to study area; full line extends further south. Black line indicates the extent of detailed profile shown in Figure A.2.42

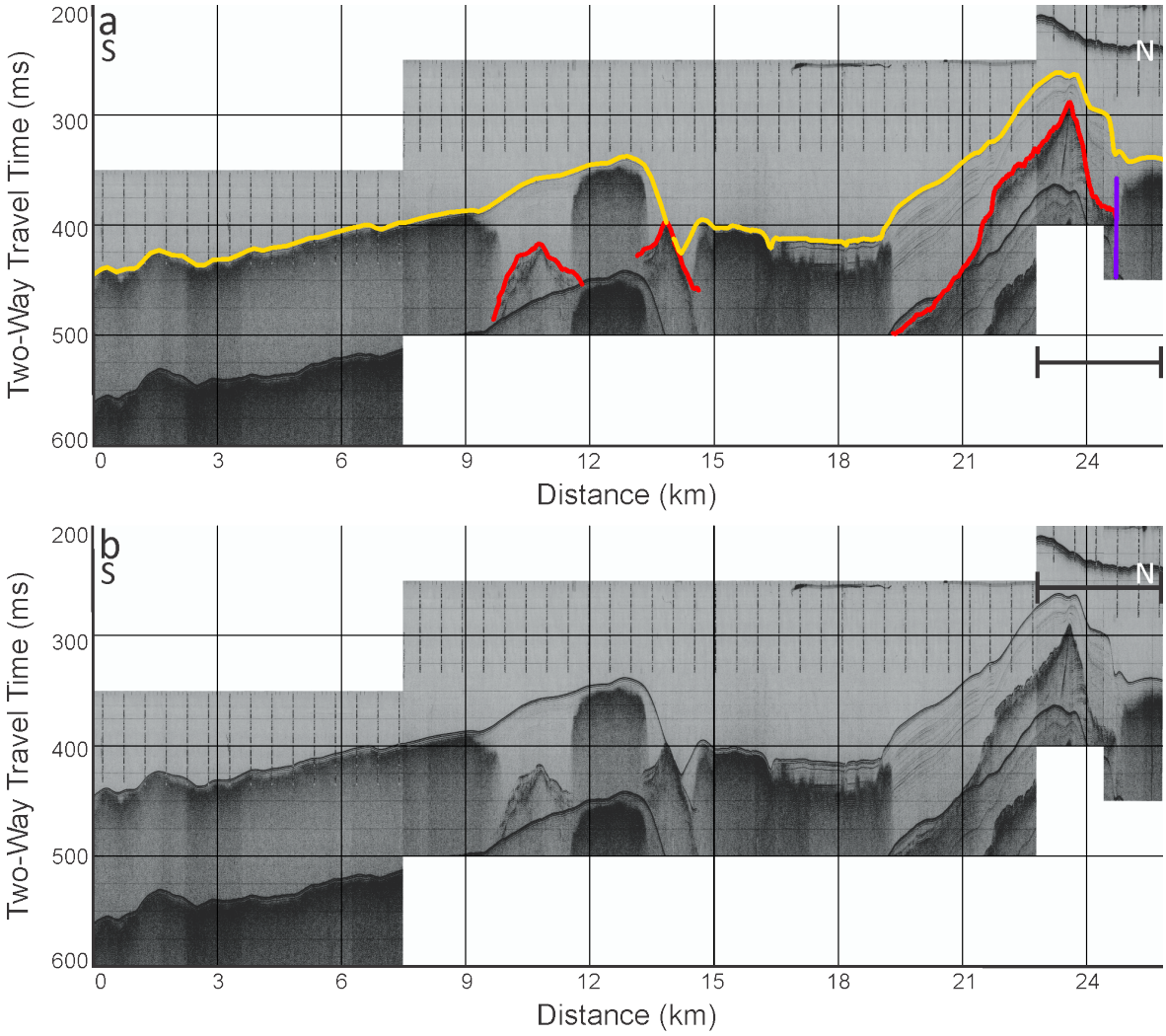


Figure A.2.41: Line A7-B8, cruise 91004PGC. Line is cropped to study area; full line extends further south. Black line indicates the extent of detailed profile shown in Figure A.2.43

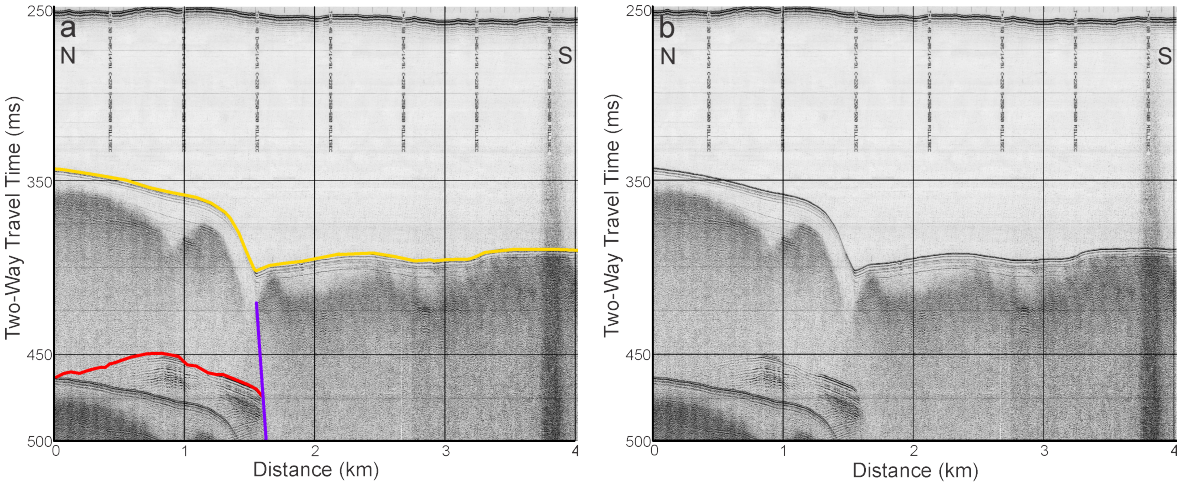


Figure A.2.42: Magnified profile of line A5-B7, cruise 91004PGC

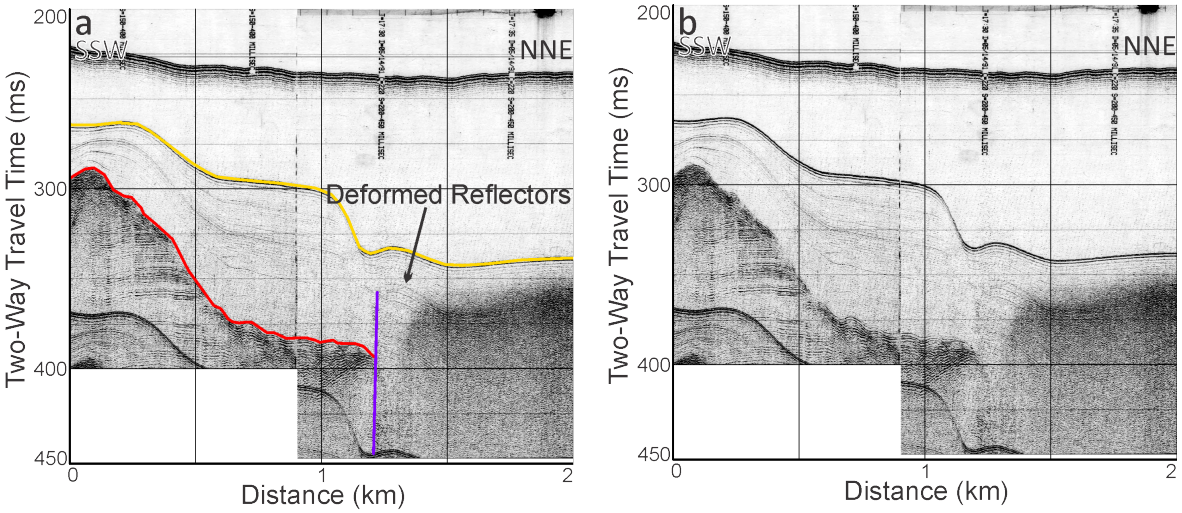


Figure A.2.43: Magnified profile of line A7-B8, cruise 91004PGC

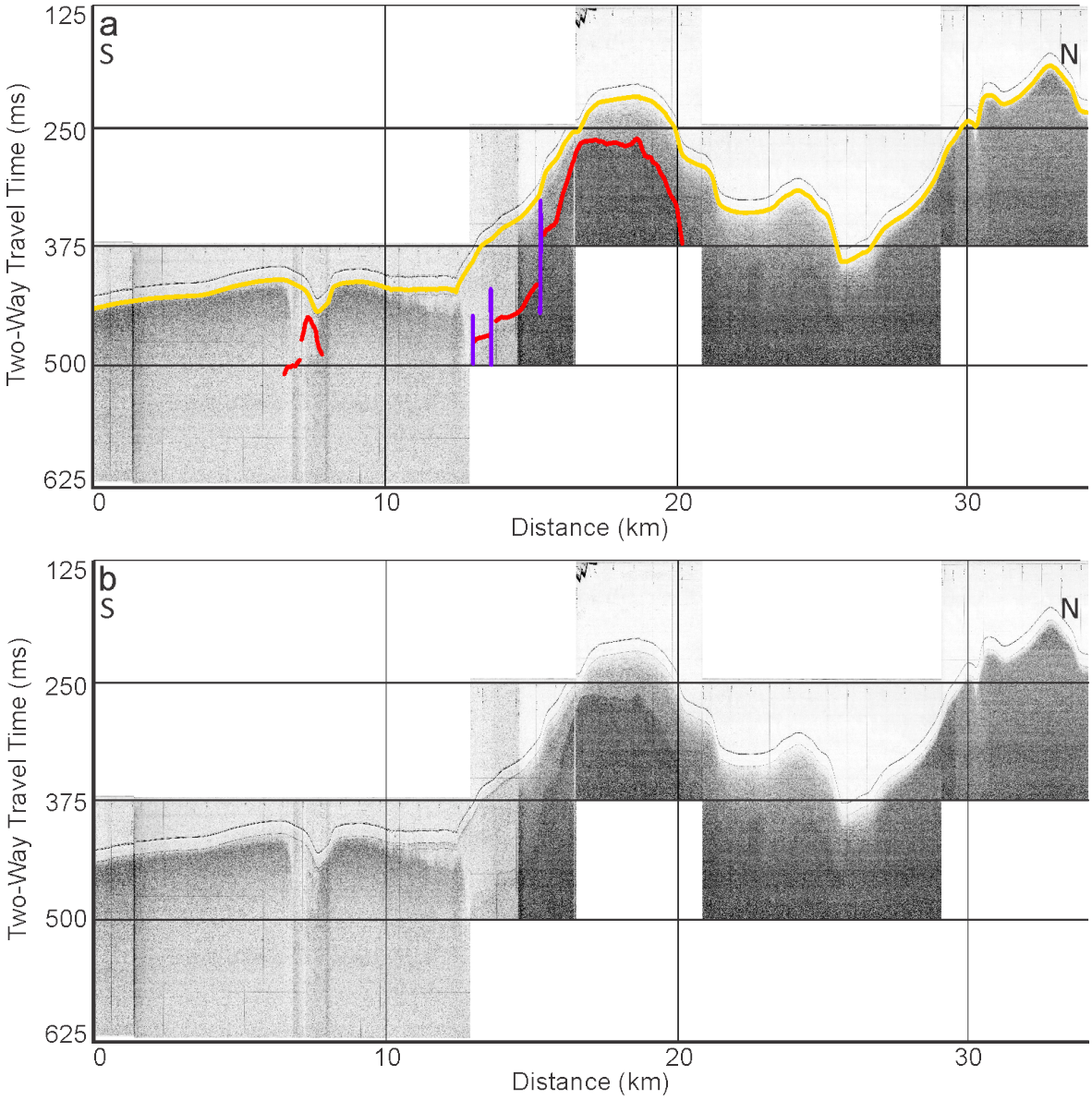


Figure A.2.44: Line A8-B11, cruise 91004PGC. Line is cropped to study area; full profile extends further south. Excluded from results due to discrepancies between the seafloor reflector in profile and seafloor relief in MBES data, suspected navigation and/or georeferencing errors.

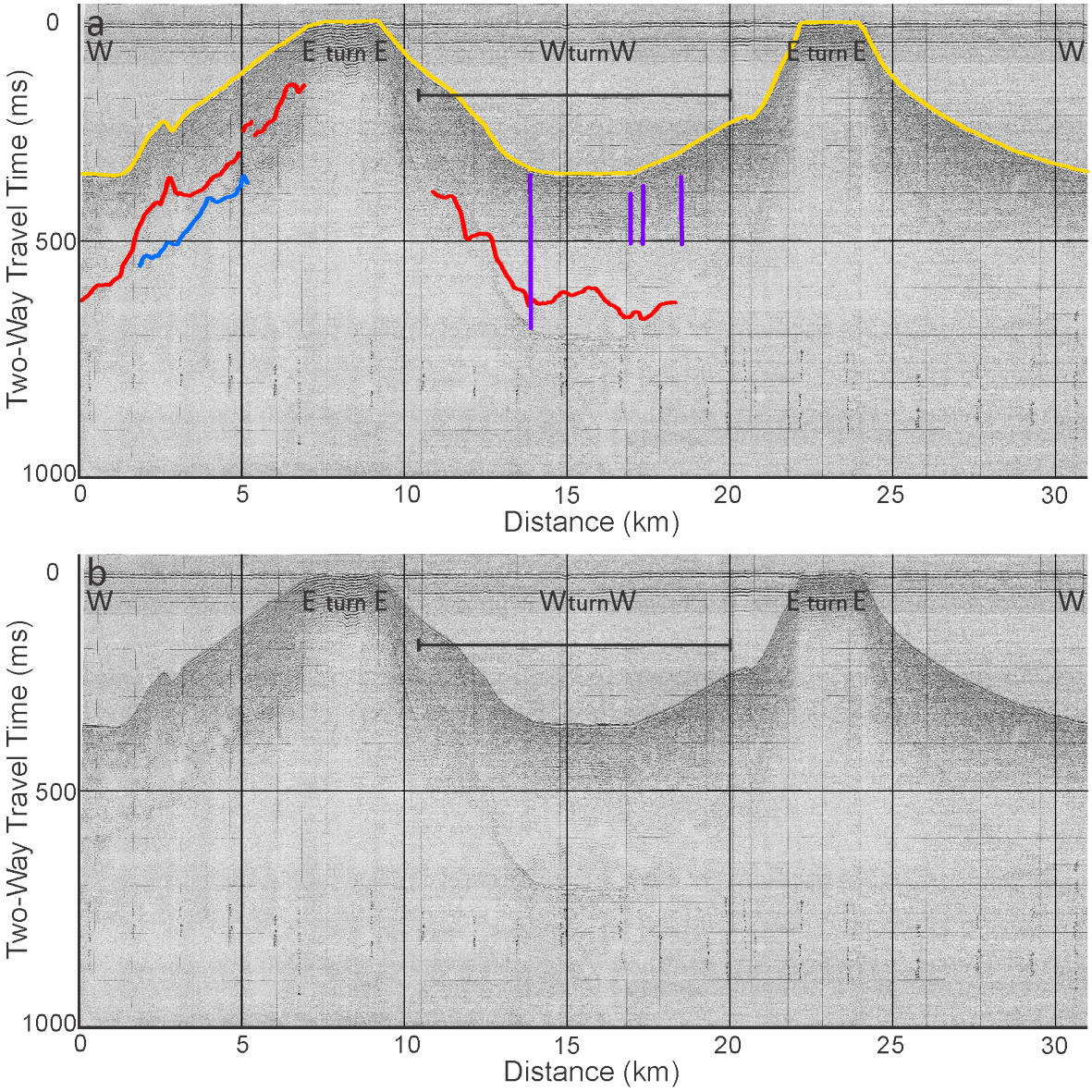


Figure A.2.45: Lines 470, 471, 472, and 473, cruise 91008PGC. Black line indicates the extent of detailed profile shown in subsequent figure.

A.2.5 Cruise ID 91008PGC

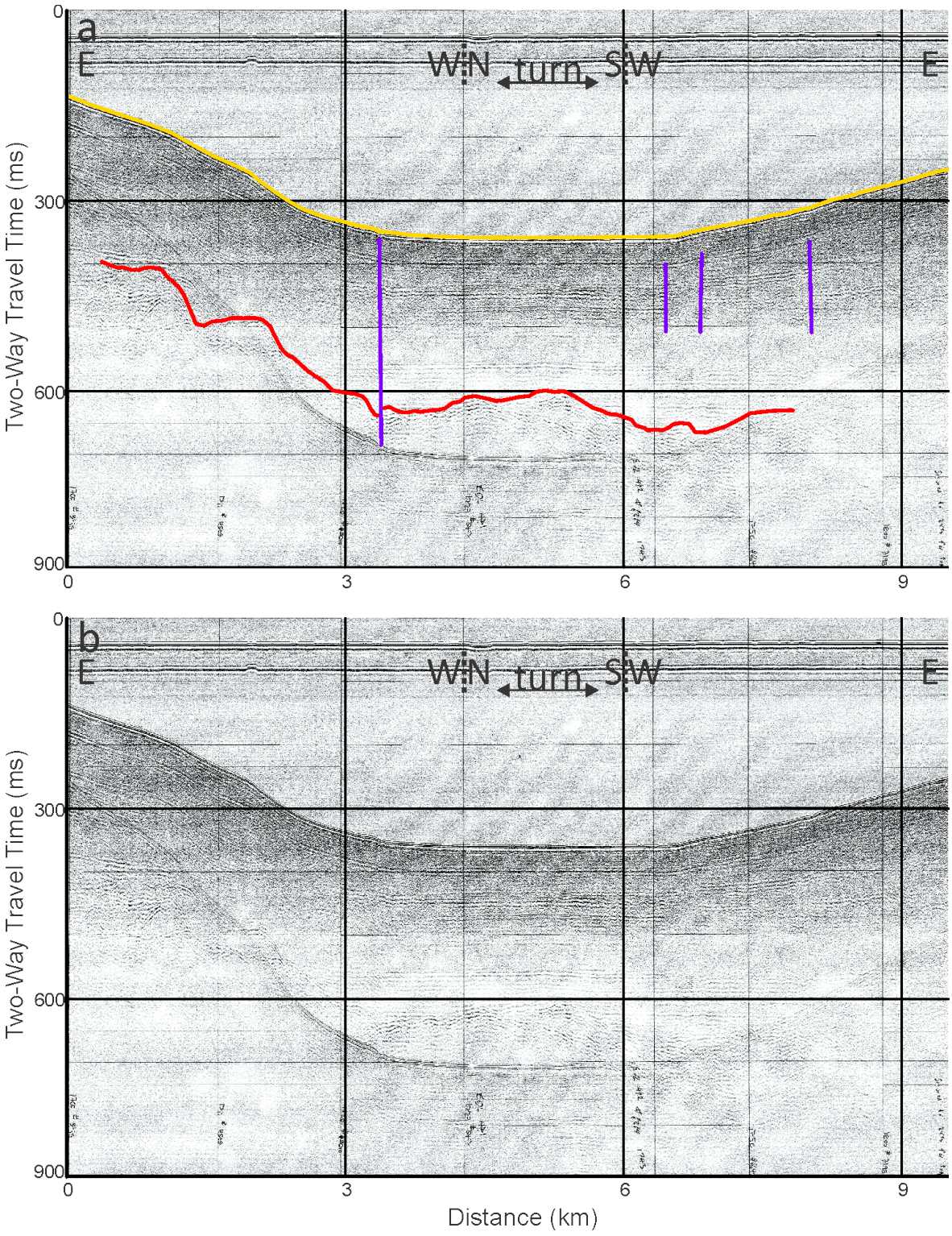


Figure A.2.46: Magnified profile of line 471, cruise 91008PGC

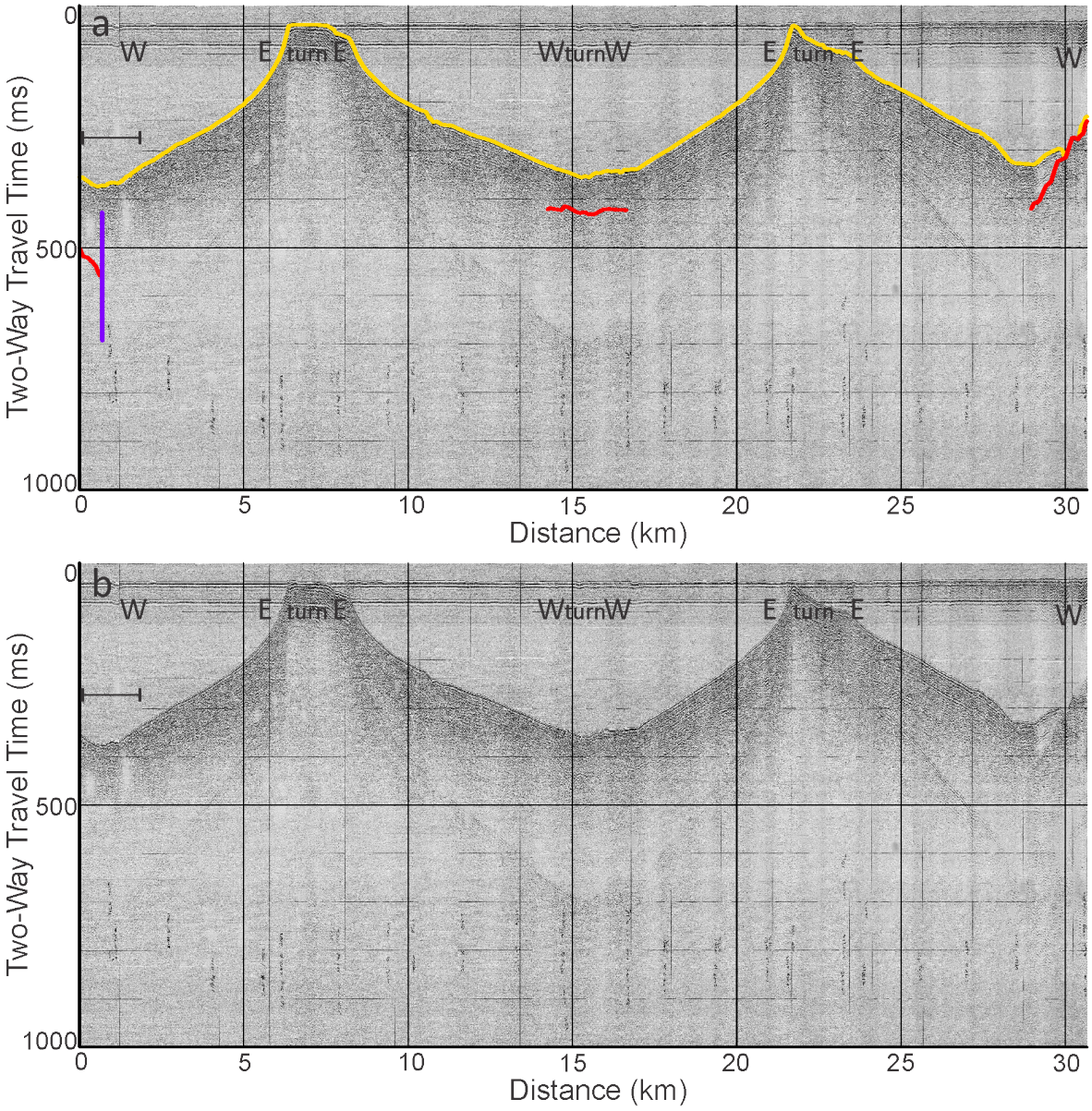


Figure A.2.47: Lines 474, 475, 476, and 477, cruise 91008PGC. Black line indicates the extent of detailed profile shown in subsequent figure.

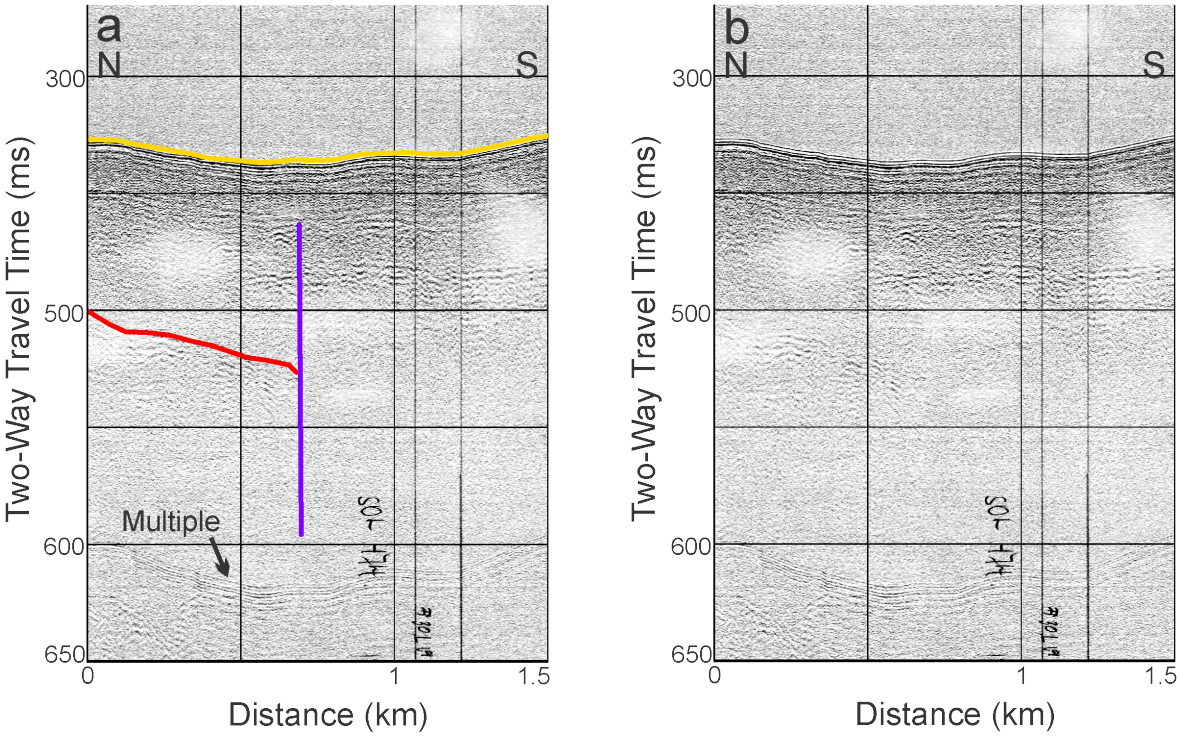


Figure A.2.48: Magnified profile of line 474, cruise 91008PGC

A.2.6 Cruise ID 95001PGC

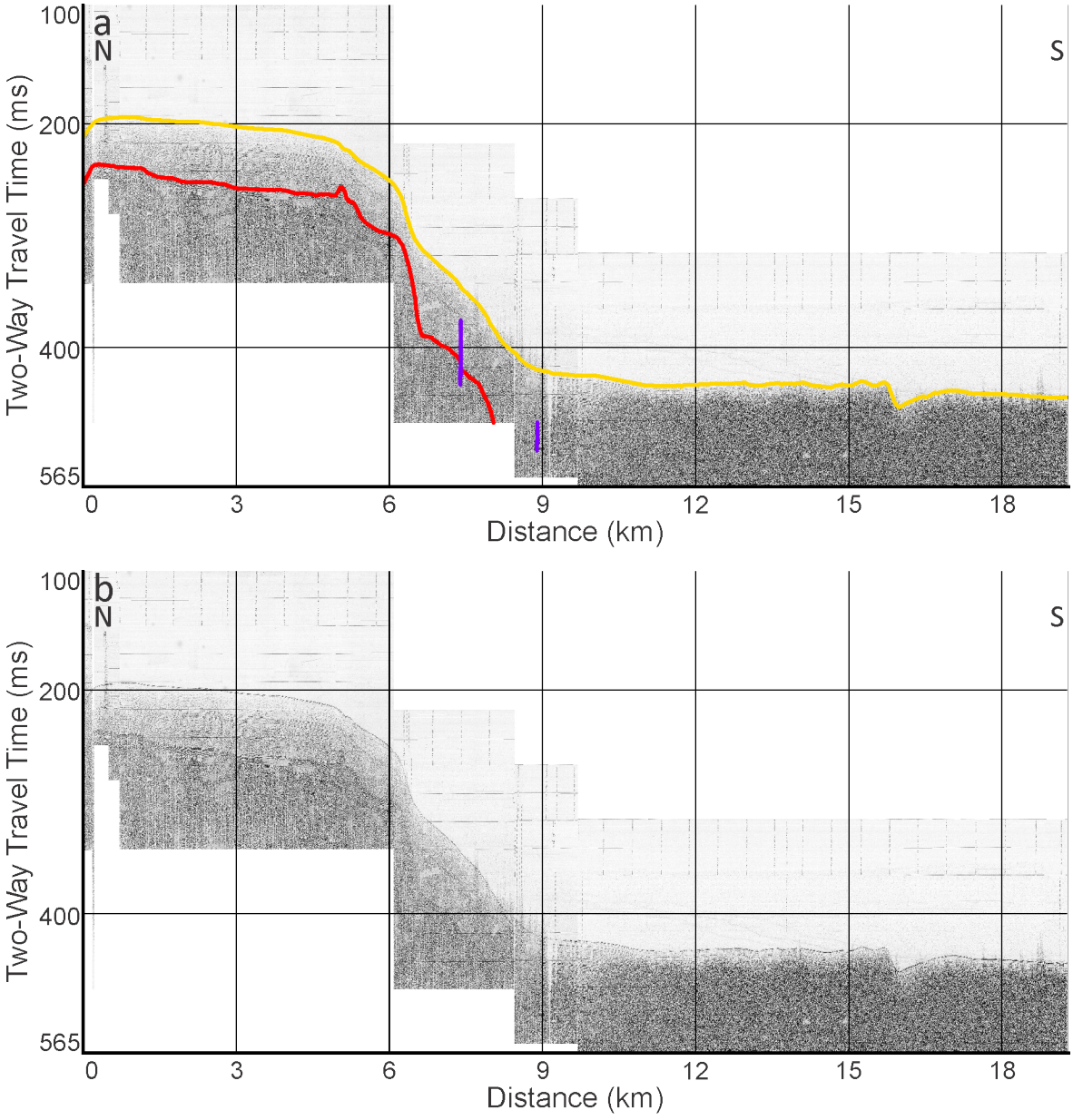


Figure A.2.49: Line 4b, cruise 95001PGC. Profile is cropped to study area; full profile extends further south.

A.2.7 Cruise ID 2002002PGC

The 2002002PGC dataset consists of 100 lines spaced 50 m apart, located over the linear pockmark chain and adjacent pockmark field (Riedel, 2002). Single-channel

airgun profiles and high-resolution DTS profiles (internal and external receivers) were collected in conjunction. Profiles include ship turns in their recording, and turns were always acquired in starboard turn mode to avoid contact between the systems (Riedel, 2002). Seismic equipment was stopped when marine mammals were observed within 100 m of the vessel or if marine mammals greater than 100 m away appeared disturbed. As a result, multiple lines have areas with missing data (Riedel, 2002). Within this appendix, lines 20 and 50a are excluded due to significant sections of missing data. For each system, every 5th line was examined, and every 10th line was worked up with interpretations, shown in the following figures.

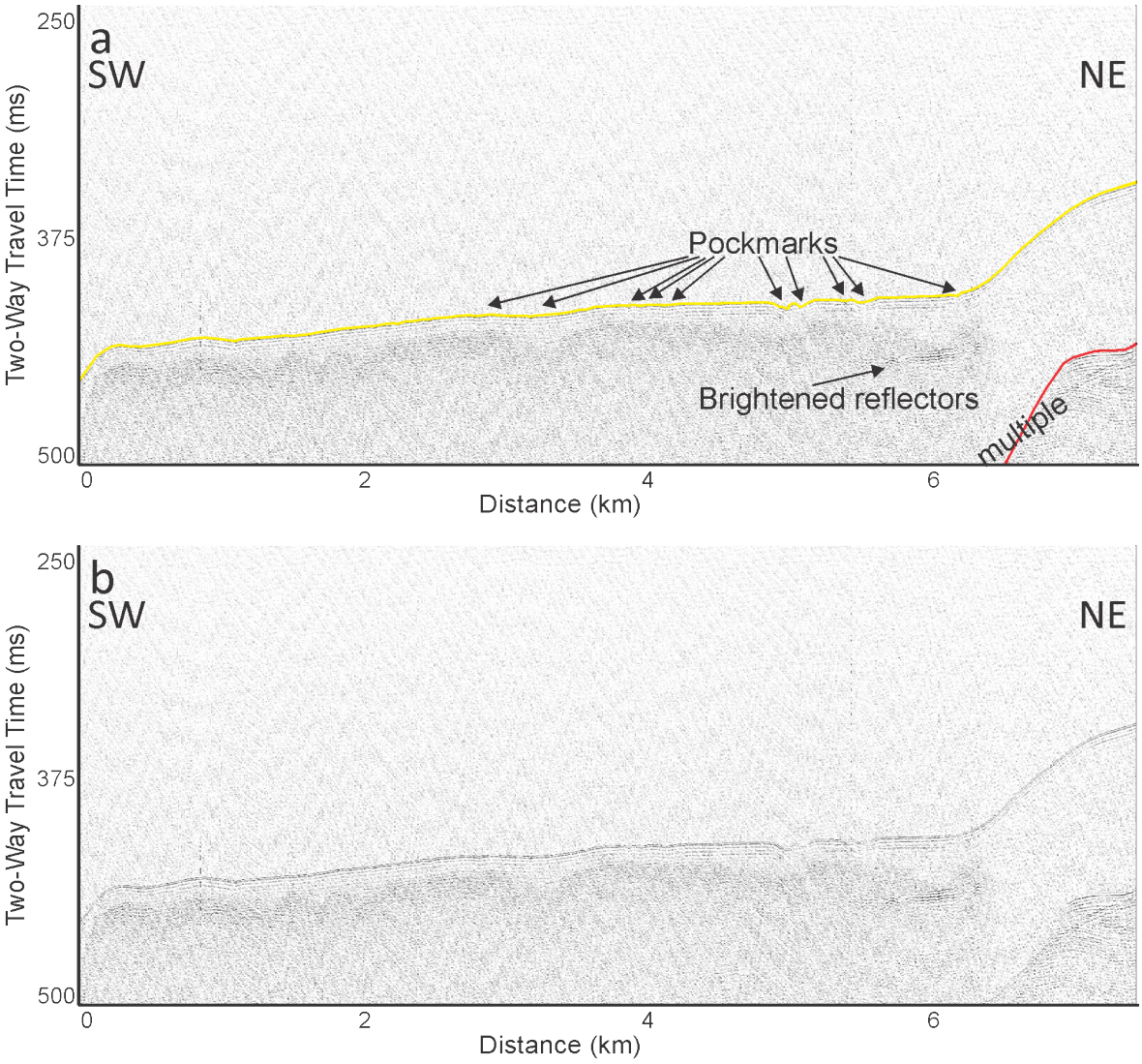


Figure A.2.50: Line 10 (Huntec DTS external), cruise 2002002PGC

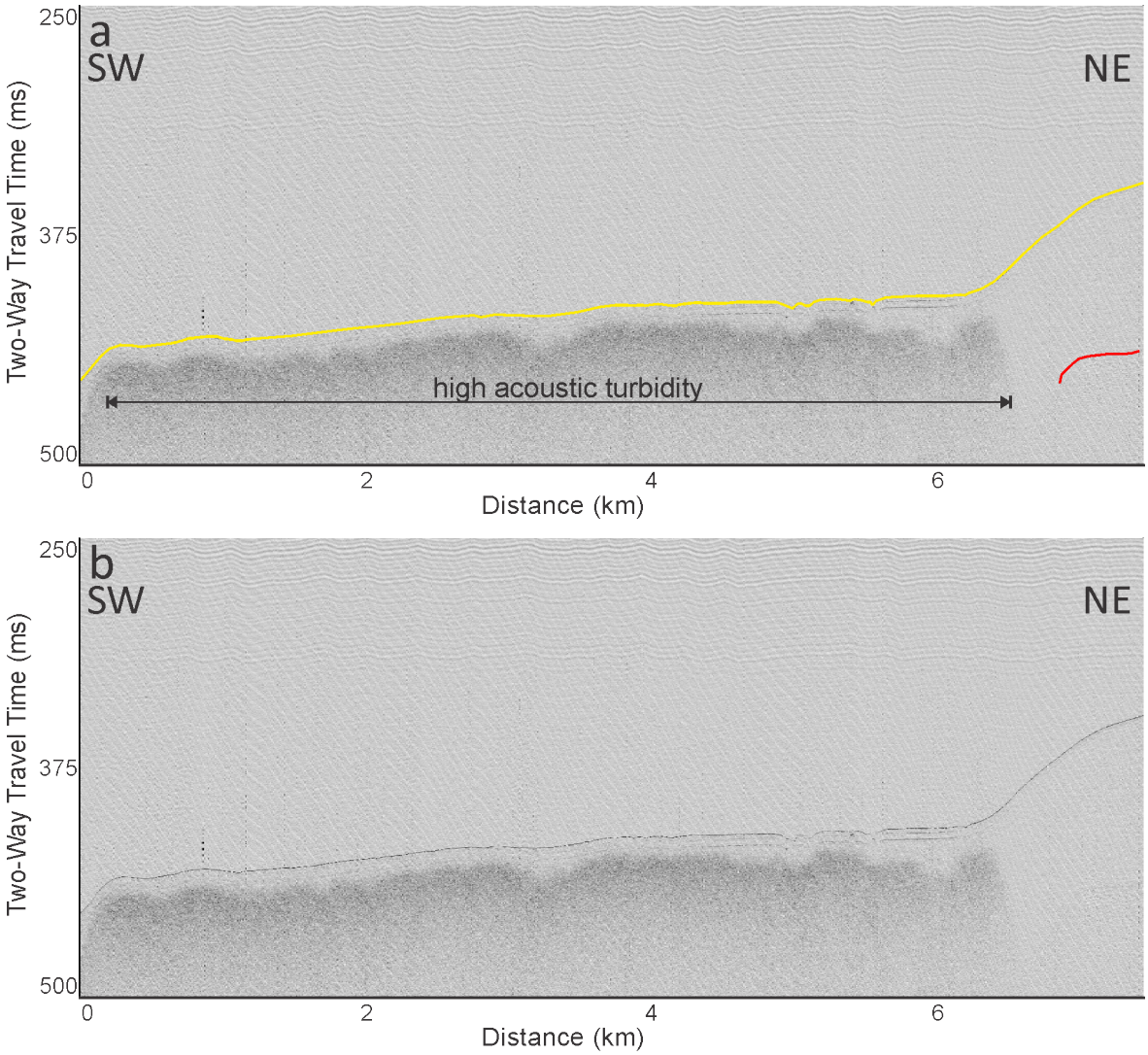


Figure A.2.51: Line 10 (Huntec DTS internal), cruise 2002002PGC

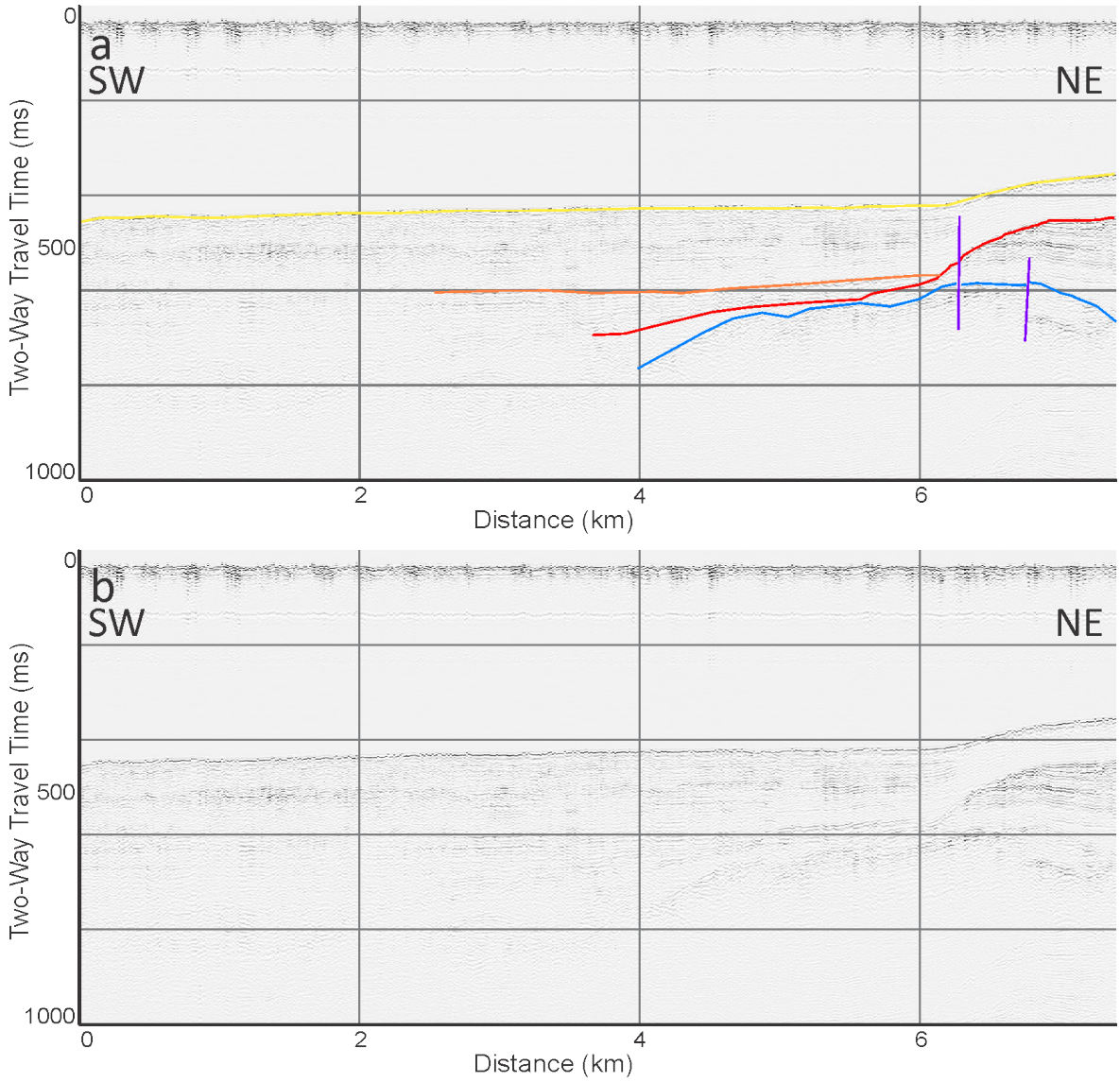


Figure A.2.52: Line 10 (airgun), cruise 2002002PGC

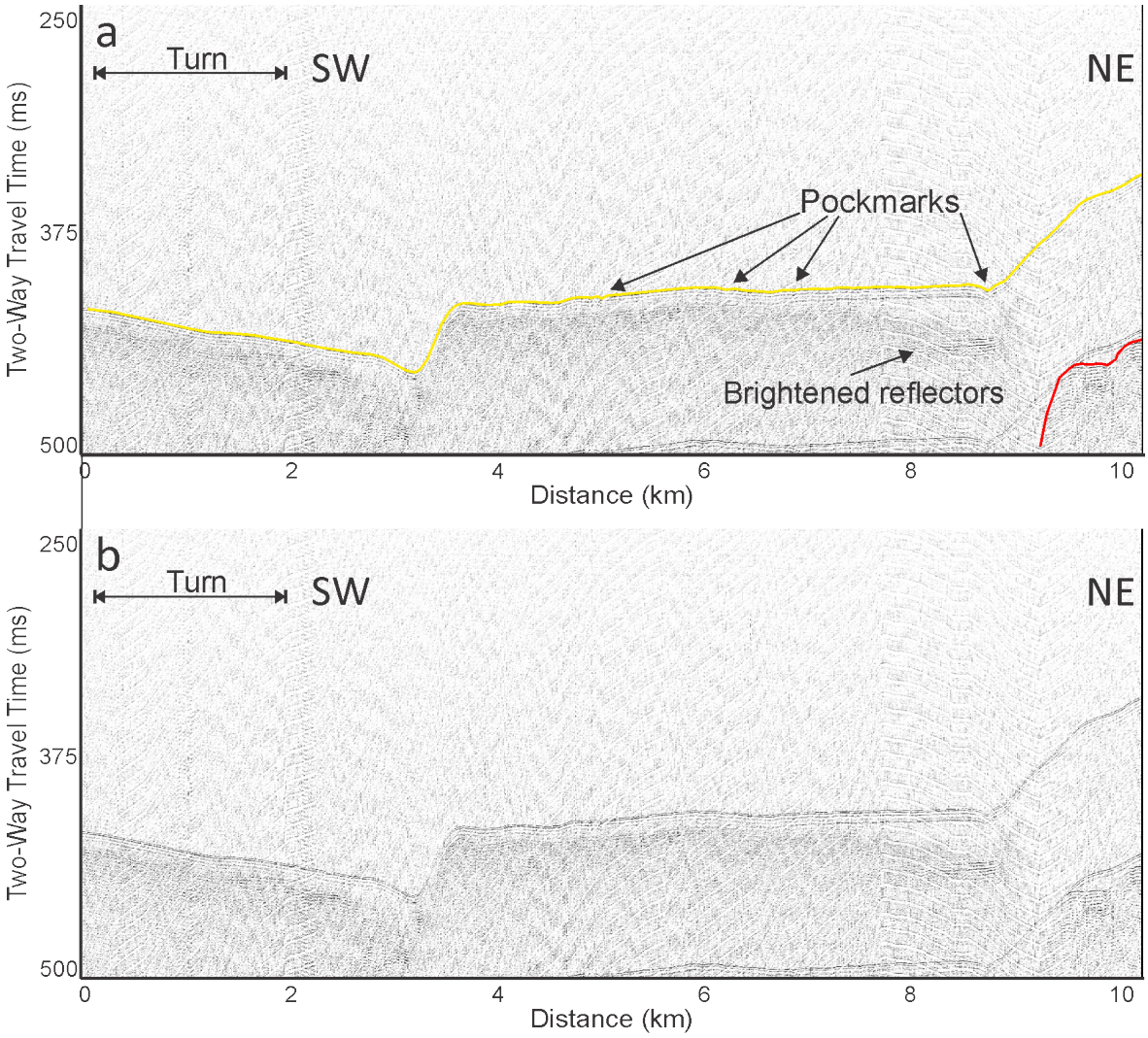


Figure A.2.53: Line 30 (Huntec DTS external), cruise 2002002PGC

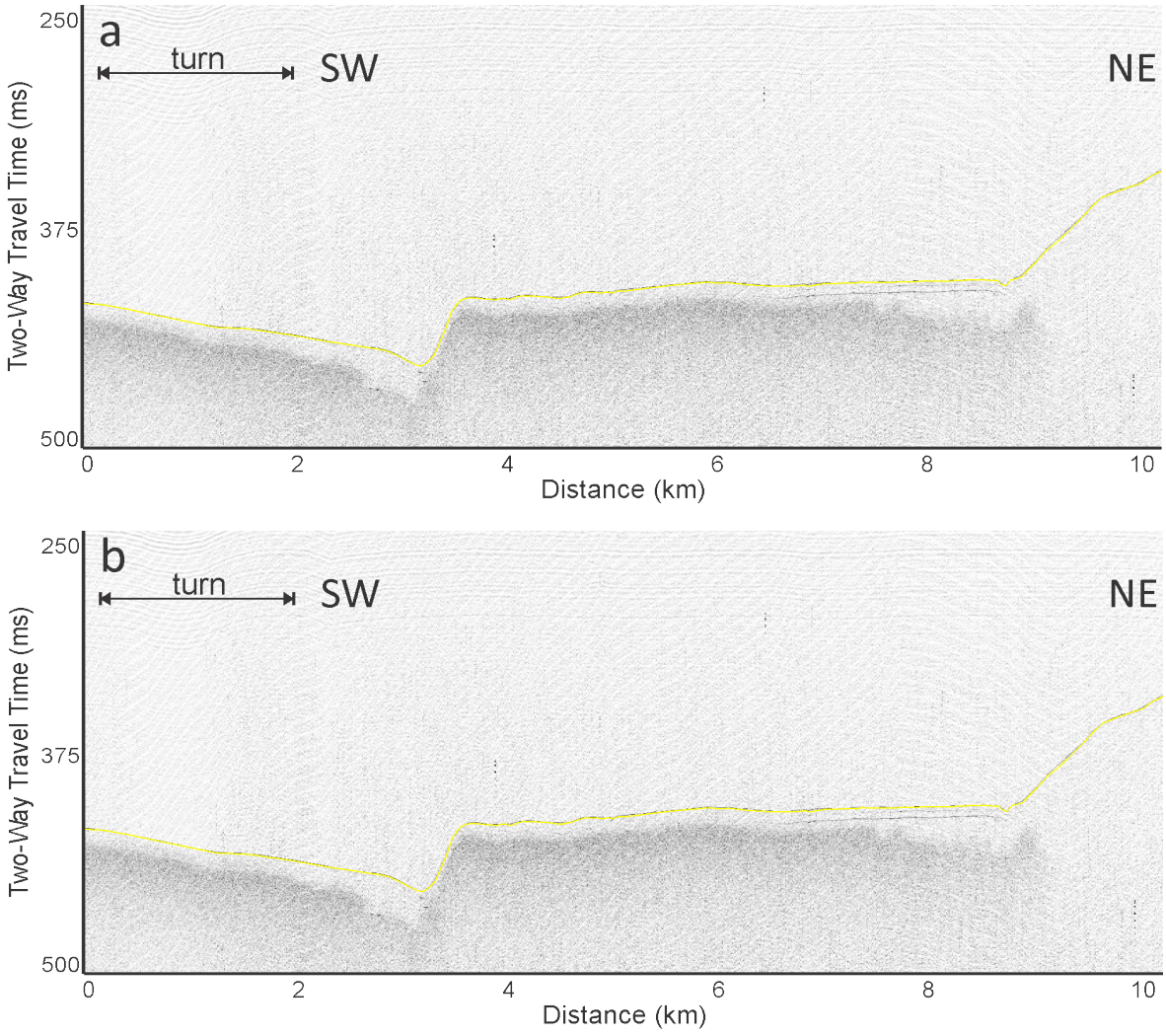


Figure A.2.54: Line 30 (Huntec DTS internal), cruise 2002002PGC

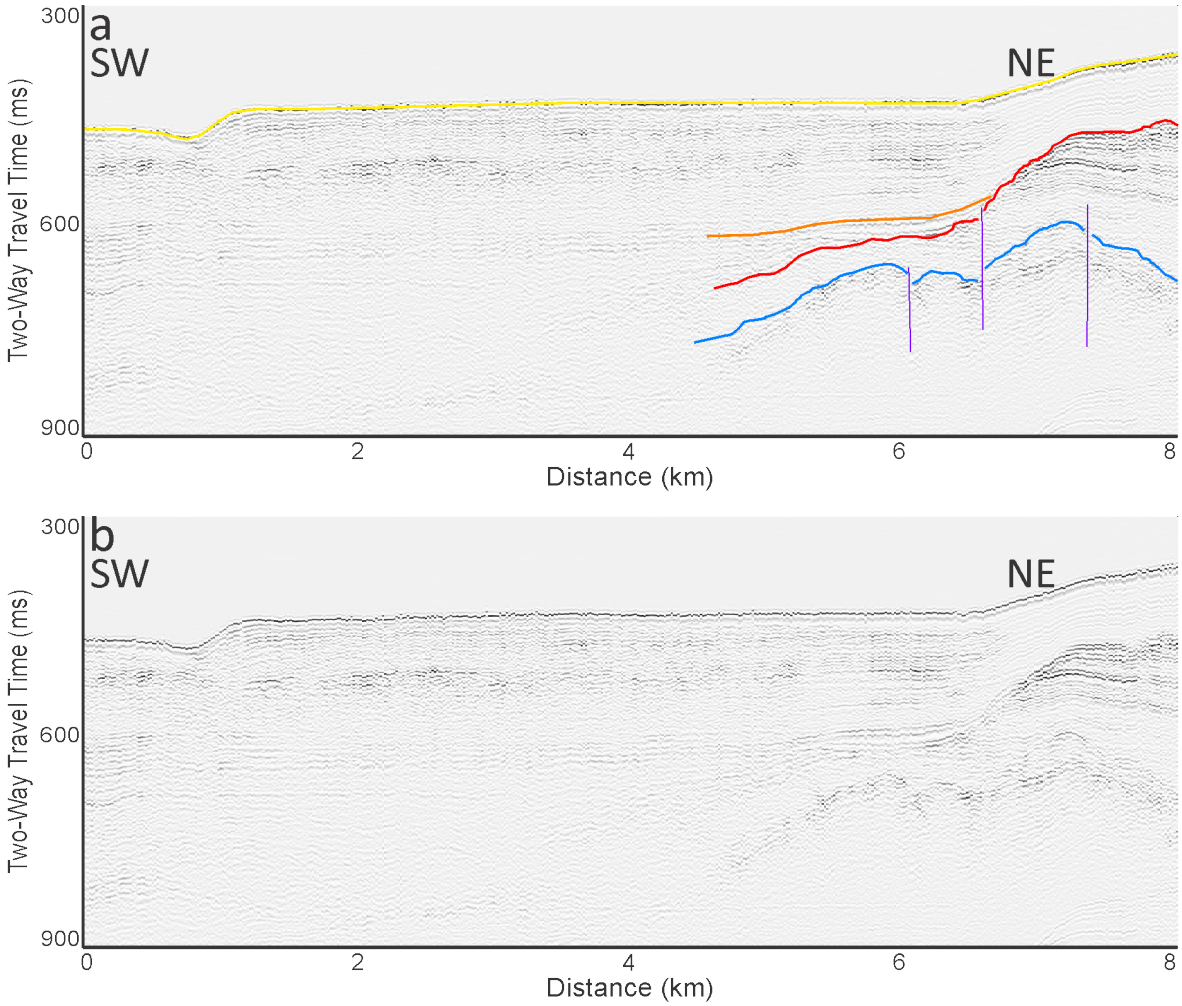


Figure A.2.55: Line 30 (airgun), cruise 2002002PGC

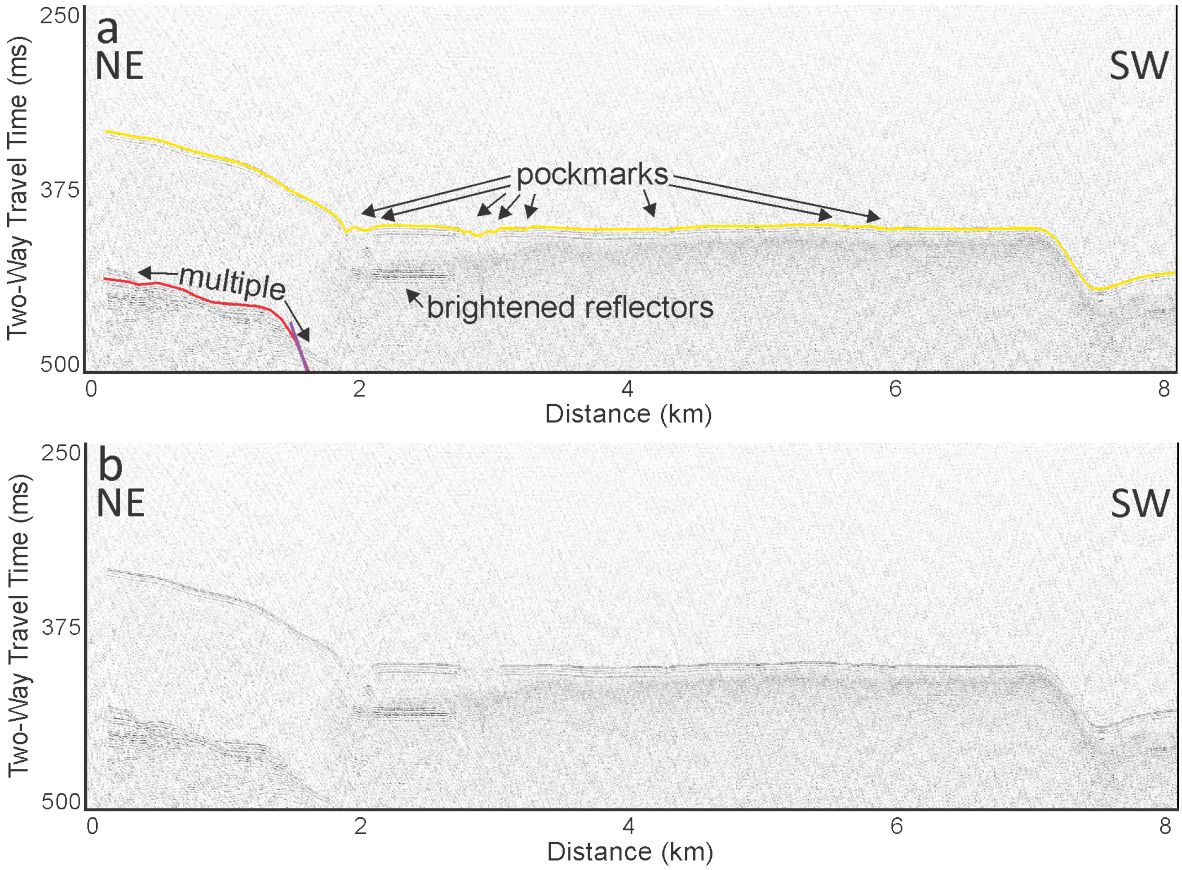


Figure A.2.56: Line 40 (Huntec DTS external), cruise 2002002PGC

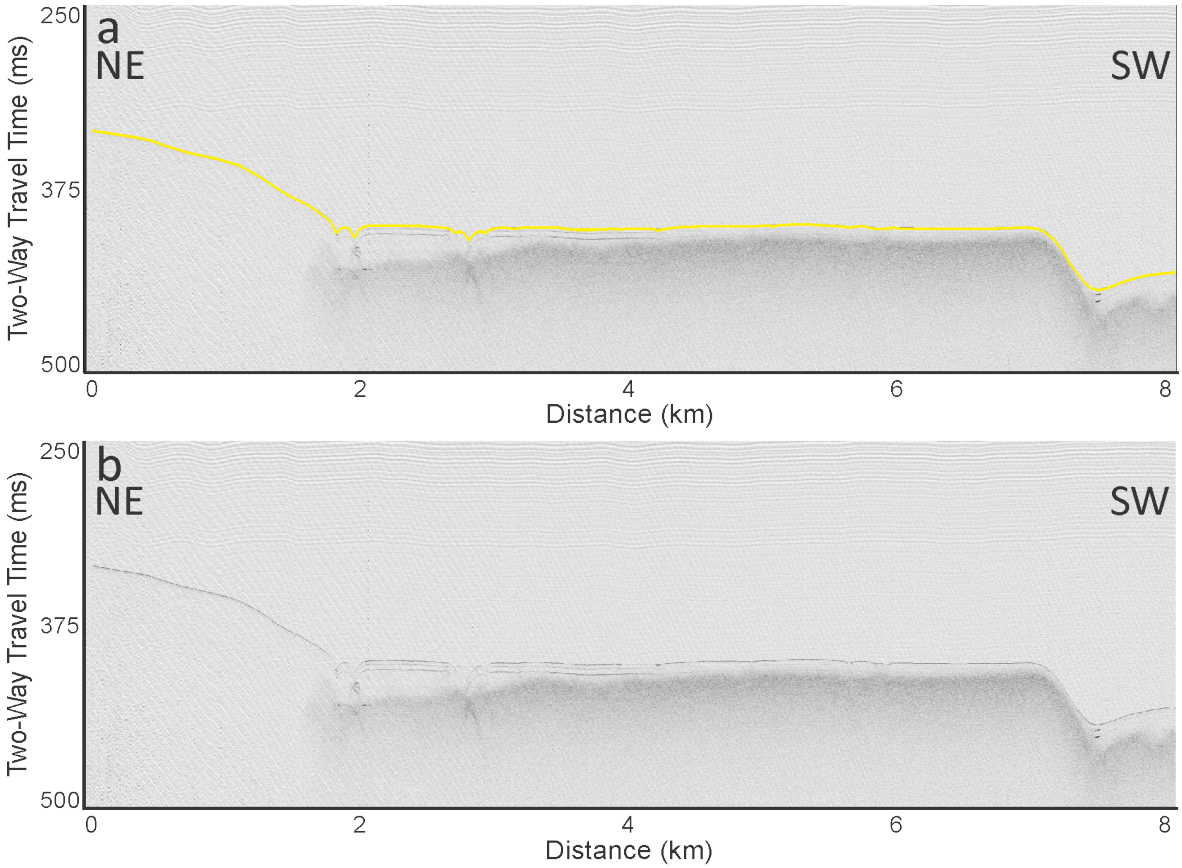


Figure A.2.57: Line 40 (Huntec DTS internal), cruise 2002002PGC

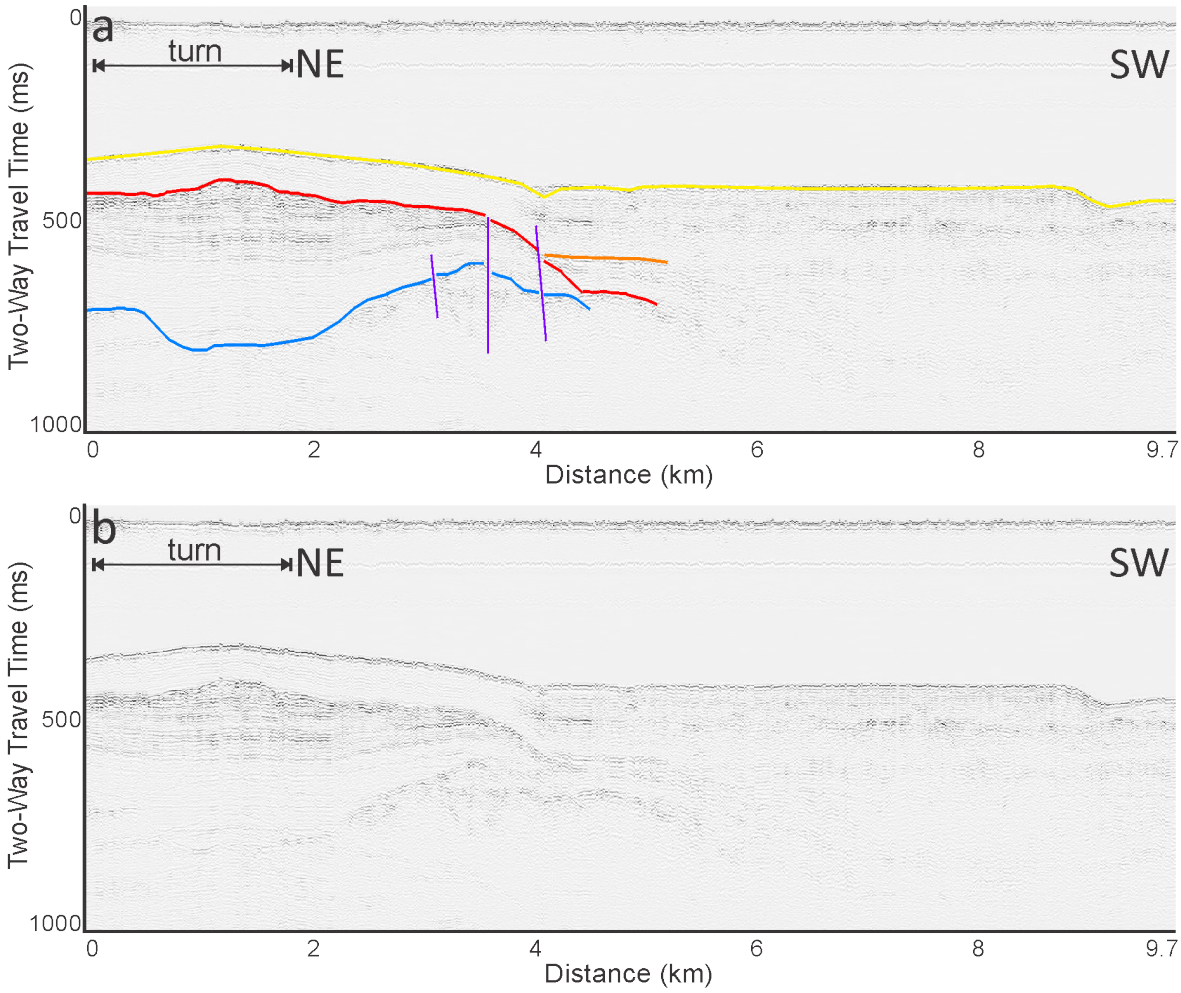


Figure A.2.58: Line 40 (airgun), cruise 2002002PGC

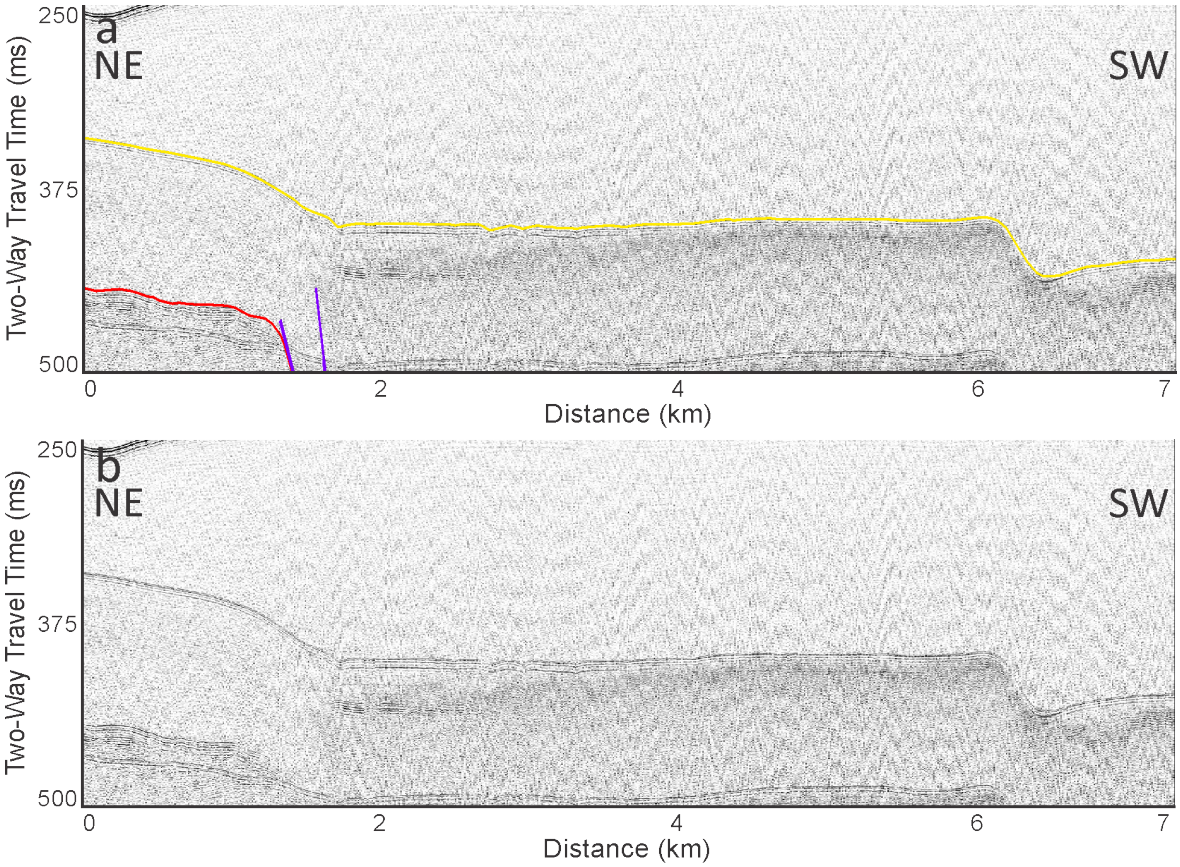


Figure A.2.59: Line 50b (Huntec DTS external), cruise 2002002PGC

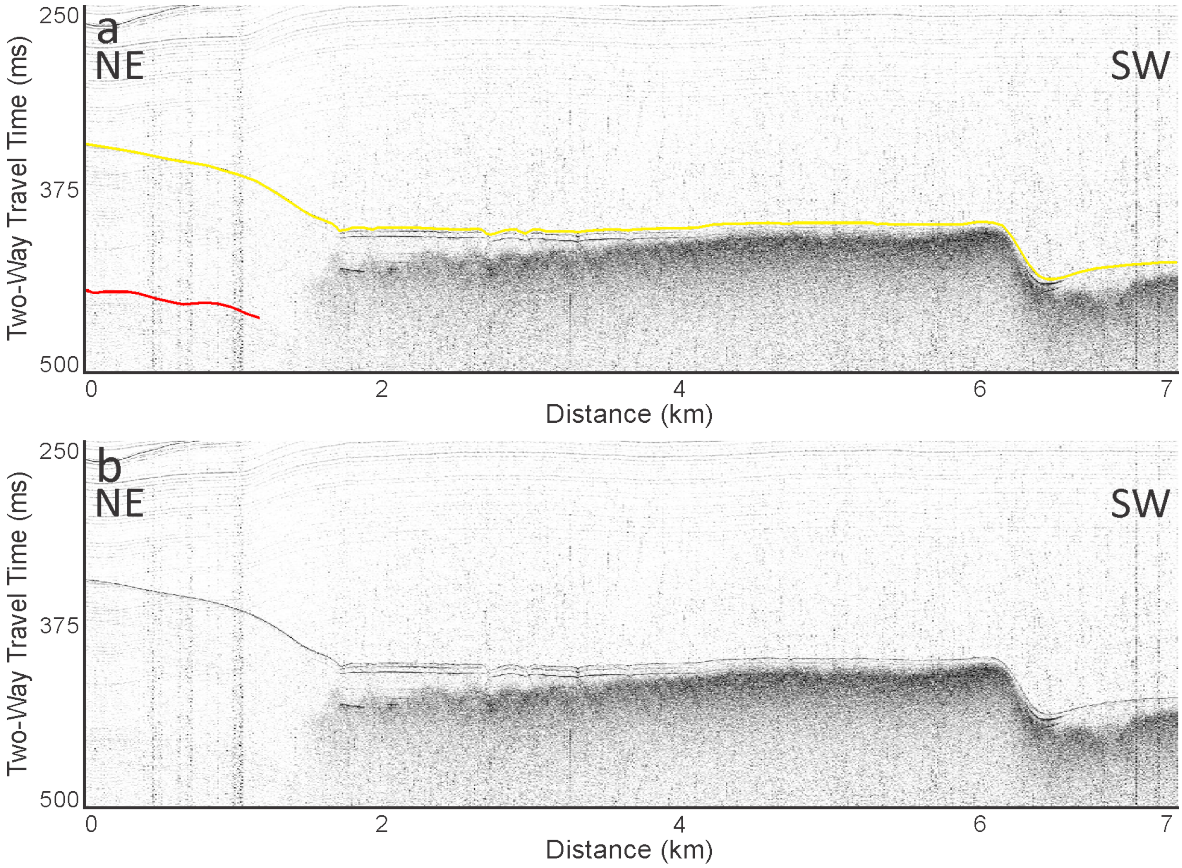


Figure A.2.60: Line 50b (Huntec DTS internal), cruise 2002002PGC

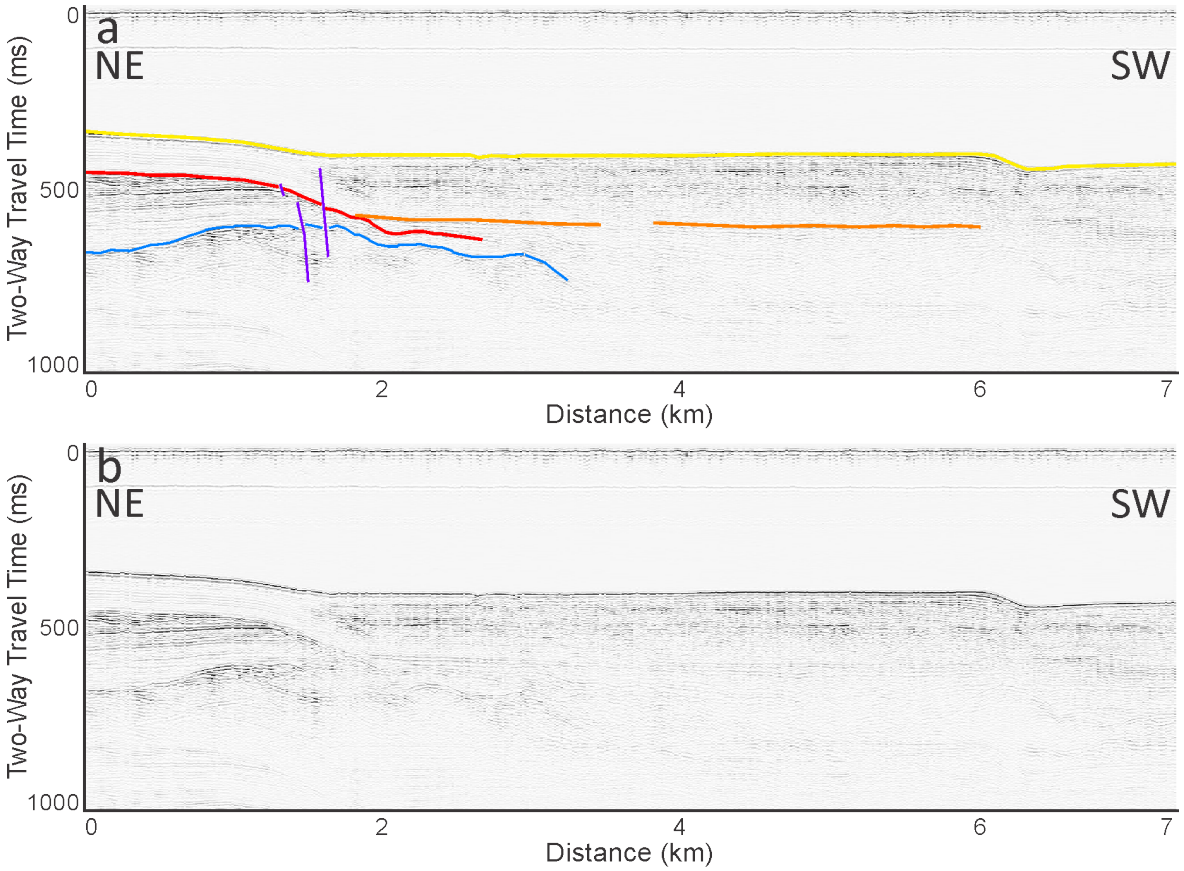


Figure A.2.61: Line 50b (airgun), cruise 2002002PGC

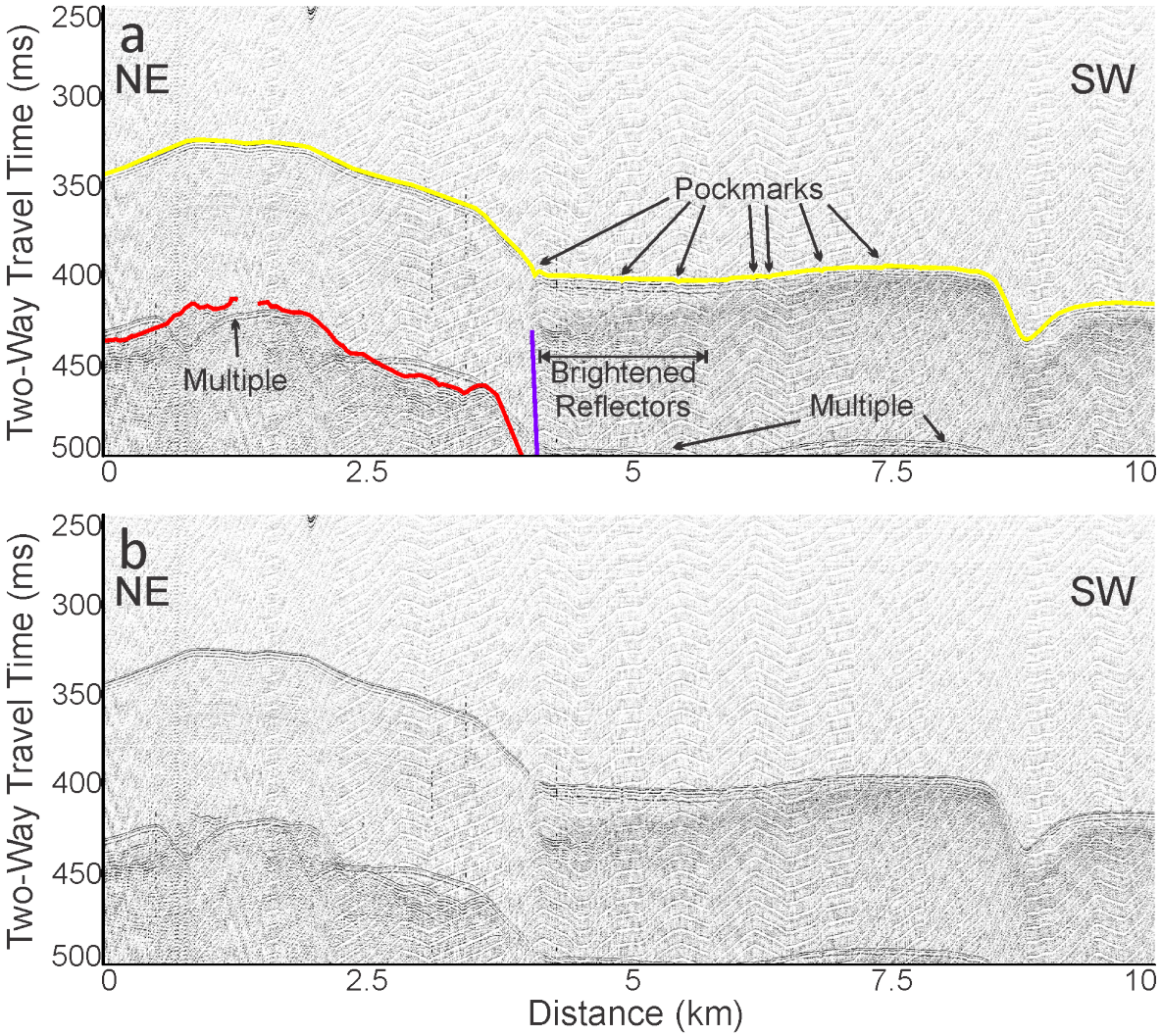


Figure A.2.62: Line 60 (Huntec DTS external), cruise 2002002PGC

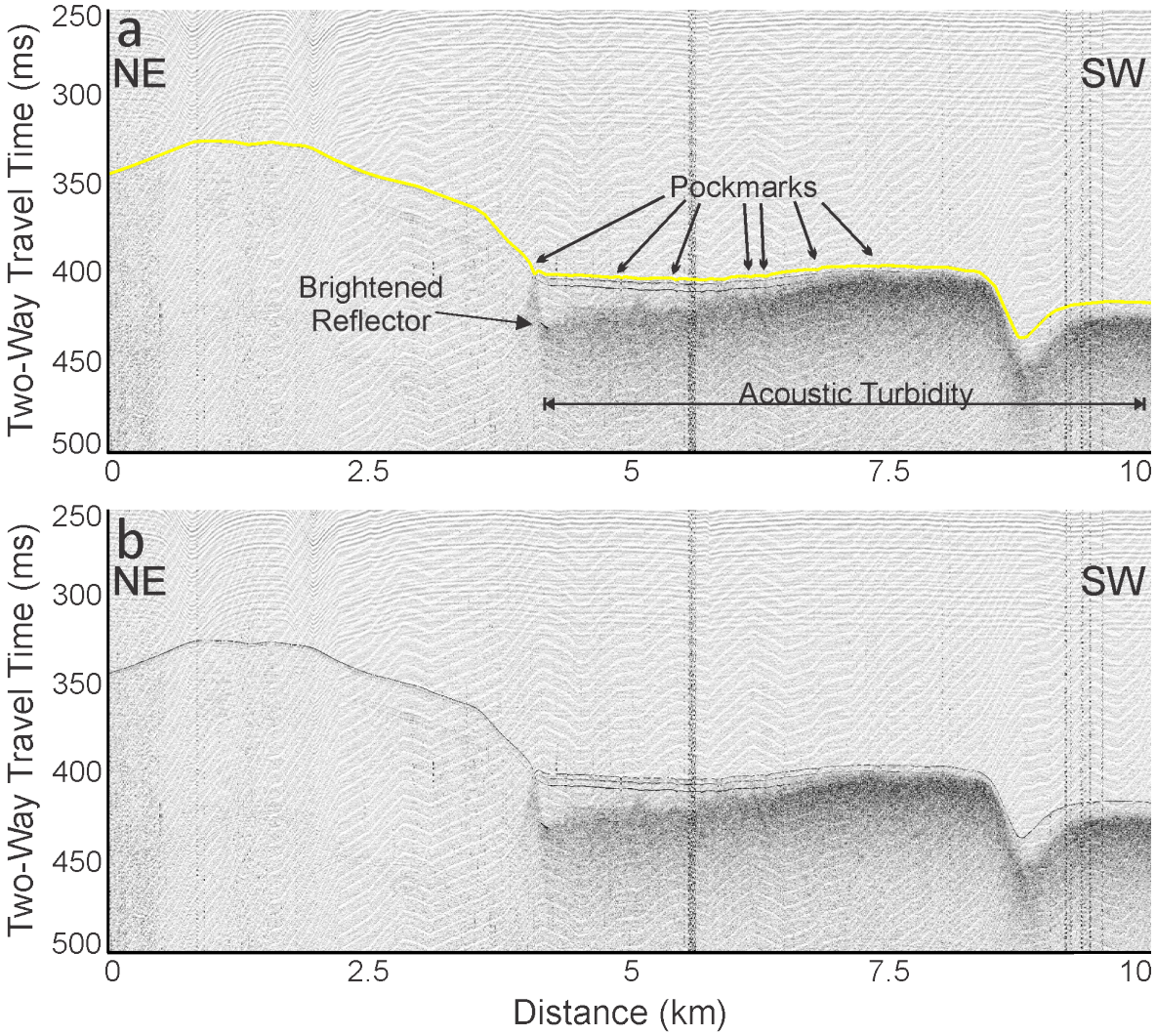


Figure A.2.63: Line 60 (Huntec DTS internal), cruise 2002002PGC

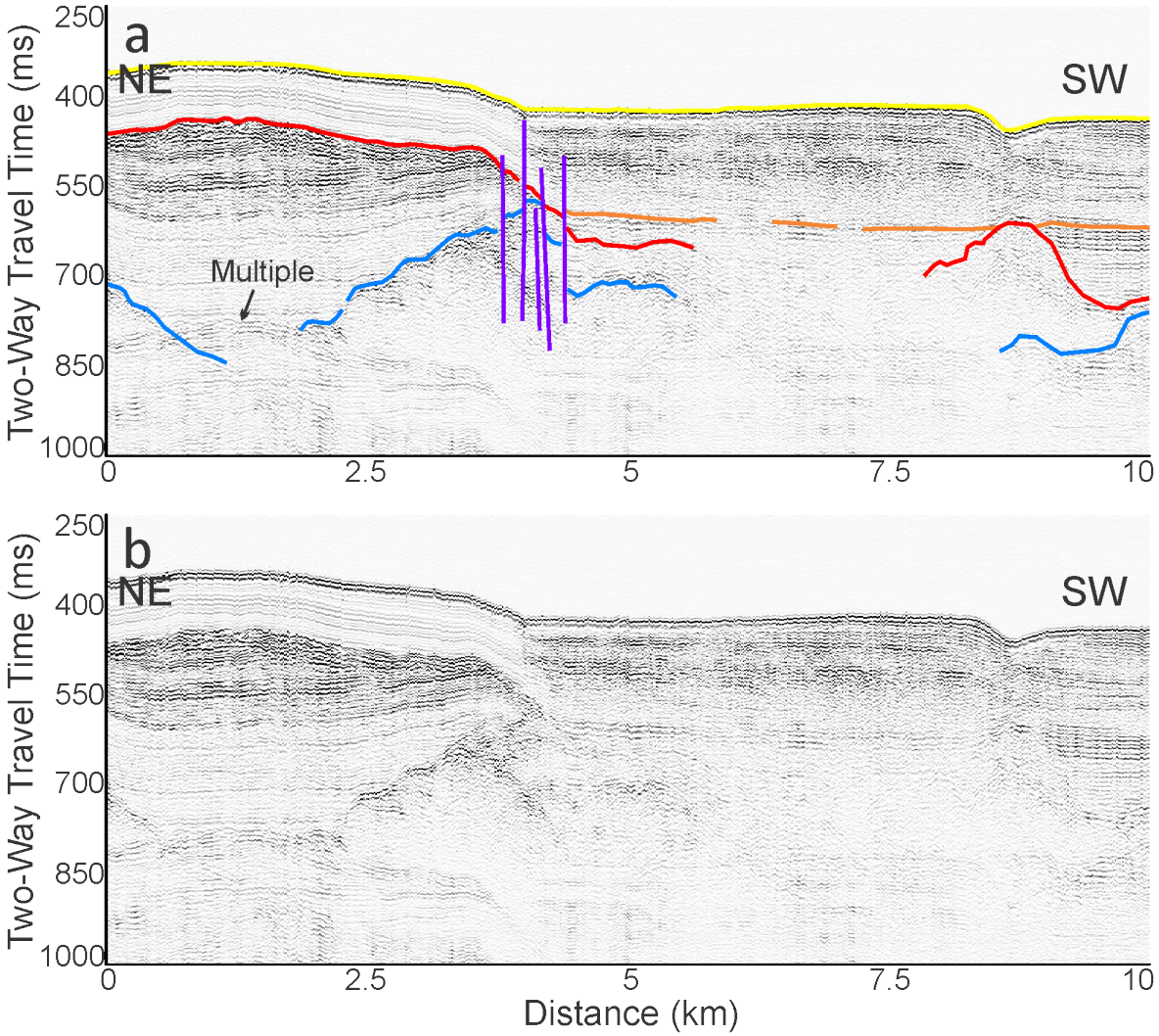


Figure A.2.64: Line 60 (airgun), cruise 2002002PGC

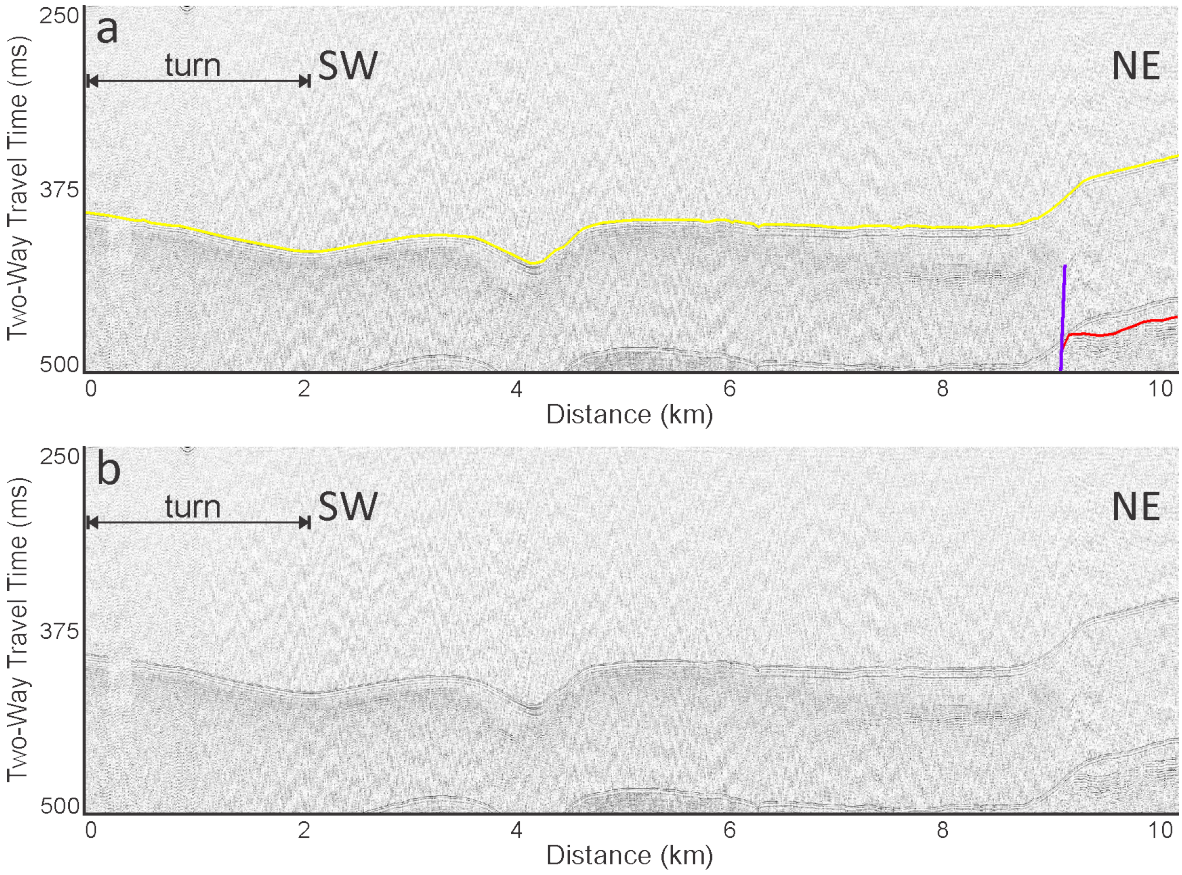


Figure A.2.65: Line 70 (Huntec DTS external), cruise 2002002PGC

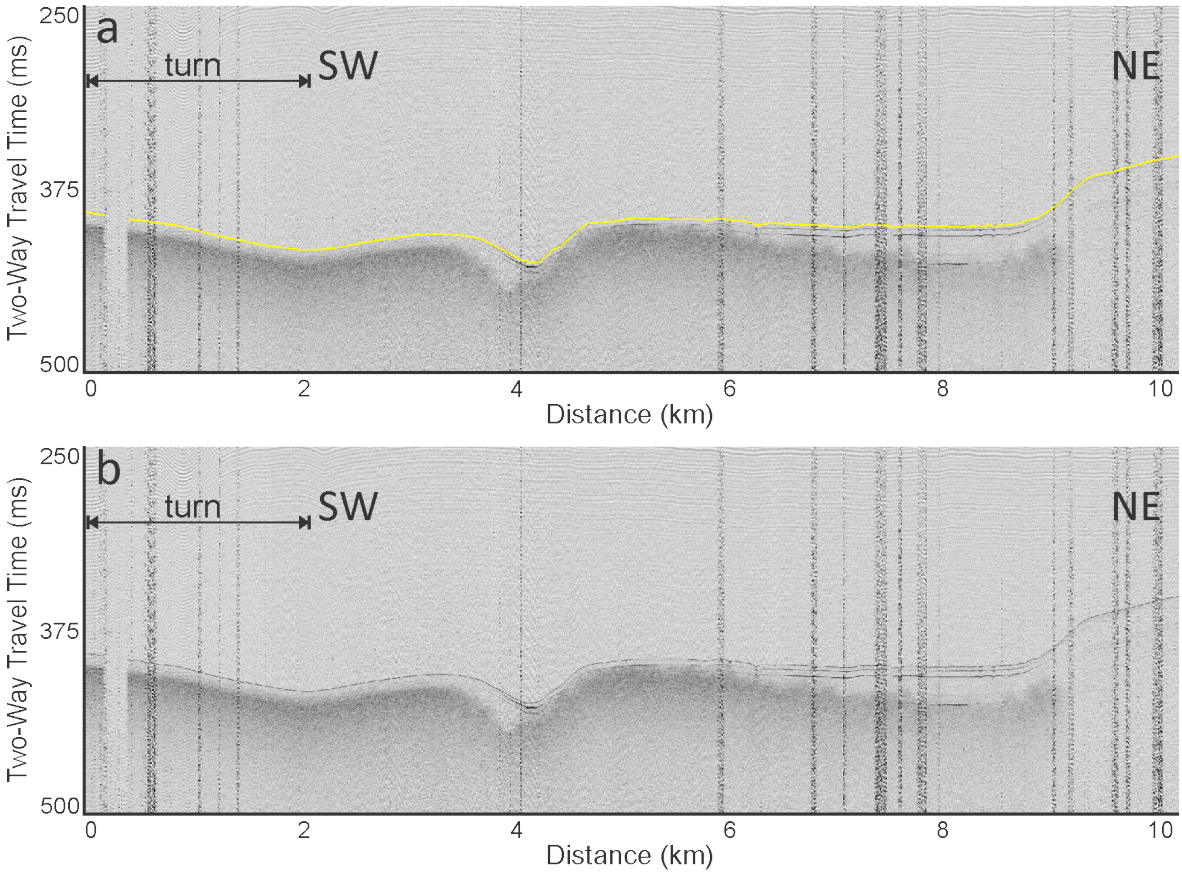


Figure A.2.66: Line 70 (Huntec DTS internal), cruise 2002002PGC

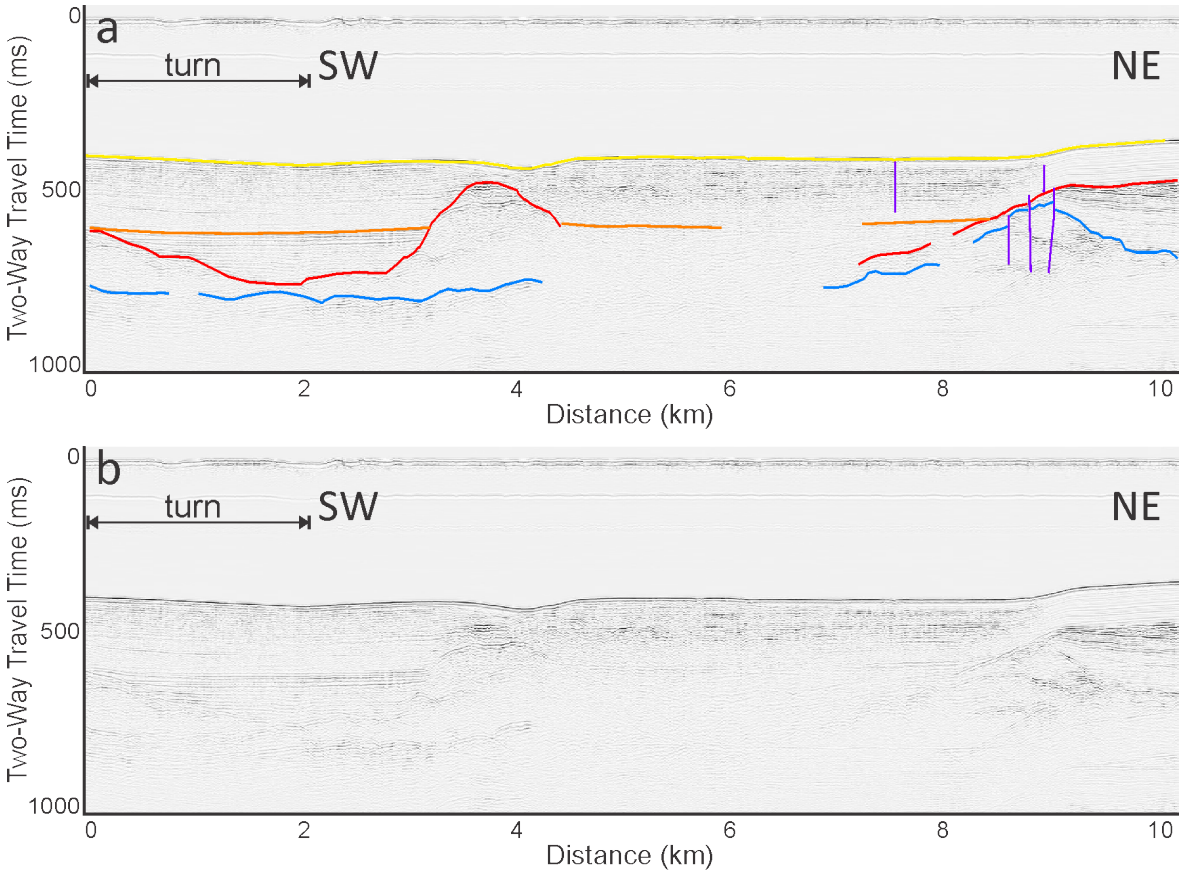


Figure A.2.67: Line 70 (airgun), cruise 2002002PGC

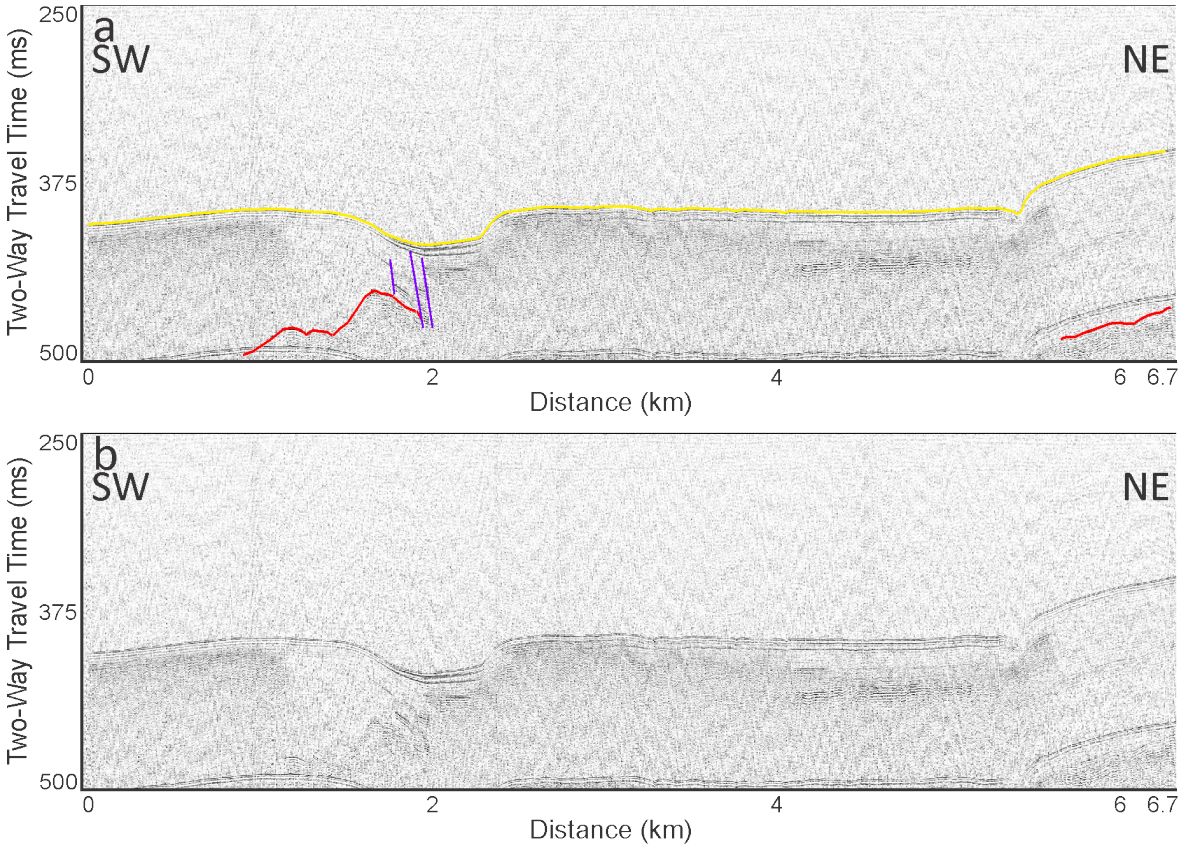


Figure A.2.68: Line 80 (Huntec DTS external), cruise 2002002PGC

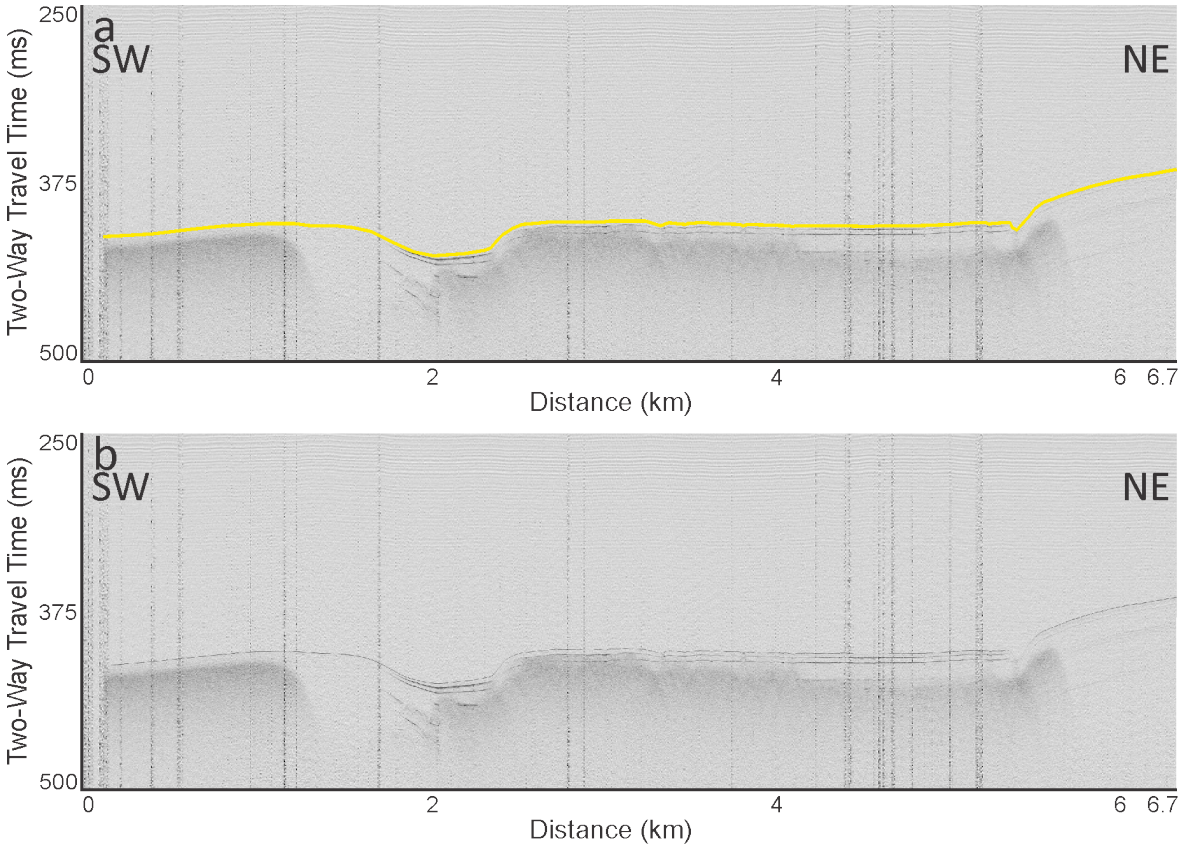


Figure A.2.69: Line 80 (Huntec DTS internal), cruise 2002002PGC

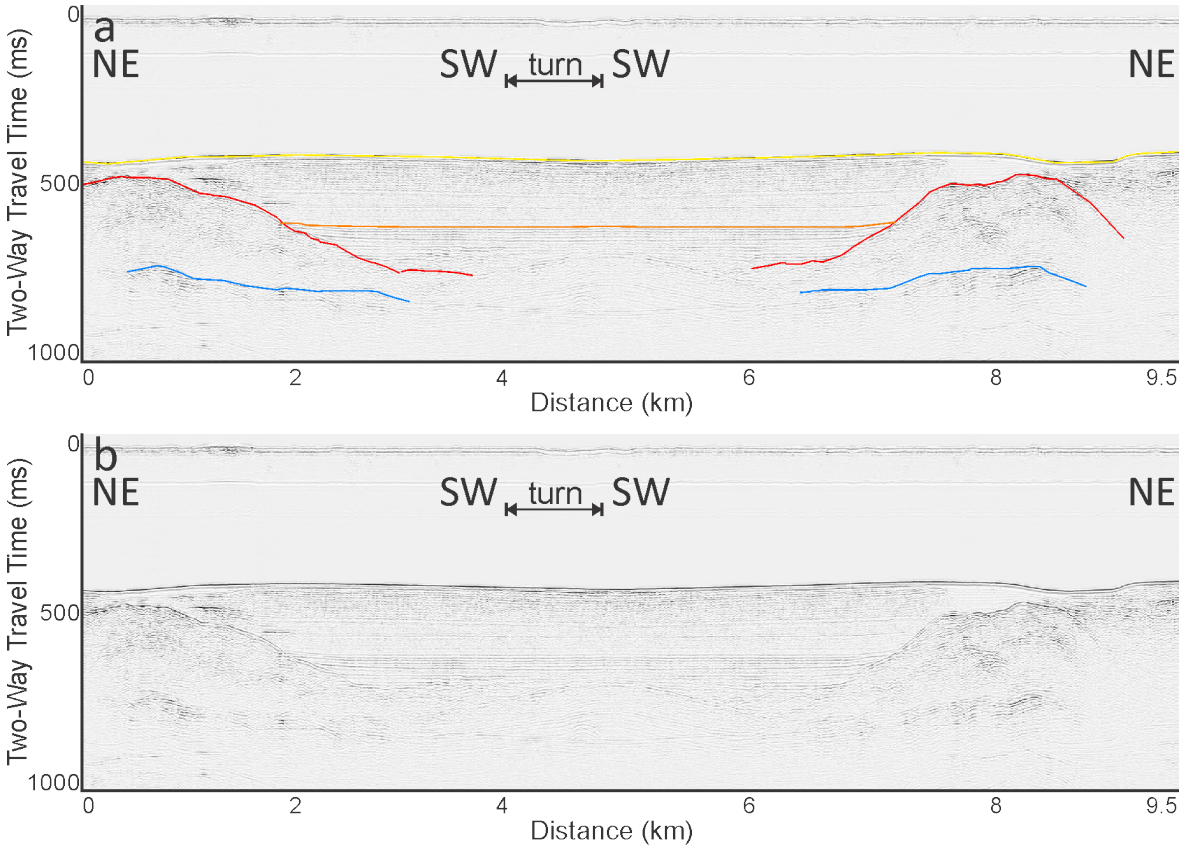


Figure A.2.70: Line 80 (airgun), cruise 2002002PGC. Profile was not fully acquired in conjunction with the Huntec internal and external profiles. The airgun line is located further southwest relative to the Huntec lines; However, the final 3 km of the airgun line and the initial 3 km of the Huntec lines were acquired simultaneously.

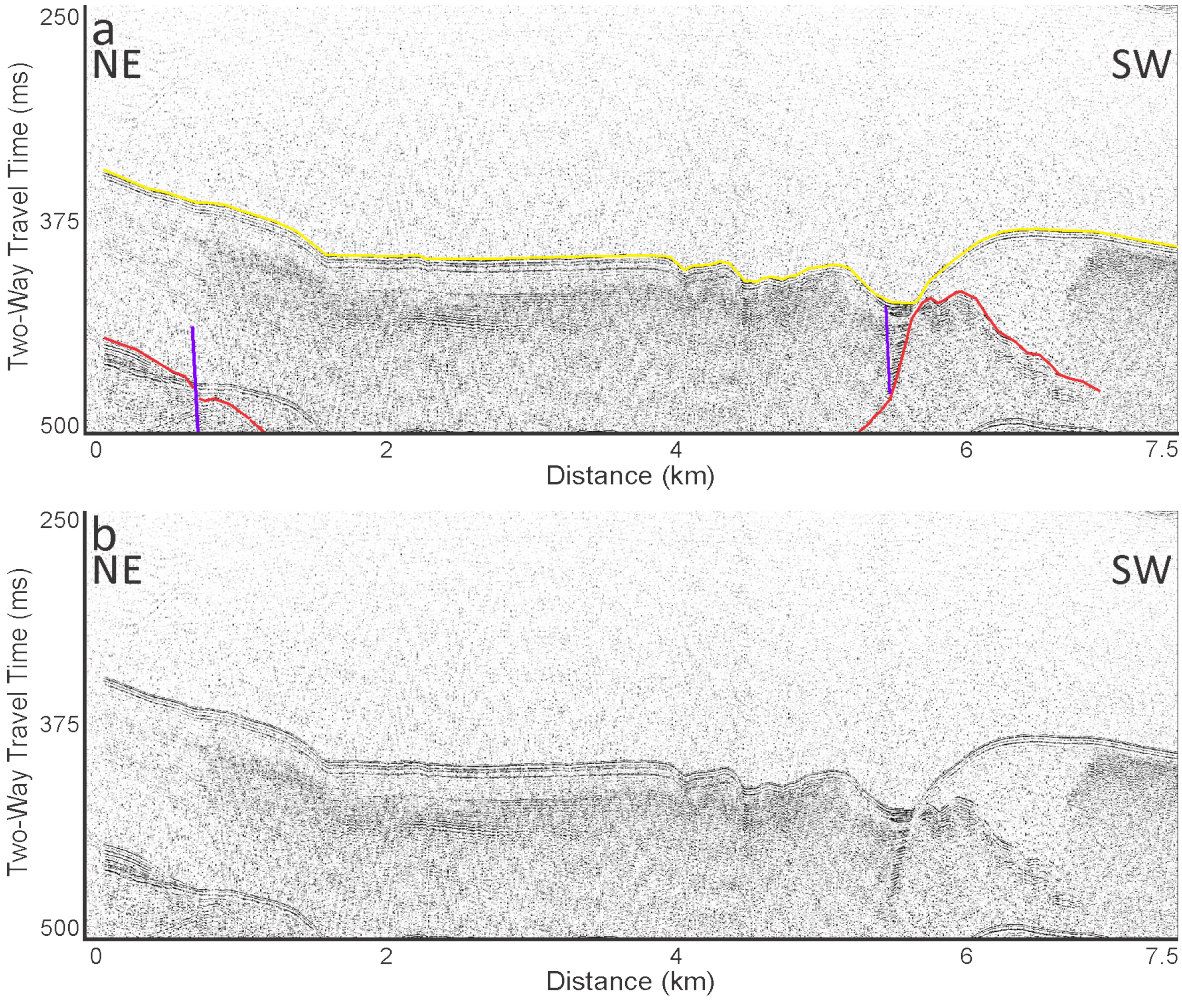


Figure A.2.71: Line 90 (Huntec DTS external), cruise 2002002PGC

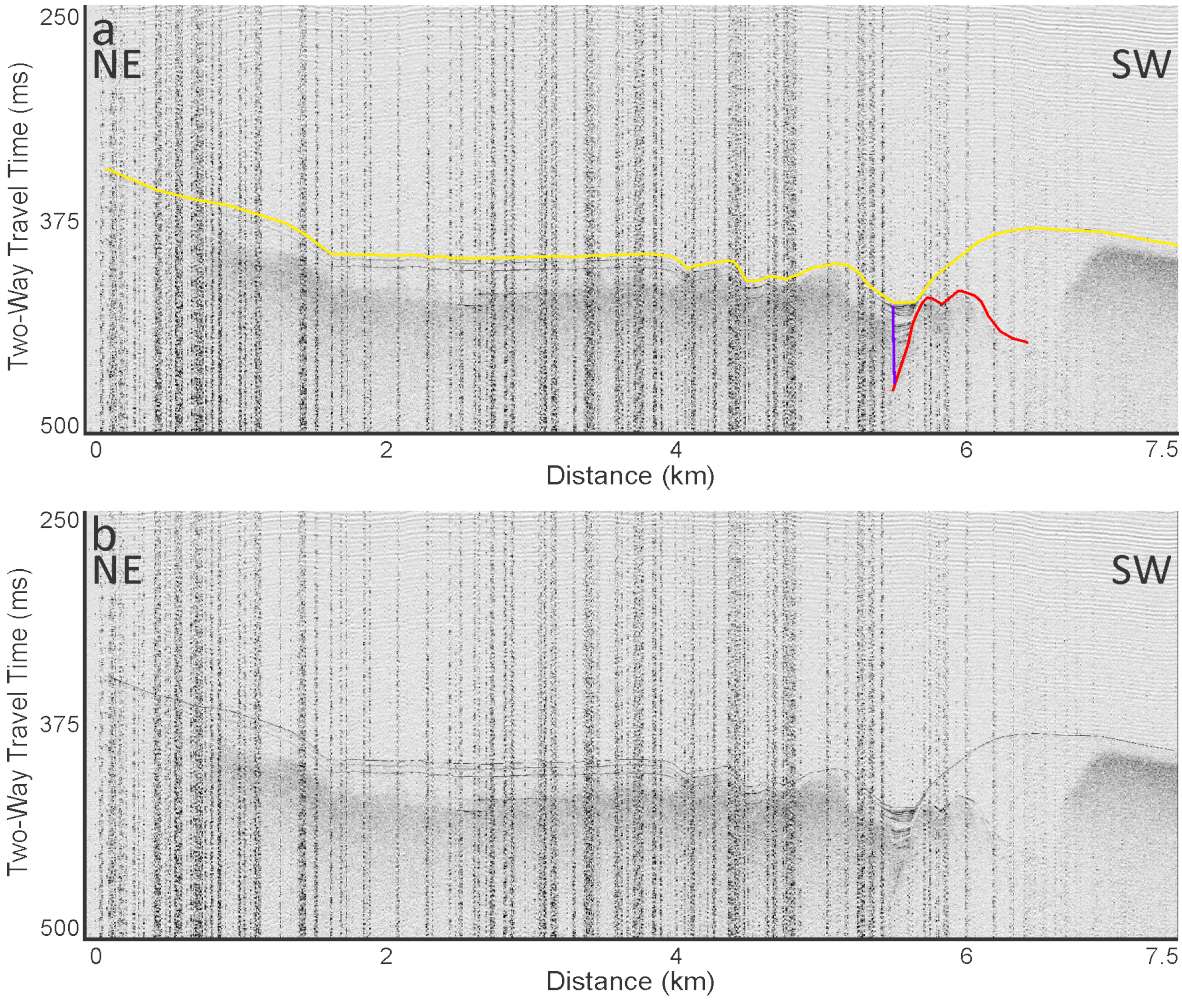


Figure A.2.72: Line 90 (Huntec DTS internal), cruise 2002002PGC

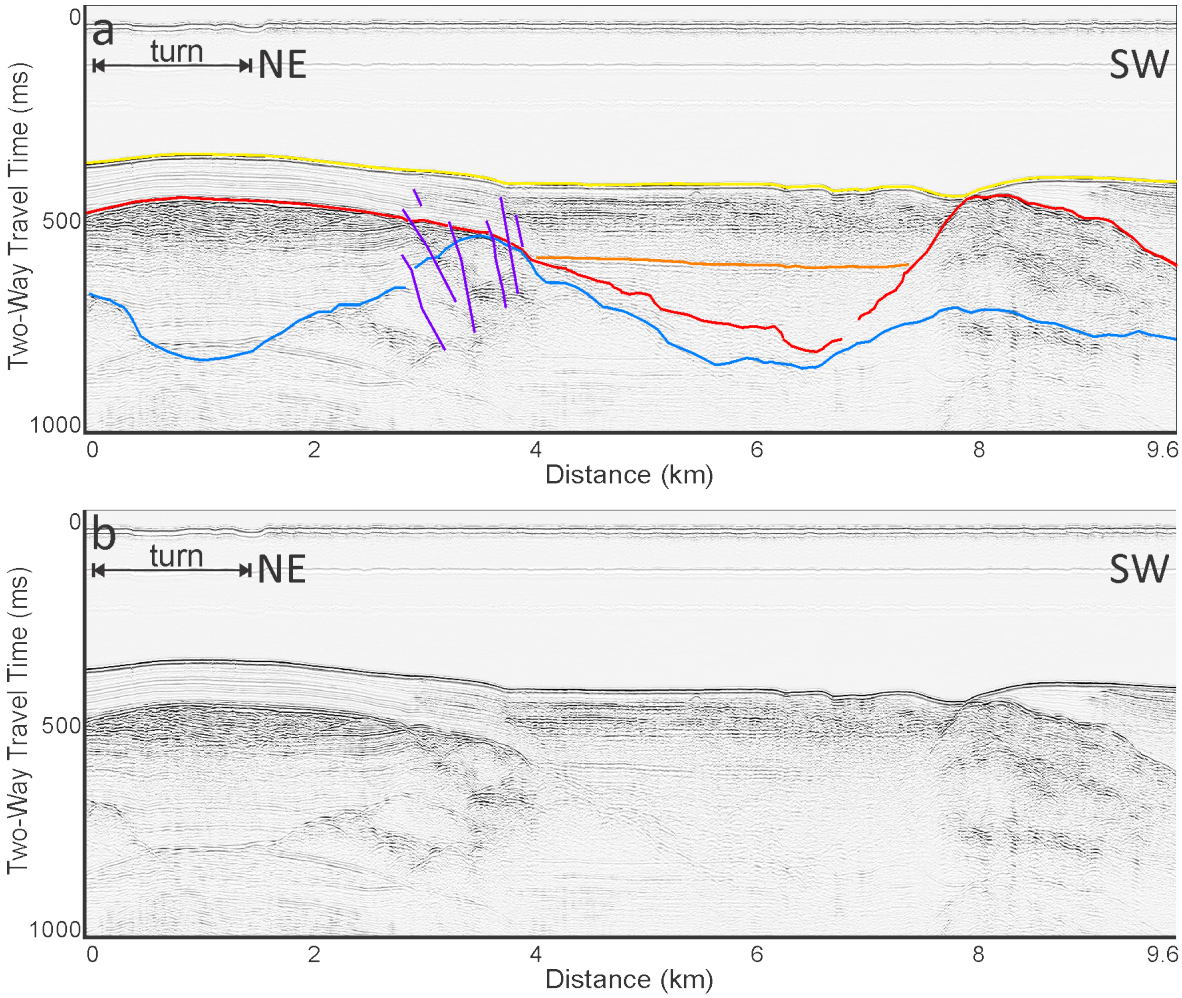


Figure A.2.73: Line 90 (airgun), cruise 2002002PGC

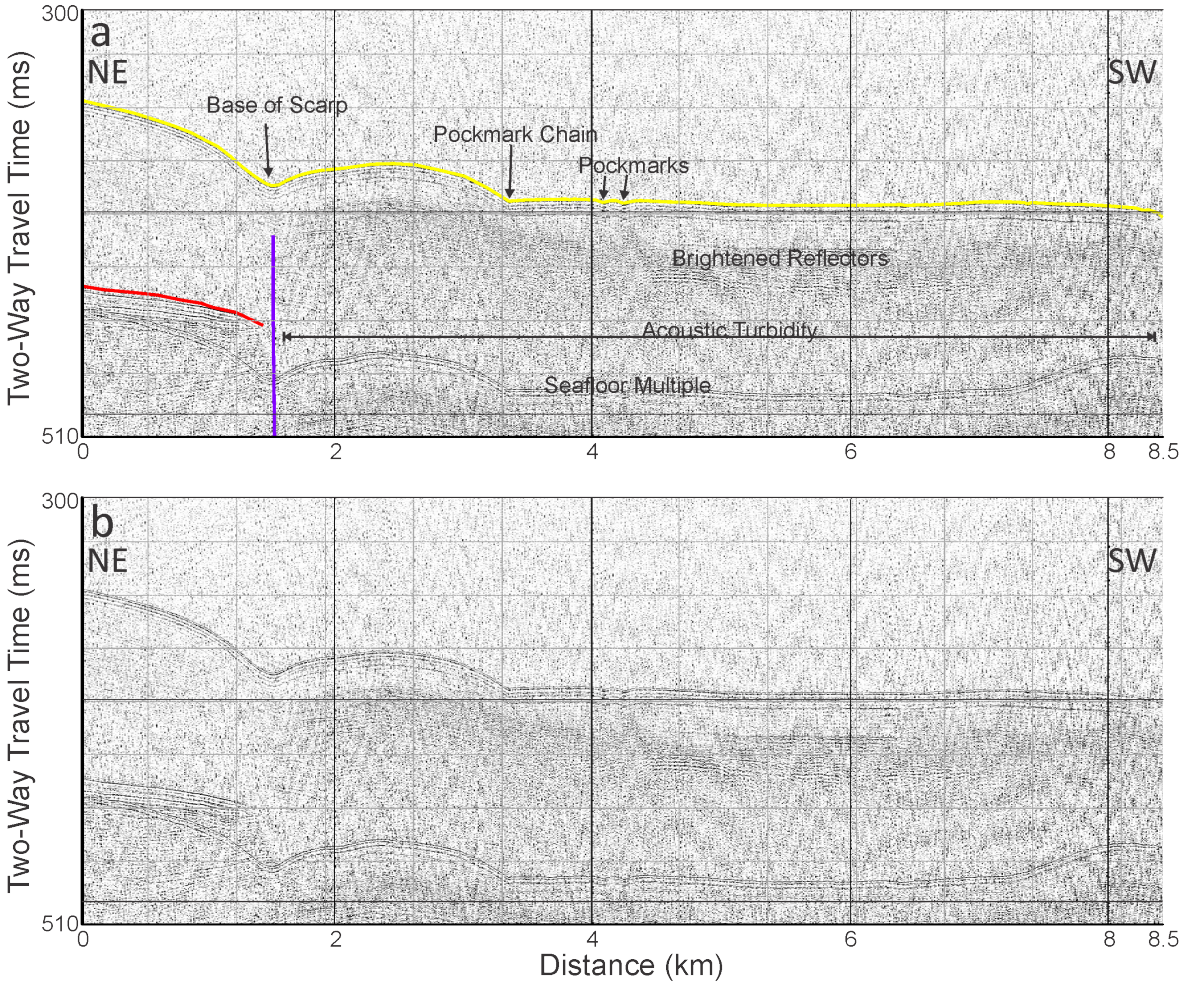


Figure A.2.74: Line 99 (Huntec DTS external), cruise 2002002PGC

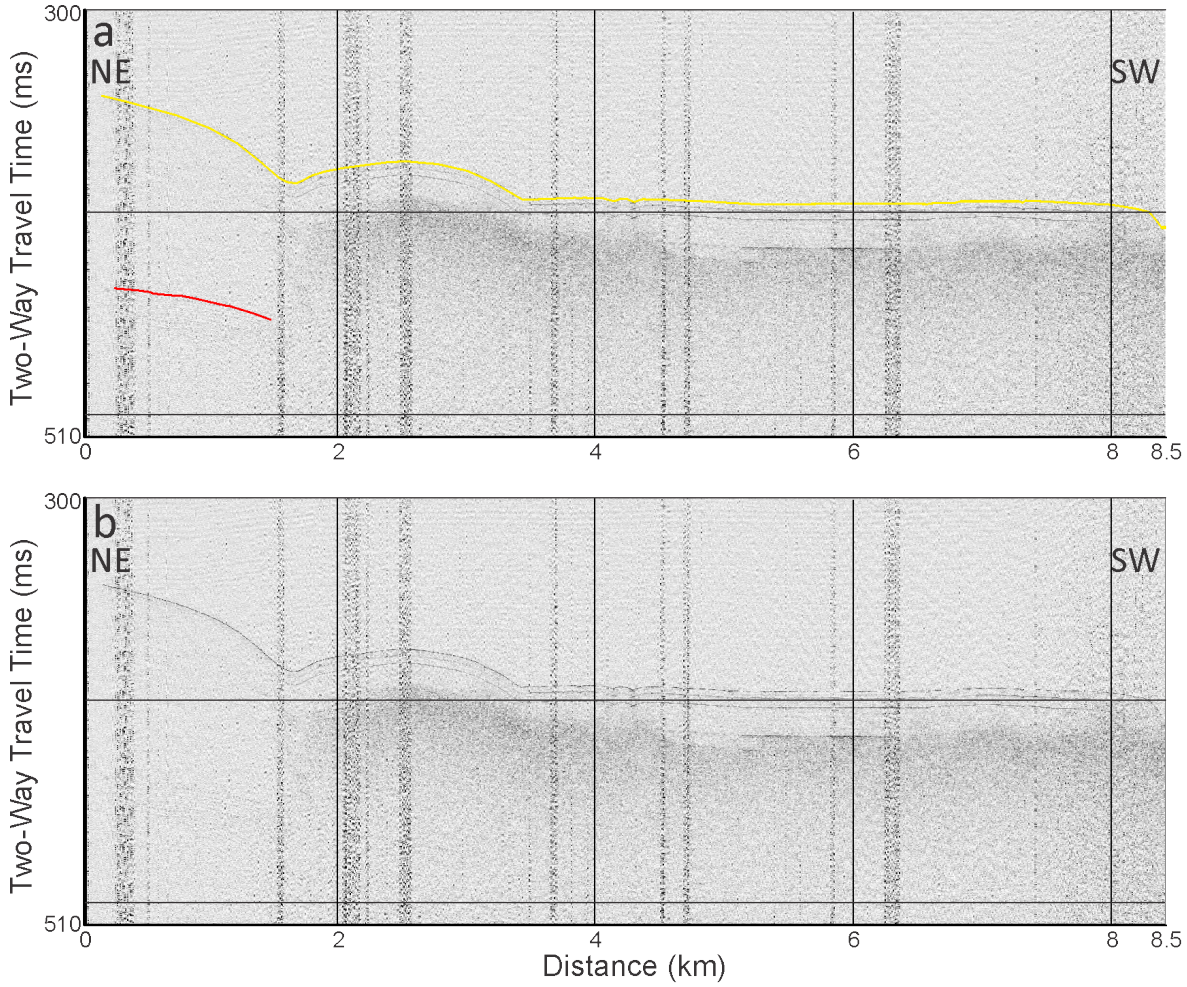


Figure A.2.75: Line 99 (Huntec DTS internal), cruise 2002002PGC

A.2.8 Cruise ID 2003002PGC

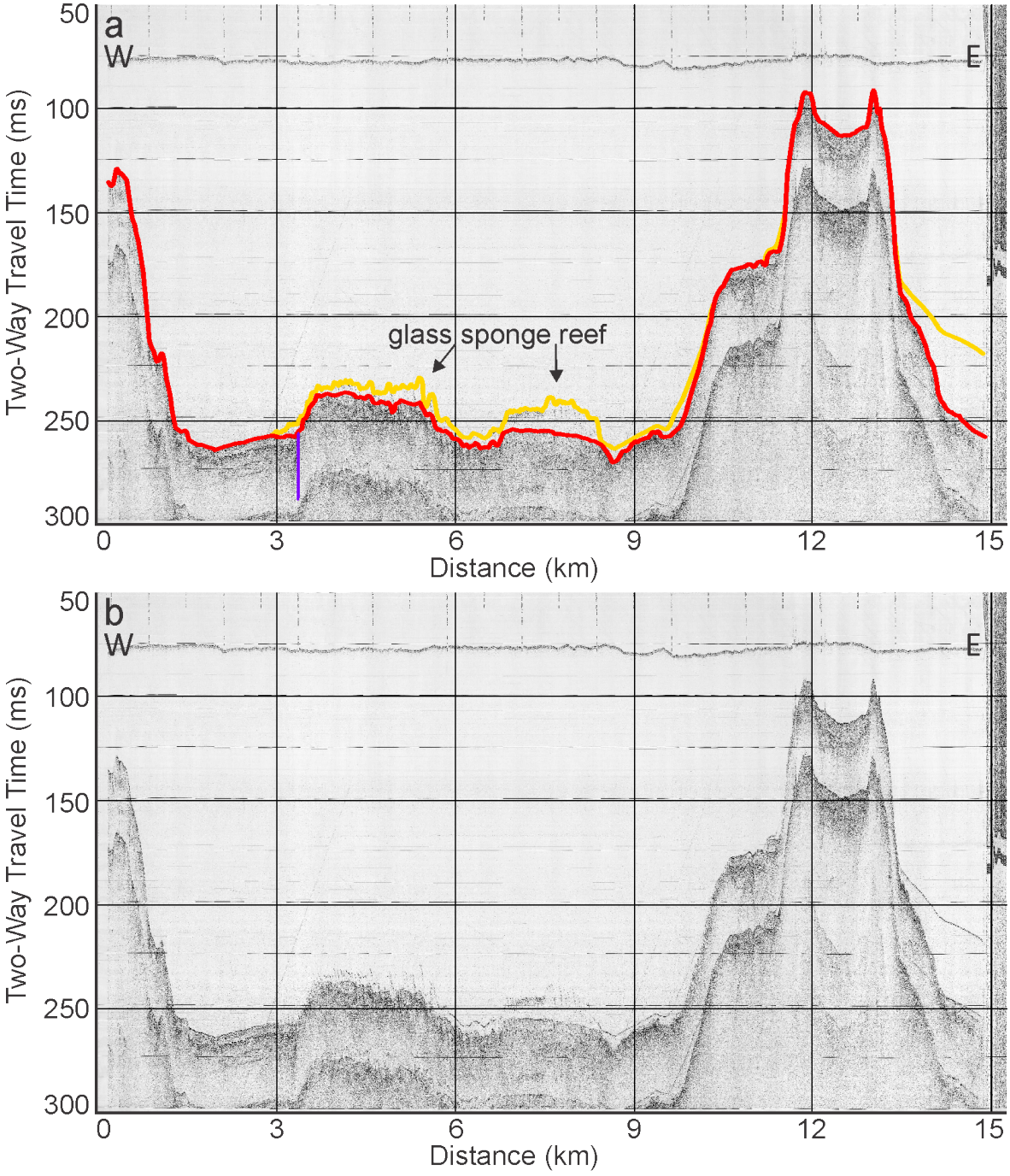


Figure A.2.76: Line 30 (Huntec DTS external), cruise 2003002PGC

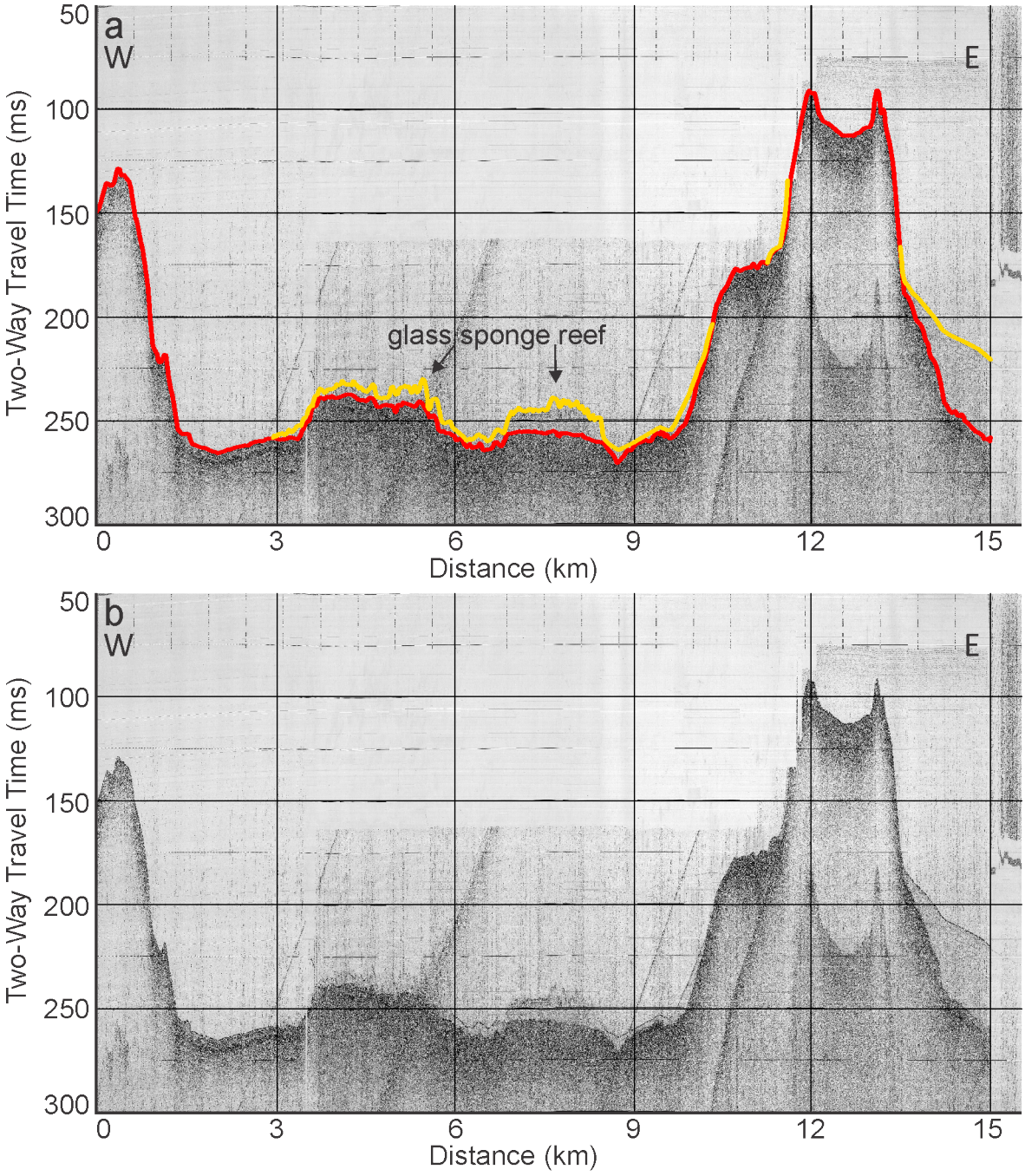


Figure A.2.77: Line 30 (Huntec DTS internal), cruise 2003002PGC

A.2.9 Cruise ID 2009009PGC

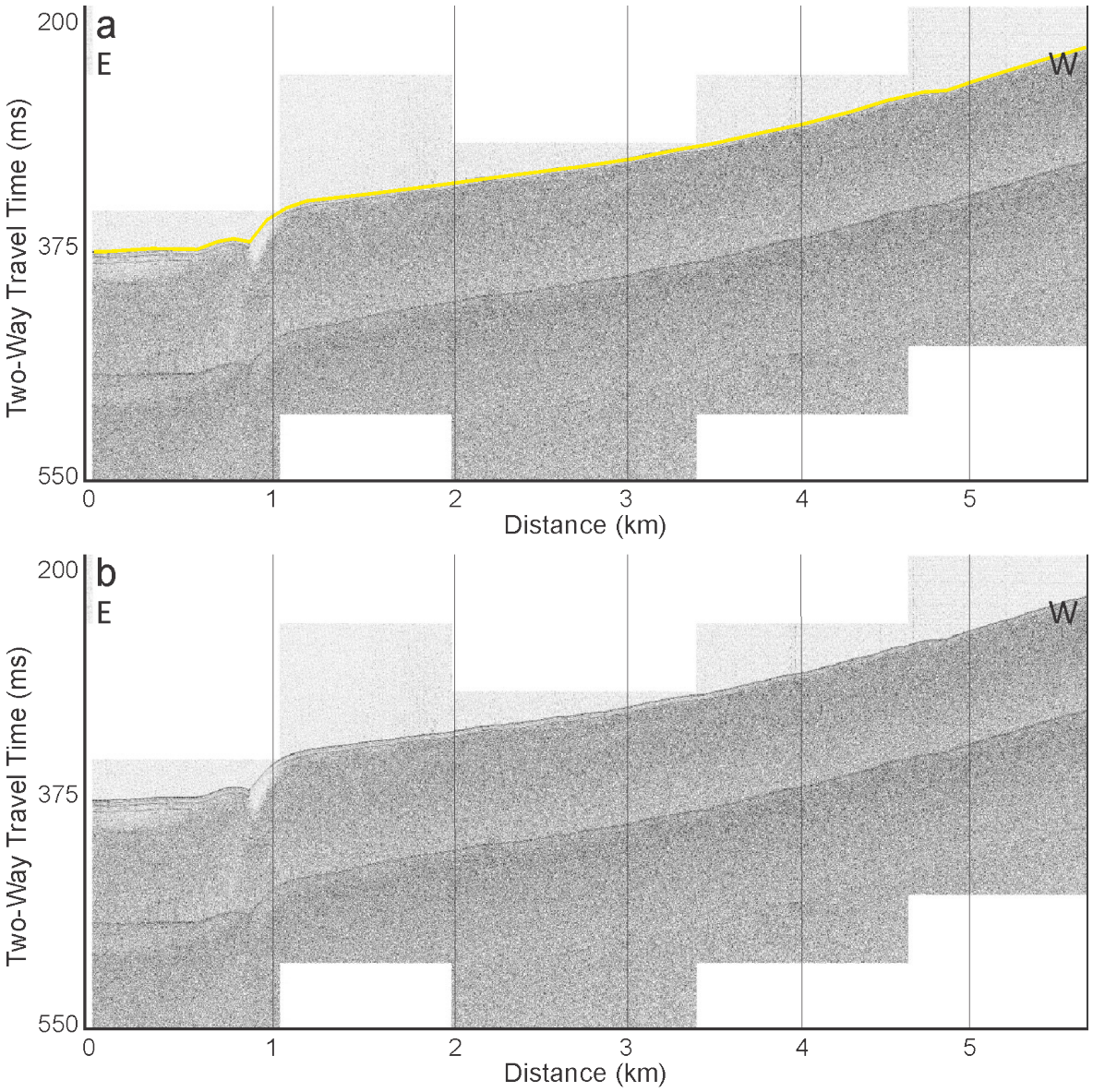


Figure A.2.78: Line DTS001, cruise 2009009PGC

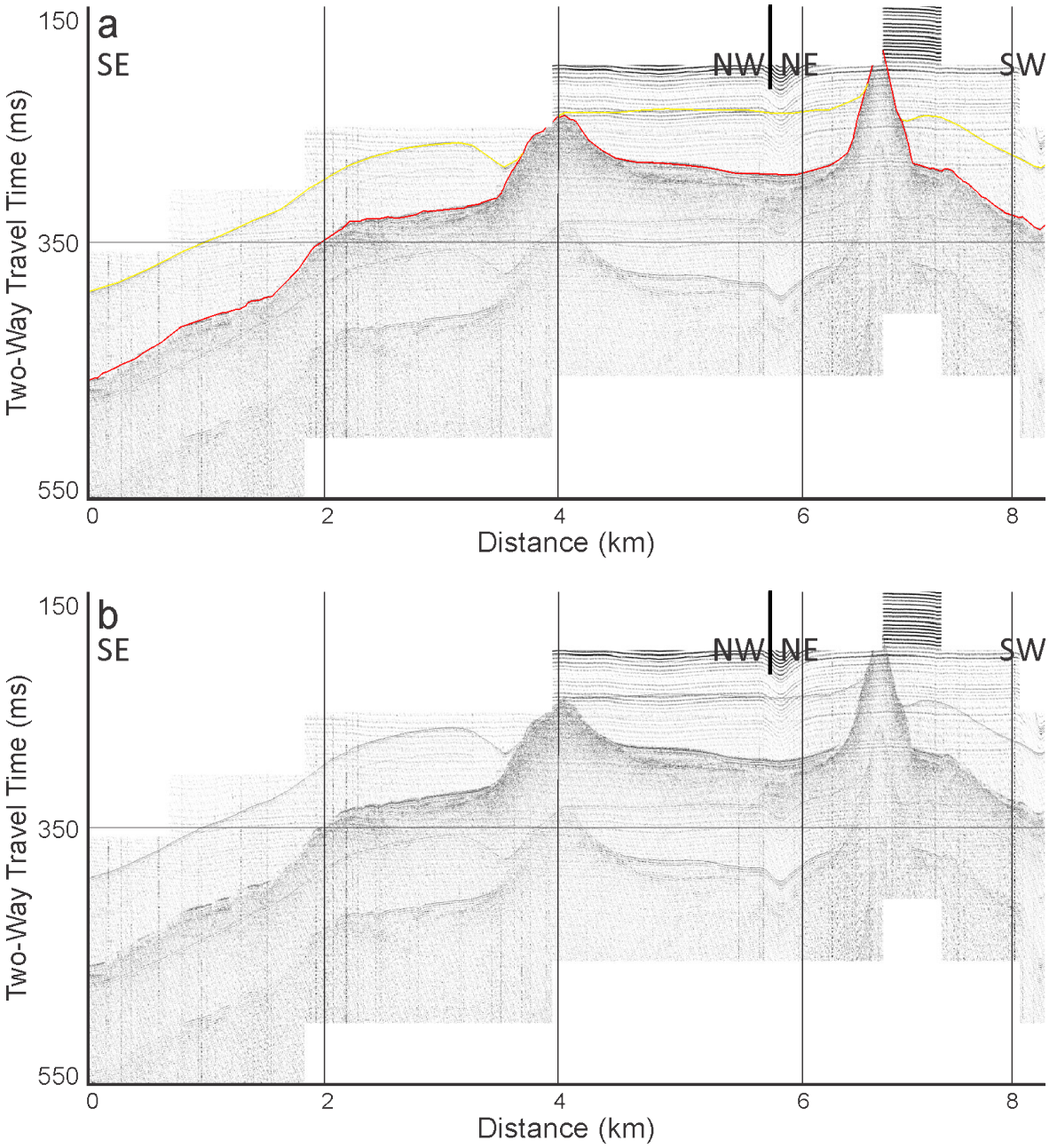


Figure A.2.79: Line DTS022 (part 1), cruise 2009009PGC. Thick lines at the top of the profile indicate locations of line turns.

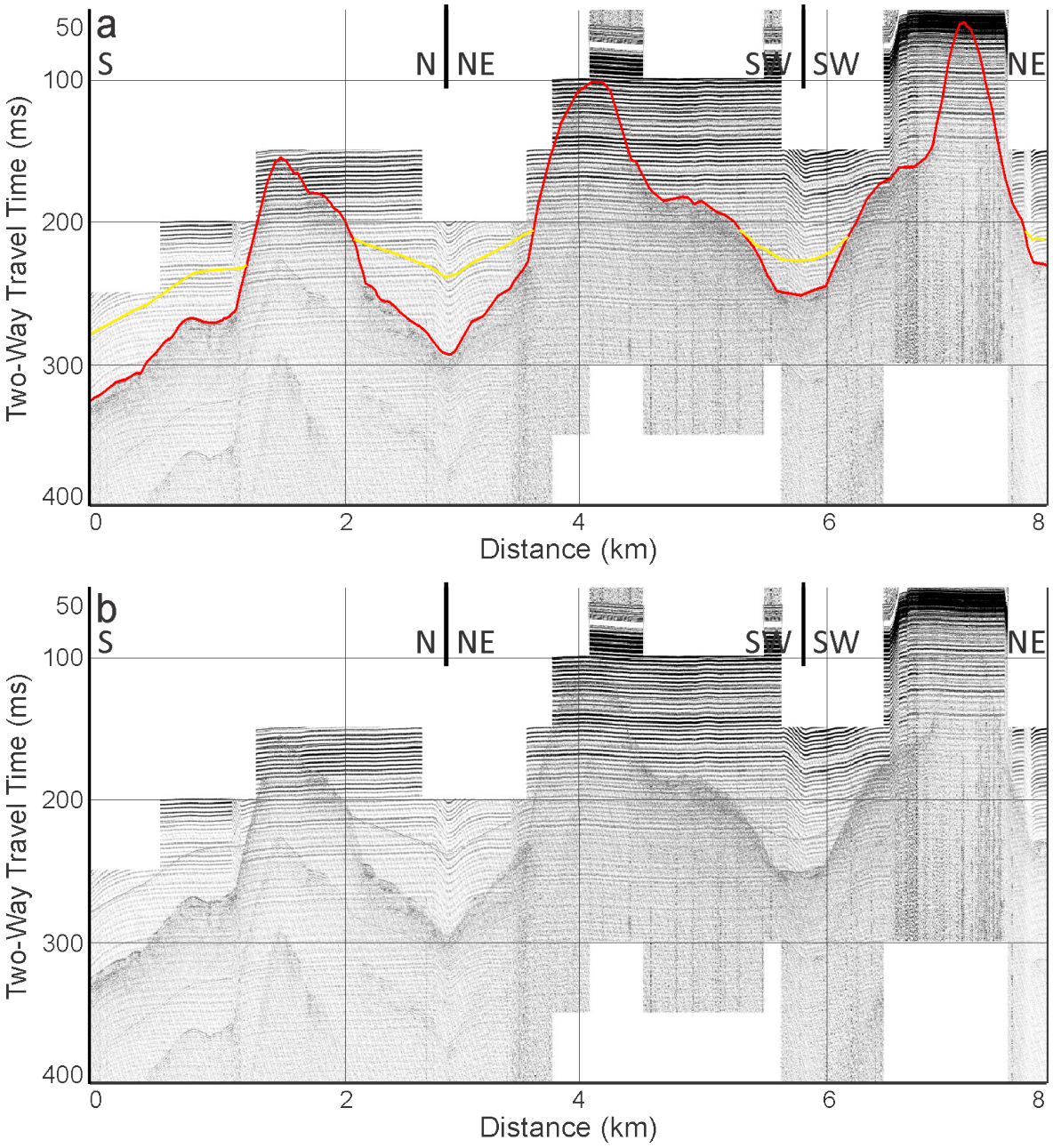


Figure A.2.80: Line DTS022 (part 2) and DTS023 (part 1), cruise 2009009PGC. Thick lines at the top of the profile indicate locations of line turns.

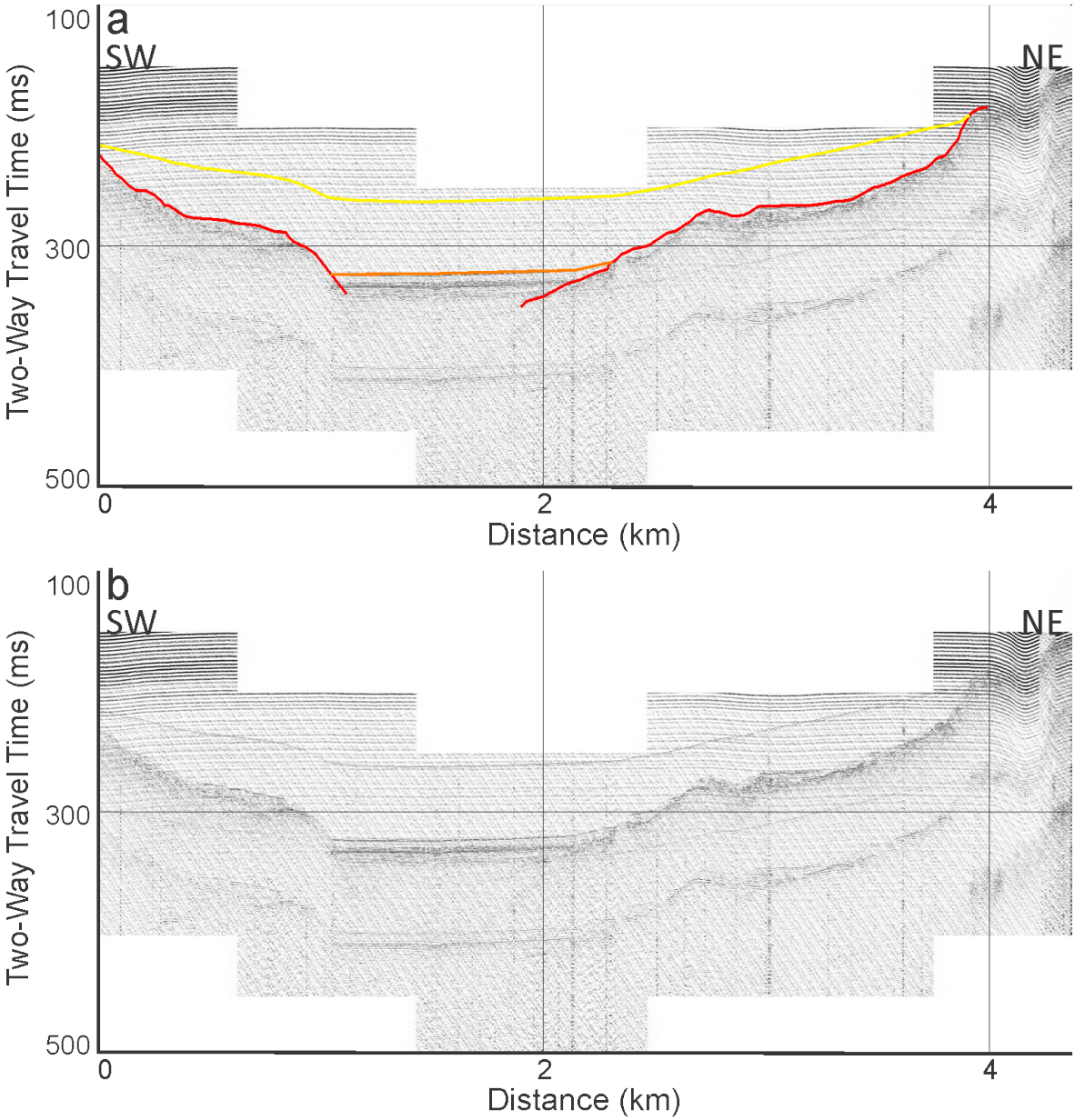


Figure A.2.81: DTS023 (part 2), cruise 2009009PGC.

A.2.10 Cruise ID 2013003PGC

Instrument data from cruise 2013003PGC includes 3.5 kHz sub-bottom profiles. A total of twenty lines were collected: one profile (Line 7-1) runs parallel to the main pockmark chain, while nineteen profiles were collected perpendicular to it. As the perpendicular profiles are largely similar in character, showing faintly stratified upper post-glacial units upslope, increased acoustic turbidity near the slope base, and seafloor pockmarks, only two representative examples are shown here alongside Line 7-1.

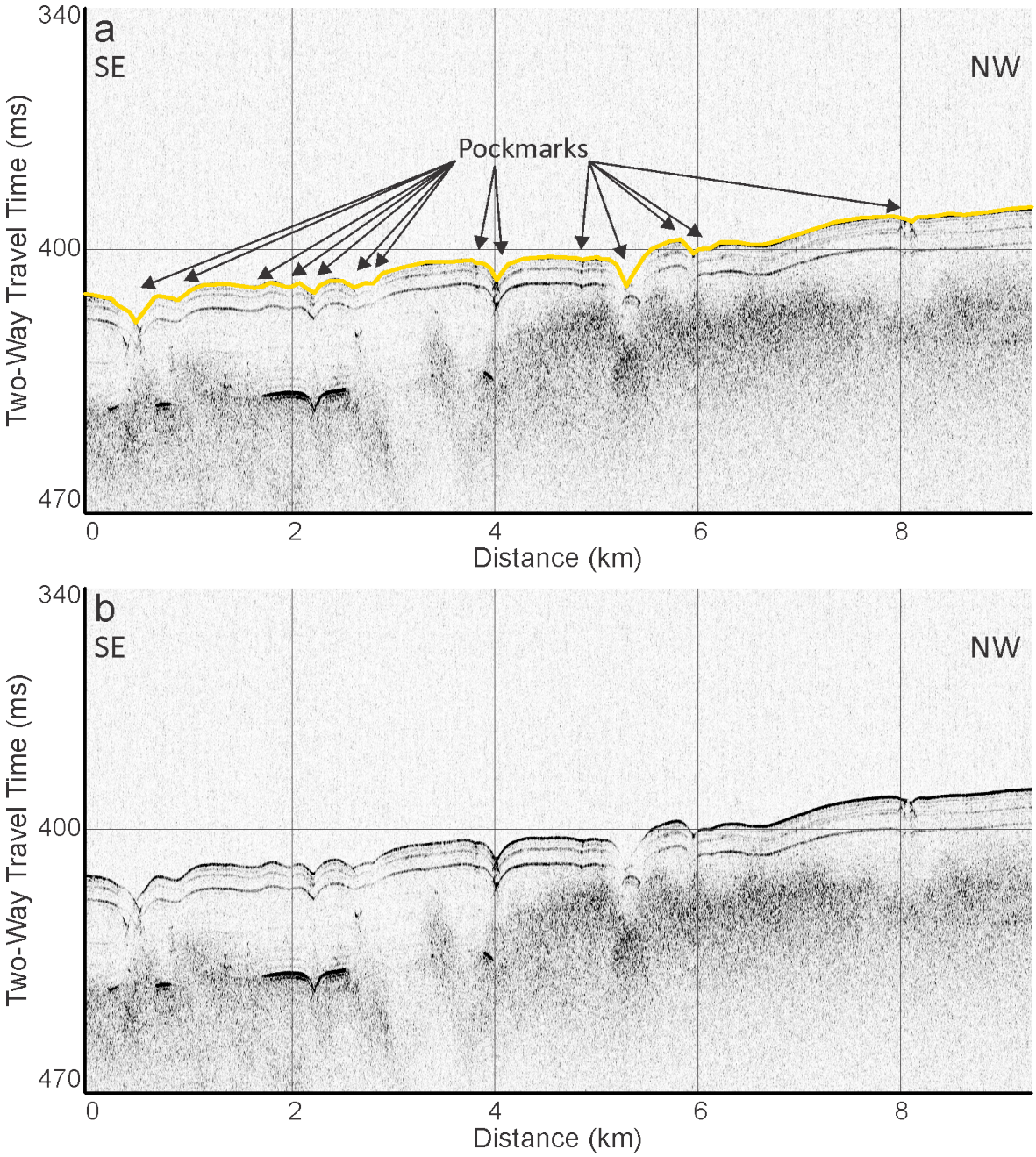


Figure A.2.82: Line 7-1, cruise 2013003PGC

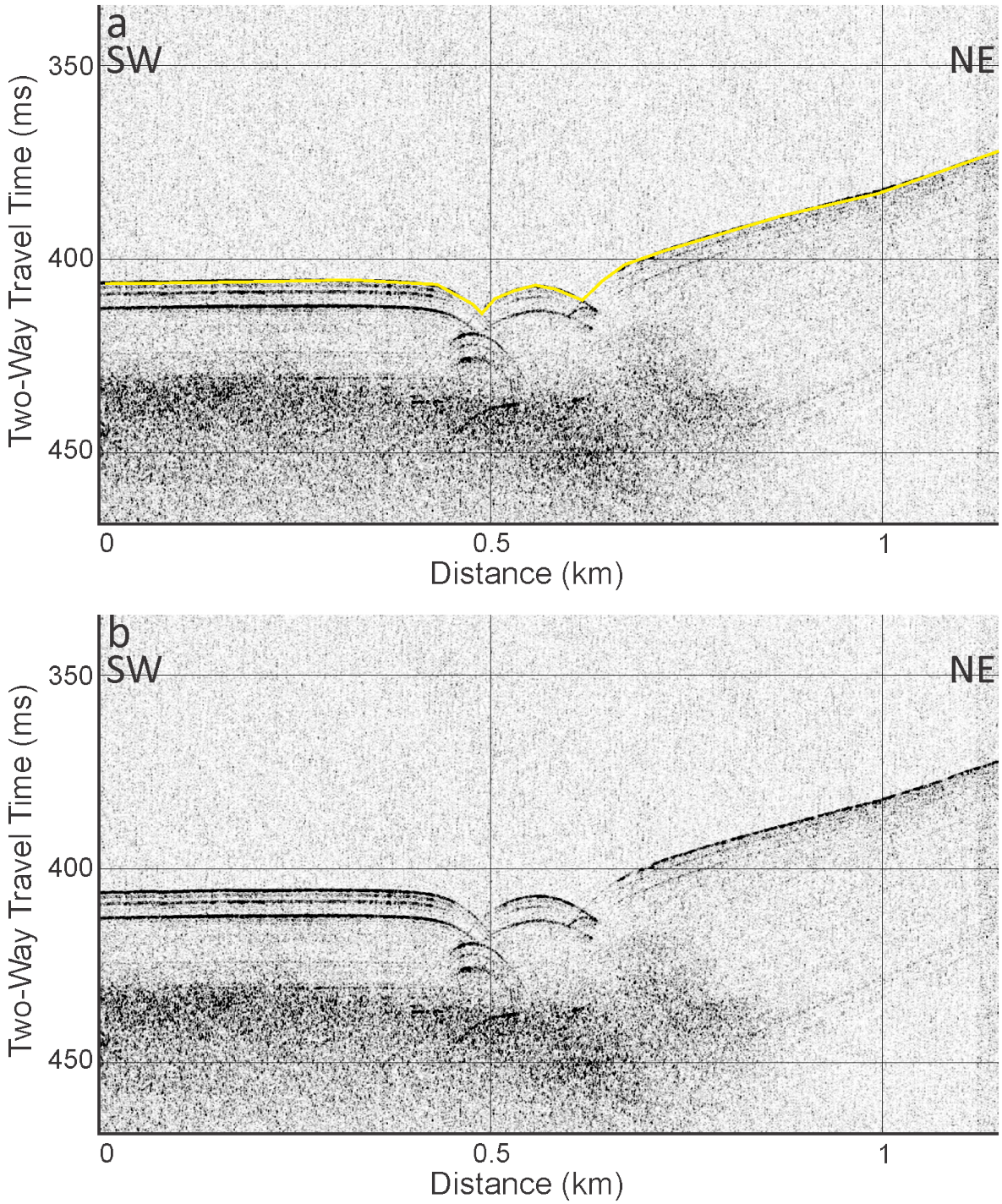


Figure A.2.83: Line WP7-8, cruise 2013003PGC

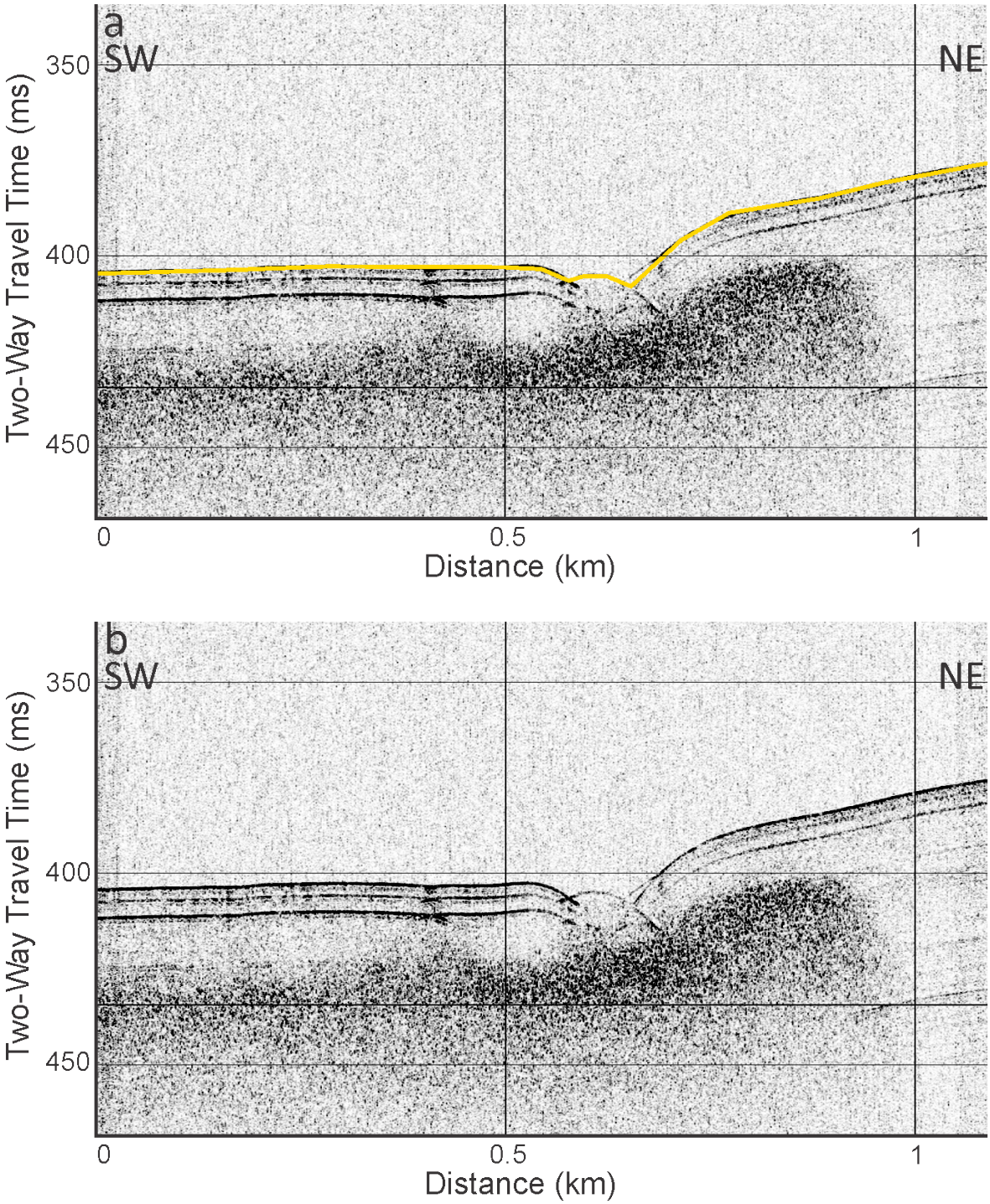


Figure A.2.84: Line WP27-28, cruise 2013003PGC

A.2.11 Cruise ID 2023004PGC

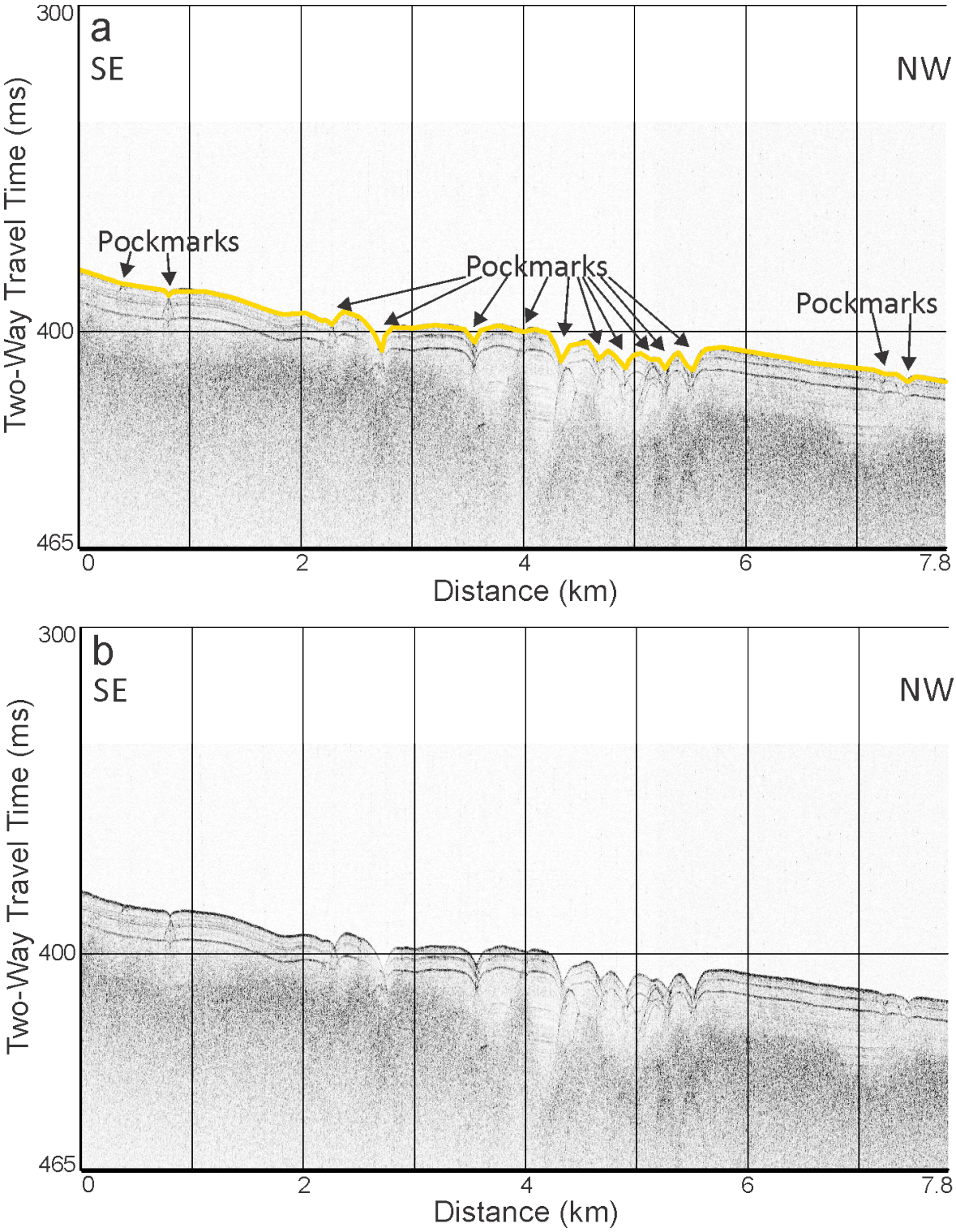


Figure A.2.85: Line 19, cruise 2023004PGC

A.2.12 Cruise ID 2024006PGC (Iona Spit Sub-bottom Dataset)

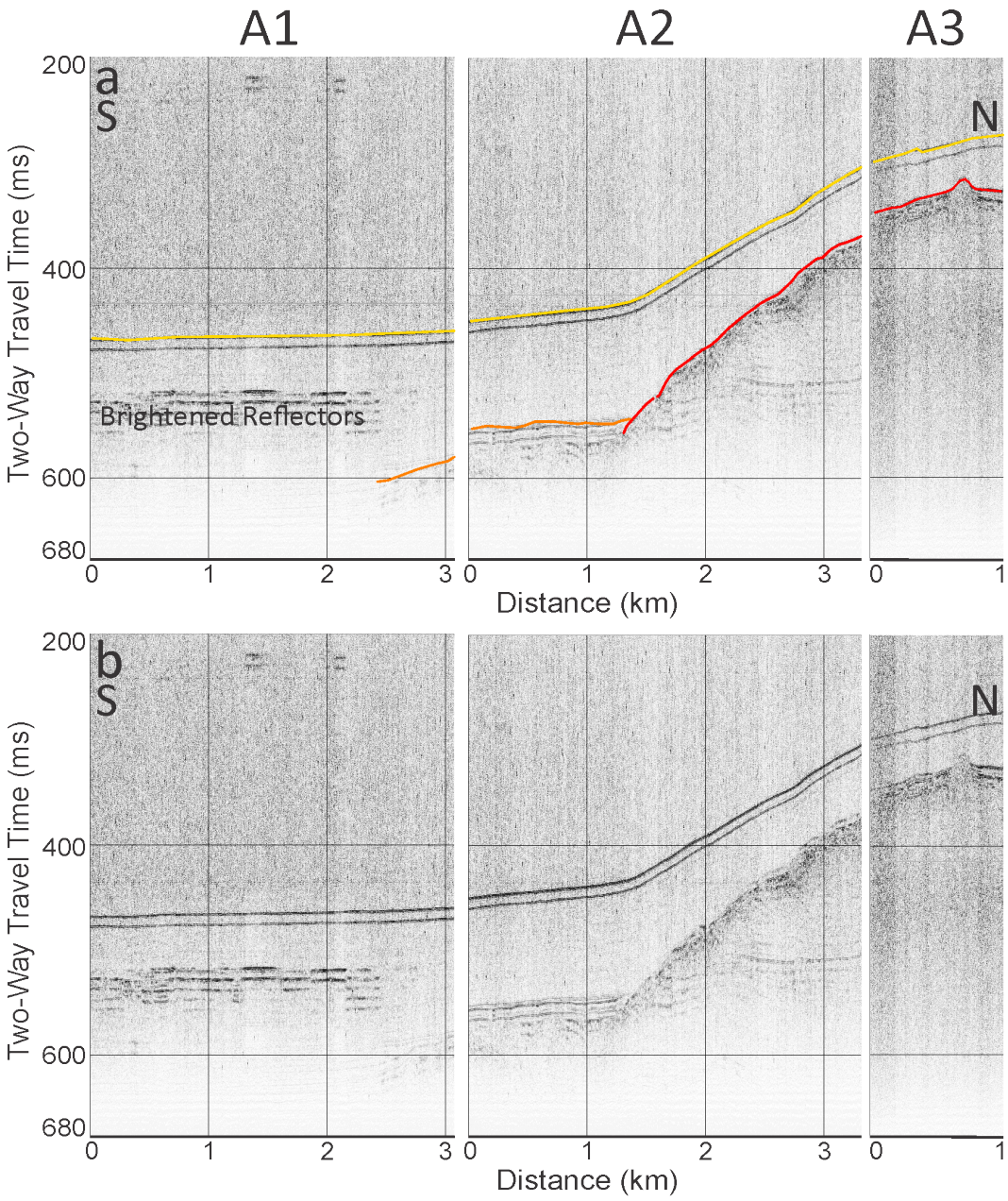


Figure A.2.86: Lines A1, A2, and A3, cruise 2024006PGC

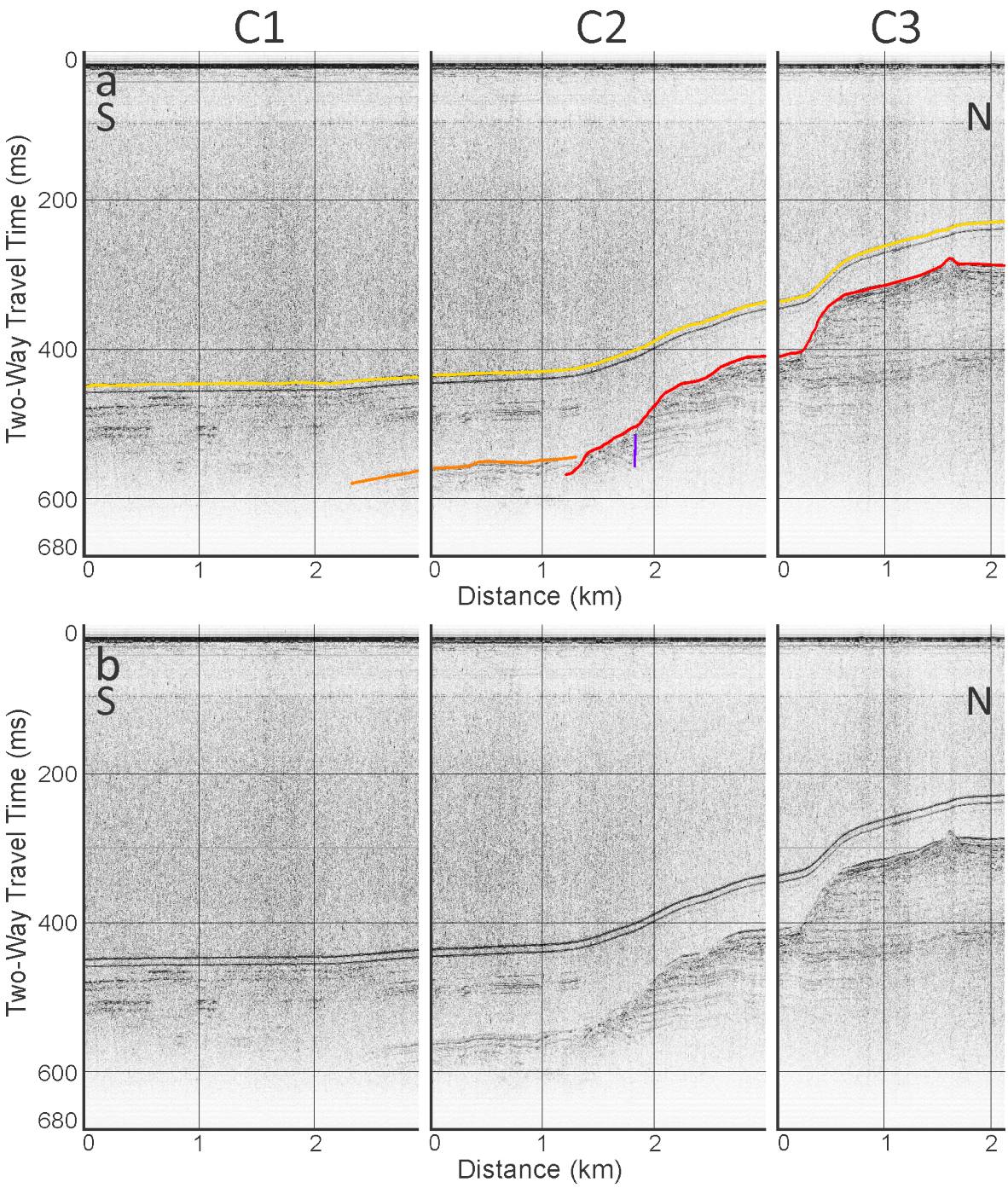


Figure A.2.87: Lines C1, C2, and C3, cruise 2024006PGC

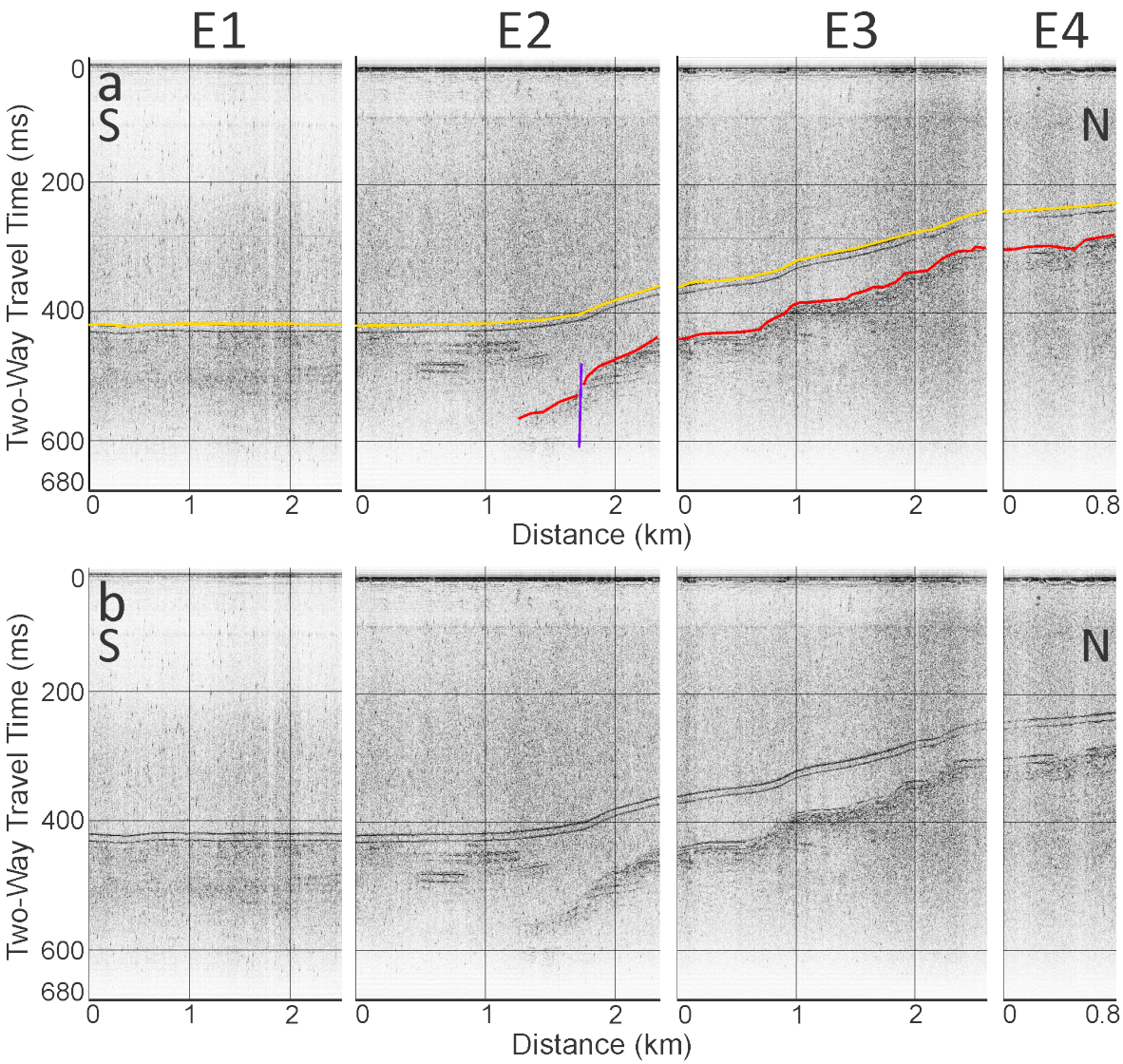


Figure A.2.88: Lines E1, E2, E3, and E4, cruise 2024006PGC

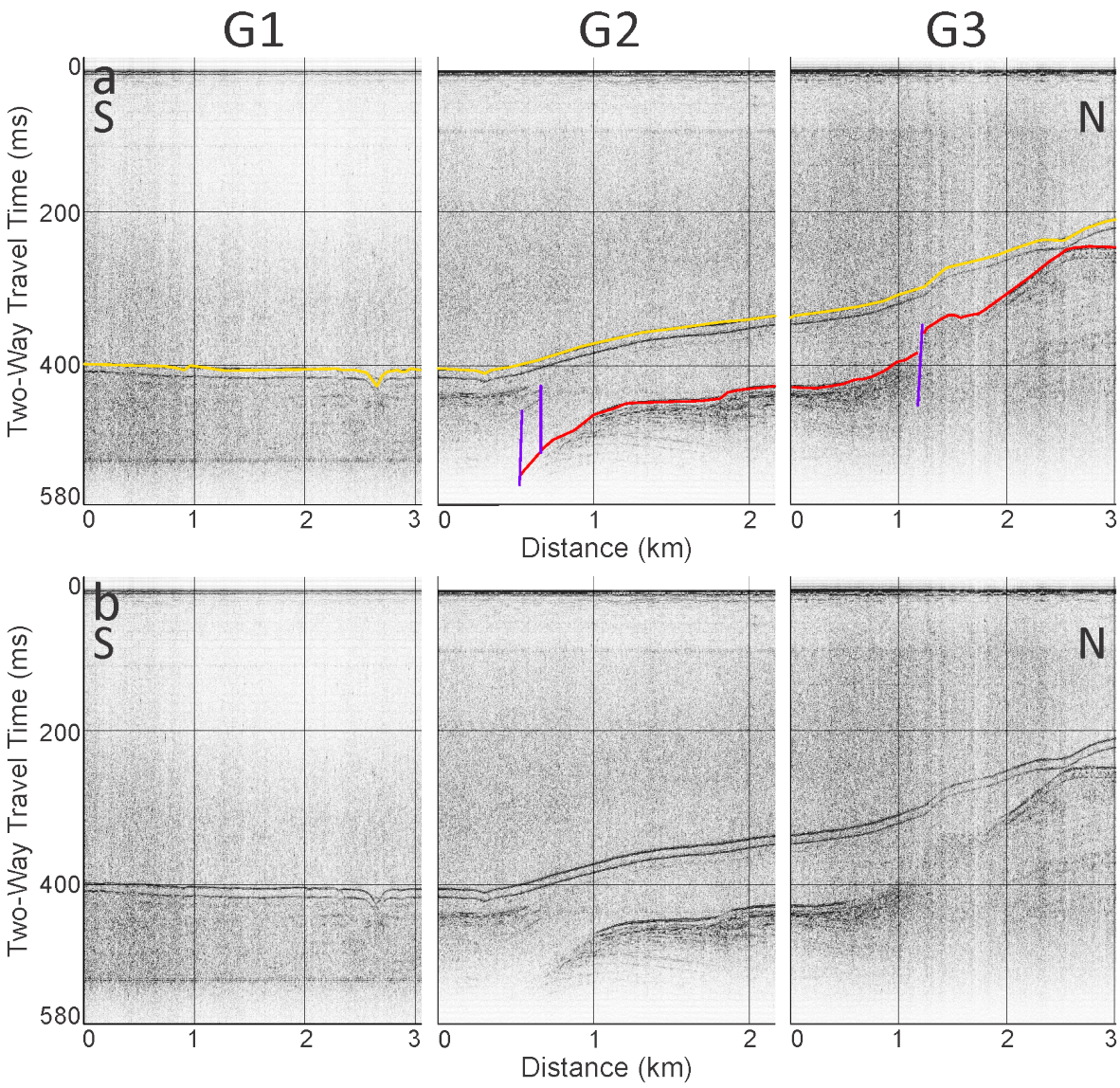


Figure A.2.89: Lines G1, G2, and G3, cruise 2024006PGC

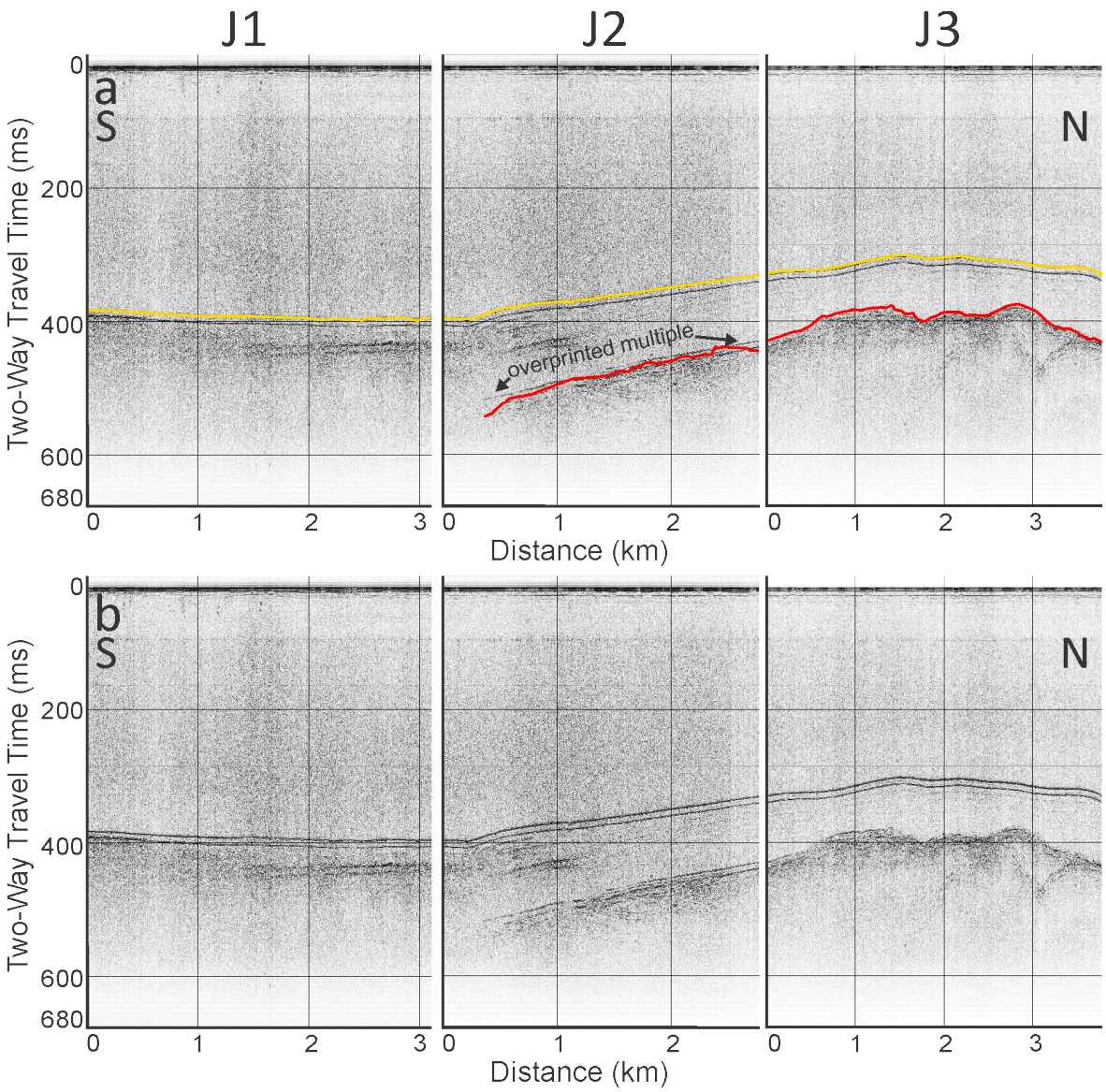


Figure A.2.90: Lines J1, J2, and J3, cruise 2024006PGC

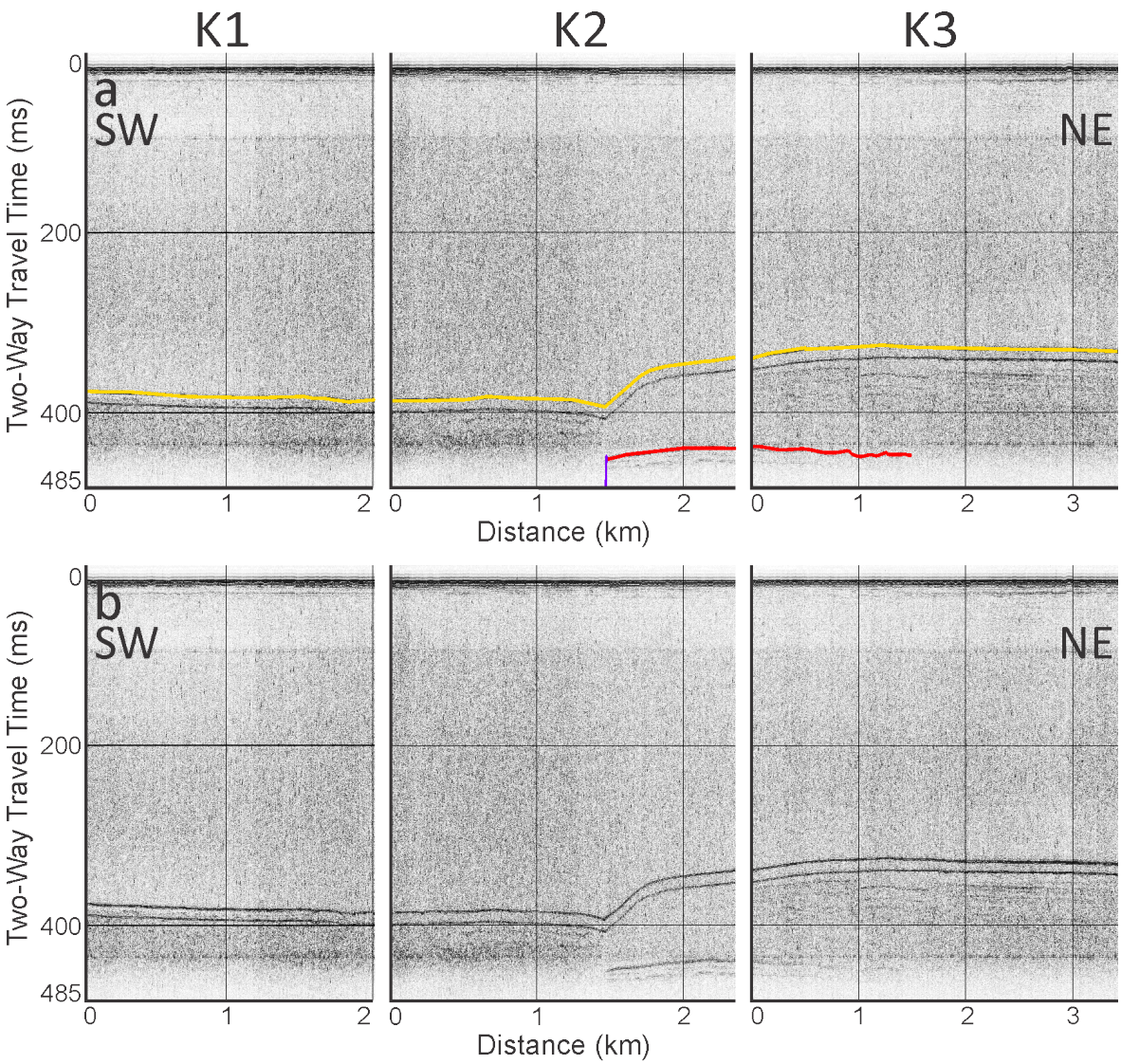


Figure A.2.91: Lines K1, K2, and K3, cruise 2024006PGC

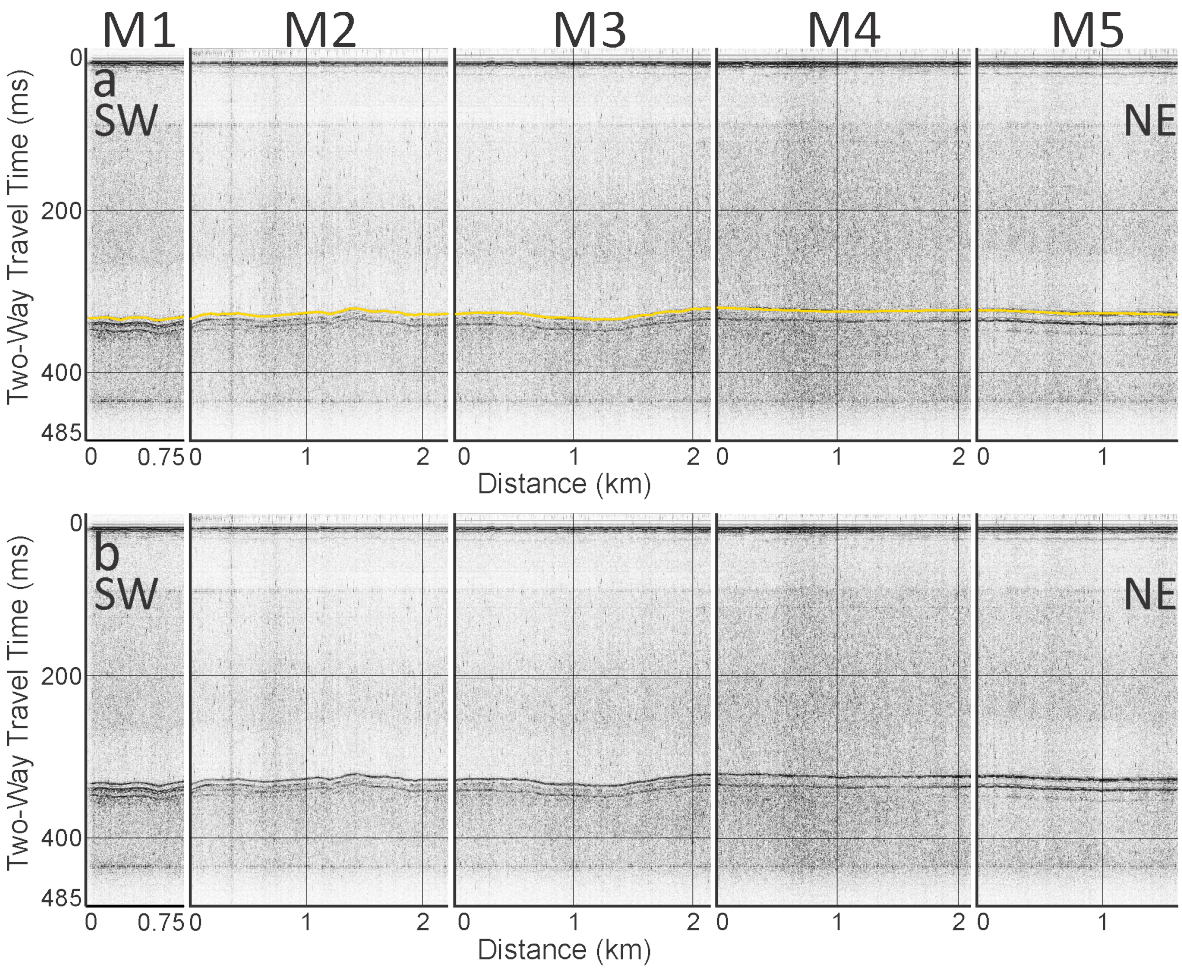


Figure A.2.92: Lines M1, M2, M3, M4, and M5, cruise 2024006PGC

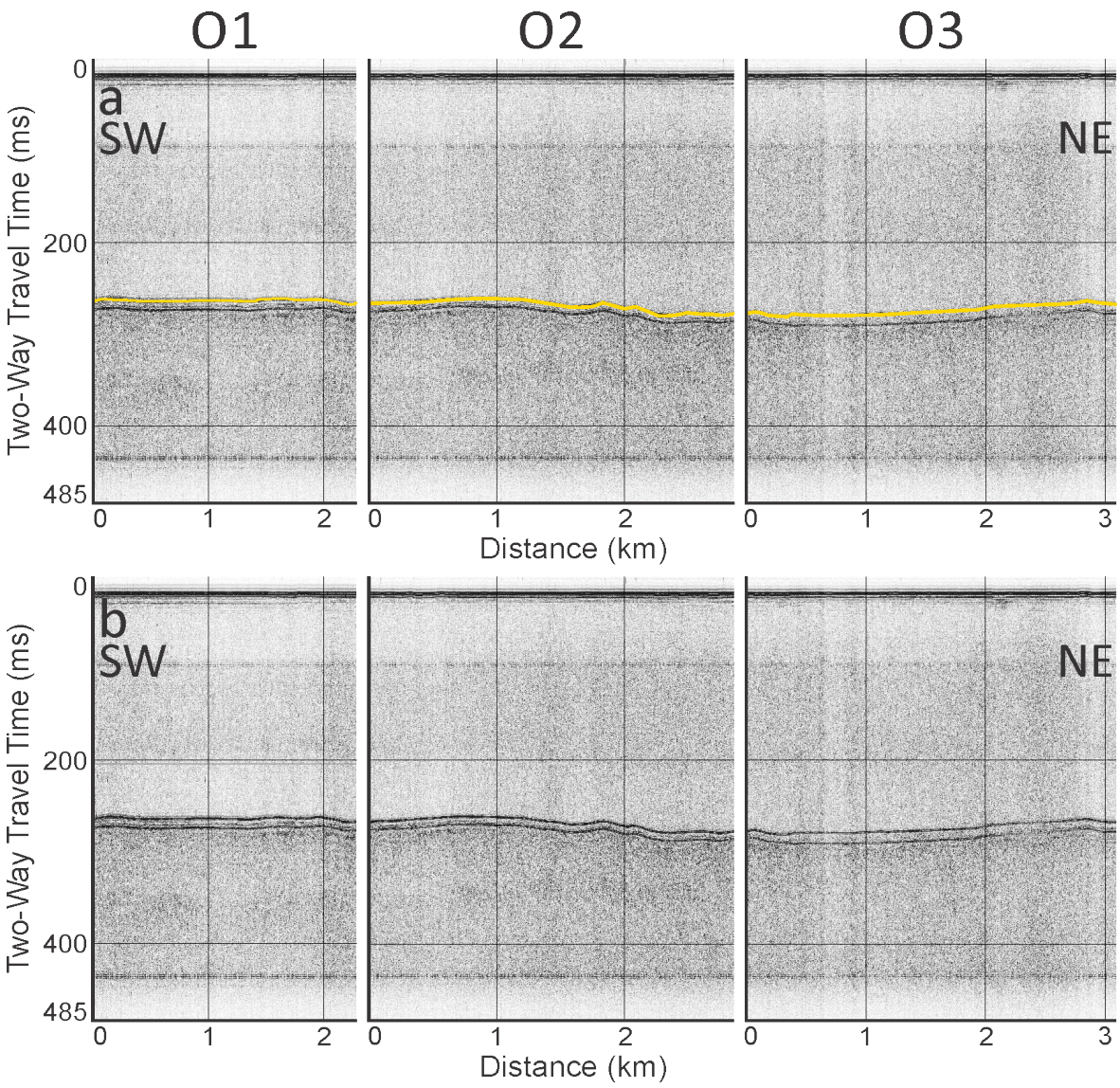


Figure A.2.93: Lines O1, O2, and O3, cruise 2024006PGC

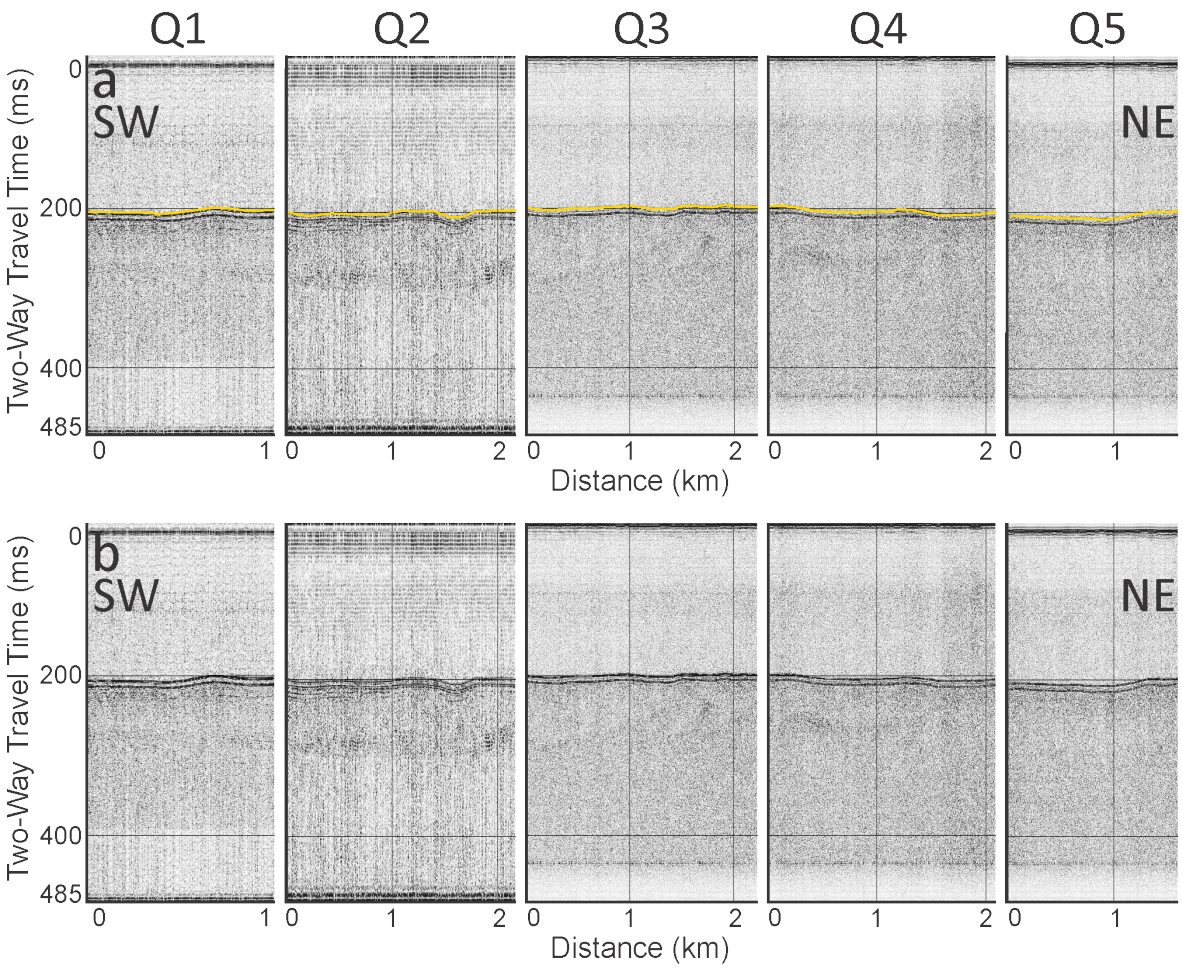


Figure A.2.94: Lines Q1, Q2, Q3, Q4, and Q5, cruise 2024006PGC

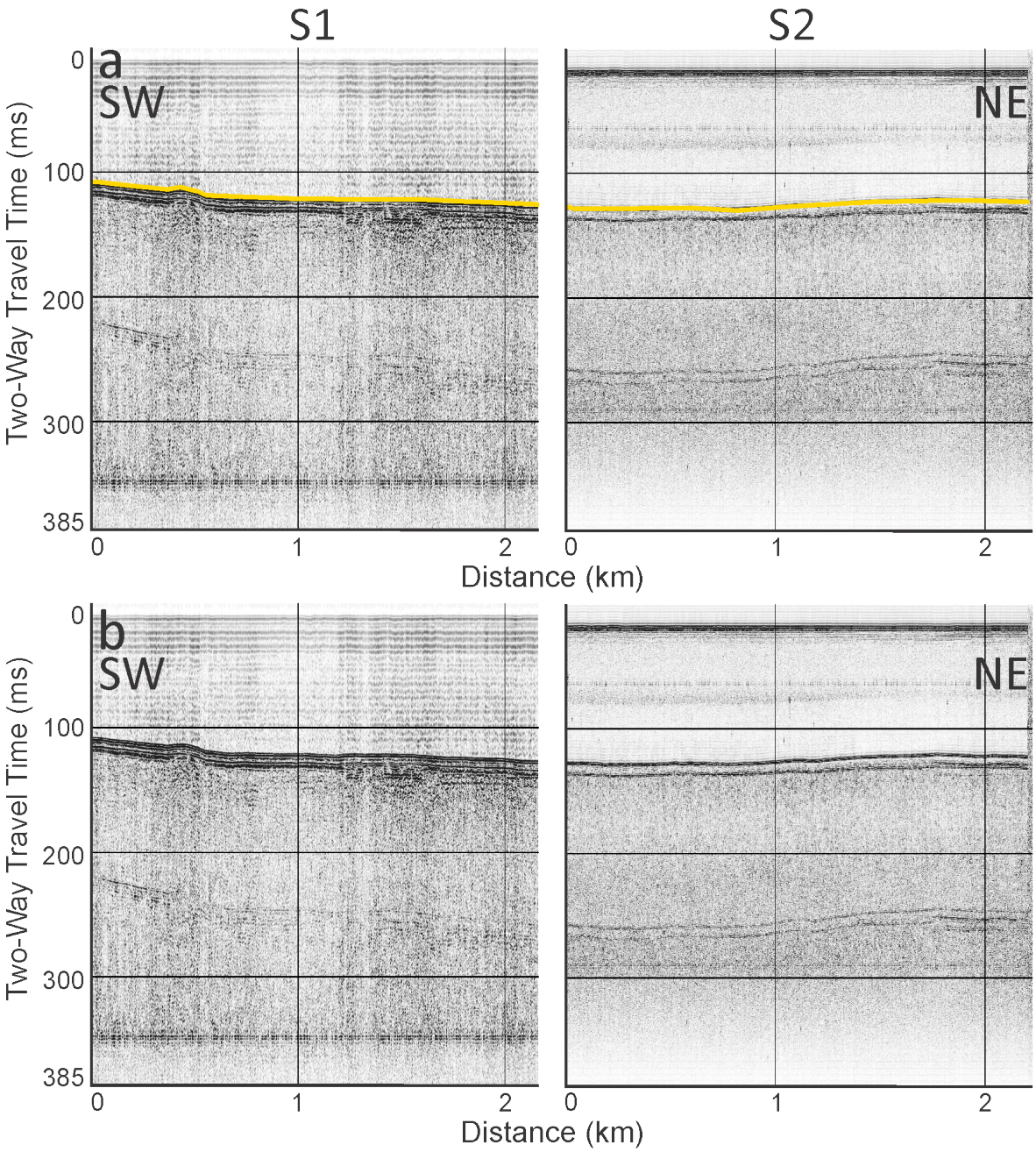


Figure A.2.95: Lines S1 and S2, cruise 2024006PGC

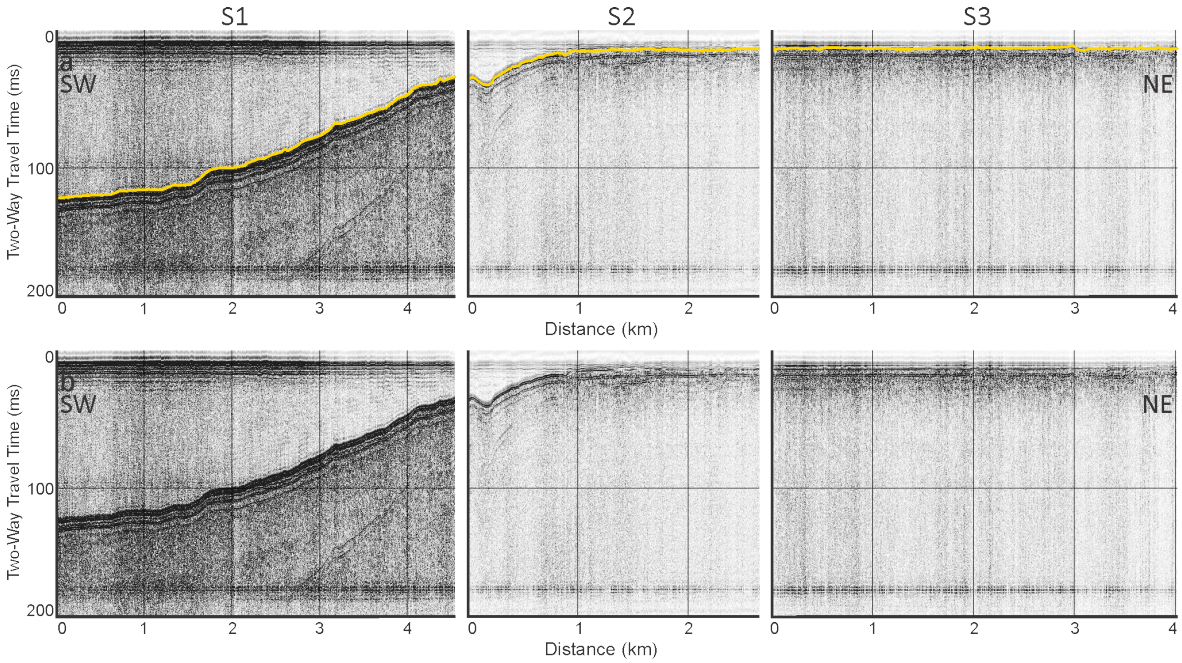


Figure A.2.96: Lines S3, S4, and S5

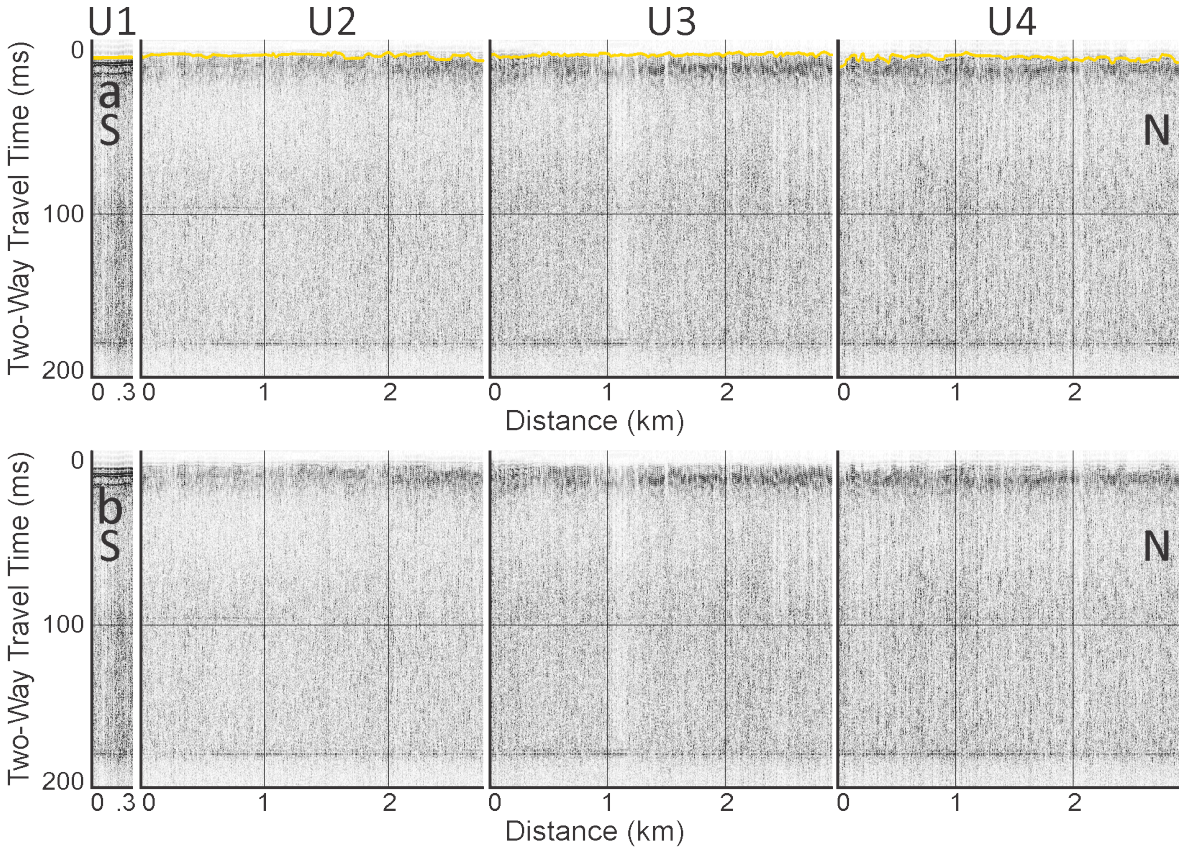


Figure A.2.97: Lines U1, U2, U3, and U4, cruise 2024006PGC

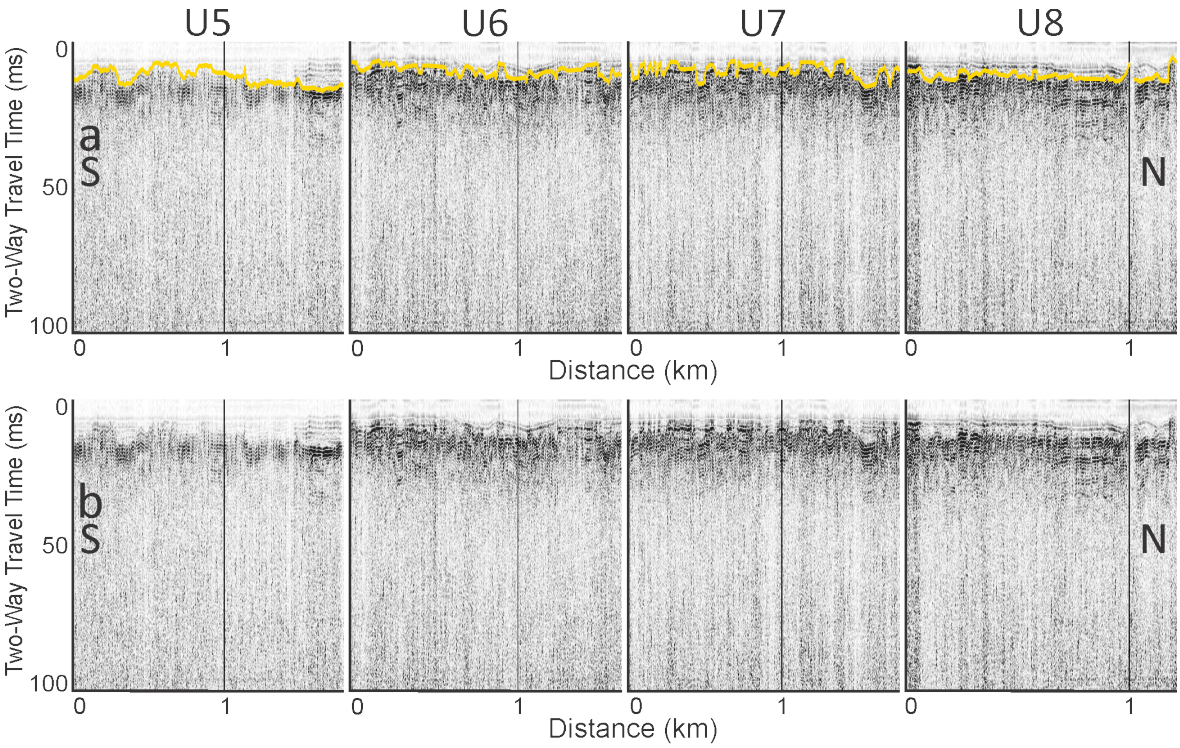


Figure A.2.98: Lines U4, U5, U6, and U7, cruise 2024006PGC

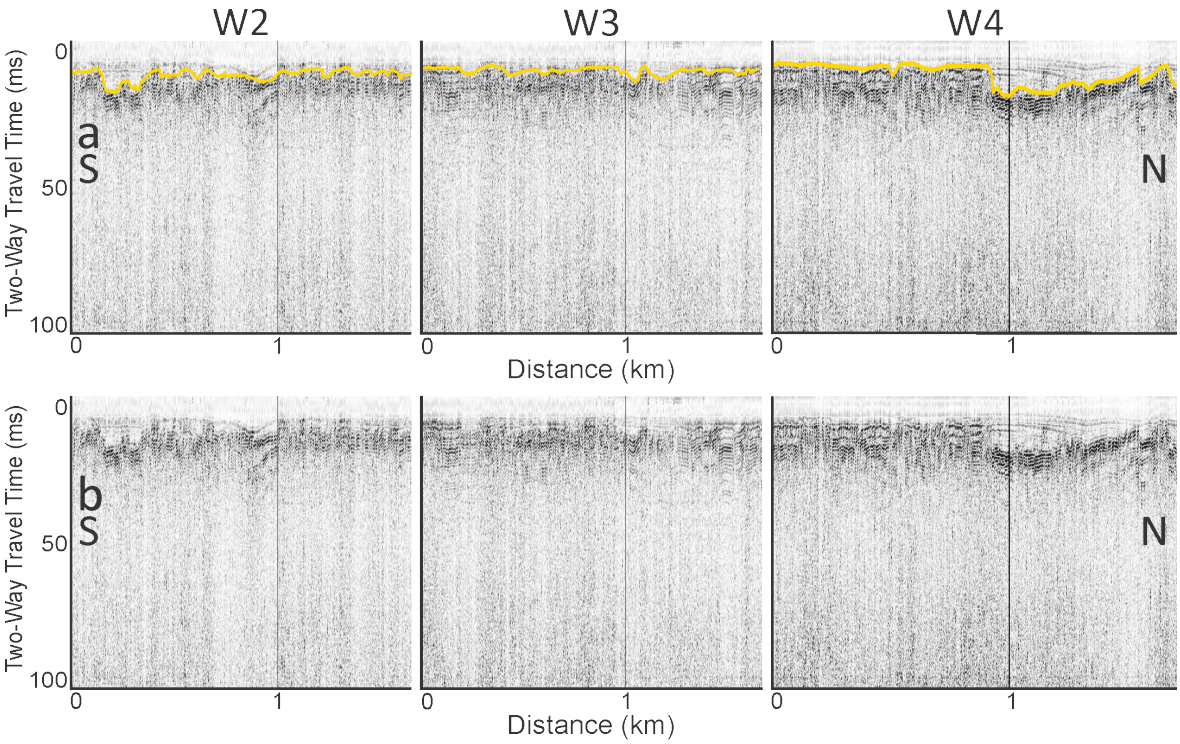


Figure A.2.99: Lines W2, W3, and W4, cruise 2024006PGC. Line W1 is excluded due to its short length.

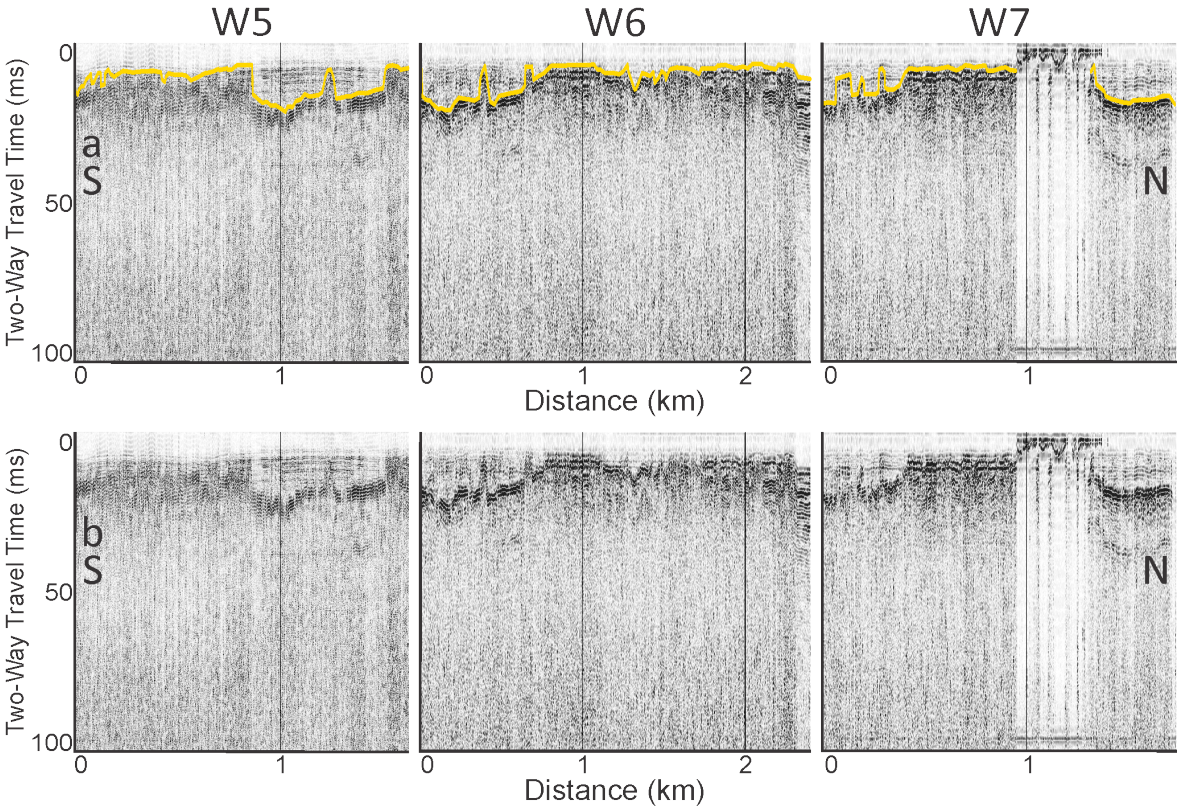


Figure A.2.100: Lines W5, W6, and W7, cruise 2024006PGC

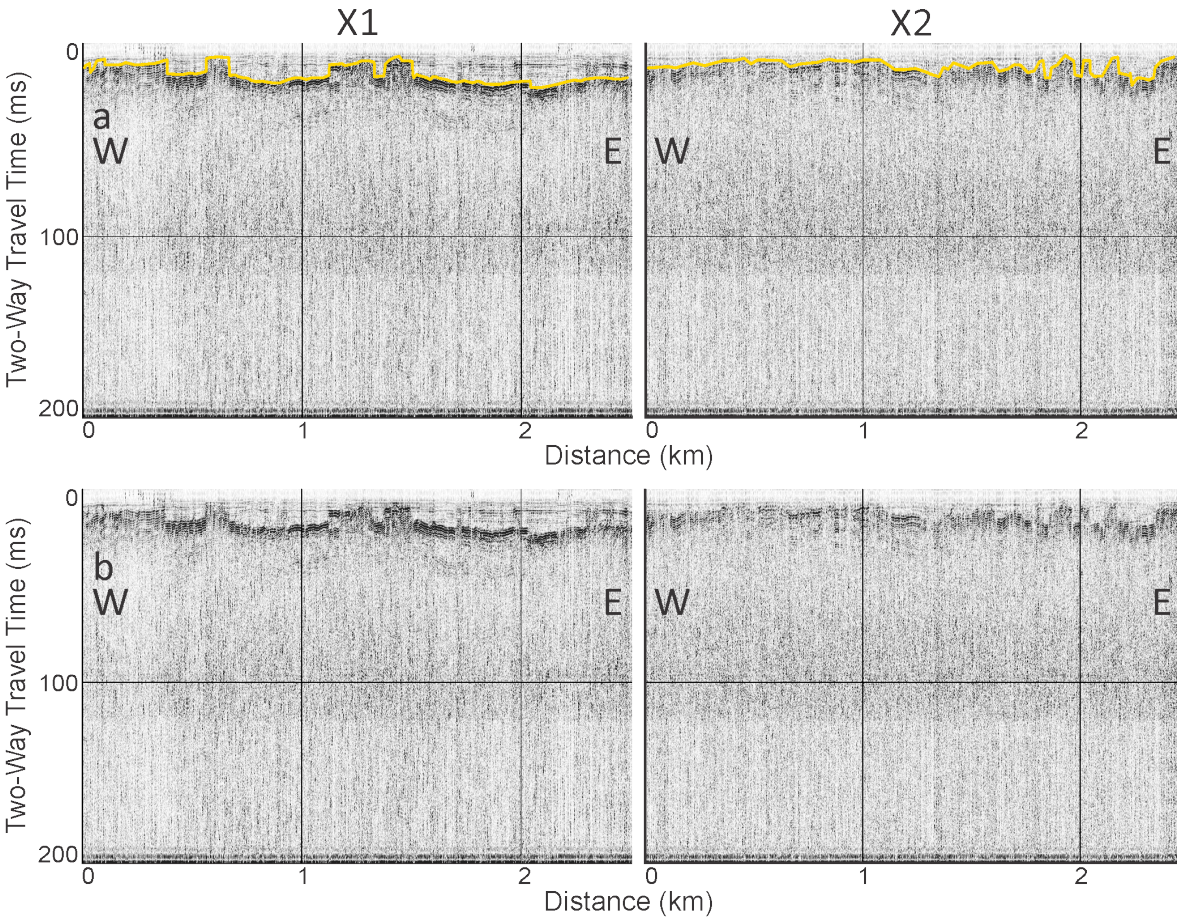


Figure A.2.101: Transit lines from U4 to W7 (X1) and U6 to W5 (X2), cruise 2024006PGC

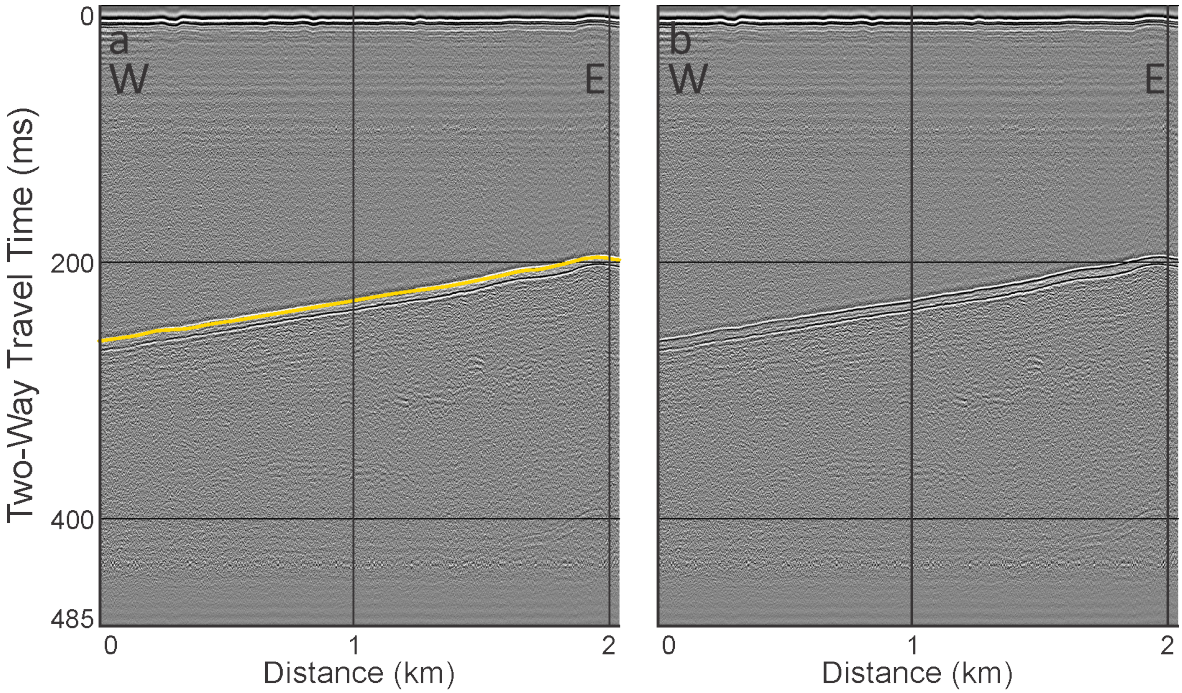


Figure A.2.102: Transit line (X3) from O3 to Q5, cruise 2024006PGC

Appendix B

Input Files for Seismic Hazard and Risk Models

B.1 Input Files for M 6.3 Strike-Slip Scenario

Rupture Inputs

```
<nrml xmlns:gml="http://www.opengis.net/gml" xmlns="http://
    openquake.org/xmlns/nrml/0.4">
<simpleFaultRupture>
<magnitude>6.3</magnitude>
<rake>180</rake>
<hypocenter lat="49.2401653" lon="-123.4517525" depth="11"/>
<simpleFaultGeometry>
<gml:LineString>
<gml:posList> -123.3576244 49.2058535 -123.3977278 49.2252749
    -123.4230478 49.2308135 -123.4517525 49.2401653
    -123.4707705 49.2485433 -123.5052376 49.2566442 </
    gml:posList>
</gml:LineString>
<dip> 75.0 </dip>
<upperSeismoDepth> 0.0 </upperSeismoDepth>
<lowerSeismoDepth> 17.0 </lowerSeismoDepth>
</simpleFaultGeometry>
</simpleFaultRupture>
</nrml>
```

Hazard Initialization

```
[general]
```

```
description = Scenario for a magnitude 6.3 strike-slip shallow
    crustal earthquake along the Central Salish Sea fault as
    outlined in thesis (Podhorodeski, 2025)
calculation_mode = scenario
random_seed = 113

[site_params]
site_model_file = ../../openquake-inputs/earthquake/sites/
    regions/site-vgrid_BC.csv

[Rupture information]
rupture_model_file = ../ruptures/
    rupture_ACM6p3_CentralSalishSeaFaultSS.xml
rupture_mesh_spacing = 4

[Calculation parameters]
gsim_logic_tree_file = ../../CanadaSHM6/OpenQuake_model_files/
    gmms/LogicTree/OQ_classes_NGASa0p3weights_activecrust.xml
truncation_level = 0
maximum_distance = 400
number_of_ground_motion_fields = 1
intensity_measure_types = PGA, SA(0.1), SA(0.2), SA(0.3), SA
    (0.5), SA(0.6), SA(1.0), SA(2.0)
```

Damage Initialization

```
[general]
description = Scenario for a magnitude 6.3 shallow strike-slip
    crustal earthquake along the Central Salish Sea fault as
    outlined in thesis (Podhorodeski, 2025)
calculation_mode = scenario_damage
random_seed = 113

[Exposure model]
exposure_file = ../../openquake-inputs/exposure/general-
    building-stock/oqBldgExp_BC.xml
```

```
[site_params]
site_model_file = ../../openquake-inputs/earthquake/sites/
    regions/site-vgrid_BC.csv

[Rupture information]
rupture_model_file = ../ruptures/
    rupture_ACM6p3_CentralSalishSeaFaultSS.xml
rupture_mesh_spacing = 4

[Calculation parameters]
gsim_logic_tree_file = ../../CanadaSHM6/OpenQuake_model_files/
    gmms/LogicTree/OQ_classes_NGASa0p3weights_activecrust.xml
truncation_level = 3.0
maximum_distance = 400
number_of_ground_motion_fields = 400

[fragility]
taxonomy_mapping_csv = ../../openquake-inputs/earthquake/
    vulnerability/CanSRM1_TaxMap_b0.csv
structural_fragility_file = ../../openquake-inputs/earthquake/
    vulnerability/structural_fragility_CAN.xml

[risk_calculation]
master_seed = 42
time_event = day
```

Risk Initialization

```
[general]
description = Scenario for a magnitude 6.3 shallow strike-slip
    crustal earthquake along the Central Salish Sea fault as
    outlined in thesis (Podhorodeski, 2025)
calculation_mode = scenario_risk
random_seed = 113

[Exposure model]
exposure_file = ../../openquake-inputs/exposure/general-
```

```
    building-stock/oqBldgExp_BC.xml

[site_params]
site_model_file = ../../openquake-inputs/earthquake/sites/
    regions/site-vgrid_BC.csv

[Rupture information]
rupture_model_file = ../ruptures/
    rupture_ACM6p3_CentralSalishSeaFaultSS.xml
rupture_mesh_spacing = 4

[Calculation parameters]
gsim_logic_tree_file = ../../CanadaSHM6/OpenQuake_model_files/
    gmms/LogicTree/OQ_classes_NGASa0p3weights_activecrust.xml
truncation_level = 3.0
maximum_distance = 400
number_of_ground_motion_fields = 400

[Vulnerability]
taxonomy_mapping_csv = ../../openquake-inputs/earthquake/
    vulnerability/CanSRM1_TaxMap_b0.csv
structural_vulnerability_file = ../../openquake-inputs/
    earthquake/vulnerability/vulnerability_structural_CAN.xml
nonstructural_vulnerability_file = ../../openquake-inputs/
    earthquake/vulnerability/vulnerability_nonstructural_CAN.
    xml
contents_vulnerability_file = ../../openquake-inputs/
    earthquake/vulnerability/vulnerability_contents_CAN.xml
```

B.2 Input Files for M 6.3 Oblique/Reverse Scenario

Rupture

```
<nrml xmlns:gml="http://www.opengis.net/gml" xmlns="http://
    openquake.org/xmlns/nrml/0.4">
```

```
<simpleFaultRupture>
<magnitude>6.3</magnitude>
<rake>135</rake>
<hypocenter lat="49.2401653" lon="-123.4517525" depth="11"/>
<simpleFaultGeometry>
<gml:LineString>
<gml:posList> -123.3576244 49.2058535 -123.3977278 49.2252749
    -123.4230478 49.2308135 -123.4517525 49.2401653
    -123.4707705 49.2485433 -123.5052376 49.2566442 </
    gml:posList>
</gml:LineString>
<dip> 75.0 </dip>
<upperSeismoDepth> 0.0 </upperSeismoDepth>
<lowerSeismoDepth> 17.0 </lowerSeismoDepth>
</simpleFaultGeometry>
</simpleFaultRupture>
</nrml>
```

Hazard Initialization

```
description = Scenario for a magnitude 6.3 oblique or reverse
    shallow crustal earthquake along the Central Salish Sea
    fault as outlined in thesis (Podhorodeski, 2025)
calculation_mode = scenario
random_seed = 113

[site_params]
site_model_file = ../../openquake-inputs/earthquake/sites/
    regions/site-vgrid_BC.csv

[Rupture information]
rupture_model_file = ../ruptures/
    rupture_ACM6p3_CentralSalishSeaFaultObl.xml
rupture_mesh_spacing = 4

[Calculation parameters]
```

```
gsim_logic_tree_file = ../../CanadaSHM6/OpenQuake_model_files/
    gmms/LogicTree/OQ_classes_NGASa0p3weights_activecrust.xml
truncation_level = 0
maximum_distance = 400
number_of_ground_motion_fields = 1
intensity_measure_types = PGA, SA(0.1), SA(0.2), SA(0.3), SA
    (0.5), SA(0.6), SA(1.0), SA(2.0)
```

Damage Initialization

```
[general]
description = Scenario for a magnitude 6.3 shallow oblique or
    reverse crustal earthquake along the Central Salish Sea
    fault as outlined in thesis (Podhorodeski, 2025)
calculation_mode = scenario_damage
random_seed = 113

[Exposure model]
exposure_file = ../../openquake-inputs/exposure/general-
    building-stock/oqBldgExp_BC.xml

[site_params]
site_model_file = ../../openquake-inputs/earthquake/sites/
    regions/site-vgrid_BC.csv

[Rupture information]
rupture_model_file = ../ruptures/
    rupture_ACM6p3_CentralSalishSeaFaultObl.xml
rupture_mesh_spacing = 4

[Calculation parameters]
gsim_logic_tree_file = ../../CanadaSHM6/OpenQuake_model_files/
    gmms/LogicTree/OQ_classes_NGASa0p3weights_activecrust.xml
truncation_level = 3.0
maximum_distance = 400
number_of_ground_motion_fields = 400
```

```
[fragility]
taxonomy_mapping_csv = ../../openquake-inputs/earthquake/
    vulnerability/CanSRM1_TaxMap_b0.csv
structural_fragility_file = ../../openquake-inputs/earthquake/
    vulnerability/structural_fragility_CAN.xml

[risk_calculation]
master_seed = 42
time_event = day
```

Risk Initialization

```
[general]
description = Scenario for a magnitude 6.3 shallow oblique or
    reverse crustal earthquake along the Central Salish Sea
    fault as outlined in thesis (Podhorodeski, 2025)
calculation_mode = scenario_risk
random_seed = 113

[Exposure model]
exposure_file = ../../openquake-inputs/exposure/general-
    building-stock/oqBldgExp_BC.xml

[site_params]
site_model_file = ../../openquake-inputs/earthquake/sites/
    regions/site-vgrid_BC.csv

[Rupture information]
rupture_model_file = ../ruptures/
    rupture_ACM6p3_CentralSalishSeaFaultObl.xml
rupture_mesh_spacing = 4

[Calculation parameters]
gsim_logic_tree_file = ../../CanadaSHM6/OpenQuake_model_files/
    gmms/LogicTree/OQ_classes_NGASa0p3weights_activecrust.xml
truncation_level = 3.0
maximum_distance = 400
```

```
number_of_ground_motion_fields = 400

[Vulnerability]
taxonomy_mapping_csv = ../../openquake-inputs/earthquake/
    vulnerability/CanSRM1_TaxMap_b0.csv
structural_vulnerability_file = ../../openquake-inputs/
    earthquake/vulnerability/vulnerability_structural_CAN.xml
nonstructural_vulnerability_file = ../../openquake-inputs/
    earthquake/vulnerability/vulnerability_nonstructural_CAN.
    xml
contents_vulnerability_file = ../../openquake-inputs/
    earthquake/vulnerability/vulnerability_contents_CAN.xml
```

B.3 Input Files for M 6.7 Strike-Slip Scenario

Rupture

```
<nrml xmlns:gml="http://www.opengis.net/gml" xmlns="http://
    openquake.org/xmlns/nrml/0.4">
<simpleFaultRupture>
<magnitude>6.7</magnitude>
<rake>180</rake>
<hypocenter lat="49.2401653" lon="-123.4517525" depth="11"/>
<simpleFaultGeometry>
<gml:LineString>
<gml:posList> -123.3576244 49.2058535 -123.3977278 49.2252749
    -123.4230478 49.2308135 -123.4517525 49.2401653
    -123.4707705 49.2485433 -123.5052376 49.2566442
    -123.5837041 49.2883218 -123.6528609 49.3200387 </
    gml:posList>
</gml:LineString>
<dip> 75.0 </dip>
<upperSeismoDepth> 0.0 </upperSeismoDepth>
<lowerSeismoDepth> 17.0 </lowerSeismoDepth>
</simpleFaultGeometry>
```

```
</simpleFaultRupture>
</nrml>
```

Hazard Initialization

```
[general]
description = Scenario for a magnitude 6.7 strike-slip shallow
    crustal earthquake along the Central Salish Sea fault as
   outlined in thesis (Podhorodeski, 2025)
calculation_mode = scenario
random_seed = 113

[site_params]
site_model_file = ../../openquake-inputs/earthquake/sites/
   regions/site-vgrid_BC.csv

[Rupture information]
rupture_model_file = ../ruptures/
   rupture_ACM6p7_CentralSalishSeaFaultSS.xml
rupture_mesh_spacing = 4

[Calculation parameters]
gsim_logic_tree_file = ../../CanadaSHM6/OpenQuake_model_files/
   gmms/LogicTree/OQ_classes_NGASa0p3weights_activecrust.xml
truncation_level = 0
maximum_distance = 400
number_of_ground_motion_fields = 1
intensity_measure_types = PGA, SA(0.1), SA(0.2), SA(0.3), SA
   (0.5), SA(0.6), SA(1.0), SA(2.0)
```

Damage Initialization

```
[general]
description = Scenario for a magnitude 6.7 shallow strike-slip
    crustal earthquake along the Central Salish Sea fault as
   outlined in thesis (Podhorodeski, 2025)
calculation_mode = scenario_damage
random_seed = 113
```

```
[Exposure model]
exposure_file = ../../openquake-inputs/exposure/general-
    building-stock/oqBldgExp_BC.xml

[site_params]
site_model_file = ../../openquake-inputs/earthquake/sites/
    regions/site-vgrid_BC.csv

[Rupture information]
rupture_model_file = ../ruptures/
    rupture_ACM6p7_CentralSalishSeaFaultSS.xml
rupture_mesh_spacing = 4

[Calculation parameters]
gsim_logic_tree_file = ../../CanadaSHM6/OpenQuake_model_files/
    gmms/LogicTree/OQ_classes_NGASa0p3weights_activecrust.xml
truncation_level = 3.0
maximum_distance = 400
number_of_ground_motion_fields = 400

[fragility]
taxonomy_mapping_csv = ../../openquake-inputs/earthquake/
    vulnerability/CanSRM1_TaxMap_b0.csv
structural_fragility_file = ../../openquake-inputs/earthquake/
    vulnerability/structural_fragility_CAN.xml

[risk_calculation]
master_seed = 42
time_event = day
```

Risk Initialization

```
[general]
description = Scenario for a magnitude 6.7 shallow strike-slip
     crustal earthquake along the Central Salish Sea fault as
    outlined in thesis (Podhorodeski, 2025)
```

```
calculation_mode = scenario_risk
random_seed = 113

[Exposure model]
exposure_file = ../../openquake-inputs/exposure/general-
    building-stock/oqBldgExp_BC.xml

[site_params]
site_model_file = ../../openquake-inputs/earthquake/sites/
    regions/site-vgrid_BC.csv

[Rupture information]
rupture_model_file = ../ruptures/
    rupture_ACM6p7_CentralSalishSeaFaultSS.xml
rupture_mesh_spacing = 4

[Calculation parameters]
gsim_logic_tree_file = ../../CanadaSHM6/OpenQuake_model_files/
    gmms/LogicTree/OQ_classes_NGASa0p3weights_activecrust.xml
truncation_level = 3.0
maximum_distance = 400
number_of_ground_motion_fields = 400

[Vulnerability]
taxonomy_mapping_csv = ../../openquake-inputs/earthquake/
    vulnerability/CanSRM1_TaxMap_b0.csv
structural_vulnerability_file = ../../openquake-inputs/
    earthquake/vulnerability/vulnerability_structural_CAN.xml
nonstructural_vulnerability_file = ../../openquake-inputs/
    earthquake/vulnerability/vulnerability_nonstructural_CAN.
    xml
contents_vulnerability_file = ../../openquake-inputs/
    earthquake/vulnerability/vulnerability_contents_CAN.xml
```

B.4 Input Files for M 6.7 Oblique/Reverse Scenario

Rupture

```
<nrml xmlns:gml="http://www.opengis.net/gml" xmlns="http://
    openquake.org/xmlns/nrml/0.4">
<simpleFaultRupture>
<magnitude>6.7</magnitude>
<rake>135</rake>
<hypocenter lat="49.2401653" lon="-123.4517525" depth="11"/>
<simpleFaultGeometry>
<gml:LineString>
<gml:posList> -123.3576244 49.2058535 -123.3977278 49.2252749
    -123.4230478 49.2308135 -123.4517525 49.2401653
    -123.4707705 49.2485433 -123.5052376 49.2566442
    -123.5837041 49.2883218 -123.6528609 49.3200387 </
    gml:posList>
</gml:LineString>
<dip> 75.0 </dip>
<upperSeismoDepth> 0.0 </upperSeismoDepth>
<lowerSeismoDepth> 17.0 </lowerSeismoDepth>
</simpleFaultGeometry>
</simpleFaultRupture>
</nrml>
```

Hazard Initialization

```
[general]
description = Scenario for a magnitude 6.7 oblique or reverse
    shallow crustal earthquake along the Central Salish Sea
    fault as outlined in thesis (Podhorodeski, 2025)
calculation_mode = scenario
random_seed = 113

[site_params]
site_model_file = ../../openquake-inputs/earthquake/sites/
    regions/site-vgrid_BC.csv
```

```
[Rupture information]
rupture_model_file = ../ruptures/
    rupture_ACM6p7_CentralSalishSeaFaultObl.xml
rupture_mesh_spacing = 4

[Calculation parameters]
gsim_logic_tree_file = ../../CanadaSHM6/OpenQuake_model_files/
    gmms/LogicTree/OQ_classes_NGASa0p3weights_activecrust.xml
truncation_level = 0
maximum_distance = 400
number_of_ground_motion_fields = 1
intensity_measure_types = PGA, SA(0.1), SA(0.2), SA(0.3), SA
    (0.5), SA(0.6), SA(1.0), SA(2.0)
```

Damage Initialization

```
[general]
description = Scenario for a magnitude 6.7 shallow oblique or
    reverse crustal earthquake along the Central Salish Sea
    fault as outlined in thesis (Podhorodeski, 2025)
calculation_mode = scenario_damage
random_seed = 113

[Exposure model]
exposure_file = ../../openquake-inputs/exposure/general-
    building-stock/oqBldgExp_BC.xml

[site_params]
site_model_file = ../../openquake-inputs/earthquake/sites/
    regions/site-vgrid_BC.csv

[Rupture information]
rupture_model_file = ../ruptures/
    rupture_ACM6p7_CentralSalishSeaFaultObl.xml
rupture_mesh_spacing = 4
```

```
[Calculation parameters]
gsim_logic_tree_file = ../../CanadaSHM6/OpenQuake_model_files/
    gmms/LogicTree/OQ_classes_NGASa0p3weights_activecrust.xml
truncation_level = 3.0
maximum_distance = 400
number_of_ground_motion_fields = 400

[fragility]
taxonomy_mapping_csv = ../../openquake-inputs/earthquake/
    vulnerability/CanSRM1_TaxMap_b0.csv
structural_fragility_file = ../../openquake-inputs/earthquake/
    vulnerability/structural_fragility_CAN.xml

[risk_calculation]
master_seed = 42
time_event = day
```

Risk Initialization

```
[general]
description = Scenario for a magnitude 6.7 shallow oblique or
    reverse crustal earthquake along the Central Salish Sea
    fault as outlined in thesis (Podhorodeski, 2025)
calculation_mode = scenario_risk
random_seed = 113

[Exposure model]
exposure_file = ../../openquake-inputs/exposure/general-
    building-stock/oqBldgExp_BC.xml

[site_params]
site_model_file = ../../openquake-inputs/earthquake/sites/
    regions/site-vgrid_BC.csv

[Rupture information]
rupture_model_file = ../ruptures/
    rupture_ACM6p7_CentralSalishSeaFaultObl.xml
```

```
rupture_mesh_spacing = 4

[Calculation parameters]
gsim_logic_tree_file = ../../CanadaSHM6/OpenQuake_model_files/
    gmms/LogicTree/OQ_classes_NGASa0p3weights_activecrust.xml
truncation_level = 3.0
maximum_distance = 400
number_of_ground_motion_fields = 400

[Vulnerability]
taxonomy_mapping_csv = ../../openquake-inputs/earthquake/
    vulnerability/CanSRM1_TaxMap_b0.csv
structural_vulnerability_file = ../../openquake-inputs/
    earthquake/vulnerability/vulnerability_structural_CAN.xml
nonstructural_vulnerability_file = ../../openquake-inputs/
    earthquake/vulnerability/vulnerability_nonstructural_CAN.
    xml
contents_vulnerability_file = ../../openquake-inputs/
    earthquake/vulnerability/vulnerability_contents_CAN.xml
```